Phase Field Modeling for Fracture with Applications to Homogeneous and Heterogeneous Materials

Mohammed Abdulrazzak Msekh

Weimar, 15. May 2017

Phase Field Modeling for Fracture with Applications to Homogeneous and Heterogeneous Materials

Phasenfeldmodellierung für Brüche mit Anwendungen auf homogene und heterogene Materialien

DISSERTATION
zur Erlangung des akademischen Grades
Doktor-Ingenieur (Dr.-Ing.)
an der Fakultät Bauingenieurwesen der Bauhaus–Universität Weimar

vorgelegt von
M.Sc. Mohammed Abdulrazzak Msekh
geboren am 02. November 1979 in Babylon, Irak
(interner Doktorand)

Mentor
Prof. Dr.-Ing. Timon Rabczuk

Weimar, 15 May 2017

Gutachter: **Prof. Dr.-Ing. Timon Rabczuk**
Institut für Strukturmechanik / Institute of Structural Mechanics.
Fakultät Bauingenieurwesen / Faculty of Civil Engineering.
Bauhaus-Universität Weimar.

Gutachter: **Prof. Dr.-Ing. Laura De Lorenzis**
Institut für Angewandte Mechanik / Institute of Applied Mechanics.
Department Bauingenieurwesen und Umweltwissenschaften / Department of Civil Engineering and Environmental Science.
Technische Universität Braunschweig.

Gutachter: **Prof. Dr. rer. nat. Tom Lahmer**
Institut für Strukturmechanik / Institute of Structural Mechanics.
Fakultät Bauingenieurwesen / Faculty of Civil Engineering.
Bauhaus-Universität Weimar.

Tag der Einreichung: 26.01.2016
Tag der Öffentlichen Disputation: 15.05.2017

To my whole family ...

Acknowledgements

First and foremost I offer my sincerest gratitude to my supervisor, Prof. Dr.-Ing. Timon Rabczuk, for his guidance and encouragement through my research work. His great interest as a supervisor is inspiring, and his wise suggestions regarding my thesis work were always very useful. It is a big honor to work under his supervision and motivation in research. Too, I would like to acknowledge Prof. Dr. Pedro Areias and Prof. Dr. Goangseup Zi for their support and collaboration during the joint work and discussions.

I am grateful for and would like to thank all my colleagues at Institute of Structural Mechanics for their help and friendly support.

I would also like to say a heartfelt thank you to my mother, brother and sisters for always believing in me, encouraging me to follow my dreams and for helping in whatever way they could during this challenging period. Beloved father, I am so happy to reach your dream for me. Thank you for the kind efforts, sufferance, and patience while you were sick and supported me to study. I pray for you daily to be in paradise and will never forget you. A precious thank you to my big family, friends, relatives and colleagues over the world for their emotional support and encouragement during my studies.

And finally to my lovely wife Dunya, my daughter Basmala, and my son Almostafa who have been by my side throughout this Ph.D., living every single challenge minute of it, and without whom, I would not have had the courage to embark on this journey, and who made it possible for me to complete what I started.

Weimar, Januar 2016 Mohammed Abdulrazzak Msekh

Abstract

The thesis presents an implementation including different applications of a variational-based approach for gradient type standard dissipative solids. Phase field model for brittle fracture is an application of the variational-based framework for gradient type solids. This model allows the prediction of different crack topologies and states. Of significant concern is the application of theoretical and numerical formulation of the phase field modeling into the commercial finite element software Abaqus in 2D and 3D. The fully coupled incremental variational formulation of phase field method is implemented by using the UEL and UMAT subroutines of Abaqus. The phase field method considerably reduces the implementation complexity of fracture problems as it removes the need for numerical tracking of discontinuities in the displacement field that are characteristic of discrete crack methods. This is accomplished by replacing the sharp discontinuities with a scalar damage phase field representing the diffuse crack topology wherein the amount of diffusion is controlled by a regularization parameter. The nonlinear coupled system consisting of the linear momentum equation and a diffusion type equation governing the phase field evolution is solved simultaneously via a Newton-Raphson approach. Post-processing of simulation results to be used as visualization module is performed via an additional UMAT subroutine implemented in the standard Abaqus viewer.

In the same context, we propose a simple yet effective algorithm to initiate and propagate cracks in 2D geometries which is independent of both particular constitutive laws and specific element technology and dimension. It consists of a localization limiter in the form of the screened Poisson equation with, optionally, local mesh refinement. A staggered scheme for standard equilibrium and screened Cauchy equations is used. The remeshing part of the algorithm consists of a sequence of mesh subdivision and element erosion steps. Element subdivision is based on edge split operations using a given constitutive quantity (either damage or void fraction). Mesh smoothing makes use of edge contraction as function of a given constitutive quantity such as the principal stress or void fraction. To assess the robustness and accuracy of this algorithm, we use both quasi-brittle benchmarks and ductile tests.

Furthermore, we introduce a computational approach regarding mechanical loading in microscale on an inelastically deforming composite material. The nanocomposites material of fully exfoliated clay/epoxy is shaped to predict macroscopic elastic and fracture related material parameters based on their fine–scale features. Two different configurations of polymer nanocomposites material (PNCs) have been studied. These configurations are fully bonded PNCs and PNCs with an interphase zone formation between the matrix and the clay reinforcement. The representative volume element of PNCs specimens with different clay weight contents, different aspect ratios, and different interphase zone thicknesses are generated by adopting Python scripting. Different constitutive models are employed for the matrix, the clay platelets, and the interphase zones. The brittle fracture behavior of the epoxy matrix and the interphase zones material are modeled using the phase field approach, whereas the stiff silicate clay platelets of the composite are designated as a linear elastic material. The comprehensive study investigates the elastic and fracture behavior of PNCs composites, in addition to predict Young's modulus, tensile strength, fracture toughness, surface energy dissipation, and cracks surface area in the composite for different material parameters, geometry, and interphase zones properties and thicknesses.

Contents

1 Introduction **1**

1.1 Introduction 1

1.2 Motivation and background 2

1.3 Objectives and overview 4

2 Literature Review **6**

2.1 Review of finite element analysis 6

2.2 Review of phase field model 6

2.3 Review of polymer nanocomposites material 11

2.3.1 Modeling of fully bonded PNCs 13

2.3.2 Modeling of PNCs with interphase zones 13

3 Phase Field Model for Quasi-Brittle Fracture **17**

3.1 Linear elastic fracture mechanics: Griffith's criterion 17

3.2 Phase field representation of crack surface 18

3.3 Governing equations and finite element model 21

3.3.1 Small strains formulation 21

3.3.2 Finite strains formulation 26

4 Abaqus Implementation of Phase Field Model in 2D and 3D **30**

4.1 Two dimensional numerical examples 32

4.1.1 Notched square plate 32

4.1.2 Three-points bending test 34

4.1.3 Notched beam with three openings 38

4.1.4 Tension test of a notched rectangular specimen with one opening . 40

4.1.5 Tension test of a notched rectangular specimen with three openings 42

4.2 Three dimensional numerical examples 45

4.2.1 Tension test of double notch specimen 46

4.2.2 Tension test of side notch specimen with different openings distribution . . . 48

5 Damage Algorithm Using the Screened Poisson Equation and Local Remeshing 52

5.1 Governing equations: constitutive integration in finite strains . . . 52

5.1.1 Integration algorithm: equilibrium and relative Green-Lagrange strain . . . 53

5.1.2 Local constitutive system . . . 57

5.1.3 Quasi-brittle model . . . 59

5.1.4 GTN model and its integration . . . 60

5.2 Arnold's MINI formulation for plasticity problems: use of relative strains 65

5.2.1 General formulation . . . 65

5.3 Regularization with the screened Poisson equation . . . 68

5.3.1 Relation with nonlocal models . . . 68

5.3.2 Weak form . . . 68

5.4 Local mesh refinement algorithm . . . 69

5.5 Numerical examples . . . 75

5.5.1 Effect of l, mesh and step size . . . 75

5.5.2 Comparison with classical phase field . . . 79

5.5.3 L-shaped panel . . . 81

5.5.4 Localization and assessment of l parameter . . . 83

5.5.5 Single edge notched beam . . . 87

5.5.6 Drilled panel . . . 90

6 Polymer Nanocomposites Properties and Modeling 95

6.1 Polymer layered silicates . . . 95

6.1.1 Montmorillonite . . . 97

6.2 Modeling of PNCs . . . 97

6.2.1 Generation of the representative volume element of PNCs . . . 98

6.2.1.1 Fully bonded PNCs . . . 98

6.2.1.2 PNCs with interphase zones . . . 101

7 Predictions of Young's Modulus, J Integral, Tensile Strength, and Surface Energy of Fully Bonded Clay/Epoxy Nanocomposites Material 103

7.1 Mechanical properties . . . 104

7.2 Predictions of fracture energy . . . 104

7.3 Numerical examples 106
7.3.1 Predictions of Young's modulus 106
7.3.2 Predictions of tensile strength and fracture toughness 113
7.3.2.1 Side notched specimen 113
7.3.2.2 Double notched specimen 117
7.3.2.3 Strain energy release rate 122
7.3.2.4 Size effect 124

8 Predictions of Young's Modulus, *J* Integral, Tensile Strength, and Surface Energy of Clay/Epoxy Nanocomposites Material with Interphase Zones 128
8.1 Mechanical properties 128
8.2 Numerical examples 130
8.2.1 Crack diffusion length (ℓ_0) of the phase field model 130
8.2.2 Predictions of Young's modulus 131
8.2.3 Predictions of tensile strength and fracture toughness 132
8.2.3.1 Surface energy dissipation of PNCs 138
8.3 Prediction of macroscopic fracture energy of PNCs 143

9 Conclusions 149
9.1 Summary of Achievements 149
9.2 Scope for future work 152

References 154

List of Figures

1.1 SEM micrographs of the fracture surface of the PNCs, a1-a2: crack initiation, b1-b2: fracture region, depicted from (1) with author's permission. 3

3.1 1D bar cut by a crack. 18
3.2 Crack phase field ϕ for different values of ℓ_0. 19
3.3 (a) Q4, 4-node quadrilateral element, (b) T3, 3-node quadrilateral element. 23
3.4 (a) C3D4, 4-node tetrahedral element, (b) C3D10, 10-node tetrahedral element. 24
3.5 Regularized crack surface in reference and deformed configurations. . . . 26

4.1 Abaqus implementation of phase field method using UEL and UMAT subroutines. 32
4.2 Geometry, loading and boundary conditions for the notched plate. 33
4.3 Notched plate tension test. Crack propagation (a)-(c) for a mesh with 86842 elements, $h = 0.002$ and $\ell_0 = 0.015$ mm. 34
4.4 Load–displacement curve for notched plate in tension. 34
4.5 Three points bending simply supported beam. Geometry, loading and boundary conditions. 35
4.7 Load–displacement curve for different values of $\mathscr{G}_c$. 36
4.8 Three points bending test. Crack propagation for a mesh with 17,363 elements, element size $h = 0.01$ *mm* with length-scale parameter $l = 0.03$ *mm*. 37
4.9 Effect of mesh size one the load–displacement curve for the three-point bending test. 38
4.10 Geometry, loading and boundary conditions for simply supported notched beam with three openings. 39

4.11 Comparison the crack patterns for the benchmark of notched three-points bending test: (a) Crack patterns with 25285 elements, $h = 0.05$ *mm* and $l = 0.2$ *mm*, (b) Crack patterns by Miehe *et al.*(2), (c) Digitized photo of crack pattern from by Bittencourt *et al.*(3). 39
4.12 Three-point bending test. Crack propagation (a)-(d) for a mesh with 25285 elements, element size $h = 0.05$ *mm* with length-scale parameter $\ell_0 = 0.15$ *mm*. 40
4.13 Notched rectangular specimen with opening. Geometry, loading and boundary conditions. 41
4.14 Notched rectangular specimen with opening tension test. Crack propagation (a)-(d) for a mesh with 17519 elements, element size $h = 3.0$ *mm* with length-scale parameter $\ell_0 = 6.5$ *mm*. 42
4.15 Notched rectangular specimen with three openings. Geometry, loading and boundary conditions. (a) openings far from the initial notch, (b)openings near the initial notch. 43
4.16 Notched rectangular specimen with three openings tension sample in Figure 4.15a. Crack propagation for a mesh with 18926 elements, element size $h = 3$ mm with length-scale parameter $\ell_0 = 8.5$ *mm*. 44
4.17 Notched rectangular specimen with three openings tension sample in Figure 4.15b. Crack propagation (a)-(d) for a mesh with 15724 elements, element size $h = 4$ mm with length-scale parameter $\ell_0 = 8.5$ mm. 45
4.18 Geometric setup and mesh of 3D DENT sample. (a) Sample dimensions and loading, (b) Mesh discretization. All dimensions are in m. 47
4.19 Crack propagation of 3D DENT sample for different load steps. SDV14= phase field. $\ell_0 = 0.06$. 47
4.20 Load–displacement curves. 48
4.21 Tension test of 3D side notched specimens with openings. (a) Loading and geometry. (b) and (c) Mesh discretization. Sample thickness is 0.1 *m*. All dimensions are in m. 49
4.22 Crack propagation of 3D side notched sample for different load steps. $\ell_0 = 0.06$ 50
4.23 Crack propagation of 3D side notched sample for different load steps. $\ell_0 = 0.06$. 51

5.1 Replacement of $\mu^\star\Delta\gamma - \langle\mu^\star\Delta\gamma + \phi\rangle$ by $\mu^\star\Delta\gamma - S(\mu^\star\Delta\gamma + \phi)$ as a function of a Error parameter ($\mu^\star = 1$ is depicted). 59

5.2 Extended GTN yield function ($y = q_1 = q_2 = q_3 = 1$) with $p = {-\mathbf{S}^T \mathbf{I}_3}/3$ and $q = \sqrt{\frac{3}{2}\mathbf{S}^T \mathbf{I}_6 \mathbf{T}_{\text{dev}} \mathbf{S}}$. 62

5.3 MINI triangle. 67

5.4 Splitting based on f and aspect ratio. 72

5.5 Element division algorithm. In **bold**: local element numbers. 73

5.6 Projection of quantities associated with coordinates $\boldsymbol{X}^n$ in the previous element $\{\boldsymbol{X}_1^o, \boldsymbol{X}_2^o, \boldsymbol{X}_3^o\}$. 74

5.7 Pulling specimen: prototype problem for parameter sensitivity. 76

5.8 Effect of l on reaction-displacement results (1000 steps, 11338 elements). Consistent units are used. 77

5.9 Effect of l on $\overline{\varepsilon}_p \times l$ at the monitored node (1000 steps, 11338 elements). Consistent units are used. 77

5.10 Effect of l on f at the monitored node (1000 steps, 11338 elements). Consistent units are used. 77

5.11 Effect of l for the pulling specimen. 77

5.12 Mesh and step size dependence. 78

5.13 Test of Ambati *et al.* (4) for phase field models assessment. 79

5.14 Test of Ambati *et al.* (4): comparison with the phase field model of Miehe and also Ambati *et al.* (4). Consistent units are used. 80

5.15 Test of Ambati *et al.*: mesh evolution with local remeshing ($l_{\min} = 5 \times 10^{-3}$ *mm*). 81

5.16 L-shaped panel: relevant data and damage region obtained from our model. 82

5.17 L-shaped panel: comparison with the results of Ambati *et al.* (4) hybrid model. 83

5.18 Two-hole specimen: data (see also Table 5.3) and localization in the inner region between the holes followed by the full-section localization and collapse ($l_{\min} = 0.2$ mm). GTN results depicted. 84

5.19 Two-hole specimen: detail of the central region crack nucleation and propagation. Undeformed configuration is used ($l_{\min} = 0.2$ *mm*). GTN results depicted. 86

5.20 Two-hole specimen: Load–displacement results for $l_{\min} = 0.2$ and $l_{\min} = 0.4$ mm. 87

5.21 Schlangen's SEN test: geometry, boundary conditions and material properties. 88

5.22 SEN test: damage distribution around the crack faces. 89

5.23 SEN test: crack path comparison. 89

5.24 SEN test: load-CMSD results: comparison with the experimental results by Schlangen (5) and effect of step and mesh sizes. 90
5.25 Drilled panel: relevant data. 92
5.26 Drilled panel: results using a coarse mesh, a fine mesh and also mesh refinement. Comparison with published results (Ambati *et al.* (4)). 93
5.27 Drilled panel: crack path comparison with the experimental crack path envelope of Ambati *et al.* (4). 93

6.1 Three different types of polymer/layered silicate nanocomposites. 96
6.2 Three and Two dimensional representation of the PNCs material. 99
6.3 Python script flow chart for the fully bonded PNCs generation. 100
6.4 Two dimensional representation of the PNCs with interphase zone. 101
6.5 Python script flow chart for the PNC including IP zone generation. 102

7.1 Nonlinear energy release rate. 105
7.2 Geometric setup of the specimen. 107
7.3 Load–displacement curves for different mesh size h, $h = 12$ nm (51334 elements), $h = 24$ nm (14890 elements), $h = 36$ nm (7755 elements). . . . 107
7.4 Load–displacement curves for different clay wt. %. 24% (51334 elements), 2.5% (53425 elements), 3% (52520 elements), 3.5% (53596 elements), 4% (53916 elements). 108
7.5 Ultimate load values for different clay wt.%. 109
7.6 Cracks patterns of the intact square PNCs specimens with different clay wt.%. SDV9 = phase field. 110
7.7 Young’s modulus versus the clay wt.%. 111
7.8 Ultimate load versus aspect ratio. 112
7.9 Cracks patterns of the intact square PNCs specimens with different aspect ratio of clay with 2% clay wt. %. SDV9 = phase field. 113
7.10 Side notch specimen geometry. 114
7.11 Cracks patterns of the side notched PNCs specimens with different initial crack length. SDV9 = phase field. 115
7.12 Load–displacement curves of PNCs with different initial crack length, $a = 375$ nm. 116
7.13 Double notch specimen geometry. 117
7.14 Cracks patterns of the double notch PNCs specimens with different clay wt.%. SDV9 = phase field. 118
7.15 Load–displacement curves for different mesh sizes, clay wt. 2%. 119

7.16 Load–displacement curves for different clay wt.%. 120
7.17 Tensile strength versus clay wt.%. 120
7.19 J integral versus clay wt.%. 121
7.18 Bulk and surface energy of PNCs with different clay wt.%. 121
7.20 Load–displacement curves for PNCs with different matrix $\mathscr{G}_c$. 122
7.21 Bulk and surface energy for PNCs with different matrix $\mathscr{G}_c$. 123
7.22 Tensile strength of PNCs versus matrix $\mathscr{G}_c$. 123
7.23 Ultimate load of PNCs versus matrix $\mathscr{G}_c$. 124
7.24 J integral versus matrix strain energy release rate $\mathscr{G}_c$. 124
7.25 Tension test of PNCs double notch specimen with different sizes. SDV9 = phase field. 125
7.26 Load–displacement curves of different size specimens. 126
7.27 Bulk and surface energy. 126

8.1 Mesh discretization 130
8.2 Load–displacement curves of PNCs samples with 2 % clay wt. and different crack diffusion lengths, $\mathscr{G}_c = 25\ N/m$, $E = 1.0\ GPa$. 131
8.3 Tensile strength versus crack diffusion length. 131
8.4 Young's modulus of PNCs for different IP thickness and properties. . . . 132
8.5 DENT sample geometric setup. 133
8.6 Load–displacement curves for samples with different clay distribution. . . 133
8.7 Crack pattern of DENT sample at different load steps for different clay distribution in samples. Distribution 1 (a–d), distribution 2 (e–h). IP=1 nm. SDV9= phase field. 134
8.8 Load–displacement curves of 1 nm IP zone thickness for different Young's modulus E and constant strain energy release rate $\mathscr{G}_c = 1.0\ N/m$. 135
8.9 PNCs tensile strength for different IP thickness and Young's modulus, $\mathscr{G}_c = 25\ N/m$. 136
8.10 PNCs tensile strength for different $\mathscr{G}_c$, thicknesses, and IP zone Young's moduli. 136
8.11 J integral versus Young's modulus of IP zone thickness. 137
8.12 J integral versus $\mathscr{G}_c$ of IP zone. 138
8.13 Surface energy for different $\mathscr{G}_c$ and E of IP. 139
8.14 Surface energy for different IP thickness and Young's modulus E. 139

8.15 Crack patterns in PNCs samples with different IP zone thicknesses. (a) 53797 elements; (b) 48091 elements; (c) 50478 elements; (d) 46834 elements. 140
8.16 Total cracks surface area of PNCs with IP = 1 *nm* and 4 *nm* with different Young's modulus. 141
8.17 Cracks surface area in IP, matrix, and PNCs. 141
8.18 DENT sample geometry and phase field, SDV9 = phase field. 142
8.19 Cracks surface area in PNCs for different depths. 142
8.20 Specimen Configuration (Matrix: $E = 1.9\ GPa$, $\nu = 0.35$, and $\mathscr{G}_c = 216\ N/m$. Clay: $E = 234\ GPa$ and $\nu = 0.25$. IP: $\mathscr{G}_c = 25\ N/m$). 143
8.21 Load–displacement curve. 144
8.22 Surface energy dissipation. 144
8.23 Crack propagation steps in the specimen. 145
8.24 Predictions of macroscopic fracture energy. 146

List of Tables

5.1 Constitutive properties for the quasi-brittle and porous model (extended GTN). . . . 64
5.2 Typical values of the parameters for the localized remeshing algorithm. . 71
5.3 Properties for 2024-T351 Aluminum 85
5.4 Mesh sizes (initial and final) and mesh evolution with time step 94

7.1 J Integral values for different samples. S1=Sample 1, S2=Sample 2, S3=Sample 3, and S4=Sample 4. 116

8.1 Elastic and fracture properties of epoxy, clay and IP zone 129

Chapter 1

Introduction

1.1 Introduction

Failure may occur for many reasons, including irregular loading or environment, defects in the materials, inadequacies in design, or inadequate construction or maintenance. Fracture analysis is a very active area of research and can provide a module to prevent failure. The prevention of failure induced by fracture is a major constraint in the design of an engineering structure. The integrity of different components of a structure can be inspected using experimental testing or numerical simulations. The numerical simulations play important roles in the design process toward testing the product because the simulations cut costs and time and improve the efficiency of the design. A great deal of research is done on the development of fracture models and its numerical implementations. The main object of fracture models is tracking the failure evolution after loading.

The task of these models is to estimate the maximum crack that a material can withstand before it fails by an analysis approach takes into consideration the overall dimensions of the structure. Many studies have clearly proven that material has failed at far below the critical stress intensity factor in linear elastic fracture mechanics because of defects in the material or micro cracks. Furthermore, analysis has proved that for any material there are two phases of crack development: the first phase is the crack initiation and the second phase is the crack growth until failure. The first phase covers the majority of fatigue life and occurs under very high cycle loading conditions, while the second phase is instantaneous. Fracture analysis includes the use of mathematical models approaches, needs the numerical tools such as finite element analysis to describe the deformations of complex geometries where the analytical methods can not handle the solution.

To date, efforts to model fracture and crack propagation have focused on two broad approaches: Discrete and continuum damage descriptions. The discrete approach incorporates a discontinuity into the displacement field that must be tracked and updated. Examples of this approach include extended finite element method (XFEM), element deletion, and cohesive zone models. The continuum damage, or smeared crack, approach incorporates a damage parameter into the model that controls the strength of the material. An advantage of this approach is that it does not require interface tracking since the damage parameter varies continuously over the domain. An alternative approach is to use a phase field to describe crack propagation.

1.2 Motivation and background

The detection of failure mechanisms in structures due to crack initiation and propagation via numerical modeling is of great importance in engineering applications, in particular in the polymer nanocomposite materials because of the complexity and cost of the experiments. Due to the special combination of the material, the expected crack path in this composite material may have curved paths or branching, depending on the clay fibers distribution in the matrix. Occasionally, the clay particles may unveil themselves as exfoliated structures during the preparation of the polymer nanocomposites (PNCs). Then, the large amount of clay in the material acts as stress concentrators which lead to the failure of the PNCs.

PNCs have received attention from materials researchers due to their promising physical, thermal, and mechanical properties in comparison to conventional composites. Thus, different polymer/clay nanocomposites come from combining different types of polymers, and also by adding clay to the polymeric matrix in order to improve properties. Knowledge of the fracture mechanics, and micro deformation of PNCs is vague; this vagueness may result from variations in both preparation procedures and obtaining the consistent micro-formation of the structure. For example, the fracture sites from the experiments of Wang *et al.* (1) are shown in Figure 1.1.

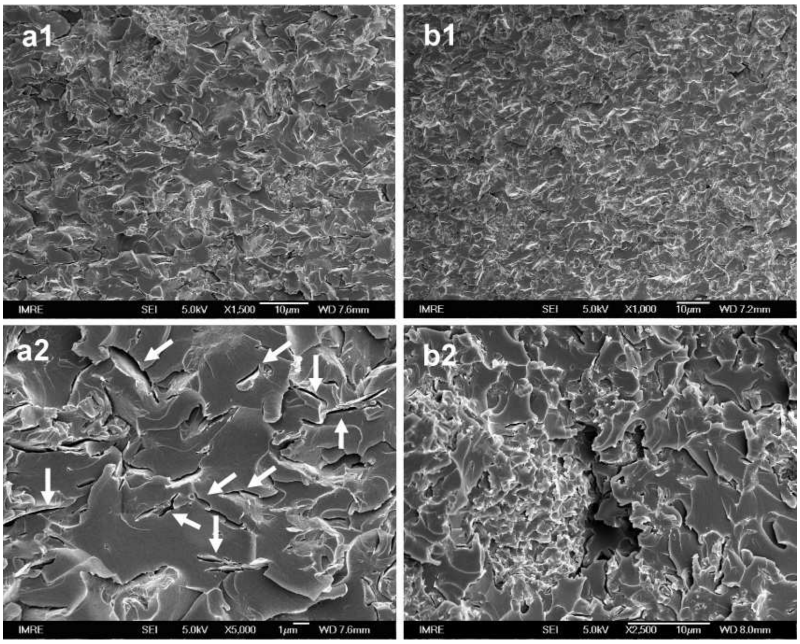

Figure 1.1: SEM micrographs of the fracture surface of the PNCs, a1-a2: crack initiation, b1-b2: fracture region, depicted from (1) with author's permission.

According to the methods used to prepare the nanocomposites, an interphase region formation may accompany the creation of PNCs. This interphase region was defined by various tests, such as X-ray, diffraction (XRD), scanning electron microscopy (SEM), and rheology (6). The precise nature of this region can be understood if accurate predictive and suitable models for the interphase behavior are used. When the understanding of this region's behavior is established, the interphase can be adapted to optimize the PNCs performance.

In material science and physics, crack propagation is an important and lasting challenge. Recently, the scientific communities have combined the concept of phase field modeling with fracture problems. The characteristic property of phase field methods is the existence of one or more phases that can be transformed into each other. In fracture, the cracks modeling in phase fields is interpreted by distinguishing between the sound state and the broken state. As usual in the phase field context, the order parameter changes between the states at the crack surfaces. Phase field model can predict the entire crack evolution, including the crack path, kinking and branching. The investigation of the nanocomposites properties and interphase region effects becomes applicable when a robust model is provided. The effect of the shape, mechanical properties, clay weight content of PNCs, and fracture properties of PNCs with or without the interphase regions can be determined using a model such as a phase field model.

The standard module of Abaqus software, for instance, supports different types of fracture criteria used for crack growth simulations. Examples of this are XFEM, critical stress at a certain distance ahead of the crack tip, critical crack opening displacement, crack length versus time, VCCT (the Virtual Crack Closure Technique), and the low-cycle fatigue criterion based on the Paris law to model quasi-static crack growth (7). These models are not ideal in PNCs simulations due to, firstly, limits in modeling the cracks kinking, branching, and perpendicular propagation. Secondly, these models require a predefined crack path by assigning master and slave surfaces during construction of the geometric model. Implementing the phase field model in the commercial software Abaqus is done to develope the software to solve complex crack fracture, and allows further use of the robust solver of the software. In addition, Abaqus provides the utility to perform the graphic user interface (GUI) through Python scripting. This feature is used to write and execute the Python script algorithm to generate the representative volume elements of the PNCs samples.

More recently, the phase field model for fracture is used in different fields and applications such as: (i) multi-physics problems (8–10), (ii) fluid transport (11), and (iii) biological tissues (12). Most of phase field approaches were applied to homogeneous materials. In this work, we use phase field model to model PNCs material which is heterogeneous. Moreover, in fracture modeling of PNCs, the molecular dynamic simulations are limited to very small sizes and not relevant to engineering applications (13). The proposed and adopted models can provide an approach for the computational design of clay/epoxy nanocomposites. In our work, we employ a mesoscopic fine-scale model accounting for the meso-structure of the composite material in order to extract the macroscopic tensile strength and J integral. The computational technique elaborated in the present work is expected to be an efficient tool for evaluating the overall size–dependent fracture behavior of PNCs.

1.3 Objectives and overview

The objectives along with the outline of presentation can be listed as follows:

Chapter 2 gives an overview of computational methods to model fracture in brittle and quasi-brittle materials. The review focuses on phase field as a variational approach to fracture. Thereafter, a review for modeling the polymer nanocomposits is introduced.

Chapter 3 demonstrates the derivation and the discretization of the phase field model for brittle fracture. The linear elastic fracture mechanics of Griffith's criterion, which is the basis of the variational approach of brittle fracture, is summarized first. Then, the theory pertaining to the diffuse representation of crack surfaces by means of a phase field, and the corresponding modification of the total potential energy functional accounting for the said field are discussed. Thereafter, we derive the appropriate expressions for the tangent stiffness matrix and right hand side vector corresponding to two- and three- dimensional elements with the additional degree of freedom per node. **Chapter 4** comprises the details for implementing the phase field method in Abaqus UEL and UMAT subroutines in addition to explain the results visualization in Abaqus viewer module. Numerical examples consist of different benchmark problems in two- and three- dimensional solids are given subsequently.

In **Chapter** 5 we present a new damage algorithm using the screened Poisson equation and local remeshing including the kinematics and constitutive laws. A specific element formulation to deal with ductile problems is described followed by presenting the main derivations for the screened Poisson equation and the weak form. Thereafter, the adopted localized remeshing algorithm leading to crack propagation is described. The numerical examples are explored to obtain a clear picture of the expected performance and likely problems.

Chapter 6 presents the physical and chemical properties of the PNCs and explains the constitutive modeling and the generation algorithm of the Representative Volume Elements (RVE) of PNCs. **Chapter 7** and **Chapter 8** predict the elastic and fracture properties of fully bonded PNCs and PNCs with formation of interphase zones around the clay platelets, respectively. The numerical examples consist of different problems to investigate the macroscopic material parameters such as the tensile strength, J integral, surface energy dissipation, and cracks surface areas in different conditions are explored in detail for each composite.

Chapter 9 concludes the thesis and mentioning the scope for the future work.

Chapter 2

Literature Review

2.1 Review of finite element analysis

The Finite Element Method (FEM) is one of the most popular and powerful numerical methods for simulating various fields in engineering and science. In solid mechanics which is a collection of physical laws, mathematical techniques and computer algorithms, FEM became necessary to study the behavior of different materials under different kinds of loading such as; mechanical, thermal, electrical, etc. FEM is a dominant discretization technique that can be interpreted from either a physical or mathematical viewpoint. The concept in the physical FEM is the subdivision of the mathematical model into divided (non-overlapped) segments of simple geometry called elements. Each element is modeled by a finite number of degrees of freedom defined as an unknown value of a function, or functions, at a set of nodal points. The outcome of the mathematical model is then approximated by the discrete model obtained by assembling the collection of all elements. The mesh size and the finite element should be selected based on the behavior of the structure (14).

2.2 Review of phase field model

The detection of failure mechanisms in structures due to crack initiation and growth via numerical modeling is of great importance in engineering applications, and has continually been the subject of attention by many researchers. The classical numerical approaches of the sharp crack discontinuity, such as the formulations of the cohesive zone modeling, interface element, or element and nodal enrichment approaches experience challenges with modeling of three-dimensional problems have crack branching. In comparison, the variational approach to phase field modeling of fracture awards new aspects towards the theoretical and computational modeling of complicated crack topologies. For example, the phase field approach for fracture avoids the modeling of discontinuities and, hence, the multi-field finite element solution scheme can be achieved in a direct manner. From the perspective of material modeling, the phase field formulation conceptually falls in line with the damage mechanics approaches. So, it can be recognized as gradient-type damage model with an individual description of the surface energy function. The recent concept of phase field enabled studying problems in different geometries and go from simple crack paths till reproducing qualitative behavior of cracks such as propagation, branching, and merging in 2D and 3D geometries with a fixed element mesh.

For brittle materials, the underlying theory is generally based on the thermodynamic framework first introduced by Griffith (15) wherein the effect of crack formation is quantified via a surface energy term that is dependent on the material surface tension, referred to as the *critical energy release rate*. A number of methods are currently available that deal specifically with numerical simulation of fracture initiation and growth. Such methods may usually be classified under one of two broad categories: *discrete* versus *smeared/diffuse* approaches.

Discrete crack models originally stemmed from the work of Ngo and Scordelis (16) and function by modifying the existing finite element mesh according to the evolution of the crack topology. In early implementations, incorporation of the crack as a geometrical entity was accomplished via node splitting which constrained the crack path to lie along element edges. This results in mesh dependency of the solution especially for complex crack patterns. Improvements to the original method were subsequently introduced in order to alleviate the mesh bias problem, for instance in the work of Ingraffea and Saouma on automatic remeshing (17). The discrete crack approach has also been successfully applied to problems involving crack propagation along material interfaces (18, 19). More recently, a 3D inter-element separation model was developed by Zhou and Molinari (20) in which a cohesive surface element is dynamically inserted between two tetrahedral elements whenever the critical stress state is reached. As with the original discrete crack model, the crack may only propagate along existing element edges. In lieu of remeshing, the issue of mesh dependency is addressed in (20) by varying the strength of the cohesive elements according to a Weibull model. A drawback of constraining crack propagation to occur only along element edges without applying additional correction is that the fracture energy is over-estimated when the true crack path deviates significantly from the corresponding element edge orientation, especially when the mesh is coarse. The extended finite element method (21, 22) based on enrichment within a partition of unity framework is another important development coming from the group of Belytschko in the late 90s, and has been the focus of intense research. In the XFEM, the crack topology is represented implicitly, usually by means of level sets. This enables cracks to propagate completely independent of the underlying mesh. The extended finite element method has been developed as an efficient alternative to remeshing techniques (23)

Furthermore, known characteristics of the phenomena being modeled are incorporated into the numerical solution space by enrichment of the standard finite element shape functions with expressions derived from benchmark analytical solutions. This endows the method with huge flexibility, such as the ability to resolve stress singularities at the crack tip as well as model the true stress behavior at the tip vicinity using a much coarser discretization than would normally be necessary in the absence of any enrichment. The implicit crack representation technique has also been successfully combined with numerical methods based on strain-smoothing as demonstrated in the work of Chen *et al.* (24), and with meshfree approaches in particular the Element Free Galerkin (see for example Rabczuk *et al.* (25)). However, XFEM is not without its disadvantages. In 2D for example, a single crack segment requires a pair of level set functions for the definition of its topology, so that computational complexity increases with the number of individual crack segments, as does the problem size due to the incorporation of additional degrees of freedom. An alternative means of discrete crack representation based on partition of unity enrichment is via cohesive segments, implemented within the finite element context by Remmers *et al.* (26), and within a meshfree setting by Rabczuk and Belytschko (27). In these methods, the crack topology is represented by a set of discrete, overlapping segments. The method may also be carried out without using shape function enrichment, as demonstrated in Rabczuk *et al.* (28). However, the implementation of XFEM for complex fracture patterns as they occur in heterogeneous materials is a tedious task. For instance, special enrichment functions are needed when the crack propagates along the clay-epoxy interface

On the other hand, the smeared crack model was pioneered by Rashid (29), who used it to perform simulations involving concrete applications. Rather than attempting to model the actual crack topology, smeared approaches incorporate the effects associated with crack formation such as stress release into the constitutive model. In an initially isotropic material, the emergence of a tensile crack alters the constitutive behavior from isotropic to orthotropic due to the loss of stiffness in the direction normal to crack, which is also referred to as the *plane of degradation*. Since no additional degrees of freedom are added, crack evolution can be simulated using standard finite element codes without modification of the initial mesh. The original model used by Rashid (29) is known as a *fixed crack* *model* due to the fact that for subsequent loadings the orientation of the POD at a given Gauss point is fixed at the orientation initially calculated when the strength criterion for cracking is met. Later on, Cope *et al.* (30) introduced the so-called *rotating crack model* wherein the orientation of the POD is adjusted to match the current major principal direction in order to account for the phenomenon of secondary cracking. It is well known that the traditional approach of utilizing a strength criterion to determine crack extension produces non-objective results owing to the presence of stress singularities at the crack tip, i.e. it is possible to advance the crack to an adjacent element with increasingly less load simply by refining the mesh (31). This problem may be overcome by adopting energetic approaches, such as constitutive models based on the *fictitious crack model* of Hillerborg *et al.* (32) which utilize the fracture energy as a material parameter in addition to the tensile strength. However this leads to another type of mesh bias problem stemming from the energy release rate being influenced by the element size. In the *Crack Band Model* proposed by Bažant and Oh (33) this issue was addressed by adjusting the value of the softening modulus based on the element size or the Gauss point tributary areas so that the correct value of the critical energy release rate is preserved during crack extension. To this end, a characteristic length parameter is introduced into the model, termed the *crack band width*. Still, this does not allow for arbitrarily large elements since a critical element size then emerges for which the softening modulus is infinite, implying a straight drop of the stress–strain curve after reaching the peak stress. Further scaling beyond this point (for elements larger than the critical size) would result in the material exhibiting spurious snap-back behavior. More details about fracture models can be found in the review paper (34).

In recent years, phase field methods for fracture simulations have been gaining popularity among researchers. Phase field methods also fall under the broader class of smeared or diffuse crack approaches, however they differ from the earlier models in their reliance on a *variational* theory of fracture. This is itself a relatively recent concept, being developed in the late 90s by Francfort and Marigo (35) to overcome certain limitations associated with the classical Griffith theory such as its inability to predict crack initiation and branching, as well as handle curved crack paths. In the variational theory, the total energy potential is assumed to include a surface term associated with the energy required for the formation of a crack. That is,

$$\Psi = \Psi^b + \Psi^s = \int_{\Omega\backslash\Gamma} \psi(\boldsymbol{\varepsilon})\, d\Omega + \int_{\Gamma} \mathscr{G}_c\, d\Gamma \tag{2.1}$$

This potential is then simultaneously minimized with respect to the displacement field and the crack geometry, with the idea being that the fracture topology evolution should occur in such a way that results in minimal potential energy. Several phase field brittle fracture approaches have been used and developed for physics, such as (36–39) where the phase field is used to model interfacial pattern formation to predict the crack for the dynamic and quasi-static fracture. Kuhn and Müller (40) also used the Ginzburg–Landau type of evolution equation and determined that the application of a phase field approach to the crack propagation is possible after taking the irreversible character of crack propagation into account. Noting that the steady state problem associated with the phase field evolution equation yields an exponential type of solution, Kuhn and Müller (41) developed new finite elements with exponential shape functions and demonstrated their superior performance in comparison to standard Lagrange elements in cases where the crack path aligns with element edges.

Further developments in mechanics field researchers were introduced by Bourdin *et al.* (42, 43), the most notable being the regularization of the sharp crack topology into a diffuse entity defined via a scalar variable (later termed the *phase field*) which serves to interpolate between cracked and intact states of the material. Bourdin *et al.* (42) utilized an evolution equation for the phase field derived from the Mumford–Shah functional for image segmentation. A modification of the original functional proposed in (42) was made by Lancioni and Royer–Carfagni (44) to handle problems involving deviatoric-type fracture. However, while their model correctly does not allow for material inter-penetration it is also unable to model crack-opening, hence limiting its applicability to cases where the dominant stress behavior is compressive. Amor *et al.* (45) improved the prior model to be able to handle crack opening by allowing degradation of stiffness corresponding to the spherical component of the stress when the value of said component is positive (signifying volumetric expansion). The significant contributions to the theory were also made by Miehe *et al.* (2, 46) in the form of a thermodynamically consistent framework for brittle mode-I fracture in the cases of both rate-independent and viscous material response. In particular, their formulation ensures local irreversibility of the phase field which permits the correct simulation of material behavior for cyclic loading. Whereas in (2) the coupled system consisting of stress equilibrium equations and the phase field evolution is solved simultaneously (with local growth of the phase field imposed via a penalty term), a staggered scheme is employed in (46) in which a local energy history field is introduced as a state variable to ensure irreversible crack growth.

Furthermore, other methods have been introduced to solve the phase field coupled system using staggered scheme rather than using FEM. Borden (47, 48) proposed the governing equation for the fourth–order phase field model supported by smooth spline functions spaces using isogeometric analysis. This work has been referenced by Dominik *et al.* (49) to speed up the computation by switching from isogeometric Galerkin to isogeometric collocation methods which improved the crack resolution. For thin shells, Amiri *et al.* (50) developed a phase field model for fracture in Kirchoff–Love thin shells using the local maximum–entropy (LME) meshfree method. For cohesive fracture, Verhoosel and Borst (51) developed a phase field model for straight crack propagation using the finite element method. This model involves three fields: the displacement field, the phase field, and an auxiliary field that represents the jump in the displacement across the crack. The third field uses as an auxiliary field which must be constantly orthogonal to the crack. This work was extended by Vignollet *et al.* (52) by using arc length method and staggered scheme. This model requires a pre–defined path for the crack. Duda *et al.* (53) introduced a mixed phase field model and gradient damage model for brittle fractures in elastic–plastic solids using FEM with a sub–stepping scheme for the time integration. The formulation shows two additional independent parameters called the phase field and the accumulated plastic strain. The technique of coupling the phase field model with plasticity can be used to analyze the interaction of plastic deformations during the surface separation. Lately, Ambati *et al.* (4) introduced a hybrid formulation for phase field model of quasi-static fracture. This formulation incorporates characteristics from both the isotropic and anisotropic models. Thus, the model does not need to split the stiffness matrix to distinguish between tension and compression cracks; the model points to a constant stiffness matrix.

2.3 Review of polymer nanocomposites material

PNCs are defined as the combination of a polymer matrix and fillers that have at least one dimension in nanometer range. PNCs have gained interest in both industrial applications and in academia due to the improvement which can be achieved in stiffness and thermal properties. One popular class of filler are nano-clays. Clay–based PNCs substantially enhance the mechanical properties of pristine polymers and drastically improve the material properties in comparison to natural polymers (54–59). PNCs are used for different purposes according to the new outcome from the combination such as: high elastic modulus (60), increasing strength (61), barrier resistance (62), flame retardancy by decreasing flammability (63), decreasing gas permeability, and reducing thermal expansion coefficient, etc. Some applications of PNCs are in aerospace engineering, automobiles, field emission and optical properties, packaging materials, medical devices, coatings, etc. (64). For example, PNCs are used in the foam of the sandwich structures of ships and aircrafts. As thermal applications, PNCs are used in electrical and electronic equipment and public transportation for heating purposes (65–67). They are also utilized as flame-retardant in manufacturing of cables to keep the mechanical properties such as elongation at break and tensile strength, whereas density is increased. More details on applications and the future trends of PNCs can be found in (68, 69).

The properties of the nanocomposites which can be achieved can be improved depending on the degree of dispersion of nanoclays. Particularly, the creation of exfoliated clay structures with the addition of a small amount of filler ($< 5\ wt.\%$). Based on the type of the polymer and the processing technique, the exfoliation/intercalation dispersion of nanoclay induces large surface area to the host epoxy/matrix. Accordingly, several improvements in the PNCs can be obtained (70). Hbaieb *et al.* (71) have shown that fully exfoliated clay is the most desirable due to the fact that clay cluster formations affect the stiffness of PNCs as well as their ability to reinforce the composite in two directions. Depending on the degree of dispersion of the clay, other benefits can be garnered from the composite (68).

There are different types of clay minerals; montmorillonite (MMT), for instance, is commonly used to prepare the polymer clay nanocomposites because of its ability to show extensive inter-layer expansion or swelling due to its particular structure. The exfoliated clay has extendable layered silicate consisting of stacks of plate-like structures $1-2\ nm$ thick and hundred nanometres in length and width and are separated by interlayer distances. These layers are organized in parallel to form stacks with a regular van der Waals gap among them, the so-called gallery structure. The platelets with an aspect ratio ranging from $50-200\ nm$ have an extremely large surface area of $750\ m^2/g$ (72, 73).

There are four strategies to experimentally synthesize the PNCs. The strategies are as follows: solution intercalation, in situ intercalative polymerisation, melt intercalation, and in-situ direct synthesis (72). Clay morphology, along with other factors such as the nano clay Young's modulus and clay volume fraction/weight content, is one of the most important factors in enhancing the stiffness of PNCs. For example, the high aspect ratios create a significant number of interfacial bonds between clays and the matrix. The interface layers become the adhesion between the heterogeneous material of the composite. In contrast, the formation of the interface layer in the PNCs is recognized through different tests. The layer has the same properties of bulk polymer far from the clay surface and a different properties near the interface layer due to the effect of the interface adhesion. This interface layer is called “interphase” and it has tiny thickness “nanometers”. This thickness makes the experiments expensive and limited; in addition, it is difficult to measure the mechanical properties of the zone due to the interactions of the stiffer clay inside the matrix under loading steps. The exact nature of this region can only be understood through developed and integrated models of the composite behavior. The interphase region can then be counted as a composite variable that itself can be altered in a rational manner to optimize composite performance.

2.3.1 Modeling of fully bonded PNCs

Experiments have been carried out to characterize the rigidity of nanocomposites by the nanoclays using different fabrication methods (74–76). However, these experiments were difficult and with contradictory results (77), motivating the use of numerical methods to gain a better understanding of nanocomposite material behavior.

For clay nanoparticles, many analytical models have been developed to quantify the fracture properties (78–80). Still, they are incapable of reliably predicting fracture–related material properties. For example, those models fail to capture the phenomenon of stress whitening observed in most relatively tough rubber-modified epoxies, or to predict the relationship between the rubber bridging mechanism. Salviato *et al.* (81) provided a multiscale model to assess the improvements in strengthening of nanoparticle filled polymers. Although, their model was concentrated on strengthening mechanisms caused by the formation of localized plastic shear bands initiated by the stress concentration around nanoparticles.

On the other hand, many numerical methods have been proposed to predict the mechanical properties of nanocomposites on different length scales (82–92). Due to the difficulty of measuring the geometrical and material properties at nano-scale and due to the significant change in the material properties from different samples, Silani *et al.* (88) and Vu-Bac *et al.* (93) proposed a stochastic analysis to predict bulk properties like Young's and shear modulus of fully exfoliated PNCs based on their fine-scale features. Rafiee *et al.* (91) and Vu-Bac *et al.* (92) numerically investigated the interaction properties between the carbon nanotubes and the polymer at different modeling scales.

2.3.2 Modeling of PNCs with interphase zones

The interfacial interaction between any heterogeneous components is an important factor that determines the properties of the composite. In composite materials, the interface is the surface boundary between any homogeneous phases in thermodynamic equilibrium (94). Interface is usually assumed as a two dimensional area. On the other hand, the intermediate phase formation between the joint surfaces of the neat epoxy and the silicate clays is referred to as *Interphase*; the interphase (IP) is a zone with a finite thickness (volume). The IP zone has different properties from the composite components. The IP properties depend on the PNCs preparation process' reactions and the conditions under which the reaction occur (6).

The IP zone position in PNCs originated at some point in the clay platelets where the clay bulk properties begin to transform into the matrix where the bulk properties of matrix resin are. In this region, different effects can be identified in the IP zone. Clay platelets may have morphological variations near their surfaces in the IP zone. Note that the surface area of defect-free platelets will be smaller than platelets containing pores and cracks on their surface area. The molecular and atomic structure of the platelet surface can differ from the bulk of the platelets themselves. This structure can be changed or broken down by chemical surface treatments. Besides, during the creation of the composite, an increase or decrease in the temperature during composite processing may eliminate certain useful surface reactivity and change the interface properties. The interaction between the clay and the matrix is influenced by the chemical and physical bonds at the interface, while the matrix composition in the IP is affected by the platelets surface. The non–interactive components and impurities of the epoxy can set the IP zone and change the local structure. The thickness of the IP zone may extend from a couple of nanometers to several nanometers. The mechanical strength, as well as chemical and thermal properties of the composite, can be deeply affected by the structure of this zone (65, 66, 95, 96). In conclusion, the IP zone energy in nanocomposite material can not be ignored due to high ratio of the IP to the volume, note that in solid mechanics the interphase/interface energy is usually negligible comparing to the bulk energy.

Fractures in polymer layered silicate (PLS) commonly occur either in the matrix or through reinforcement material actions that causes the debonding. In the case of matrix fracture, voiding or cavitation can occur during deformation of the neat epoxy (97). On the other hand, local interfacial damage in the clay area might promote debonding the silicate from the epoxy matrix (98). Accordingly, the properties of the composites depend on the matrix and the filler adhesion.

The IP zone properties, thickness, and volume can affect the PNCs properties considerably due to the major role of the clay nanofillers. In addition, IP zone determination is necessary because this zone produces the advantages of the PLS by transferring the stress from the polymeric matrix to the platelets, which will yield a high modulus and strength in the composite. Experiments attempting to measure the IP zone thickness and its mechanical properties were done by Zita *et al.* (6, 99). They show that the estimation of the contact surface between the silicate and the matrix is difficult. Experiments have also shown that this estimation neglects the interactions which developed in composites consisting of uncoated or modified silicates. Some models take into consideration the formation of the IP, either by assuming a finite thickness and homogeneous IP zone properties or considering that the properties are changing continuously from phase to another (100). In carbon nanotubes, the IP zone is considered in work of Rafiee *et al.* (101, 102). Analytically, mathematical models could be easily applied to *rounded nanoclay particles* rather than the *layered silicate*, such as the models used, to predict the tensile modulus of nanocomposites and assume the thickness and modulus of IP by Ji *et al.* (103) and Pukanszky (104) and recently by Zare *et al.* (105, 106).

Mortazavi *et al.* (107) investigated the IP effects on the elastic modulus and the thermal conductivity of PNCs by using a three-dimensional finite element with linear elastic material modeling. Samandari and Khatibi (108) extracted the elastic modulus of PNCs through the nanoclay inclusion modulus and its shape using analytical models. The shape of that uniformly distributed inclusions were spherical, cylindrical, and platelet. Fertig and Garnich (109) used a linear elastic material phase for the matrix, clay flake inclusion, and IP. The clay flakes were assumed to be parallel to each other in a single group. In terms of failure modeling at the interface, Chia *et al.* (110, 111) studied the effects of interfaces on the mechanical properties of nanocomposites; they considered the IP zone a critical factor in the property enhancement of polymer nanocomposites, while the interface properties of the nanoclay and the matrix strongly constrain the stiffness of the nanocomposite. They also modeled the clay gallery failure behavior with a cohesive law (112).

Molecular dynamics models of PNCs are limited to extremely small sizes. Multi-scale modeling can play a crucial role in the design of PNCs (113). Sheng *et al.*(114) developed a multiscale model that accounts for the hierarchical morphology of nanoclay and measures the elastic modulus as a function of the epoxy and the clay's properties and structure. The hierarchical structure of nanoclay assumes the representations of the nanoclay at multiple length scales, such as particle, multi-layer stack, and repeated cell structure. While the elements of interest such as carbon nanotubes and nanoclay sheets are represented in atomic level thickness for the analytical/numerical micromechanical models. This is to provide an accurate description of mechanical properties using continuum level models and choosing a measurable scale to the particle thickness and their spacing. Recently, Chen *et al.* (115) and Song *et al.* (116) developed a hierarchical multiscale approach to study the splitting failure of intercalated silicate in nylon 6/clay nanocomposites. The damage in the IP and the gallery of the intercalated silicate layers is realized by interfacial degradation using cohesive modeling (34, 117, 118), while the bulk of the epoxy was modeled by the GTN model. Pereira *et al.* (119) determined the mechanical, thermal, and barrier properties of PNCs using molecular dynamics, dissipative particles dynamics, and finite element method at different length scales. In this context, the review article by Zeng *et al.* (13) concluded that there are challenges in developing a multi-scale method, including theories and computational tools to represent the future of computer simulation and modeling of PNCs. These developments are important to the improvement the simulation techniques at individual time and length scales. Moreover, the development of methods on a broader time and length scale spanning from quantum mechanical domain to the macroscopic domain while considering the interaction properties of various components such as the nanofiller and the polymer (120).

Chapter 3

Phase Field Model for Quasi-Brittle Fracture

This chapter shows the derivation of the governing balance equations for phase field fracture in physical and material space, in addition to discretizing the model into finite element method in 2D and 3D.

3.1 Linear elastic fracture mechanics: Griffith's criterion

The first law of thermodynamics, is equal to the energy conservation in the control volume Ω_t.

$$\frac{d}{dt}(\Psi^{\text{int}}(\Omega_t) + \Psi^{k}(\Omega_t)) = \Psi^{ext}(\Omega_t) + \Psi^{h}(\Omega_t) \ , \tag{3.1}$$

where Ψ^{int}, $\Psi^{k}(\Omega_t)$, $\Psi^{ext}(\Omega_t$, and $\Psi^{h}(\Omega_t)$ are the rate of internal energy, rate of kinetic energy, external energy, and heat supply energy respectively. The fracture energy approach of Griffith (15) provided a new term to the above energy balance which is required for the fracture process $\Psi^{s} = \mathscr{G}_c \, d\Gamma$ and become

$$\dot{\Psi}^{\text{int}} + \dot{\Psi}^{k} + \dot{\Psi}^{s} = \Psi^{ext} + \Psi^{h} \ . \tag{3.2}$$

This assumption of quasi static fracture, where the cracks propagate slowly, the kinetic energy can be neglected in addition to the heat supply energy, assuming there is no heat conduction, the energy balance can be given as

$$\dot{\Psi}^{\text{int}} + \dot{\Psi}^{s} = \Psi^{ext} \ , \tag{3.3}$$

If the body forces potential written as $\Pi = \Psi^{\text{int}} + \Psi^{s}$, the total potential can be equals to

$$\frac{d\Pi}{dt} + \frac{\Psi^{s}}{dt} = 0 \ . \tag{3.4}$$

Considering the crack extension area is infinitesimal. Equation 3.4 can be reformed as

$$\left(\frac{d\Pi}{dA} + \frac{\Psi^{s}}{dA}\right)\frac{dA}{dt} = 0 \ . \tag{3.5}$$

If the term $\frac{-d\Pi}{dA}$ is the release of potential energy $\mathscr{G}$, and the term $\frac{\Psi^{s}}{dA}$ is the fracture surface energy $\mathscr{G}_c$. Equation 3.5 simplifies to

$$(\mathscr{G}_c - \mathscr{G})\dot{A} = 0 \ . \tag{3.6}$$

Griffith has invited this energy relations to find the condition of the crack initiation propagation which is $\mathscr{G}_c = \mathscr{G}$.

The above energetic approach is limited to stable crack propagation with time and it loses the crack detection when the energy release rate $\mathscr{G}$ exceeds the critical energy release rate $\mathscr{G}_c$, in addition to the restriction of predicting the crack path and cracks branching and kinking.

3.2 Phase field representation of crack surface

Let us consider the 1D problem consisting of an infinitely long cylindrical bar (constant cross-sectional area A) that is aligned along the x-axis and fully cut by a crack at $x = a$ as shown in Fig. 3.1. The surface energy dissipated by the formation of the said crack may be calculated simply as the product of the critical energy release rate $\mathscr{G}_c$ and the crack surface equal to the cross sectional area of the bar, i.e.

$$\Psi^{s} = \int_{\Gamma_s} \mathscr{G}_c \, d\Gamma = \mathscr{G}_c A \ . \tag{3.7}$$

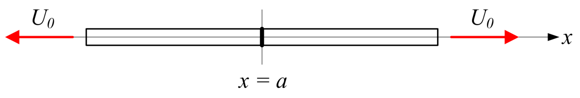

Figure 3.1: 1D bar cut by a crack.

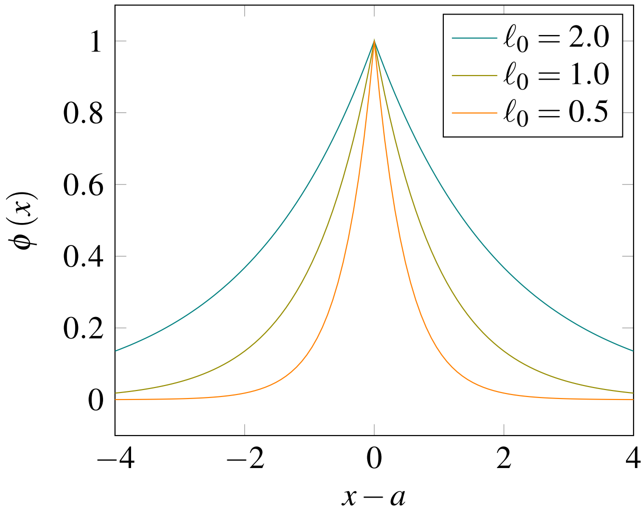

Figure 3.2: Crack phase field ϕ for different values of ℓ_0.

However such a calculation implies knowledge of the crack path, and while this is trivial in 1D, the actual crack topology is needed in higher dimensions to be able to compute the value of A. An alternative is to smooth out the crack such that the surface energy can be calculated as a domain integral. As demonstrated in Miehe *et al.* (2), this can be accomplished by introducing a scalar field variable to represent the diffuse crack of the form

$$\phi(x) = \exp\left(\frac{-|x-a|}{\ell_0}\right) , \tag{3.8}$$

where $\phi(x)$ is denoted as the crack phase field, and ℓ_0 is a parameter that controls the amount of "diffusion" of the crack. It can be seen that $\phi(x) \in [0,1]$, with 0 representing a completely intact state of the material, and 1 a fully broken state. The crack phase field for the 1D problem described above is shown in Fig. 3.2 for different values of ℓ_0. It should be emphasized that ℓ_0 does not represent the actual "width" of the diffuse crack. On the contrary, the form of expression (3.8) means that the crack is smoothed out over the *entire* domain, since $\phi(x)$ is never actually zero. Furthermore, while (3.8) may not be the only possible expression for describing the diffuse crack, the choice of functions is not entirely arbitrary. In particular, $\phi(x)$ should be symmetric, as well as monotonically decay to zero as we move away from the crack location. That is,

$$\phi(x) \to 0 \text{ as } x \to \pm\infty . \tag{3.9a}$$

$$\phi'(x) \to 0 \text{ as } x \to \pm\infty . \tag{3.9b}$$

Taking derivatives of (3.8), we obtain

$$\begin{aligned}\phi'(x) &= -\frac{\operatorname{sgn}(x-a)}{\ell_0}\exp\left(-\frac{|x-a|}{\ell_0}\right) ,\\ \phi''(x) &= \left[\frac{\operatorname{sgn}(x-a)}{\ell_0}\right]^2\exp\left(-\frac{|x-a|}{\ell_0}\right) ,\\ &= \frac{1}{\ell_0^2}\exp\left(-\frac{|x-a|}{\ell_0}\right) = \frac{1}{\ell_0^2}\phi(x) .\end{aligned} \tag{3.10}$$

These derivatives are undefined at $x=a$, however for $x \neq a$ the expression in (3.8) satisfies the ODE

$$-\phi''(x) + \frac{1}{\ell_0^2}\phi(x) = 0 , \tag{3.11}$$

as reported in (2). The weak formulation corresponding to the above equation along with the derivative boundary conditions given in (3.9b) is

$$0 = \int_{-\infty}^{\infty} v'\phi' + \frac{1}{\ell_0^2}v\phi \, dx , \tag{3.12}$$

where v represents some test function. The associated quadratic functional is then given by

$$I(\phi) = \int_{-\infty}^{\infty} \frac{1}{2}\left[(\phi')^2 + \frac{1}{\ell_0^2}\phi^2\right] dx . \tag{3.13}$$

The construction of $I(\phi)$ implies that (3.11) along with (3.9b) constitute the Euler–Lagrange equations associated with the variational problem

$$\phi^\star = \arg\inf_{\phi \in W}\{I(\phi)\} , \tag{3.14}$$

in which W is the set of functions satisfying (3.9b) along with the internal condition $\phi(a) = 1$. Furthermore, $\phi^\star$ is none other than the function given in (3.8). Plugging this into the functional in (3.13) yields

$$I(\phi^\star) = \int_{-\infty}^{\infty} \frac{1}{\ell_0^2}\exp\left(-\frac{2|x-a|}{\ell_0}\right) dx = \frac{1}{\ell_0} . \tag{3.15}$$

Hence we can define a function

$$\gamma(\phi) = \frac{1}{2}\left[\ell_0(\phi')^2 + \frac{1}{\ell_0}\phi^2\right] , \tag{3.16}$$

which is simply the integrand of (3.13) scaled by ℓ_0 so that the regularized surface energy may now be written as a domain integral:

$$\Psi^s = \mathscr{G}_c\int_\Omega \gamma(\phi)\, d\Omega = \mathscr{G}_c\int_A\int_{-\infty}^{\infty}\gamma(\phi)\, dx\, dA = \mathscr{G}_c A . \tag{3.17}$$

Correspondingly, the bulk energy is recast as

$$\Psi^b = \int_\Omega g(\phi)\, \psi^e(\varepsilon)\, d\Omega\,, \tag{3.18}$$

in which $g(\phi)$ is known as the *stress degradation function*. A common form obtained from (2) and other works is

$$g(\phi) = (1-\phi)^2 + k\,, \tag{3.19}$$

where k is a parameter chosen to be as small as possible while at the same time keeping the system of equations well-conditioned. It is worthwhile to note that parameter a representing the crack location does not appear in (3.17), which means that no preliminary estimation of the crack path is required. This endows the phase field model with enormous flexibility, such as the automatic nucleation, branching and merging of cracks. The expression given in (3.16) may be readily extended to 2D and 3D, with the relevant form being

$$\gamma(\phi) = \frac{1}{2}\left[\ell_0 \frac{\partial \phi}{\partial x_i}\frac{\partial \phi}{\partial x_i} + \frac{1}{\ell_0}\phi^2\right]\,, \tag{3.20}$$

where $i = 1, \ldots, d$ with d being the number of dimensions.

3.3 Governing equations and finite element model

3.3.1 Small strains formulation

By using the results from the previous section, the total potential energy functional can be written as

$$\Psi(\phi,\mathbf{u}) = \int_\Omega \left[(1-\phi)^2 + k\right] \psi(\boldsymbol{\varepsilon})\, d\Omega + \int_\Omega \frac{\mathscr{G}_c}{2}\left[\ell_0 \nabla\phi\cdot\nabla\phi + \frac{1}{\ell_0}\phi^2\right] d\Omega\,, \tag{3.21}$$

where for a linear-elastic material,

$$\psi(\boldsymbol{\varepsilon}) = \frac{1}{2}\lambda\,\varepsilon_{kk}\varepsilon_{ll} + \mu\varepsilon_{ij}\varepsilon_{ij}\,, \tag{3.22}$$

with λ and μ being the Láme constants. We confine ourselves to the case of small strains, i.e.

$$\varepsilon_{ij} = \frac{1}{2}\left(\partial u_i/\partial x_j + \partial u_j/\partial x_i\right)\,. \tag{3.23}$$

The governing equations are obtained as follows: we first define the first variation of the external work increment (dropping terms that evaluate to zero) as

$$\delta W_{\text{ext}} = \int_\Omega b_j \delta u_j\, d\Omega + \int_{\partial\Omega} h_j \delta u_j\, d\partial\Omega \tag{3.24}$$

where b_j and h_j are the components of the body force and boundary traction respectively. On the other hand, the variation of the internal energy increment is given by

$$\delta W_{\text{int}} = \delta \Psi = \frac{\partial \Psi}{\partial \varepsilon_{ij}} \delta \varepsilon_{ij} + \frac{\partial \Psi}{\partial \phi} \delta \phi \tag{3.25}$$

which for the case of (3.21) yields

$$\delta \Psi = \int_{\Omega} \left[(1-\phi)^2 + k \right] \sigma_{ij} \delta \varepsilon_{ij} \, d\Omega + \int_{\Omega} -2(1-\phi)\, \delta\phi\, \psi(\boldsymbol{\varepsilon})\, d\Omega + \int_{\Omega} \mathscr{G}_c \left(\ell_0 \frac{\partial \phi}{\partial x_i} \frac{\partial \delta \phi}{\partial x_i} + \frac{1}{\ell_0} \phi \delta \phi \right) d\Omega \tag{3.26}$$

By appropriate transfer of differentiation between variables, it can be shown that the above expression is equivalent to

$$\delta \Psi = \int_{\partial\Omega} \left[(1-\phi)^2 + k \right] n_i \sigma_{ij} \delta u_j \, d\partial\Omega - \int_{\Omega} \left[(1-\phi)^2 + k \right] \frac{\partial \sigma_{ij}}{\partial x_i} \delta u_j \, d\Omega + \int_{\Omega} -2(1-\phi)\, \delta\phi\, \psi(\boldsymbol{\varepsilon})\, d\Omega + \int_{\partial\Omega} \frac{\partial \phi}{\partial x_i} n_i \delta \phi \, d\partial\Omega + \int_{\Omega} \mathscr{G}_c \left(-\ell_0 \frac{\partial^2 \phi}{\partial x_i \partial x_i} \delta \phi + \frac{1}{\ell_0} \phi \delta \phi \right) d\Omega \tag{3.27}$$

where n_i denote the components of the unit vector normal to the surface $\partial\Omega$. We then combine the terms in (3.24) and (3.27), imposing that $\delta W_{int} - \delta W_{ext} = 0$ should hold for arbitrary values of δu_i and $\delta \phi$. This leads to the strong form of the governing equations:

$$\left[(1-\phi)^2 + k \right] \frac{\partial \sigma_{ij}}{\partial x_i} + b_j = 0 \text{ in } \Omega \tag{3.28a}$$

$$\left[(1-\phi)^2 + k \right] n_i \sigma_{ij} = h_j \text{ on } \partial\Omega_h \tag{3.28b}$$

$$u_j = \bar{u}_j \text{ on } \partial\Omega_u \tag{3.28c}$$

$$-\mathscr{G}_c \ell_0 \frac{\partial^2 \phi}{\partial x_i \partial x_i} + \left[\frac{\mathscr{G}_c}{\ell_0} + 2\psi(\boldsymbol{\varepsilon}) \right] \phi = 2\psi(\boldsymbol{\varepsilon}) \text{ in } \Omega \tag{3.28d}$$

$$\frac{\partial \phi}{\partial x_i} n_i = 0 \text{ on } \partial\Omega \tag{3.28e}$$

The above shows a coupled system consisting of the modified stress equilibrium equation (3.28a) and the phase field evolution equation (3.28d). Equations (3.28b) and (3.28c) are the natural and essential boundary conditions associated with (3.28a), while the last equation is the natural boundary condition associated with (3.28d). Note that while satisfaction of (3.28e) seems trivial, it implies an upper limit to the choice of the regularization parameter ℓ_0 with respect to the domain such that the phase field sufficiently decays to zero at the boundary.

Since the finite element model is based on the weak form, it is more convenient to work with eqs. (3.24) and (3.26) directly. Utilizing the Voigt notation in 2D and 3D settings, the primary variables can be discretized as follows

$$\mathbf{u} = \sum_{I=1}^{m} \mathbf{N}_I^{\mathbf{u}} \mathbf{u}_I, \quad \phi = \sum_{I=1}^{m} N_I \phi_I \tag{3.29}$$

in which

$$\mathbf{N}_I^{\mathbf{u}} = \begin{bmatrix} N_I & 0 \\ 0 & N_I \end{bmatrix} \tag{3.30}$$

where N_I denotes the shape function associated with node I, and $\mathbf{u}_I = \left\{u_x, u_y, u_z\right\}_I^{\mathrm{T}}$ and ϕ_I are the displacement and phase field values at node I. In 2D we have chosen to employ the standard 4-node quadrilateral element (Q4 or CPE4 in Abaqus) using four integration points and 3-node quadrilateral element (T3 or CPE3 in Abaqus) using one integration point as shown in Figure 3.3 , while in 3D, we have chosen the linear tetrahedron element (Tet4 or C3D4 in Abaqus) using one integration point and quadratic tetrahedron element (Tet10 or C3D10 in Abaqus) using four integration points as shown in Figure 3.4.

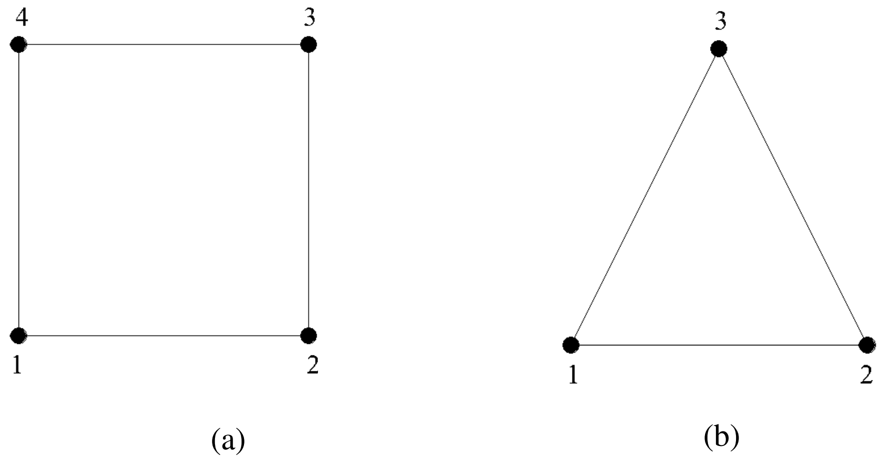

Figure 3.3: (a) Q4, 4-node quadrilateral element, (b) T3, 3-node quadrilateral element.

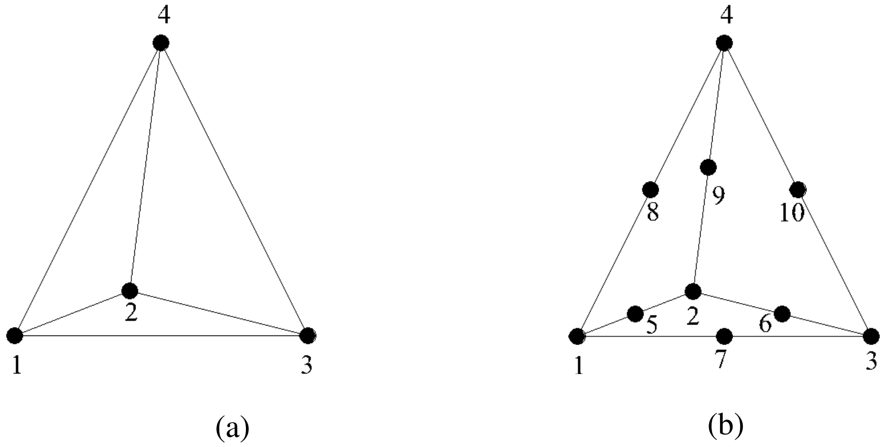

Figure 3.4: (a) C3D4, 4-node tetrahedral element, (b) C3D10, 10-node tetrahedral element.

The corresponding derivative quantities are given by

$$\boldsymbol{\varepsilon} = \sum_{I=1}^{m} \mathbf{B}_I^{\mathbf{u}} \mathbf{u}_I, \quad \nabla\phi = \sum_{I=1}^{m} \mathbf{B}_I^{\phi} \phi_I \tag{3.31}$$

with

$$\mathbf{B}_I^{\mathbf{u}} = \begin{bmatrix} N_{I,x} & 0 & 0 \\ 0 & N_{I,y} & 0 \\ 0 & 0 & N_{I,z} \\ 0 & N_{I,z} & N_{I,y} \\ N_{I,z} & 0 & N_{I,x} \\ N_{I,y} & N_{I,x} & 0 \end{bmatrix} \quad \mathbf{B}_I^{\phi} = \begin{bmatrix} N_{I,x} \\ N_{I,y} \\ N_{I,z} \end{bmatrix} \tag{3.32}$$

Correspondingly, the test functions and there derivatives are discretized as

$$\begin{aligned} \delta\mathbf{u} &= \sum_{I=1}^{m} \mathbf{N}_I^{\mathbf{u}} \delta\mathbf{u}_I, \quad \delta\phi = \sum_{I=1}^{m} N_I \delta\phi_I \\ \delta\boldsymbol{\varepsilon} &= \sum_{I=1}^{m} \mathbf{B}_I^{\mathbf{u}} \delta\mathbf{u}_I, \quad \nabla\delta\phi = \sum_{I=1}^{m} \mathbf{B}_I^{\phi} \delta\phi_I \end{aligned} \tag{3.33}$$

Using the above expressions and invoking the arbitrariness of the test functions, we obtain the external force from (3.24) as

$$\mathbf{f}_{I\text{ext}}^{\mathbf{u}} = \int_{\Omega} \mathbf{N}_I^{\mathbf{u}T} \mathbf{b}\, d\Omega + \int_{\partial\Omega} \mathbf{N}_I^{\mathbf{u}T} \mathbf{h}\, d\Omega \tag{3.34}$$

Likewise, the internal forces are obtained from (3.26) as

$$\mathbf{f}^{\mathbf{u}}_{I\mathrm{int}} = \int_{\Omega} \left[(1-\phi)^2 + k \right] \mathbf{B}^{\mathbf{u}\,T}_I \boldsymbol{\sigma}\, d\Omega \tag{3.35}$$

so that the discrete equations corresponding to stress equilibrium may be expressed as via the following residual:

$$\begin{aligned} \mathbf{r}^{\mathbf{u}}_I &= \mathbf{f}^{\mathbf{u}}_{I\mathrm{int}} - \mathbf{f}^{\mathbf{u}}_{I\mathrm{ext}} \\ &= \int_{\Omega} \left[(1-\phi)^2 + k \right] \mathbf{B}^{\mathbf{u}\,T}_I \boldsymbol{\sigma}\, d\Omega - \int_{\Omega} \mathbf{N}^{\mathbf{u}\,T}_I \mathbf{b}\, d\Omega - \int_{\partial\Omega} \mathbf{N}^{\mathbf{u}\,T}_I \mathbf{h}\, d\Omega \end{aligned} \tag{3.36}$$

On the other hand, the residual corresponding to the evolution of the phase field is given by

$$r^{\phi}_I = \int_{\Omega} \mathscr{G}_c \ell_0 \mathbf{B}^{\phi\,T}_I \nabla\phi\, d\Omega + \left[\frac{\mathscr{G}_c}{\ell_0} + 2\psi(\boldsymbol{\varepsilon}) \right] N_I \phi\, d\Omega - \int_{\Omega} 2N_I \psi(\boldsymbol{\varepsilon})\, d\Omega \tag{3.37}$$

We seek the solution for which the $\mathbf{r}^{\mathbf{u}} = \mathbf{0}$ and $\mathbf{r}^{\phi} = 0$. Due to the nonlinear nature of the residuals with respect to $\mathbf{u}$ and ϕ, we employ an incremental-iterative strategy utilizing the Newton–Raphson approach in conjunction with a parametrization based on a fictitious time t:

$$\left\{ \begin{array}{c} \mathbf{u} \\ \boldsymbol{\phi} \end{array} \right\}_{t+\Delta t} = \left\{ \begin{array}{c} \mathbf{u} \\ \boldsymbol{\phi} \end{array} \right\}_{t} - \left[\begin{array}{cc} \mathbf{K}^{\mathbf{uu}} & \mathbf{K}^{\mathbf{u}\phi} \\ \mathbf{K}^{\phi\mathbf{u}} & \mathbf{K}^{\phi\phi} \end{array} \right]^{-1}_{t} \left\{ \begin{array}{c} \mathbf{r}^{\mathbf{u}} \\ \mathbf{r}^{\phi} \end{array} \right\}_{t} \tag{3.38}$$

in which

$$\mathbf{K}^{\mathbf{uu}}_{IJ} = \frac{\partial \mathbf{r}^{\mathbf{u}}_I}{\partial \mathbf{u}_J} = \int_{\Omega} \left[(1-\phi)^2 + k \right] \mathbf{B}^{\mathbf{u}\,T}_I \mathbf{C} \mathbf{B}^{\mathbf{u}}_J\, d\Omega \tag{3.39a}$$

$$\mathbf{K}^{\mathbf{u}\phi}_{IJ} = \frac{\partial \mathbf{r}^{\mathbf{u}}_I}{\partial \phi_J} = \int_{\Omega} -2(1-\phi) \mathbf{B}^{\mathbf{u}\,T}_I \boldsymbol{\sigma} N_J\, d\Omega \tag{3.39b}$$

$$\mathbf{K}^{\phi\mathbf{u}}_{IJ} = \frac{\partial \mathbf{r}^{\phi}_I}{\partial \mathbf{u}_J} = \int_{\Omega} -2(1-\phi) N_I \boldsymbol{\sigma}^T \mathbf{B}^{\mathbf{u}}_J\, d\Omega \tag{3.39c}$$

$$\mathbf{K}^{\phi\phi}_{IJ} = \frac{\partial \mathbf{r}^{\phi}_I}{\partial \phi_J} = \int_{\Omega} \mathscr{G}_c \ell_0 \mathbf{B}^{\phi\,T}_I \mathbf{B}^{\phi}_J\, d\Omega + \left[\frac{\mathscr{G}_c}{\ell_0} + 2\psi(\boldsymbol{\varepsilon}) \right] N_I N_J\, d\Omega \tag{3.39d}$$

It should be noted that the above system does not guarantee irreversible evolution of the phase field, i.e. that $\phi_{t+\Delta t} \geq \phi_t$. This can be approximately enforced by introducing a penalty term to the phase field equation as described in Miehe *et al.* (2). Let us define the following function

$$\langle x \rangle_- = \left\{ \begin{array}{ll} -x, & x < 0 \\ 0, & x \geq 0 \end{array} \right. \tag{3.40}$$

A suitable penalty term can be constructed as

$$P\left(\dot{\phi}\right) = \frac{\eta}{n\Delta t}\left\langle \dot{\phi}\right\rangle_{-}^{n} \tag{3.41}$$

where n is a positive integer which in the present work is taken to be equal to 2, and $\dot{\phi} = \phi_{t+\Delta t} - \phi_t$. The parameter η controls the magnitude of the penalty term, and should be set to a value that is large enough to sufficiently enforce the irreversibility condition, but not too large as to result in an ill-conditioned system. The residual and the system Jacobian are then modified as follows:

$$r_I^{\phi} = \int_{\Omega} \mathscr{G}_c \ell_0 \mathbf{B}_I^{\phi T} \nabla \phi \, d\Omega + \left[\frac{\mathscr{G}_c}{\ell_0} + 2\psi\left(\boldsymbol{\varepsilon}\right)\right] N_I \phi \, d\Omega - \int_{\Omega} 2N_I \left[\psi\left(\boldsymbol{\varepsilon}\right) - \frac{\eta}{n\Delta t}\left\langle \dot{\phi}\right\rangle_{-}^{n}\right] d\Omega \tag{3.42}$$

$$\mathbf{K}_{IJ}^{\phi\phi} = \int_{\Omega} \mathscr{G}_c \ell_0 \mathbf{B}_I^{\phi T} \mathbf{B}_J^{\phi} \, d\Omega + \left[\frac{\mathscr{G}_c}{\ell_0} + 2\psi\left(\boldsymbol{\varepsilon}\right)\right] N_I N_J \, d\Omega + \int_{\Omega} \frac{\eta}{\Delta t}\left\langle \dot{\phi}\right\rangle_{-}^{n-1} N_I N_J \, d\Omega \tag{3.43}$$

3.3.2 Finite strains formulation

In the finite strain context, the fracture of solids can be represented by the deformation field that maps the material point $\mathbf{X}$ to the spatial points $\mathbf{x} = \mathbf{g}(\mathbf{X},t)$ and ϕ is the crack phase field at time t (see Figure 3.5).

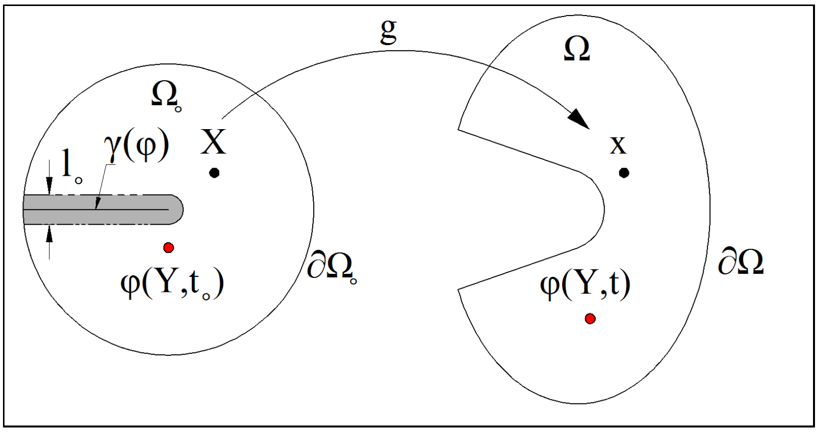

Figure 3.5: Regularized crack surface in reference and deformed configurations.

The deformation gradient $\mathbf{F}$ when $(\nabla_0 = \frac{\partial}{\partial \mathbf{X}})$ is defined as:

$$\mathbf{F} = \nabla_0 \mathbf{x}, \tag{3.44}$$

The global energy storage functional will have the form:

$$\Psi(\mathbf{F},\phi) = \Psi^b(\mathbf{F},\phi) + \Psi^s(\phi). \tag{3.45}$$

Correspondingly, the bulk energy is expressed as

$$\Psi^b(\mathbf{F},\phi) = \int\limits_{\Omega_0} \psi(\mathbf{F},\phi,\nabla_0\phi)d\Omega_0 \ , \tag{3.46}$$

where $\psi(\mathbf{F},\phi,\nabla_0\phi) = g(\phi)\psi_0(\mathbf{F})$ in which

$$\psi_0(\mathbf{F}) = \frac{\mu}{2}[\mathrm{tr}[\mathbf{F}^T\mathbf{F}]-3] - \mu\ln(\det\mathbf{F}) + \frac{\lambda}{2}[\ln(\det\mathbf{F})]^2 \ , \tag{3.47}$$

is the strain energy density for the hyperelastic compressible neo-Hookean material with elastic strain energy

The first variation of the free energy function can be written as

$$\delta\Psi = \int\limits_{\Omega_0} \left[\frac{\partial\psi}{\partial\mathbf{F}} : \delta\mathbf{F} + \frac{\partial\psi}{\partial\phi}\delta\phi\right] d\Omega_0 + \int\limits_{\Omega_0} \mathscr{G}_c\delta\gamma d\Omega_0 \ , \tag{3.48}$$

The external virtual work increment is given by

$$\delta W_{ext} = \int\limits_{\Omega_0} \mathbf{b_0}\cdot\delta\mathbf{x}d\Omega_0 + \int\limits_{\partial\Omega_0} \mathbf{h_0}\cdot\delta\mathbf{x}d\partial\Omega_0 \ , \tag{3.49}$$

where $\mathbf{b_0}$ and $\mathbf{h_0}$ are the components of the body force and boundary traction, respectively. The first variation of the internal energy increment is given by

$$\delta W_{\mathrm{int}} = \delta\Psi = \int\limits_{\Omega_0} \left[g(\phi)\left(\mu(\mathbf{F}-\mathbf{F}^{-T}) + \lambda\ln(\det\mathbf{F})\mathbf{F}^{-T}\right) : \delta\mathbf{F} + g'(\phi)\psi_0\delta\phi\right] d\Omega_0 + \int\limits_{\Omega_0} \mathscr{G}_c\left(\ell_0\nabla_0\phi\cdot\nabla_0\delta\phi + \frac{\phi\delta\phi}{\ell_0}\right) d\Omega_0 \tag{3.50}$$

which yields with (3.48)

$$\delta\Psi = \int\limits_{\Omega_0} \left[g(\phi)\frac{\partial\psi_0}{\partial\mathbf{F}} : \delta\mathbf{F} + g'(\phi)\psi_0\delta\phi\right] d\Omega_0 + \int\limits_{\Omega_0} \mathscr{G}_c\delta\gamma d\Omega_0 \ , \tag{3.51}$$

$$\frac{\partial\psi_0}{\partial\mathbf{F}} = \mu(\mathbf{F}-\mathbf{F}^{-T}) + \lambda\ln(\det\mathbf{F})\mathbf{F}^{-T} \ , \tag{3.52}$$

$$\mathbf{P} := g(\phi)\frac{\partial\psi_0}{\partial\mathbf{F}} \ , \tag{3.53}$$

$$\delta\Psi = \int\limits_{\Omega_0} \left[\mathbf{P} : \delta\mathbf{F} + g'(\phi)\psi_0\delta\phi\right] d\Omega_0 + \int\limits_{\Omega_0} \mathscr{G}_c \delta\gamma d\Omega_0 \ , \tag{3.54}$$

The second variation of the internal energy increment is given as:

$$\Delta\delta\Psi = \int\limits_{\Omega_0} \left(\delta\mathbf{F} : [\boldsymbol{C}_{iJkL}] : \Delta\mathbf{F} + \frac{\partial\mathbf{P}}{\partial\phi} : \delta\mathbf{F}\Delta\phi\right) d\Omega_0 + \int\limits_{\Omega_0} \left[2\Delta\phi\,\psi_0 - 2\,(1-\phi)\,\frac{\partial\psi_0}{\partial\mathbf{F}} : \Delta\mathbf{F}\right] \delta\phi d\Omega_0 + \int\limits_{\Omega_0} \mathscr{G}_c \left[\ell_0 \nabla_0\Delta\phi . \nabla_0\delta\phi + \frac{\Delta\phi\delta\phi}{\ell_0}\right] d\Omega_0 \tag{3.55}$$

where

$$\boldsymbol{C}_{iJkL} := \frac{\partial P_{iJ}}{\partial F_{kL}} = g(\phi)\left[\mu\left(\delta_{ik}\delta_{JL} + F_{iL}^{-T}F_{kJ}^{-T}\right) + \lambda\left(F_{iJ}^{-T}F_{kL}^{-T} - \ln(\det\mathbf{F})F_{iL}^{-T}F_{kJ}^{-T}\right)\right] \ , \tag{3.56}$$

$$\frac{\partial\mathbf{P}}{\partial\phi} = g'(\phi)\frac{\partial\psi_0}{\partial\mathbf{F}} = g'(\phi)\left(\mu(\mathbf{F} - \mathbf{F}^{-T}) + \lambda\ln(\det\mathbf{F})\mathbf{F}^{-T}\right) \ . \tag{3.57}$$

The FEM discretization of the deformation field and phase field is given by:

$$\mathbf{X} = \sum_{a=1}^{n} N_a(\boldsymbol{\xi})\mathbf{X}_a, \quad \mathbf{x} = \sum_{a=1}^{n} N_a(\boldsymbol{\xi})\mathbf{x}_\mathbf{a}, \quad \phi = \sum_{a=1}^{n} N_a(\boldsymbol{\xi})\phi_a \ , \tag{3.58}$$

where N_a denotes the shape function associated with node a, and $\boldsymbol{\xi} = [\xi_1, \xi_2, \xi_3]^T$ represents the element local coordinates. $\mathbf{X}$, $\mathbf{x}$, and ϕ are the initial configuration, deformed configuration field and the phase field values at node a. The deformation gradient and the phase field gradient are given by

$$\Delta\mathbf{F} = \sum_{a=1}^{n} \Delta\mathbf{x}_\mathbf{a} \otimes \nabla_0 N_a, \quad \Delta\mathbf{x} = \sum_{a=1}^{n} N_a(\boldsymbol{\xi})\Delta\mathbf{x}_\mathbf{a}, \quad \Delta\phi = \sum_{a=1}^{n} N_a(\boldsymbol{\xi})\Delta\phi_a \ . \tag{3.59}$$

The corresponding test functions and derivatives equivalents of the variables are interpolated using the same spaces as:

$$\delta\mathbf{x} = \sum_{a=1}^{n} N_a(\boldsymbol{\xi})\delta\mathbf{x_a}, \quad \delta\phi = \sum_{a=1}^{n} N_a(\boldsymbol{\xi})\delta\phi_a, \tag{3.60}$$

$$\delta\mathbf{F} = \sum_{a=1}^{n} \delta\mathbf{x_a}\otimes\nabla_0 N_a(\boldsymbol{\xi}), \nabla_0\delta\phi = \sum_{a=1}^{n} \nabla_0 N_a(\boldsymbol{\xi})\delta\phi_a, \quad \nabla_0\Delta\phi = \sum_{a=1}^{n} \nabla_0 N_a(\boldsymbol{\xi})\Delta\phi_a \,. \tag{3.61}$$

Substituting Equations (3.58) – (3.60) into the weak form and invoking the arbitrariness of the test functions, the internal forces obtained from (3.48) as

$$\begin{aligned} \mathbf{R}^{\mathbf{x}}_a &= \int\limits_{\Omega_0} \mathbf{P}\cdot\nabla_0 N_a d\Omega_0 - \int\limits_{\Omega_0} N_a \mathbf{b}_0 d\Omega_0 - \int\limits_{\partial\Omega_0} N_a \mathbf{h}_0 d\partial\Omega_0 \\ \mathrm{R}^{\phi}_a &= \int\limits_{\Omega_0} -2(1-\phi)\psi_0 N_a d\Omega_0 + \int\limits_{\Omega_0} \mathscr{G}_c \ell_0 \nabla_0\phi\cdot\nabla_0 N_a + \frac{\phi N_a}{\ell_0} d\Omega_0 \,. \end{aligned} \tag{3.62}$$

We employ the Newton-Raphson approach to solve the nonlinear nature of the residuals:

$$\begin{bmatrix} \mathbf{K}^{\mathbf{xx}} & \mathbf{K}^{\mathbf{x}\phi} \\ \mathbf{K}^{\phi\mathbf{x}} & \mathbf{K}^{\phi\phi} \end{bmatrix} \begin{bmatrix} \Delta\mathbf{x} \\ \Delta\phi \end{bmatrix} = - \begin{bmatrix} \mathbf{R}^{\mathbf{x}} \\ \mathbf{R}^{\phi} \end{bmatrix} , \tag{3.63}$$

in which

$$\mathbf{K}^{\mathbf{xx}} = \int\limits_{\Omega_0} \left(\frac{\partial N_a}{\partial X_J} \boldsymbol{C}_{iJkL} \frac{\partial N_b}{\partial X_L} \right) d\Omega_0 \tag{3.64a}$$

$$\mathbf{K}^{\mathbf{x}\phi} = \int\limits_{\Omega_0} \frac{\partial P_{iJ}}{\partial\phi} \frac{\partial N_a}{\partial X_J} N_b d\Omega_0 \tag{3.64b}$$

$$\mathbf{K}^{\phi\mathbf{x}} = \int\limits_{\Omega_0} -2(1-\phi) N_a \frac{\partial\psi_0}{\partial F_{iJ}} \frac{\partial N_b}{\partial X_J} d\Omega_0 \tag{3.64c}$$

$$\mathbf{K}^{\phi\phi} = \int\limits_{\Omega_0} \left(2N_a N_b \psi_0 + \mathscr{G}_c \left(\ell_0 \frac{\partial N_a}{\partial X_I} \frac{\partial N_b}{\partial X_I} + \frac{N_a N_b}{\ell_0} \right) \right) d\Omega_0 \,. \tag{3.64d}$$

Chapter 4

Abaqus Implementation of Phase Field Model in 2D and 3D

The scope of this chapter is to illustrate the implementation of the phase field method for simulating brittle mode-I fracture within the Abaqus software (7) using UEL and UMAT subroutines in two and three dimensional problems. Abaqus /Standard allows for five different types of fracture criteria to be used for crack-growth simulations. These are: critical stress at a certain distance ahead of the crack tip, critical crack opening displacement, crack length versus time, VCCT (the Virtual Crack Closure Technique), and the low-cycle fatigue criterion based on the Paris law for modeling quasi-static crack growth. However all of these models require a predefined crack path and the definition of two distinct but initially bonded contact surfaces along which the crack will propagate. This implies the inclusion of master and slave surfaces during construction of the geometric model, as well as the specification of node sets to identify the initially bonded part of slave surfaces. Clearly, a phase field approach offers the advantages of avoiding the aforementioned complications related to geometry construction and meshing as well as offering the ability to model multiple crack initiation, branching, and coalescence for complex structures in which no prior knowledge of the crack paths are available.

The system of equations resulting from the finite element model (chapter 3) is nonlinear, so one must resort to incremental-iterative schemes for calculating the solution. We have chosen to implement the above-mentioned model within the software Abaqus in order to take advantage of its built-in nonlinear solver using the Newton-Raphson algorithm as well as automatic time-stepping schemes.

With regard to the phase field model for brittle fracture in 2D, we define 3 and 4 nodes triangular and quadrilateral elements with 3 degrees of freedom per node, which are denoted as u_x, u_y and ϕ. While in 3D we define 4 and 10 nodes tetrahedral elements with 4 degrees of freedom per node which are u_x, u_y, u_z, and ϕ. These elements are implemented using the UEL subroutine in Abaqus, UEL subroutine allows for user-defined calculation of element tangent stiffness matrices as well as nodal force vectors (right hand side). The constitutive behavior at the element Gauss points is evaluated by a call to a material function that is defined within the UEL subroutine. Hence, the user-programmed UEL subroutine is called for each element, which in turn makes several calls to the material function according to the number of Gauss points per element. The UEL subroutine interfaces with standard arrays defined in the Abaqus environment for the retrieval of dependent variable values such as the displacement and phase field, as well as the storage of internal/state variables associated with each Gauss point.

One drawback to using UEL subroutines is that post-processing and visualization of the results are not straightforward. In particular, it is not possible to display the results of in the Abaqus Viewer; for example, because element shape functions are user-defined, the software can no longer automatically extrapolate variables from Gauss points to the element nodes. One way to address this problem is by coding a python script that accesses the database to obtain (and if necessary, recalculate) results in such a way that is compatible with some existing element type in the Abaqus library. Alternatively, element results can be stored as state-dependent variables (121), which are valid if the connectivity and shape functions of the user-defined element are the same as those of a pre existing Abaqus implementation. Otherwise, there will be errors arising from the differences between the element formulations. We have employed the latter approach in this work, as the shape functions for our user defined elements are simply the standard CPE4, CPE3, C3D4, and C3D10 shape functions of Abaqus elements. Visualization is implemented by utilizing a second, *fictitious* mesh consisting of native Abaqus elements that match the original mesh of user-defined elements.

The material for the overlaid mesh is defined via a UMAT user subroutine, which is also used for computing stresses and tangent moduli at the integration points. The material parameters are selected such that there is no resistance to strain; for instance, we use an elastic material with Young's modulus set near to machine precision (10^{-15}). The state variables for the integration points are stored in the array STATEV which is accessible through the UMAT subroutine. These variables are originally calculated within the UEL subroutine and stored in the built-in array SVARS that is accessible through that subroutine. Transfer of values from SVARS to the STATEV array is accomplished by making use of the `common` statement. Figure 4.1 shows the relation between the different subroutines.

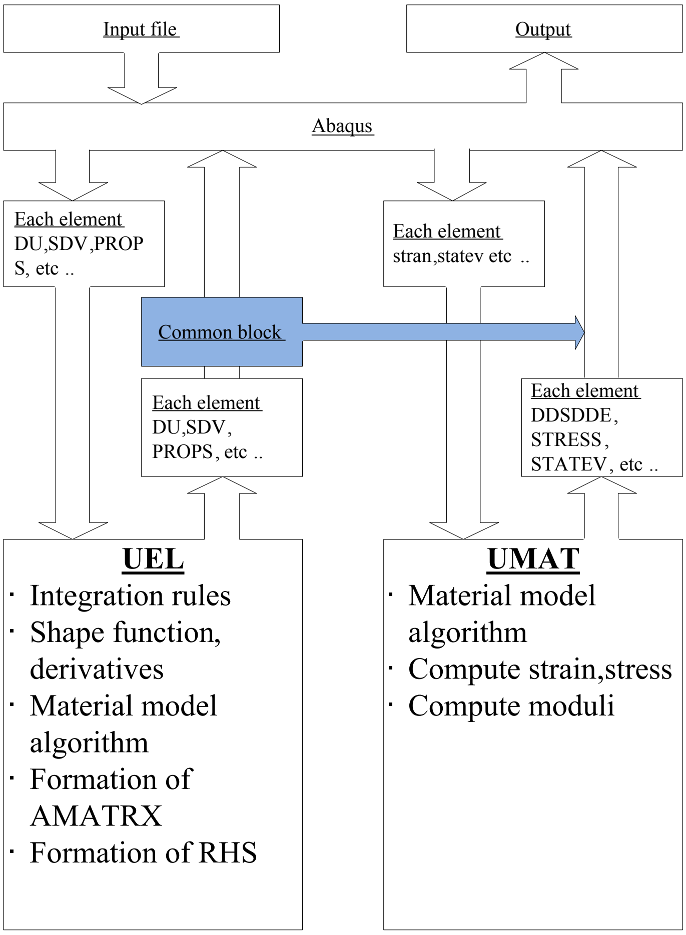

Figure 4.1: Abaqus implementation of phase field method using UEL and UMAT subroutines.

4.1 Two dimensional numerical examples

4.1.1 Notched square plate

The problem of a square plate with an initial notch subjected to tensile loading has been analyzed in Miehe *et al.* (2, 46), Borden (47) using Isogeometric Analysis, and Hesch and Weinberg (122). The geometric setup as well as loading conditions are shown in Figure 4.2. In the present work, the notch is modeled as an actual feature of the geometry. Alternatively, it is possible to avoid having to include the notch in the geometry by solving the steady state problem

$$-\ell_0 \nabla^2 \phi + \frac{1}{\ell_0}\phi = 0 \tag{4.1}$$

over the entire square plate, subject to homogeneous natural boundary conditions plus an internal condition of $\phi = 1$ at the notch. The geometry is meshed using 86842 elements with manual refinement resulting in an effective element size of $h = 0.005$ *mm* within the expected crack propagation zone. Young's modulus and Poisson's ratio were chosen to be equal to 210 *GPa* and 0.2 respectively, while the critical energy release rate $\mathscr{G}_c$ was set to a value of 2.7 N/mm.

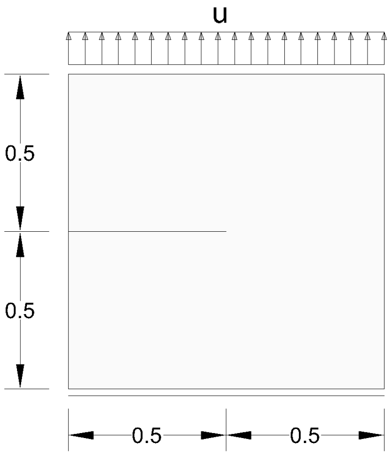

Figure 4.2: Geometry, loading and boundary conditions for the notched plate.

The applied loading consists of an imposed displacement at the top portion of the plate, with the bottom of the plate fixed. The loading is applied incrementally and linearly with respected to time by using the command `AMPLITUDE = RAMP` in the Abaqus input file. The initial time increment was chosen to be $\Delta u_0 = 10^{-2}$ *mm*, with succeeding increments being allowed to vary according to the automatic time stepping scheme available in Abaqus, but with a minimum allowed time increment of 10^{-7} *mm*. A value of 0.015 *mm* was selected for the crack regularization parameter ℓ_0, following the recommendation in Miehe *et al.* (2) that ℓ_0 should be more than twice the characteristic element length in order to properly resolve the crack. The crack propagation at different time steps is shown in Figure 4.3(a-c), and the resulting load–displacement curve is given in Figure 4.4. The results are compared with the recent work of Hesch and Weinberg (122).

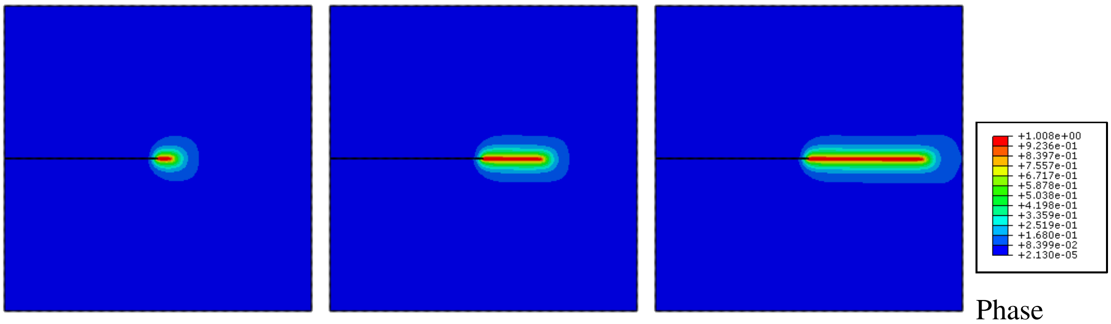

(a) (b) (c) Phase field

Figure 4.3: Notched plate tension test. Crack propagation (a)-(c) for a mesh with 86842 elements, $h = 0.002$ and $\ell_0 = 0.015$ mm.

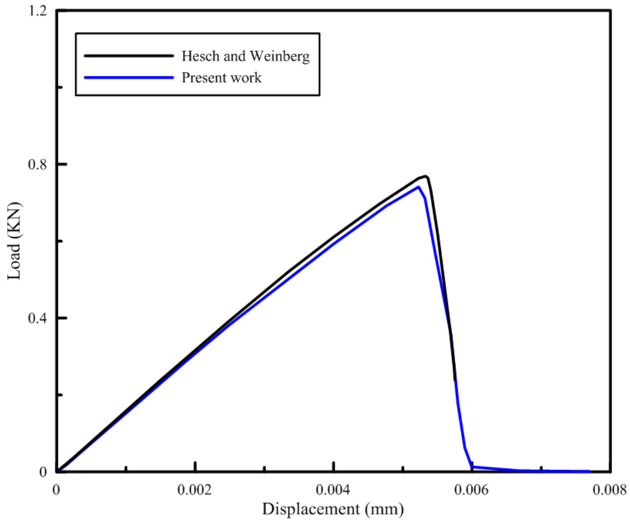

Figure 4.4: Load–displacement curve for notched plate in tension.

4.1.2 Three-points bending test

The aim of this benchmark is to test the model in a bending problem and verify the crack propagation. Figure 4.5 shows the geometric setup of the benchmark with the loading conditions. The benchmark descretized into (17,363) quadrilateral elements with an effective mesh size $h = 0.01$ *mm* in the refined region near the initial notch. The material parameters are used as $E = 20.8$ *GPa* and $\nu = 0.3$. The critical energy release rate is $\mathscr{G}_c = 5$ N/mm. The load applied in a one step with a minimum load increment ($\Delta u = 1 \times 10^{-7}$ *mm*) and maximum load increment ($\Delta u = 1 \times 10^{-2}$ *mm*) using the automatic time incrementation of Abaqus.

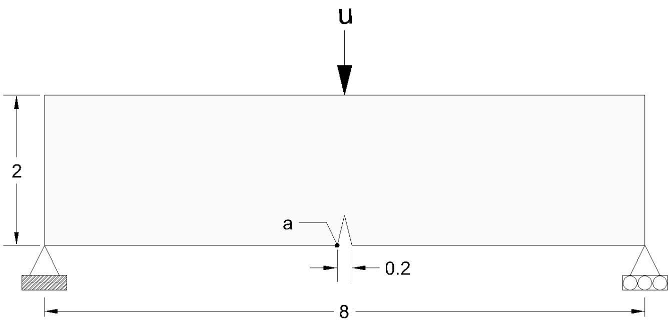

Figure 4.5: Three points bending simply supported beam. Geometry, loading and boundary conditions.

The mesh discretization is shown in Figure 4.6 with element edge lengths equal to 0.01 *mm* at the expected crack path and 0.25 *mm* at areas well removed from the crack trajectory.

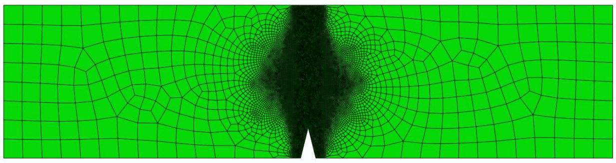

Figure 4.6: Mesh refinement of the three points bending sample.

Figure 4.7 shows the load deflection curve of a reference point (a) in Figure 4.5 and it is compared with different values of the energy release rate $\mathscr{G}_c$.

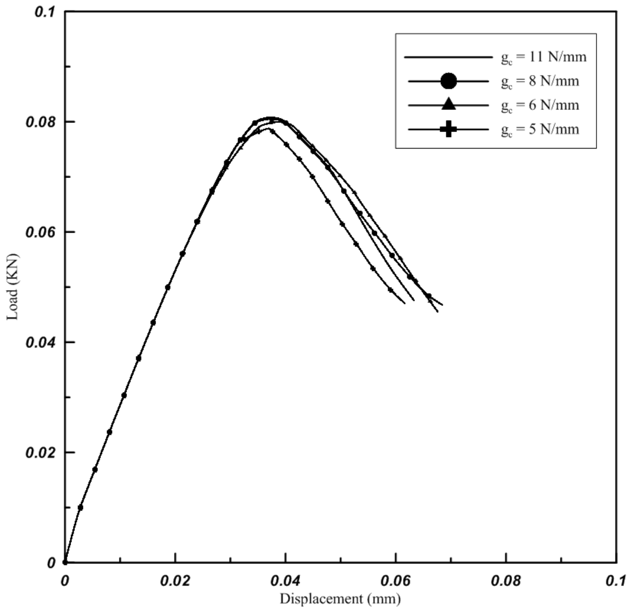

Figure 4.7: Load–displacement curve for different values of $\mathscr{G}_c$.

Figure 4.7 shows the effect of increasing the value of $\mathscr{G}_c$ on the value of the collapse load. The progression of the crack at several load levels is shown in Figure 4.8.

(a) time step = 0.24.

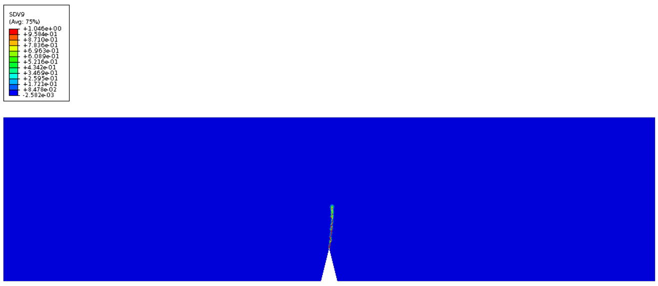

(b) time step = 0.38.

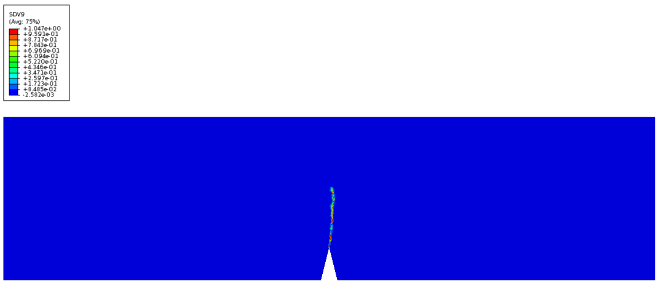

(c) time step = 0.51.

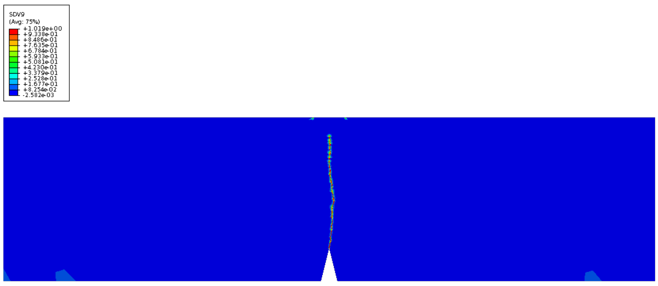

(d) time step = 1.0.

Figure 4.8: Three points bending test. Crack propagation for a mesh with 17,363 elements, element size $h = 0.01$ *mm* with length-scale parameter $l = 0.03$ *mm*.

In Figure 4.9 different simulations are carried out to show the comparison of the load–displacement curve for different values of element edge sizes at the crack path vicinity.

The edge sizes used varied from 0.008 *mm*, 0.006 *mm* and 0.005 *mm* with the corresponding number of elements being 24,400, 31,944 and 34,711 respectively. The material parameters are $E = 20.8$ *GPa* and $\nu = 0.3$ and the energy release rate is $\mathscr{G}_c = 5\ N/mm$ with length scale parameter $\ell_0 = 0.015\ mm$.

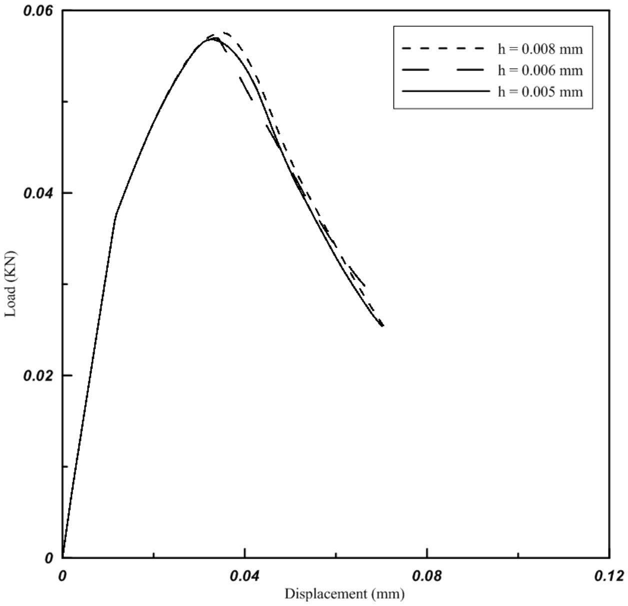

Figure 4.9: Effect of mesh size one the load–displacement curve for the three-point bending test.

4.1.3 Notched beam with three openings

The Ingraffea–Bittencourt benchmark is one of the most popular examples for validating curved crack patterns. The experimental testing was carried out by Ingraffea and Grigoriu(123), with subsequent numerical modeling by Bittencourt *et al.*(3). The geometry and the loading of the problem are given in Figure 4.10. In the present study, we have used the following values for material parameters: Young's modulus $E = 20\ GPa$, Poisson ratio $\nu = 0.3$, and critical energy release rate $\mathscr{G}_c = 1\ N/mm$.

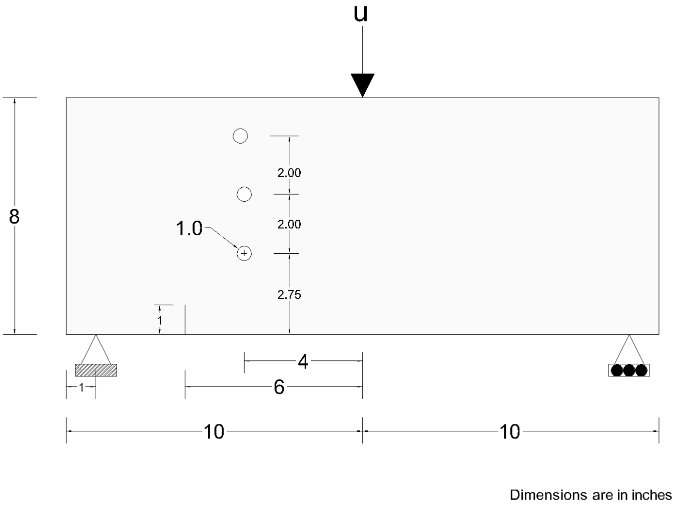

Figure 4.10: Geometry, loading and boundary conditions for simply supported notched beam with three openings.

Figure 4.11 compares the results of present study with the experimental crack pattern as well as numerical results from Miehe *et al.*(2) and shows that the present Abaqus implementation is able to predict the correct trajectory of a curved crack.

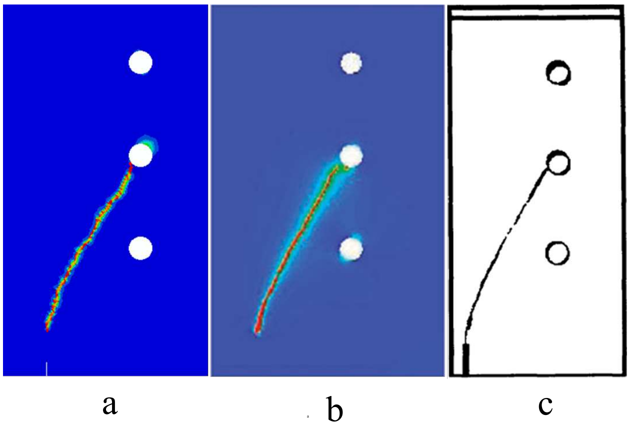

Figure 4.11: Comparison the crack patterns for the benchmark of notched three-points bending test: (a) Crack patterns with 25285 elements, $h = 0.05$ *mm* and $l = 0.2$ *mm*, (b) Crack patterns by Miehe *et al.*(2), (c) Digitized photo of crack pattern from by Bittencourt *et al.*(3).

Figure 4.12 shows four different time steps of crack propagation with 25285 elements which are used in simulations.

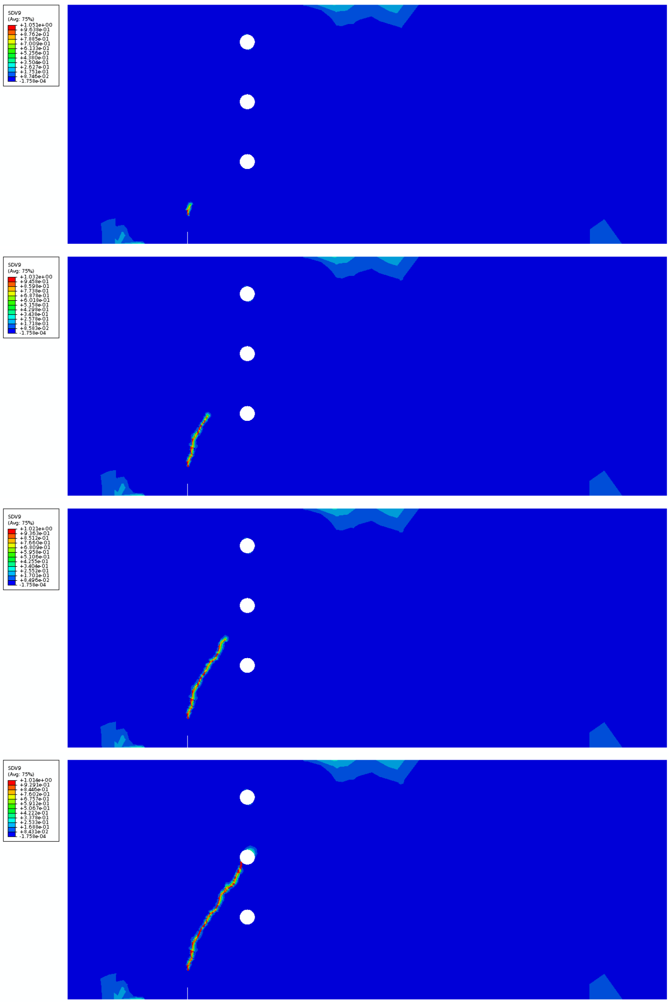

Figure 4.12: Three-point bending test. Crack propagation (a)-(d) for a mesh with 25285 elements, element size $h = 0.05\ mm$ with length-scale parameter $\ell_0 = 0.15\ mm$.

4.1.4 Tension test of a notched rectangular specimen with one opening

In the following setup, we investigate the influence of the presence of openings to the resulting crack trajectory for a square plate subjected to tension. The numerical specimen consists of a notched rectangular plate with one opening, for which the geometry, boundary conditions and loading are given in Figure 4.13.

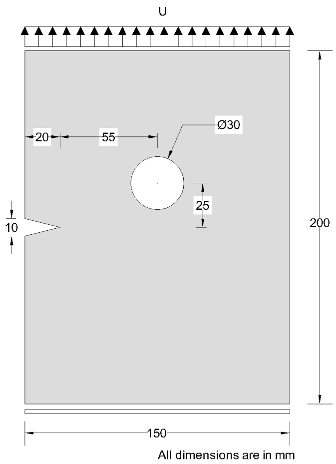

Figure 4.13: Notched rectangular specimen with opening. Geometry, loading and boundary conditions.

The setup is discretized using 17519 quadrilateral elements of effective size $h = 3$ *mm* and material properties $E = 18$ *GPa* and $\nu = 0.2$. The length-scale parameter selected to be $\ell_0 = 6.5$ *mm*. Figure 4.14 shows the crack propagation during the load increments. A state of stress is developed in the present setup, and in 4.14c the tip of the propagating has reached a location in the specimen that is nearly stress-free resulting in crack arrest. Propagation then resumes in the vertical direction as the failure load for the specimen is reached, as shown in Figure 4.14d.

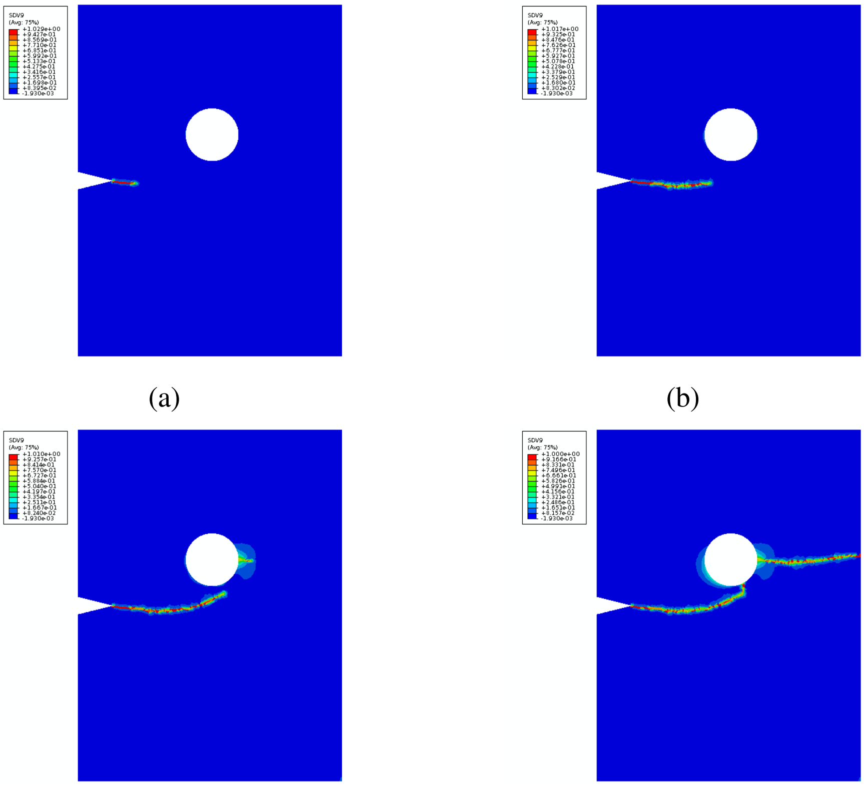

(a) (b)

(c) (d)

Figure 4.14: Notched rectangular specimen with opening tension test. Crack propagation (a)-(d) for a mesh with 17519 elements, element size $h = 3.0$ *mm* with length-scale parameter $\ell_0 = 6.5$ *mm*.

4.1.5 Tension test of a notched rectangular specimen with three openings

The next example demonstrates the effect of varying proximities of openings in altering the path of propagation of a crack. To do this we simulate two samples consisting of notched rectangular plates, each with three circular openings with centers aligned on a single horizontal line. In the first specimen, this line is situated 40 *mm* from the horizontal line emanating from the notch, while in the second specimen the distance has been reduced to 20 *mm* as shown in Figure 4.15 along with the applied loading and boundary conditions.

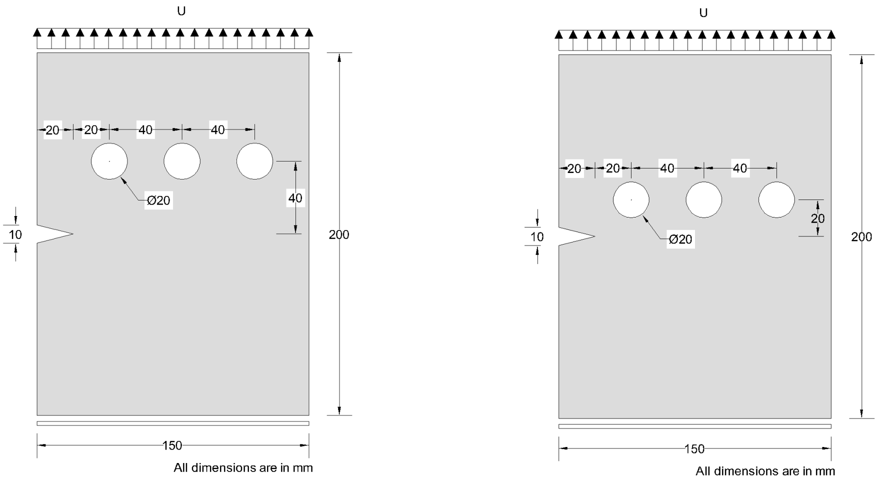

(a)

(b)

Figure 4.15: Notched rectangular specimen with three openings. Geometry, loading and boundary conditions. (a) openings far from the initial notch, (b)openings near the initial notch.

It can be seen in Figure 4.16 that for holes situated significantly far away from the notch line the crack propagation is virtually unaffected by the presence of such features, whereas for sufficiently close openings the crack path is altered.

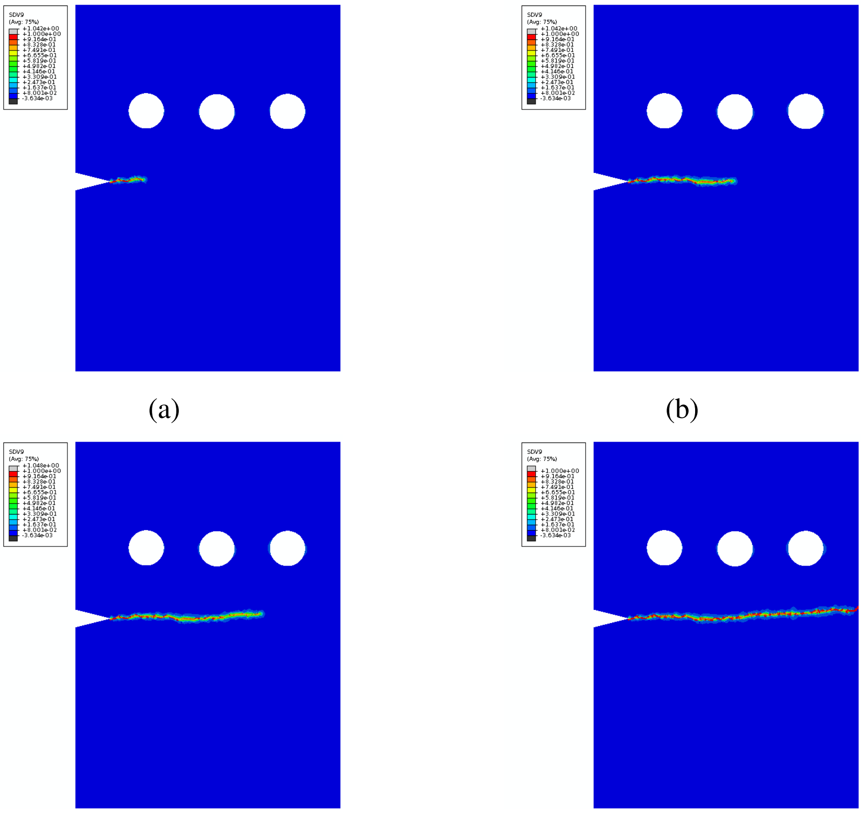

(a)

(b)

(c)

(d)

Figure 4.16: Notched rectangular specimen with three openings tension sample in Figure 4.15a. Crack propagation for a mesh with 18926 elements, element size $h = 3$ mm with length-scale parameter $\ell_0 = 8.5\ mm$.

We can also see from 4.17 that the presence of the opening nearest to the notch causes a kinking of the crack path just below it, however it is not near enough to the notch line as to arrest the crack propagation; this occurs just below the second opening along with the initiation of a new crack segment similar to what was observed in the previous example.

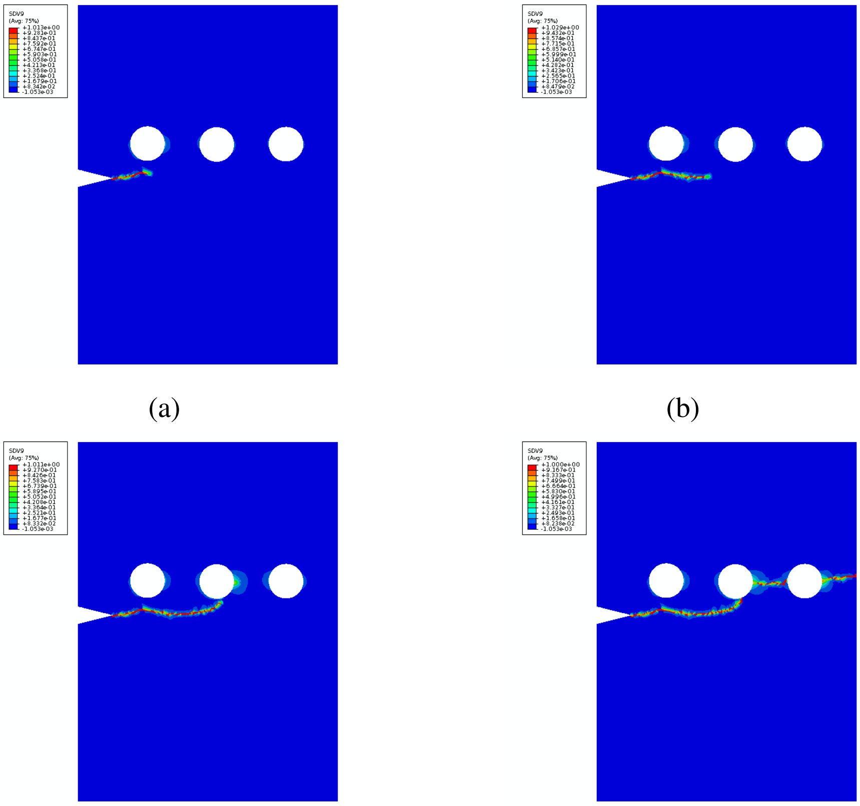

(a) (b)

(c) (d)

Figure 4.17: Notched rectangular specimen with three openings tension sample in Figure 4.15b. Crack propagation (a)-(d) for a mesh with 15724 elements, element size $h = 4$ mm with length-scale parameter $\ell_0 = 8.5$ mm.

The current example along with the preceding one shows a highlights another important strength of the phase field method, specifically that the initiation of a crack does not require the introduction of a notch, and that a crack may initiate anywhere within the geometry of a given body.

4.2 Three dimensional numerical examples

The extension to a 3D phase field model is straightforward and, unlike other crack propagation models, does not need special considerations. In other models, special considerations must be made for brittle fracture models, and the finite element modeling is required since the displacement field may have jump discontinuities at the crack. These considerations are addressed by using remeshing techniques to update the mesh after each crack increment to set the new geometry of discontinuity. Extended finite element method (XFEM) was introduced as an alternative approach, and, through the use of displacement shape functions with an enrichment based on partition of unity method, avoids having to use remeshing techniques. To date, it is very difficult to model complex patterns of cracks in 2D and 3D.

The fully coupled system of phase field model in 3D is implemented in Abaqus with implicit time integration using Newton–Raphson technique. The linear tetrahedron element (C3D4) and quadratic tetrahedron element (C3D10) are implemented in UEL and UMAT subroutines.

Different problems using linear and quadratic tetrahedron element types are determined in the following numerical examples.

4.2.1 Tension test of double notch specimen

The DENT sample in Figure 4.18 is used as a benchmark and discretized using C3D4 and C3D10 elements. The sample has been subjected to tension loading by a displacement with a minimum increment of $\Delta u = 10^{-7}$ and maximum increment of $\Delta u = 10^{-3}$. The material properties are designated as 210 GPa for the modulus of elasticity and 0.25 for Poisson's ratio. The strain energy release rate $\mathscr{G}_c$ is 1.0 N/m. The load–displacement curves of the test are exhibited in Figure 4.20. The results reveal that there is no variation between either element types. The crack propagation steps for various load steps for the two element types are shown in Figure 4.19.

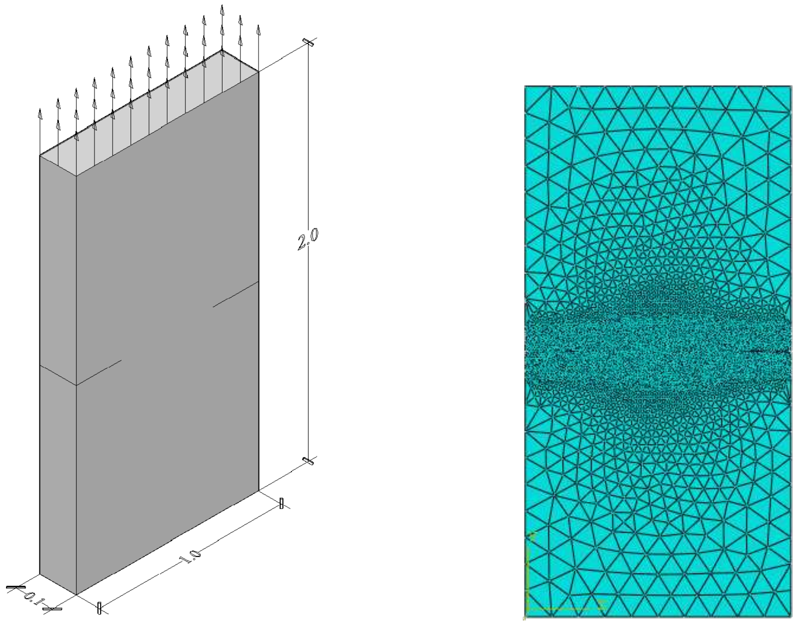

(a) (b)

Figure 4.18: Geometric setup and mesh of 3D DENT sample. (a) Sample dimensions and loading, (b) Mesh discretization. All dimensions are in m.

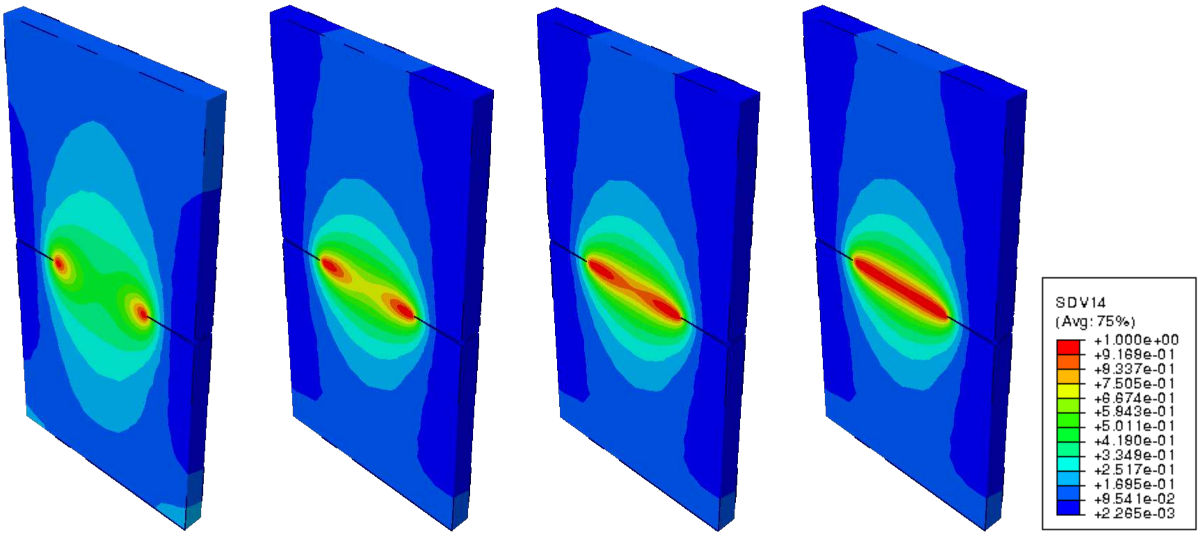

(a) (b) (c) (d)

Figure 4.19: Crack propagation of 3D DENT sample for different load steps. SDV14= phase field. $\ell_0 = 0.06$.

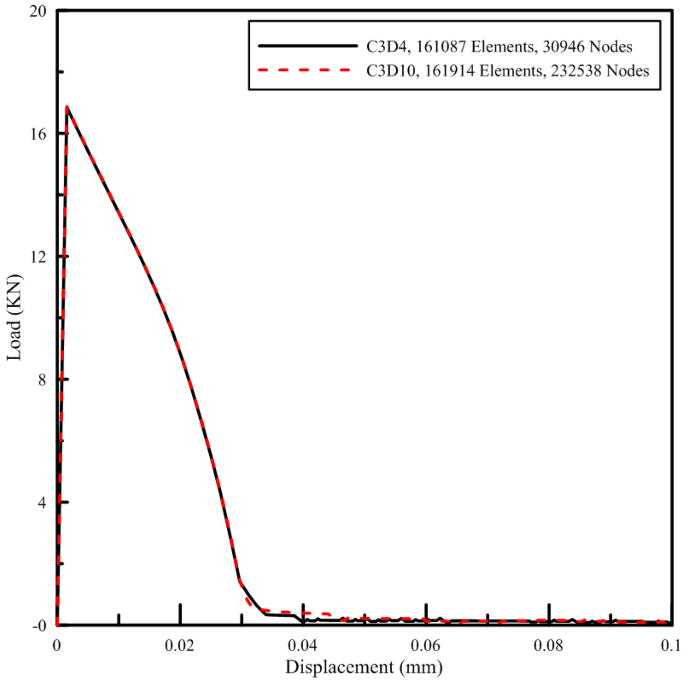

Figure 4.20: Load–displacement curves.

4.2.2 Tension test of side notch specimen with different openings distribution

To test the phase field method capability to cracks propagation in 3D, two samples with different opening distributions are tested. Figure 4.21 shows the geometry, loading, and mesh descritization of the sample. Both samples have the same properties and boundary conditions; however, one of the openings is positioned at different coordinates to track the change in crack path. The samples are subjected to tension from above and pinned from bottom. The Young's modulus of the samples is 210 GPa and Poisson's ratio is 0.3. The strain energy release rate $\mathscr{G}_c$ is 1.0 N/m. Figures 4.22 and 4.23 show the crack propagation steps and how the crack turns towards the voids.

An interesting phenomenon can be observed in crack propagation in both samples, wherein the propagation of the original crack that emanates from the notch of the plate stops at the same time that a new crack segment initiates at the right and left sides of the nearest opening. This occurrence may understood by noting that for an infinite plate with a circular opening subjected to uniform vertical tension, the upper and lower portion of hole must be essentially stress free, whereas the left and right portions are under a tension stress concentration factor of 3. A similar state of stress is developed in the present setup, and in both cases the tip of the propagating crack reaches a location in the specimen that results in crack arrest. Propagation then resumes between the openings.

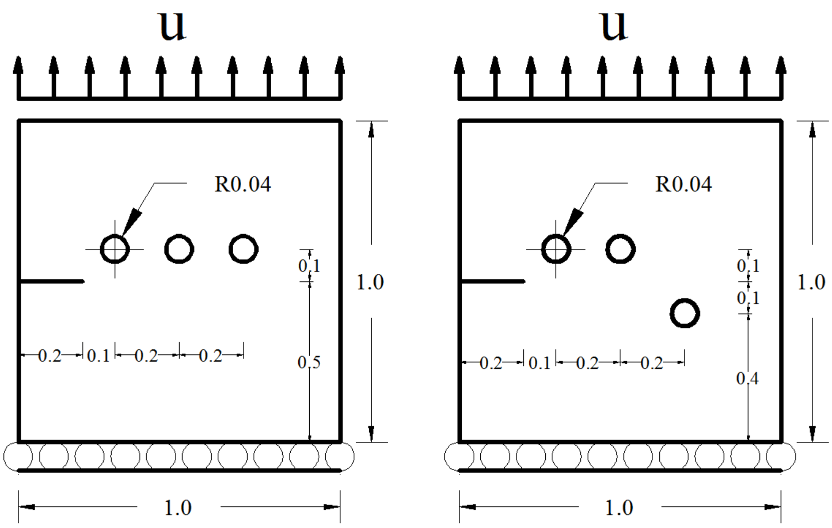

(a)

(b) 94614 Nodes, 503382 Elements.

(c) 100071 Nodes, 532683 Elements.

Figure 4.21: Tension test of 3D side notched specimens with openings. (a) Loading and geometry. (b) and (c) Mesh discretization. Sample thickness is 0.1 m. All dimensions are in m.

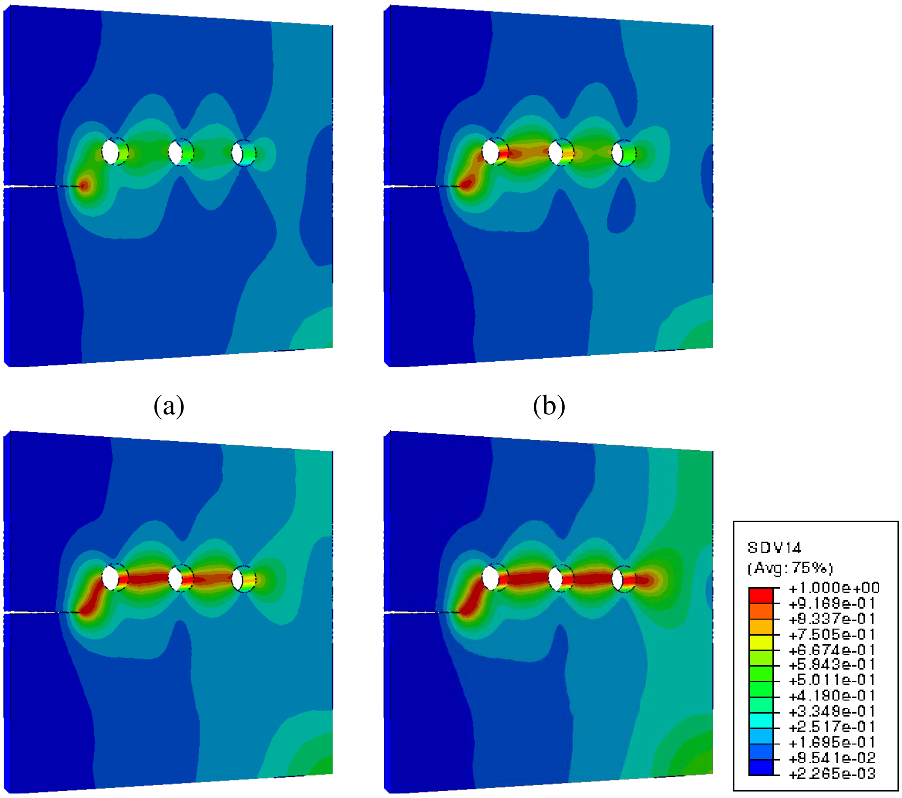

(a) (b)

(c) (d)

Figure 4.22: Crack propagation of 3D side notched sample for different load steps. $\ell_0 = 0.06$

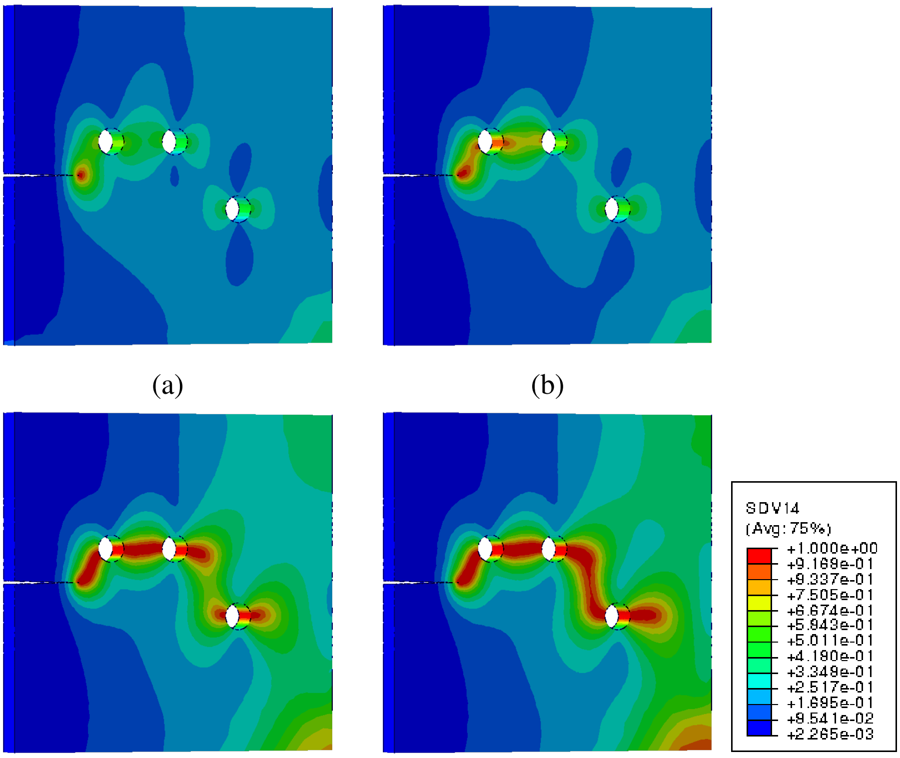

(a) (b)

(c) (d)

Figure 4.23: Crack propagation of 3D side notched sample for different load steps. $\ell_0 = 0.06$.

Conclusion

We have presented a procedure for the implementation of the phase field model within the commercial FE code Abaqus for two- and three- dimensional fracture problems. We have given several numerical examples in 2D and 3D; they were solved and demonstrated the merits of the implementation. In particular the ability of the phase field method to realize non-trivial crack topologies with minimal additional input into the mesh, such as refining the discretization at the vicinity of the expected crack. Mesh refinement is needed to fulfill the requirements regarding the ratio of element sizes to the chosen characteristic length of the phase field diffusion. This ratio should not be greater than 0.5 (2).

Chapter 5

Damage Algorithm Using the Screened Poisson Equation and Local Remeshing

In this chapter, we aim generality with respect to element technology and choose a purely constitutive algorithm which produces either a damage value (in quasi-brittle problems) or a void fraction value (in ductile problems) that also serves as an indicator of material collapse (124). This has been titled *continuum approach to fracture* (125) and we explore it in this work. With this approach, pre-cracks or pre-notches are unnecessary and explicit calculation of crack paths is not performed. Regularization is adopted in the form of a staggered algorithm for the strain with the screened Poisson equation (see, e.g. (126)). To ensure a reasonable solution and an accurate crack path, we use local remeshing when required. A staggered approach (constrained equilibrium analysis, screened Poisson equation, detection, recursive local remeshing, node repositioning, variable transfer) is introduced.

5.1 Governing equations: constitutive integration in finite strains

This section outlines the general material framework used for the computational crack propagation technique herein envisaged, which will be subsequently particularized for different constitutive laws, namely: (1) quasi-brittle material (section 5.1.3) and (2) extended GTN (section 5.1.4). The relevant constitutive quantities are determined solving a general nonlinear constitutive system.

5.1.1 Integration algorithm: equilibrium and relative Green-Lagrange strain

Cauchy equations of equilibrium for a rotated reference configuration are obtained from the corresponding *spatial* equilibrium (derivations for the latter are shown in Ogden (127)). Using standard notation, we write the spatial equilibrium equations as

$$\frac{\partial \sigma_{ij}}{\partial x_{a_j}} + b_i = 0 \tag{5.1}$$

with the Cauchy tensor components σ_{ij} $(i, j = 1, 2, 3)$. In (5.1) i is the direction index and j is the facet index. The components of the body force vector are b_i. In (5.1), coordinates x_{a_j} are the spatial, or deformed, coordinates of a given point under consideration. In addition, the following natural and essential boundary conditions hold on each part of the boundary $\Gamma_a = \Gamma_a^t \cup \Gamma_a^u$ where Γ_a^t is the natural boundary and Γ_a^u is the essential boundary:

$$\bar{\boldsymbol{t}} = \boldsymbol{\sigma} \cdot \boldsymbol{\nu} \quad \text{on} \quad \Gamma_a^t \tag{5.2}$$

$$\bar{\boldsymbol{u}} = \boldsymbol{u} \quad \text{on} \quad \Gamma_a^u \tag{5.3}$$

where $\bar{\boldsymbol{t}}$ is the known stress vector on Γ_a^t where $\boldsymbol{\nu}$ is the outer normal and $\bar{\boldsymbol{u}}$ is the known displacement field on Γ_a^u. It is assumed that (5.1) and (5.2-5.3) are satisfied for a time parameter $t_a \in [0, T]$ with T being the total time of analysis and for a point with position $\boldsymbol{x}_a \in \Omega_a$ belonging to the deformed position domain at the time of analysis. Natural boundary Γ_a^t is evolving in the sense that cracks create boundaries with known $\bar{\boldsymbol{t}}$. Equilibrium configuration corresponds to the domain Ω_a and is identified by the subscript a. In tensor notation, equation (5.1) can be presented as:

$$\boldsymbol{\nabla} \cdot \boldsymbol{\sigma}^T + \boldsymbol{b} = \boldsymbol{0} \tag{5.4}$$

with $\boldsymbol{\nabla} = \partial/\partial \boldsymbol{x}_a$ being the spatial gradient *operator*. After multiplication by the velocity field $\dot{\boldsymbol{u}}$, integration in the deformed configuration Ω_a and application of integration by parts component-wise, we obtain the following power form ($\dot{W}_{\text{int}}$ is the internal and $\dot{W}_{\text{ext}}$

is the external power):

$$\underbrace{\int_{\Omega_a} \boldsymbol{\sigma} : \boldsymbol{L} \mathrm{d}\Omega_a}_{\dot{W}_{\mathrm{int}}} = \underbrace{\int_{\Omega_a} \boldsymbol{b} \cdot \dot{\boldsymbol{u}} \mathrm{d}\Omega_a + \int_{\Gamma_a^t} \bar{\boldsymbol{t}} \cdot \dot{\boldsymbol{u}} \mathrm{d}\Gamma_a}_{\dot{W}_{\mathrm{ext}}} \tag{5.5}$$

where $\boldsymbol{L}$ is the velocity gradient: $\boldsymbol{L} = \frac{\partial \dot{\boldsymbol{x}}_a}{\partial \boldsymbol{x}_a} = \frac{\partial \dot{\boldsymbol{u}}}{\partial \boldsymbol{x}_a}$. $\boldsymbol{L}$ can be decomposed in a symmetric part ($\boldsymbol{D}$, called strain rate) and a skew-symmetric part ($\boldsymbol{W}$, called vorticity), $\boldsymbol{L} = \boldsymbol{D} + \boldsymbol{W}$. Since $\boldsymbol{\sigma}$ has a symmetric component matrix, integrating in the initial configuration (subscript 0, which corresponds to the domain Ω_0), we obtain:

$$\dot{W}_{\mathrm{int}} = \int_{\Omega_0} \boldsymbol{\tau} : \boldsymbol{D} \mathrm{d}\Omega_0 \tag{5.6}$$

where $\boldsymbol{\tau} = J\boldsymbol{\sigma}$ is the Kirchhoff stress tensor with $J = \det \boldsymbol{F}$ with $\boldsymbol{F}$ being the deformation gradient. In the corotational case, we can rotate the Kirchhoff stress and the strain rate to obtain:

$$\dot{W}_{\mathrm{int}} = \int_{\Omega_0} \left(\boldsymbol{R}_{0a}^T \boldsymbol{\tau} \boldsymbol{R}_{0a}\right) : \left(\boldsymbol{R}_{0a}^T \boldsymbol{D} \boldsymbol{R}_{0a}\right) \mathrm{d}\Omega_0 \tag{5.7}$$

From each element nodal arrangement, we use three directions, where $\bar{e}_{1a}$, $\bar{e}_{2a}$ and $\bar{e}_{3a}$ to define $\boldsymbol{R}_{0a}$ as:

$$\boldsymbol{R}_{0a} = [\bar{e}_{1a}, \bar{e}_{2a}, \bar{e}_{3a}] \tag{5.8}$$

where each column is a unit vector and $\bar{\boldsymbol{e}}_{ia} \cdot \bar{\boldsymbol{e}}_{ja} = \delta_{ij}$. We then use the following convention for writing tensors: the bold symbol indicates tensor *components*. Therefore, the frame where the tensor components are defined is identified as a superscript. For example, the second-order tensor $\boldsymbol{S}_{ab}$ with the equilibrium configuration Ω_a and reference configuration Ω_b has the following components in frame c:$\boldsymbol{S}_{ab}^c$. If global frame 0 is adopted, component transformation between frame 0 and frame c follows:

$$\boldsymbol{S}_{ab}^c = \boldsymbol{R}_{c0} \boldsymbol{S}_{ab}^0 \boldsymbol{R}_{c0}^T \tag{5.9}$$

Generalizing (5.9), *change of basis* from d to c results in the following transformation:

$$\boldsymbol{S}_{ab}^c = \boldsymbol{R}_{cd} \boldsymbol{S}_{ab}^d \boldsymbol{R}_{cd}^T \tag{5.10}$$

In addition, change in *reference* configuration reads:

$$\boldsymbol{S}^0_{ac} = \boldsymbol{R}_{bc}\boldsymbol{S}^0_{ab}\boldsymbol{R}^T_{bc} \tag{5.11}$$

Using (5.11) and transformation (5.10) for coinciding reference configuration and frame,

$$\boldsymbol{S}^c_{ac} = \boldsymbol{S}^b_{ab} \tag{5.12}$$

From the relation between the time derivative right Cauchy-Green tensor $\boldsymbol{C}$ and the strain rate $\boldsymbol{D}$, we obtain:

$$\dot{\boldsymbol{C}} = 2\boldsymbol{F}^T\boldsymbol{D}\boldsymbol{F} \tag{5.13}$$

J. Simo (128) derived the following one-step scheme for integrating the strain rate in frame 0, producing the following "strain" from integration of $\boldsymbol{D}$:

$$\boldsymbol{e}^0_{ab,\beta} \cong \frac{1}{2}\boldsymbol{F}^T_{b\beta}\left[\boldsymbol{F}^T_{a\beta}\boldsymbol{F}_{a\beta} - \boldsymbol{I}\right]\boldsymbol{F}_{b\beta} \tag{5.14}$$

Using the previous power conjugacy (5.7) ($\boldsymbol{\tau} = J\boldsymbol{\sigma}$), internal power can be written as:

$$\dot{W}_{\text{int}} = \int_{\Omega_0} \boldsymbol{S}^0_{a0} : \boldsymbol{D}^0_{a0}\mathrm{d}\Omega_0$$

where $\boldsymbol{S}^0_{a0} = \boldsymbol{R}^T_{0a}\boldsymbol{\tau}^0_a\boldsymbol{R}_{0a}$ and $\boldsymbol{D}^0_{a0} = \boldsymbol{R}^T_{0a}\boldsymbol{d}^0_a\boldsymbol{R}_{0a}$. Using an hypoelastic relation, stress updating is performed as:

$$\boldsymbol{S}^0_{a0} = \boldsymbol{S}^0_{b0} + \Delta\check{\boldsymbol{S}}_a(\boldsymbol{R}_{\beta 0}\boldsymbol{e}^0_{ab,\beta}\boldsymbol{R}^T_{\beta 0})$$

where $\Delta\check{\boldsymbol{S}}_a$ is a function of the strain $\boldsymbol{e}^0_{ab,\beta}$. This term $\Delta\check{\boldsymbol{S}}_a$ is called the constitutive part of the stress. However, since $\boldsymbol{S}^0_{a0} = \boldsymbol{S}^b_{ab}$ and $\boldsymbol{S}^0_{b0} = \boldsymbol{S}^b_{bb}$, we have:

$$\boldsymbol{S}^b_{ab} = \boldsymbol{S}^b_{bb} + \Delta\check{\boldsymbol{S}}_a(\boldsymbol{R}_{\beta 0}\boldsymbol{e}^0_{ab,\beta}\boldsymbol{R}^T_{\beta 0})$$

In the case $\beta = b$, the result for (5.14) is:

$$\boldsymbol{S}^b_{ab} = \boldsymbol{S}^b_{bb} + \Delta\check{\boldsymbol{S}}_a(\boldsymbol{e}^b_{ab}) \tag{5.15}$$

with

$$\boldsymbol{e}^b_{ab} \cong \frac{1}{2}\boldsymbol{R}_{b0}\left[\boldsymbol{F}^T_{ab}\boldsymbol{F}_{ab} - \boldsymbol{I}\right]\boldsymbol{R}^T_{b0} \tag{5.16}$$

We now insert the Jacobian for configuration Ω_b in (5.15) as:

$$\underbrace{\frac{1}{J_{b0}}\boldsymbol{S}^{b}_{ab}}_{\boldsymbol{S}^{\star b}_{ab}} = \underbrace{\frac{1}{J_{b0}}\boldsymbol{S}^{b}_{bb}}_{\boldsymbol{\sigma}^{b}_{b}} + \frac{1}{J_{b0}}\Delta\check{\boldsymbol{S}}_{a}(\boldsymbol{e}^{b}_{ab}) \tag{5.17}$$

Defining

$$\boldsymbol{S}^{\star b}_{ab} = \frac{1}{J_{b0}}\boldsymbol{S}^{b}_{ab} \tag{5.18}$$

then we obtain the Cauchy stress in configuration Ω_a and frame a as:

$$\boldsymbol{\sigma}^{a}_{a} = \boldsymbol{S}^{\star a}_{aa} = \frac{1}{J_{a0}}\boldsymbol{S}^{a}_{aa} = \frac{1}{J_{a0}}\boldsymbol{S}^{b}_{ab} = \frac{J_{b0}}{J_{a0}}\boldsymbol{S}^{\star b}_{ab} \tag{5.19}$$

If $\Delta\check{\boldsymbol{S}}_{a}(\boldsymbol{e}^{b}_{ab})$ is homogeneous of degree one, then it follows that:

$$\boldsymbol{S}^{\star b}_{ab} = \boldsymbol{\sigma}^{b}_{b} + \Delta\check{\boldsymbol{S}}_{a}\left(\tilde{\boldsymbol{e}}^{b}_{ab}\right)$$

where

$$\tilde{\boldsymbol{e}}^{b}_{ab} = \frac{1}{J_{b0}}\boldsymbol{e}^{b}_{ab} \tag{5.20}$$

For symmetric tensors, such as $\boldsymbol{S}^{\star b}_{ab}$ and $\boldsymbol{e}^{b}_{ab}$, it is preferable to use the Voigt notation. Upright bold symbols denote Voigt form of symmetric tensors, for example:

$$\mathbf{S}^{\star b}_{ab} = \mathrm{Voigt}[\boldsymbol{S}^{\star b}_{ab}] \tag{5.21}$$

The full algorithm is given in Table 1.

Algorithm 1 General relative Lagrangian formulation (Voigt notation adopted).

Given $\boldsymbol{F}^{b}_{ab}$, $\mathbf{e}^{b}_{ab}$ (*both in frame b*), $\boldsymbol{R}_{0b}$ and $\boldsymbol{R}_{0a}$ (*both in frame* 0) Recovered from storage $\boldsymbol{F}^{b}_{b0}$, $\boldsymbol{\sigma}^{0}_{b}$, $\mathbf{e}^{b}_{b0}$ ($\boldsymbol{\sigma}_{b}$ is stored in frame 0 for purpose of representation)	
Represent Cauchy stress in frame *b*	$\boldsymbol{\sigma}^{b}_{b}=\mathscr{V}_{S}\left(\boldsymbol{R}^{T}_{0b}\right)\boldsymbol{\sigma}^{0}_{b}$
Relevant Jacobian determinants	$J_{b0}=\det\boldsymbol{F}^{b}_{b0}$ $J_{ab}=\det\boldsymbol{F}^{b}_{ab}$
Relative rotation and total deformation gradient update	$\boldsymbol{R}_{ab}=\boldsymbol{R}^{T}_{0a}\boldsymbol{R}_{0b}$ $\boldsymbol{F}^{b}_{a0}=\boldsymbol{F}^{b}_{ab}\boldsymbol{F}^{b}_{b0}$
Total strain update	$\mathbf{e}^{b}_{a0}=\mathbf{e}^{b}_{b0}+\mathscr{V}_{E}\left(\boldsymbol{F}^{bT}_{b0}\right)\mathbf{e}^{b\circ}_{ab}$
Corrected relative strain	$\tilde{\boldsymbol{e}}^{b}_{ab}=\frac{1}{J_{b0}}\boldsymbol{e}^{b}_{ab}$
Determine $\mathbf{S}^{\star b}_{ab}=\boldsymbol{\sigma}^{b}_{b}+\Delta\check{\mathbf{S}}_{a}\left(\tilde{\mathbf{e}}^{b}_{ab}\right)$ along with sensitivity $\mathscr{C}_{ab}=\frac{1}{J_{b0}}\frac{\partial\Delta\check{\mathbf{S}}_{a}}{\partial\tilde{\mathbf{e}}^{b}_{ab}}$	
Determine strain in frame *a*	$\mathbf{e}^{a}_{a0}=\mathscr{V}_{E}\left(\boldsymbol{R}_{ab}\right)\mathbf{e}^{b}_{a0}$
Determine deformation gradient in frame *a*	$\boldsymbol{F}^{a}_{a0}=\boldsymbol{R}_{ab}\boldsymbol{F}^{b}_{a0}\boldsymbol{R}^{T}_{ab}$
Determine Cauchy stress in frame 0	$\boldsymbol{\sigma}^{0}_{a}=\frac{1}{J_{ab}}\mathscr{V}_{S}\left(\boldsymbol{R}_{0a}\right)\mathbf{S}^{\star b}_{ab}$
Store $\boldsymbol{F}^{a}_{a0}$, $\boldsymbol{\sigma}^{0}_{a}$, $\mathbf{e}^{a}_{a0}$ Return $\mathbf{S}^{\star b}_{ab}$ and $\mathscr{C}_{ab}$	

5.1.2 Local constitutive system

We determine the relevant constitutive quantities by solving a *general* nonlinear *constitutive* system. Omitting the frame superscript, it reduces to the root finding for the following nonlinear system:

$$\boldsymbol{\varphi}\left(\underbrace{\mathbf{S}_{ab}}_{\text{Unknown}};\underbrace{\mathbf{e}_{ab}}_{\text{Known}};\underbrace{\boldsymbol{\chi}_{a}}_{\text{Internal var.}}\right)=\mathbf{0} \tag{5.22}$$

where $\boldsymbol{\chi}_a$ is the internal variable vector. For the present application, it is defined as:

$$\boldsymbol{\chi}_a=\left\{\begin{array}{c}\varepsilon_p\\ f_a\end{array}\right\} \tag{5.23}$$

where ε_p is the effective strain and f_a is the damage variable. Newton iteration for (5.22) provides, in general, the solution for the constitutive unknowns $\mathbf{S}_{ab}$ and $\boldsymbol{\chi}_a$. A smoothed version of (5.22) is introduced by using the Chen-Mangasarian replacement functions, which depend on a parameter `Error` such that (129):

$$\lim_{\texttt{Error}\to 0}\boldsymbol{\varphi}_{\texttt{Error}}=\boldsymbol{\varphi} \tag{5.24}$$

Newton iteration on (5.22), using $\boldsymbol{\varphi}_{\texttt{Error}}$ as a replacement provides the following scheme:

$$\underbrace{\left[\begin{array}{cc}\dfrac{\partial\boldsymbol{\varphi}_{\texttt{Error}}}{\partial\mathbf{S}_{ab}} & \dfrac{\partial\boldsymbol{\varphi}_{\texttt{Error}}}{\partial\boldsymbol{\chi}_{a}}\end{array}\right]}_{\boldsymbol{J}}\left\{\begin{array}{c}\Delta\mathbf{S}_{ab}\\ \Delta\boldsymbol{\chi}_a\end{array}\right\}=-\boldsymbol{\varphi}_{\texttt{Error}} \tag{5.25}$$

After achieving solution using the Newton scheme (5.25), we calculate the sensitivities from the following equation:

$$\left\{\begin{array}{c}\mathrm{d}\mathbf{S}_{ab}\\ \mathrm{d}\boldsymbol{\chi}_a\end{array}\right\}=-\boldsymbol{J}^{-1}\left[\frac{\partial\boldsymbol{\varphi}_{\texttt{Error}}}{\partial\mathbf{e}_{ab}}\right]\mathrm{d}\mathbf{e}_{ab} \tag{5.26}$$

Specifically (with further details being given in (129)), an elasto-plastic system is therefore given by:

$$\boldsymbol{\varphi}(\boldsymbol{S}_{ab};\mathbf{e}_{ab})=\left\{\begin{array}{c}\mathbf{e}_{ab}-\mathscr{C}_{\text{linear}}^{-1}\Delta\check{\mathbf{S}}_{ab}-\mathbf{n}\Delta\gamma\\ \mu^{\star}\Delta\gamma-\langle\mu^{\star}\Delta\gamma+\phi\rangle_{\texttt{Error}}\\ \Delta\boldsymbol{\chi}_a-\Delta\gamma\omega(\boldsymbol{\chi}_a)\end{array}\right\} \tag{5.27}$$

where $\Delta\gamma$ is the plastic multiplier increment, $\mu^{\star}$ is a dimensional parameter described in (129) and the smooth ramp function of Chen and Mangasarian (130) is used for the third equation, which depends on `Error`. Function ϕ in (5.27) is the yield function and ω are

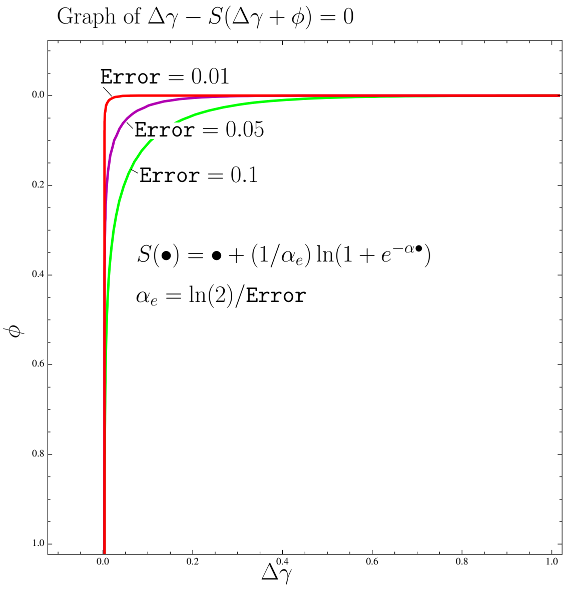

Figure 5.1: Replacement of $\mu^\star\Delta\gamma - \langle\mu^\star\Delta\gamma + \phi\rangle$ by $\mu^\star\Delta\gamma - S(\mu^\star\Delta\gamma + \phi)$ as a function of a Error parameter ($\mu^\star = 1$ is depicted).

the internal variable evolution functions. In addition, the flow vector $\mathbf{n}$ is also required for the flow rule, and it is defined as

$$\mathbf{n} = \frac{\partial\phi}{\partial\mathbf{S}_{ab}} \tag{5.28}$$

Figure 5.1 shows the effect of `Error` in the satisfaction of the complementarity condition. The reason for a unique treatment for *all* yield functions is that any particular yield function is inserted by means of ϕ, $\mathbf{n}$ and derivatives of $\mathbf{n}$. In (5.27), function $\omega(\boldsymbol{\chi}_a)$ is the internal variable evolution function, such that:

$$\dot{\boldsymbol{\chi}}_a = \dot{\gamma}\omega(\boldsymbol{\chi}_a) \tag{5.29}$$

5.1.3 Quasi-brittle model

For the quasi-brittle model, we use the following yield function and hardening law:

$$\phi_{\mathrm{QB}}(y, \mathbf{S}) = \max_{\sigma_I}\left(\det\left[\mathbf{S} - \sigma_I \boldsymbol{I}\right] = 0\right) - y \tag{5.30}$$

$$y = \sigma_{\max}\exp\left(-\frac{\varepsilon_{pa}\sigma_{\max} l}{\mathscr{G}_c}\right) \tag{5.31}$$

and $f = 1 - \frac{y}{E\varepsilon_p}$ where the effective strain $\varepsilon_{pa} = \varepsilon_1$ corresponds to the principal maximum strain. In (5.31), $\sigma_{\max}$ is the maximum stress and $\mathscr{G}_c$ is the fracture energy (mode I) and l is the length scale parameter. This is a Rankine-type yield function with softening, noting that length scale is incorporated in the softening law. To ensure consistence with other models, we identify f as the damage constitutive variable.

5.1.4 GTN model and its integration

The version of the Gurson-Tvergaard-Needleman model introduced by Reis *et al.* (131) is rewritten here in non-dimensional form:

$$\phi_{\mathrm{GTN}}(y, \mathbf{S}, f_\star) = \frac{3\mathbf{S}^T \mathbf{I}_6 \mathbf{T}_{\mathrm{dev}} \mathbf{S}}{2y^2} - \left[1 + q_3 f_\star^2 - 2q_1 f_\star \cosh\left(\frac{q_2 \mathbf{S}^T \mathbf{I}_3}{2y}\right)\right] \tag{5.32}$$

where $\mathbf{I}_6$ is given by:

$$\mathbf{I}_6 = \begin{bmatrix} 1 & 0 & 0 & 0 & 0 & 0 \\ 0 & 1 & 0 & 0 & 0 & 0 \\ 0 & 0 & 1 & 0 & 0 & 0 \\ 0 & 0 & 0 & 2 & 0 & 0 \\ 0 & 0 & 0 & 0 & 2 & 0 \\ 0 & 0 & 0 & 0 & 0 & 2 \end{bmatrix} \tag{5.33}$$

and $\mathbf{T}_{\mathrm{dev}}$ is the deviatoric projection matrix:

$$\mathbf{T}_{\mathrm{dev}} = \frac{1}{3} \begin{bmatrix} 2 & -1 & -1 & 0 & 0 & 0 \\ -1 & 2 & -1 & 0 & 0 & 0 \\ -1 & -1 & 2 & 0 & 0 & 0 \\ 0 & 0 & 0 & 3 & 0 & 0 \\ 0 & 0 & 0 & 0 & 3 & 0 \\ 0 & 0 & 0 & 0 & 0 & 3 \end{bmatrix} \tag{5.34}$$

In addition, $\mathbf{I}_3$ is the Voigt form of the second-order identity matrix:

$$\mathbf{I}_3 = \begin{bmatrix} 1 & 0 & 0 & 0 & 0 & 0 \\ 0 & 1 & 0 & 0 & 0 & 0 \\ 0 & 0 & 1 & 0 & 0 & 0 \\ 0 & 0 & 0 & 0 & 0 & 0 \\ 0 & 0 & 0 & 0 & 0 & 0 \\ 0 & 0 & 0 & 0 & 0 & 0 \end{bmatrix} \tag{5.35}$$

The effective void fraction $f_\star$ is a function of the current void fraction f. We use the nucleation part of the void fraction following the work of Chu and Needleman (132) using the normal distribution:

$$\dot{f}_N = \frac{f_N}{S_N\sqrt{2\pi}}\exp\left[-\frac{1}{2}\left(\frac{\varepsilon_{pa}-\varepsilon_N}{S_N}\right)^2\right]\dot{\varepsilon}_p \tag{5.36}$$

where f_N, S_N and ε_N are constitutive properties for the nucleation (N) part of the *void fraction* law. The classical void growth term of Gurson (133) is adopted:

$$f_G = 1-\exp(-\varepsilon_v) \tag{5.37}$$

where ε_v is the trace of deformation. In addition, the shear part of Xue and Nahshon (134–136) are combined to obtain the following term:

$$f_S = \frac{3q_6}{2}\left(\frac{6}{\pi}\right)^{\frac{1}{3}}\left(1-54\frac{\det^2\left[\boldsymbol{S}_{\text{dev}}\right]}{\left(\mathbf{S}^T\mathbf{I}_6\mathbf{T}_{\text{dev}}\mathbf{S}\right)^3}\right)f^{\frac{1}{3}}\varepsilon_{pa}^2 \tag{5.38}$$

Including the initial void fraction, f_0, then the total f follows the following *closed-form* laws from the above classical relations:

$$f = \underbrace{f_0+\frac{f_N}{2}\left[\text{ERF}\left(\frac{\varepsilon_N}{S_N\sqrt{2}}\right)-\text{ERF}\left(\frac{\varepsilon_N-\varepsilon_p}{S_N\sqrt{2}}\right)\right]+1-\exp\left(-\varepsilon_v\right)}_{\overline{f}}+ \tag{5.39}$$

$$\underbrace{\frac{3q_6}{2}\left(\frac{6}{\pi}\right)^{\frac{1}{3}}\left(1-54\frac{\det^2\left[\boldsymbol{S}_{\text{dev}}\right]}{\left(\mathbf{S}^T\mathbf{I}_6\mathbf{T}_{\text{dev}}\mathbf{S}\right)^3}\right)\overline{f}^{\frac{1}{3}}\varepsilon_{pa}^2}_{f_S} \tag{5.40}$$

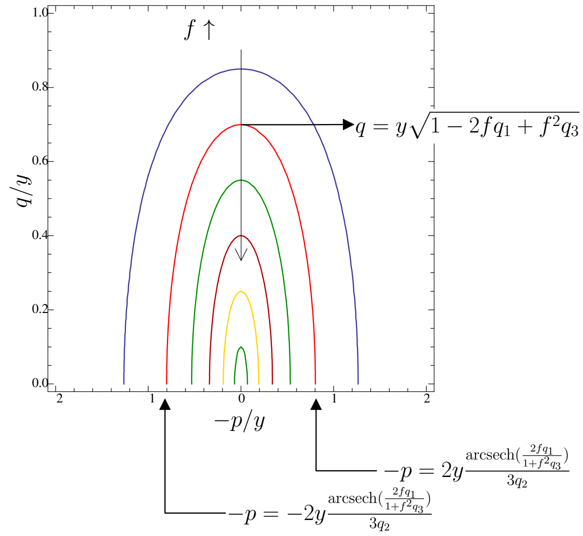

Figure 5.2: Extended GTN yield function ($y = q_1 = q_2 = q_3 = 1$) with $p = -\mathbf{S}^T\mathbf{I}_3/3$ and $q = \sqrt{\frac{3}{2}\mathbf{S}^T\mathbf{I}_6\mathbf{T}_{\text{dev}}\mathbf{S}}$.

The additional property q_6 controls the void growth in shear. A depiction of (5.32) with is shown in Figure 5.2. The GTN model is symmetric with respect to the trace of **S**. The effect of increasing f can be observed as a uniform reduction in radius of the yield surface.

The error function ERF($\bullet$) results from closed-form integration of the Gaussian curve, is available in several open-source libraries, and is defined as:

$$\text{ERF}(\bullet) = \frac{2}{\sqrt{\pi}} \int_0^{\bullet} e^{-t^2} \text{d}t \tag{5.41}$$

Two distinct types of effective plastic strain are adopted[1], ε_v and ε_p. The latter being given as:

$$\dot{\varepsilon}_p = \frac{\dot{\gamma}}{(1-f)y} \mathbf{S}_{ab}^T \mathbf{n} \tag{5.42}$$

Integration of constitutive quantities follow the unconditionally stable backward-Euler scheme:

$$\varepsilon_{pa} = \varepsilon_{pb} + \frac{\Delta\gamma}{(1-f)y} \mathbf{S}_{ab}^T \mathbf{n} \tag{5.43}$$

---

[1] No power-consistent closed-form solution exists for the effective plastic strain in the *classical* Gurson model.

In addition, we have the trace of the flow vector, which is used to obtain ε_v:

$$\dot{\varepsilon}_v = \dot{\gamma}\left(\mathbf{n}^T \mathbf{I}_3\right) \tag{5.44}$$

It is straightforward to obtain the critical f_f, corresponding to collapse, which is given by:

$$f_f = \frac{q_1 + \sqrt{q_1^2 - q_3}}{q_3} \tag{5.45}$$

The effective void fraction $f_\star$ is calculated according to the additional property f_c, using the Tvergaard-Needleman modification (137):

$$f_\star = \begin{cases} f, & f < f_c \\ f_c + \frac{f_f - f_c}{f_m - f_c}\left(f - f_c\right) & f_c \leq f \leq f_m \\ f_f & f > f_m \end{cases} \tag{5.46}$$

The effective void fraction (5.46) is used in the yield function, and is not updated as is the case of f.

Summary of properties for constitutive models

Constitutive properties of the quasi-brittle and the ductile model are shown in Table 5.1.

Table 5.1: Constitutive properties for the quasi-brittle and porous model (extended GTN).

	Quasi-brittle	**GTN**
Elastic properties	E, ν	E, ν
Hardening law	$y = \sigma_{\max} \exp\left(-\frac{\varepsilon_p \sigma_{\max} l_{\min}}{G_F}\right)$	$y \equiv y_0 + K_h \varepsilon_p^n$ where y_0, K_h and n are hardening properties
Initial void fraction	0	f_0
Void fraction properties	$\sigma_{\max}$	q_1
	$\mathscr{G}_c$	q_2
		q_3
Nucleation		f_N
		S_N
		ε_N
Shear		q_6
Coalescence		f_c
		f_m

5.2 Arnold's MINI formulation for plasticity problems: use of relative strains

5.2.1 General formulation

Due to the number of constraints present in low-order elements and the inability of displacement-based elements to separate incompressibility constraints from quadrature points (138, 139). Usually, mixed elements are a solution for avoiding locking in quasi-incompressible problems. The low-order MINI element by Douglas Arnold (140), see also Bathe (141) for a similar two-field method, is based on a formulation where:

Pressure is linearly interpolated using the corner nodes.

An internal shape function, called a bubble, enriches the velocity or displacement fields.

This passes the inf-sup condition and is easily extended to finite strains (142). Since Cauchy stress is calculated from the constitutive stress $\mathbf{S}_{ab}^{\star b}$ as:

$$\boldsymbol{\sigma}_a^a = \frac{1}{J_{ab}} \mathbf{S}_{ab}^{\star b} \tag{5.47}$$

Cauchy pressure is obtained as:

$$p_a = -\frac{\left(\mathbf{S}_{ab}^{\star b}\right)^T \mathbf{I}_3}{3 J_{ab}} \tag{5.48}$$

We can therefore write $\mathbf{S}_{ab}^{\star b}$ in Voigt form as a sum of deviatoric and pressure terms:

$$\mathbf{S}_{ab}^{\star b} = -J_{ab} p_a \mathbf{I}_3 + \mathbf{T}_{\text{dev}} \mathbf{S}_{ab}^{\star b} \tag{5.49}$$

where $\mathbf{T}_{\text{dev}}$ is the following sparse matrix (plane strain and axisymmetric cases):

$$\mathbf{T}_{\text{dev}} = \begin{bmatrix} \frac{2}{3} & -\frac{1}{3} & -\frac{1}{3} & 0 \\ -\frac{1}{3} & \frac{2}{3} & -\frac{1}{3} & 0 \\ -\frac{1}{3} & -\frac{1}{3} & \frac{2}{3} & 0 \\ 0 & 0 & 0 & 1 \end{bmatrix} \tag{5.50}$$

In terms of power balance, we use the following relation, where $\widetilde{\mathbf{S}}^{\star b}_{ab}$ depends on the independent pressure $\widetilde{p}$. It corresponds to a classical two-field variational principle:

$$\underbrace{\int_{\Omega_b} \left(\widetilde{\mathbf{S}}^{\star b}_{ab}\right)^T \dot{\mathbf{e}}^{b}_{ab} \mathrm{d}\Omega_b + \int_{\Omega_b} \left(J_{ab}\widetilde{p} + \frac{\left(\mathbf{S}^{\star b}_{ab}\right)^T \mathbf{I}_3}{3} \right) \dot{\widetilde{p}} \mathrm{d}\Omega_b}_{\dot{W}_{\text{int}}} = \dot{W}_{\text{ext}} \tag{5.51}$$

where the relative Jacobian J_{ab} is used to ensure correct volume calculation. We note that the product $J_{ab}\widetilde{p}$ cannot be used as an unknown field. In (5.51), we have the following quantities:

$$\widetilde{\mathbf{S}}^{\star b}_{ab} = -J_{ab}\widetilde{p}\mathbf{I}_3 + \mathbf{T}_{\text{dev}}\mathbf{S}^{\star b}_{ab} \tag{5.52}$$

Discretization follows the standard MINI *triangular* formulation:

$$\boldsymbol{u}(\boldsymbol{\xi}) = \sum_{K=1}^{4} N_K(\boldsymbol{\xi})\,\boldsymbol{u}_K \tag{5.53}$$

where $\boldsymbol{\xi}$ are the parent-domain coordinates of the triangle. Independent pressure $\widetilde{p}$ is interpolated using the corner nodes:

$$\widetilde{p}(\boldsymbol{\xi}) = \sum_{K=1}^{3} N_K(\boldsymbol{\xi})\,\widetilde{p}_K \tag{5.54}$$

$$N_1(\boldsymbol{\xi}) = 1 - \xi_1 - \xi_2 \tag{5.55a}$$

$$N_2(\boldsymbol{\xi}) = \xi_1 \tag{5.55b}$$

$$N_3(\boldsymbol{\xi}) = \xi_2 \tag{5.55c}$$

The bubble function is given by:

$$N_4(\boldsymbol{\xi}) = \xi_1\xi_2(1 - \xi_1 - \xi_2) \tag{5.55d}$$

For the calculation of the stiffness matrix, the variation of (5.51) is required. Not all quantities are determined by hand-derivation, and we use Mathematica (143) with the AceGen (144) add-on to calculate some derivatives. Using (5.51), we obtain:

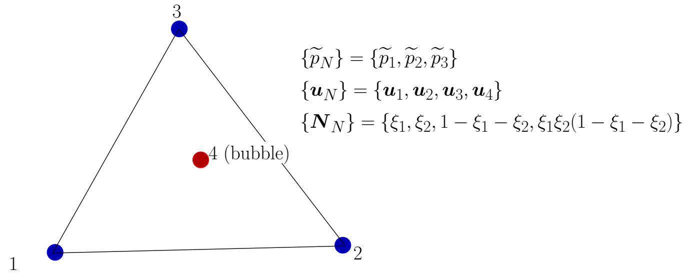

Figure 5.3: MINI triangle.

$$\begin{aligned} \mathrm{d}\dot{W}_{\text{int}} &= \int_{\Omega_b} \left(\left(\mathrm{d}\widetilde{\mathbf{S}}^{\star b}_{ab} \right)^T \dot{\mathbf{e}}^b_{ab} + \left(\widetilde{\mathbf{S}}^{\star b}_{ab} \right)^T \mathrm{d}\dot{\mathbf{e}}^b_{ab} \right) \mathrm{d}\Omega_b && (5.56) \\ &\quad + \int_{\Omega_b} \left(\mathrm{d}J_{ab}\widetilde{p} + J_{ab}\mathrm{d}\widetilde{p} + \frac{\left(\mathrm{d}\mathbf{S}^{\star b}_{ab}\right)^T \mathbf{I}_3}{3} \right) \dot{\widetilde{p}}\mathrm{d}\Omega_b && (5.57) \end{aligned}$$

where the following notation was used:

$$\begin{aligned} \mathrm{d}\mathbf{S}^{\star b}_{ab} &= \mathscr{C}_{ab}\mathrm{d}\mathbf{e}^b_{ab} && (5.58) \\ \mathrm{d}\widetilde{\mathbf{S}}^{\star b}_{ab} &= \mathbf{T}_{\text{dev}}\mathscr{C}_{ab}\mathrm{d}\mathbf{e}^b_{ab} - \mathrm{d}J_{ab}\widetilde{p}\mathbf{I}_3 - J_{ab}\mathrm{d}\widetilde{p}\mathbf{I}_3 && (5.59) \end{aligned}$$

Specifically, the terms $\mathrm{d}\mathbf{e}^b_{ab}$ and $\mathrm{d}J_{ab}$ are determined by AceGen. A depiction representing the degree-of-freedom distribution of a MINI triangle is presented in Figure 5.3.

Specifics of axisymmetric and plane-strain triangles

Dimensional reduction for plane-strain requires careful consideration of out-of-plane stress, which is in general non-null. We therefore explicitly enforce the plane-strain condition by setting 13 and 23 components of both stress and strain as zero, but including the out-of-plane stress $\left[\widetilde{\boldsymbol{S}}^{\star b}_{ab}\right]_{33}$ as active. Therefore, for plane strain, we only omit out-of-plane shear components of stress and strain. In the axisymmetric case, we use reduced integration, which is sufficient to remove locking in the near-incompressible case.

5.3 Regularization with the screened Poisson equation

5.3.1 Relation with nonlocal models

The classical screened Poisson equation (126) (typically named Helmholtz-like, (145, 146)) is adopted to regularize the otherwise ill-posed equilibrium problem in the presence of strain softening (147). Using an additional field, $\overline{\varepsilon}_p$, we perform a coupling with the constitutive-based ε_p as:

$$l^2\left(\nabla_b^2\overline{\varepsilon}_p\right):\boldsymbol{I}=\overline{\varepsilon}_p-\varepsilon_p \tag{5.60}$$

with the following boundary condition:

$$\nabla_b\overline{\varepsilon}_p\cdot\boldsymbol{n}_b=0 \quad \text{in}\,\Gamma_b \tag{5.61}$$

which was established by Lasry and Belytschko (148) who used an explicit version of this model. In (5.60), ∇_b^2 is the Laplacian with respect to the coordinates in configuration Ω_b. This allows the diffusion effect of (5.60) without the well-known (146) flattening effect. The solution of this equation in spherical coordinates is well known:

$$\overline{\varepsilon}_p(\boldsymbol{x}_b)=\int_{\Omega_b}\underbrace{\left(\frac{e^{-\frac{\|\boldsymbol{x}_b-\boldsymbol{x}'_b\|}{l}}}{4\pi l^2\|\boldsymbol{x}_b-\boldsymbol{x}'_b\|}\right)}_{W(\boldsymbol{x}_b,\boldsymbol{x}'_b)}\varepsilon_p(\boldsymbol{x}'_b)\mathrm{d}\boldsymbol{x}'_b \tag{5.62}$$

where $\boldsymbol{x}'_b$ is the integration variable. We note that $\overline{\varepsilon}_p$ is a weighted average of ε_p. The weight function $W(\boldsymbol{x}_b,\boldsymbol{x}'_b)$ in (5.62) shows a dependence on the characteristic length l and also that the support is the whole domain Ω_b. $\overline{\varepsilon}_p(\boldsymbol{x}_b)$ given by equation (5.62) is a weighted average and therefore mesh size only affects the local quantity ε_p which is not directly responsible for softening, as f depends on $\overline{\varepsilon}_p(\boldsymbol{x}_b)$.

5.3.2 Weak form

We use a staggered scheme to regularize the strain-softening problem. We introduce a triangular element that implements equation (5.60) using the following weak form using the previous rate notation:

$$\dot{W}_{\varepsilon_p} = \int_{\Omega_b} \left[-l^2 \left(\nabla_b \overline{\varepsilon}_p \cdot \nabla_b \dot{\overline{\varepsilon}}_p \right) + \left(\varepsilon_p - \overline{\varepsilon}_p \right) \dot{\overline{\varepsilon}}_p \right] \mathrm{d}\Omega_b \tag{5.63}$$

where, in terms of discretization, $\overline{\varepsilon}_p = \sum_{K=1}^{3} N_K(\boldsymbol{\xi})\overline{\varepsilon}_{pK}$ where $N_K(\boldsymbol{\xi})$ are the classical shape functions and $\overline{\varepsilon}_{pK}$ are the nodal unknowns for the regularization element. Linearization of (5.63) follows:

$$\mathrm{d}\dot{W}_{\varepsilon_p} = \int_{\Omega_b} \left[-l^2 \left(\nabla_b \mathrm{d}\overline{\varepsilon}_p \cdot \nabla_b \dot{\overline{\varepsilon}}_p \right) - \mathrm{d}\overline{\varepsilon}_p \dot{\overline{\varepsilon}}_p \right] \mathrm{d}\Omega_b \tag{5.64}$$

The implementation is performed with Mathematica (143) and AceGen software (144).

5.4 Local mesh refinement algorithm

The local remeshing technique is presented as Algorithm 2. Five major steps are performed (1. edge marking, 2. node and element creation, 3. element marking, 4. element deactivation, 5. mesh smoothing and mapping). Note that the undeformed or initial configuration is used for remeshing.

Algorithm 2 Localized remeshing Algorithm.

- Mark edges for splitting based on a convex interpolation of f(Figure 5.4).
- Mark edges for splitting based on the aspect ratio of adjacent elements (Figure 5.4).

- Create new nodes in the center of marked edges (Figure 5.5)
- Create new elements by subdivision of elements with marked edges (Figure 5.5).

- Mark elements for unloading based on f_e and $\dot{f}_e$: if $\dot{f}_e > 0$ and $f_e \geq (1 - tol_3)\, f_{\max}$.
- Mark elements for unloading based on the number of neighbor unloaded elements (greater or equal to two).

- Deactivate marked elements (set the internal forces to null vector) If any element was deactivated, shift displacement/load parameter so that unloading of the structure occurs.

- Perform mesh smoothing.
- Map degrees-of-freedom and history variables for the new mesh.

Splitting edges is much simpler than rotating edges (149) and duplicating tip nodes since no specific crack path tracking is required. Concerning the tolerances, Table 5.2 shows typical values (used in this work). We note that only two parameters are required from the analyst: tol_3 and $l_{\min}$.

Table 5.2: Typical values of the parameters for the localized remeshing algorithm.

Symbol	Interpretation	Typical Value
tol_1	Ratio of lengths, below which an edge is splitted	0.70
tol_2	Ratio between length of the largest edge and the sum of the other two lengths above which the largest edge is splitted.	0.95
tol_3	Percentage of maximum damage or void fraction above which the element is deactivated	$0.04^{\star}$
$l_{\min}$	Minimum edge length	⊛
*User-overridable		
⊛User -defined		

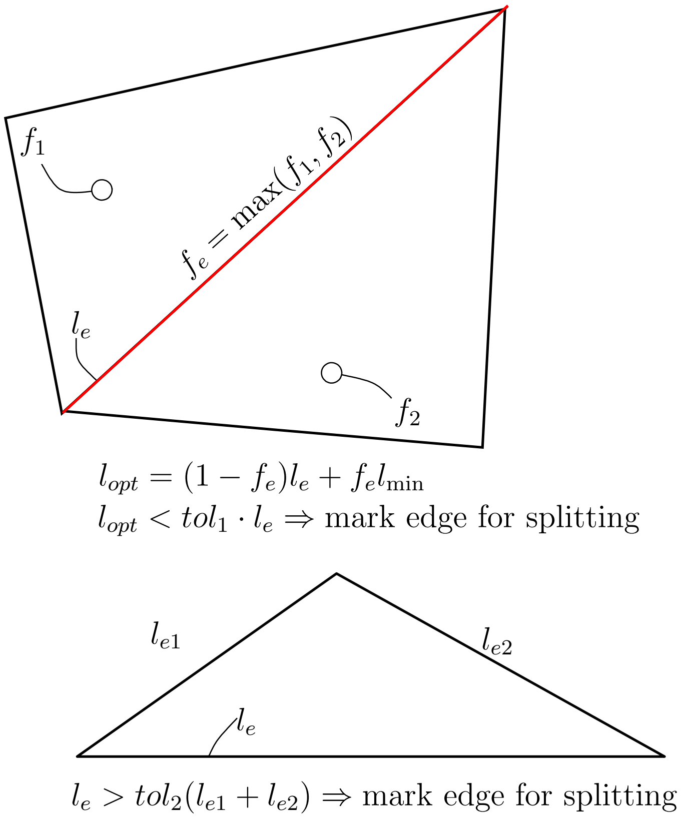

Figure 5.4: Splitting based on f and aspect ratio.

We use a nodal smoothing based on the weighted Laplacian method (150) using length ratios as weights:

$$\boldsymbol{X}_K = \frac{1}{\sum_{I=1}^{N_n} \alpha_{KI}} \sum_{I=1}^{N_n} \alpha_{KI} \boldsymbol{X}_{KI} \tag{5.65}$$

where I is a given node number connected to node K by an element, N_n is the number of nodes connected to K, and

$$\alpha_{KI} = \frac{\|\boldsymbol{X}_I - \boldsymbol{X}_K\|}{\|\boldsymbol{X}_I - \boldsymbol{X}_K\|(1 - \zeta_I) + l_{\min}\zeta_I} \tag{5.66}$$

$$\zeta_I = f^I_{\max} \tag{5.67}$$

where $f^I_{\max}$ is the maximum damage parameter value of elements sharing node I.

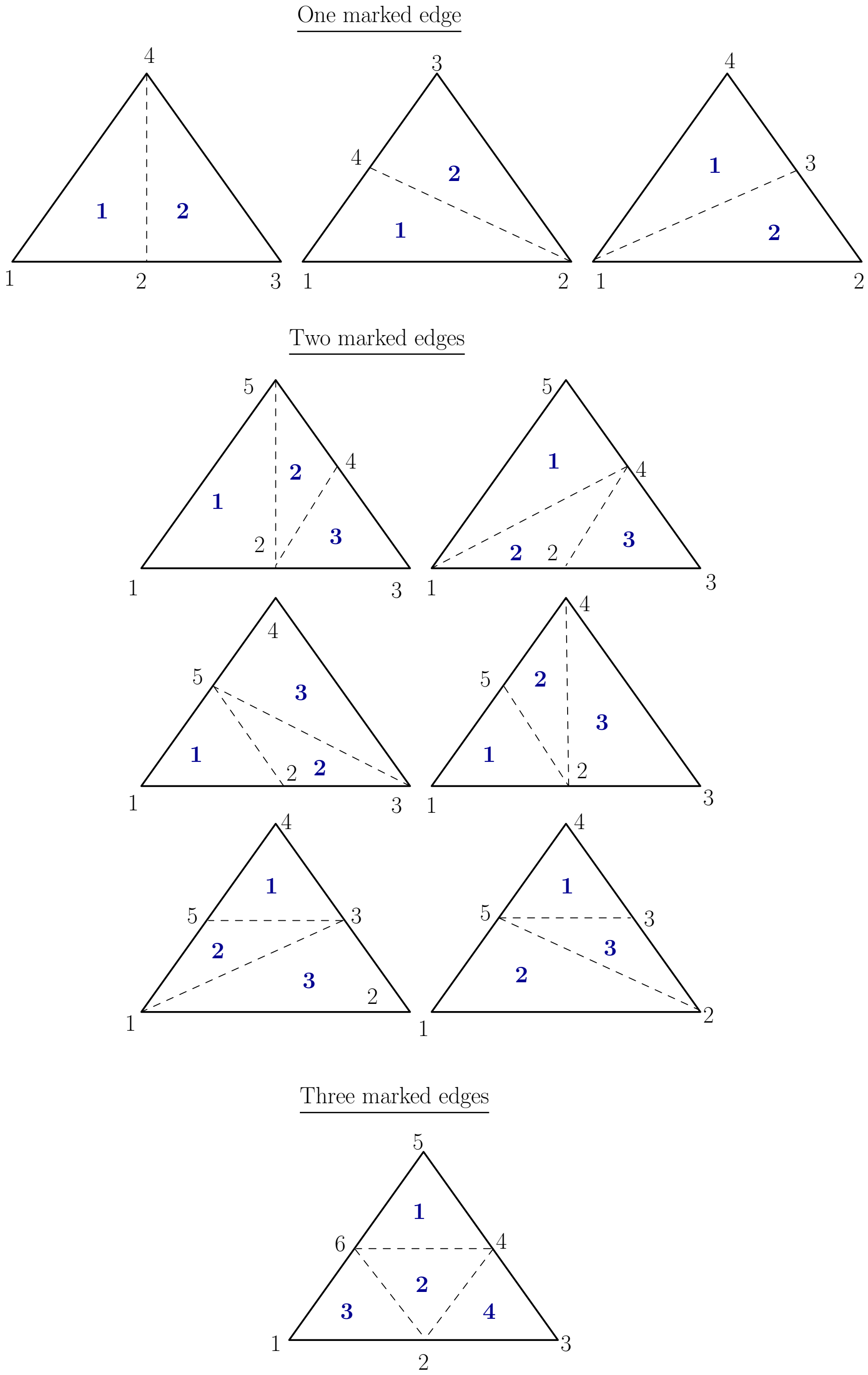

Figure 5.5: Element division algorithm. In **bold**: local element numbers.

Mapping between meshes is strictly geometric and consists of the following two stages:

- Finding the element in the previous mesh where the centroid of *each element* in the current mesh falls. Then *copy* the constitutive history data.

- Finding the element in the previous mesh where each node of the current mesh falls. Then *interpolate* the degrees-of-freedom.

The projection of a given node or a given centroid with coordinates $\boldsymbol{X}^n$ of the current mesh on the previous mesh (o) is performed as follows. First, the parent-domain coordinates are determined determining quantities $\boldsymbol{a}$, $\boldsymbol{b}$ and $\boldsymbol{c}$:

$$\boldsymbol{a} = \boldsymbol{X}_3^o - \boldsymbol{X}^n \tag{5.68}$$

$$\boldsymbol{b} = \boldsymbol{X}_3^o - \boldsymbol{X}_1^o \tag{5.69}$$

$$\boldsymbol{c} = \boldsymbol{X}_3^o - \boldsymbol{X}_2^o \tag{5.70}$$

and then solving the following system for ξ_1 and ξ_2:

$$\begin{bmatrix} \boldsymbol{b}\cdot\boldsymbol{b} & \boldsymbol{b}\cdot\boldsymbol{c} \\ \boldsymbol{b}\cdot\boldsymbol{c} & \boldsymbol{c}\cdot\boldsymbol{c} \end{bmatrix} \left\{ \begin{array}{c} \xi_1 \\ \xi_2 \end{array} \right\} = \left\{ \begin{array}{c} \boldsymbol{a}\cdot\boldsymbol{b} \\ \boldsymbol{a}\cdot\boldsymbol{c} \end{array} \right\} \tag{5.71}$$

If $(\xi_1,\xi_2) \in [0,1]\times[0,1]$ then $\boldsymbol{X}^n$ projects in triangle $\{\boldsymbol{X}_1^o,\boldsymbol{X}_2^o,\boldsymbol{X}_3^o\}$. A depiction of this projection is shown in Figure 5.6.

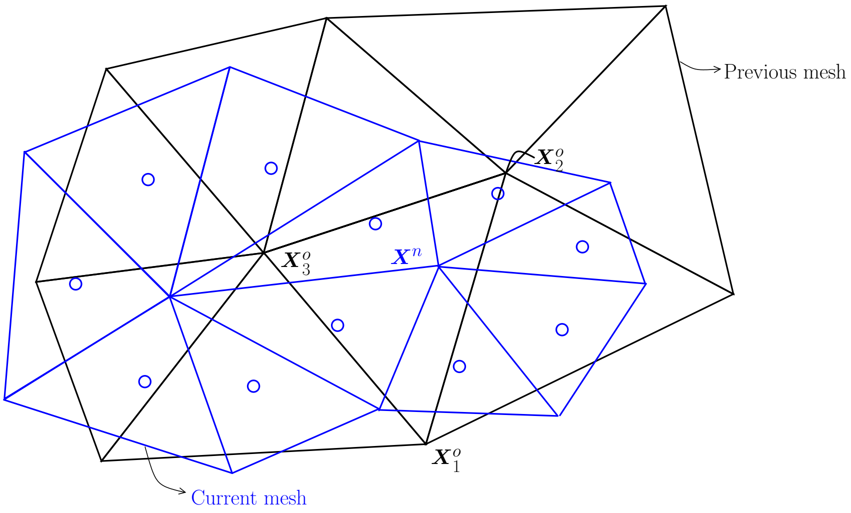

Figure 5.6: Projection of quantities associated with coordinates $\boldsymbol{X}^n$ in the previous element $\{\boldsymbol{X}_1^o,\boldsymbol{X}_2^o,\boldsymbol{X}_3^o\}$.

5.5 Numerical examples

All numerical tests were solved with an in-house software (124) with the formulations shown in previous sections. In terms of discretization, MINI (140) elements were implemented to comply with the relative Green-Lagrange strains. Internal degrees-of-freedom of mixed elements are condensed out. Two types of solution control were used: imposed displacement and crack mouth sliding displacement (CMSD). Local mesh refinement is used in some of the problems, according to what was described in section 5.4. Although relatively fine meshes are employed, mesh refinement is still required for the erosion process to ensure a well defined crack.

5.5.1 Effect of l, mesh and step size

We are concerned with robustness and reproducibility of results with strain softening. Mesh dependence is expected for nonlinear problems and to be acute for unregularized strain softening problems. With the prototype problem described in Figure 5.7, we assess the effect of solution parameters in the results (for the quasi-brittle constitutive model). Since load-displacement results are known to be sensitive to mesh (in unregularized methods) and length scale (in gradient-enhanced algorithms, (146)), these two effects are assessed. Staggered schemes can be sensitive to step size and this is also inspected here. In terms of results, Figure 5.7 shows the effect of l in the spreading of void fraction (f) around the damaged region. We note that the support of f is also affected by the use of l in equation 5.31. Quantitatively, Figure 5.11 shows the effect of l on the load–displacement diagram, on $\overline{\varepsilon}_p \times l$ and f at the monitored node. We also inspect mesh size and step size dependence in Figure 5.12.

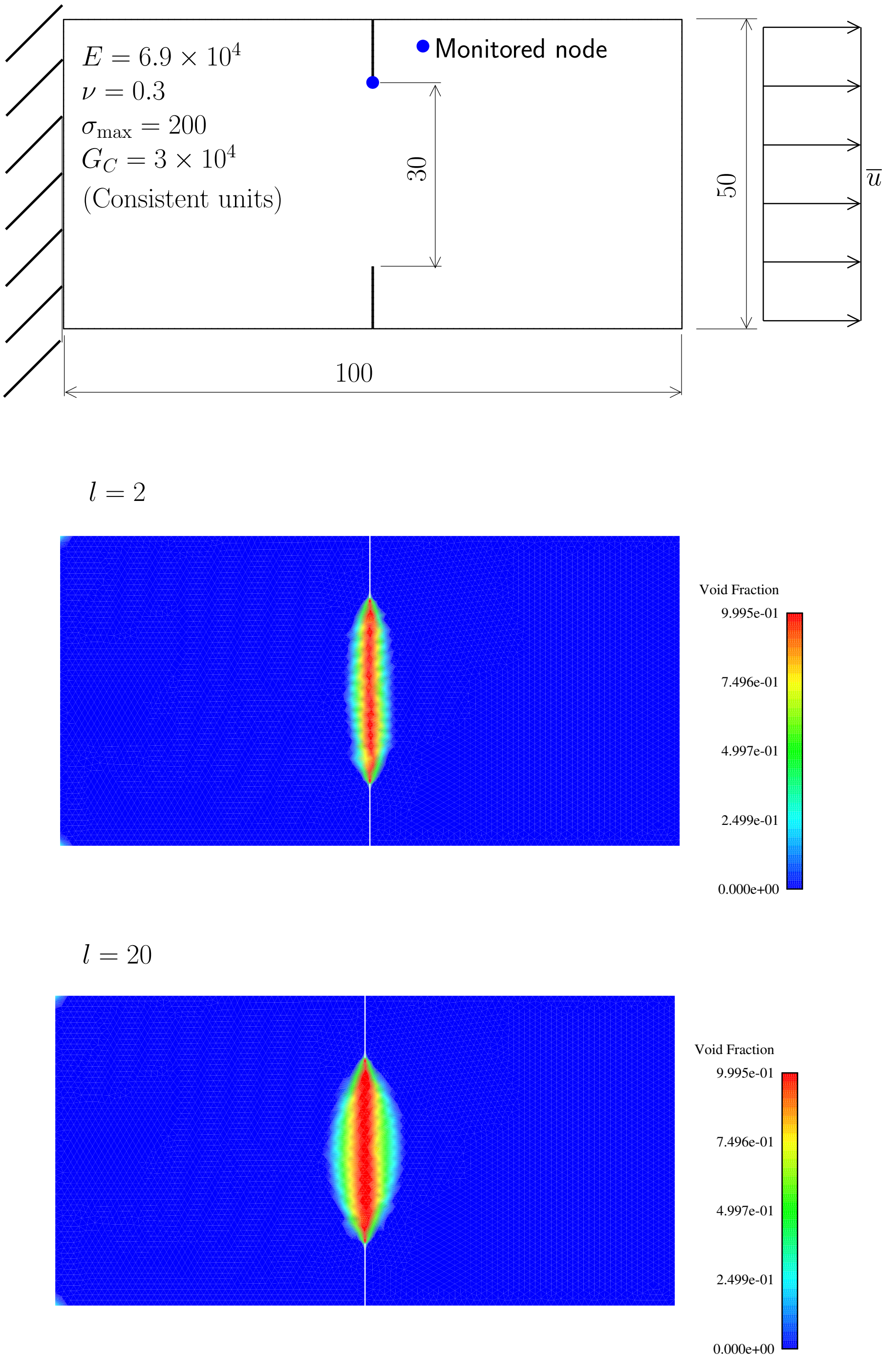

Figure 5.7: Pulling specimen: prototype problem for parameter sensitivity.

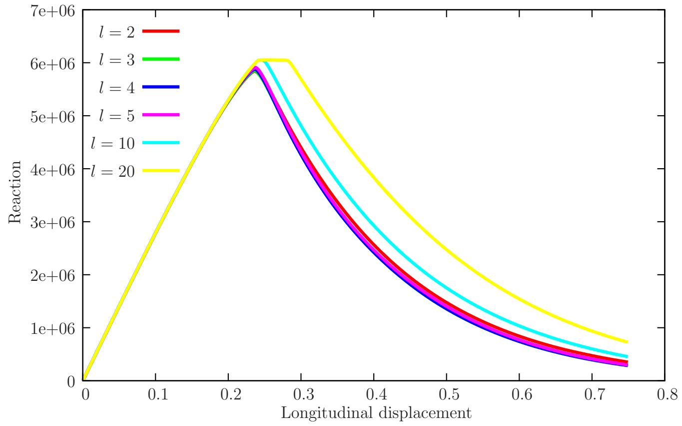

Figure 5.8: Effect of l on reaction-displacement results (1000 steps, 11338 elements). Consistent units are used.

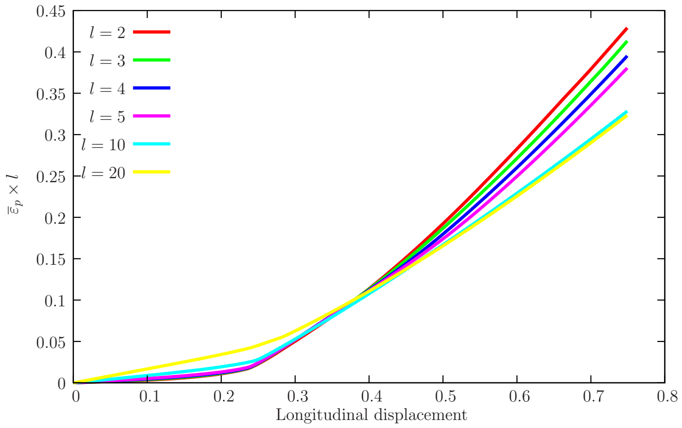

Figure 5.9: Effect of l on $\overline{\varepsilon}_p \times l$ at the monitored node (1000 steps, 11338 elements). Consistent units are used.

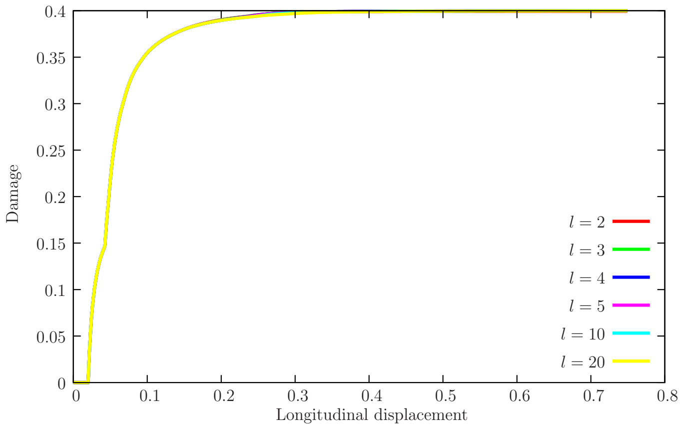

Figure 5.10: Effect of l on f at the monitored node (1000 steps, 11338 elements). Consistent units are used.

Figure 5.11: Effect of l for the pulling specimen.

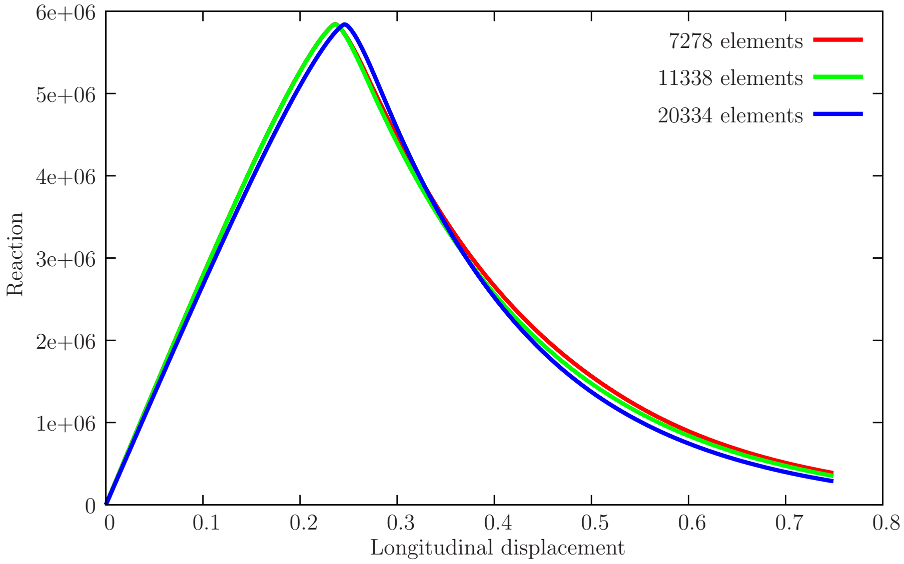

(a) Mesh size dependence ($l = 2$, 1000 steps). Errors in integrated $\mathscr{G}_c$ from the reaction–displacement curves are: 22.1%, 18.3% and 16.8% for 7278, 11338 and 20334 triangular elements, respectively. Consistent units are used.

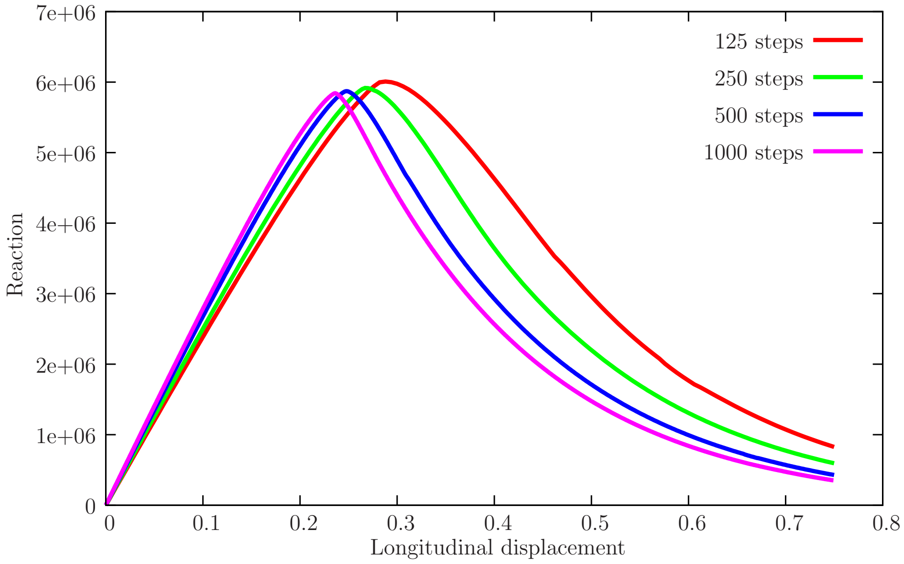

(b) Step size dependence ($l = 2$, 11338 elements). Consistent units are used.

Figure 5.12: Mesh and step size dependence.

Conclusions can be drawn from this problem:

- Length scale l has a moderate effect on the results and this effect is further reduced for lower values of l. Particularly, results for $l \in [2, 5]$ are nearly indistinguishable.

- Mesh size independence is extraordinary: nearly mesh-independent results are obtained.
- Step size has, in general, a relatively significant effect on the results. This is caused by the staggered algorithm which is known to produce some drifting. However, for sufficiently small step sizes, the dependence is attenuated.

5.5.2 Comparison with classical phase field

This problem was proposed by Ambati *et al. (4)* with the goal of comparing their hybrid model with Miehe's anisotropic model (2). We perform a comparison with both the classical phase field model of Miehe (2, 46) and the hybrid model of Ambati *et al.* (4). Modes I and II are tested (identified here as Case I and Case II, respectively). Relevant data for this problem is shown in Figure 5.13 along with damage contour plots for the two cases. We use an initial mesh containing 22763 elements 11633 nodes. Local remeshing evolution is shown in Figure 5.15 and comparisons with reported results are shown in Figure 5.14 for several values of the time step. Very good agreement can be observed with a limited step-size dependence for sufficiently small steps.

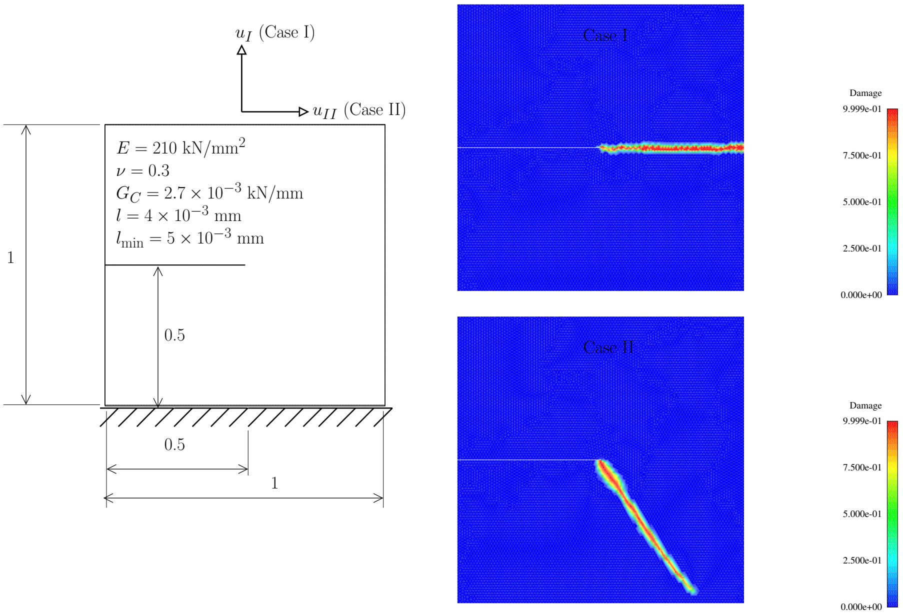

Figure 5.13: Test of Ambati *et al.* (4) for phase field models assessment.

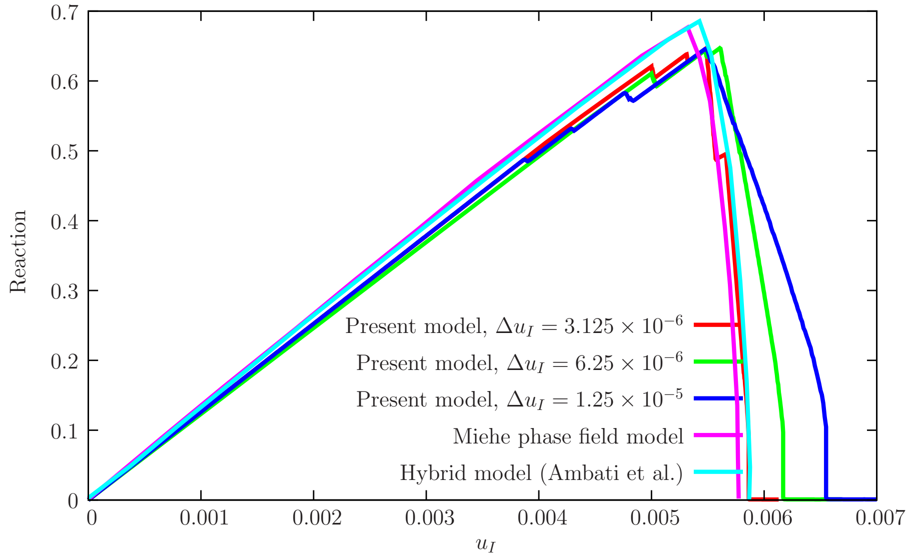

(a) Case I

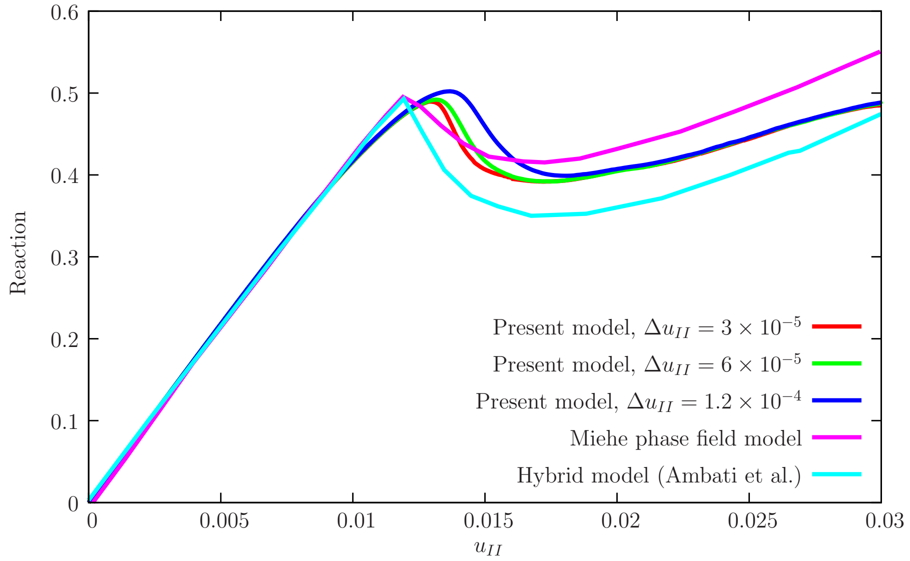

(b) Case II

Figure 5.14: Test of Ambati *et al.* (4): comparison with the phase field model of Miehe and also Ambati *et al.* (4). Consistent units are used.

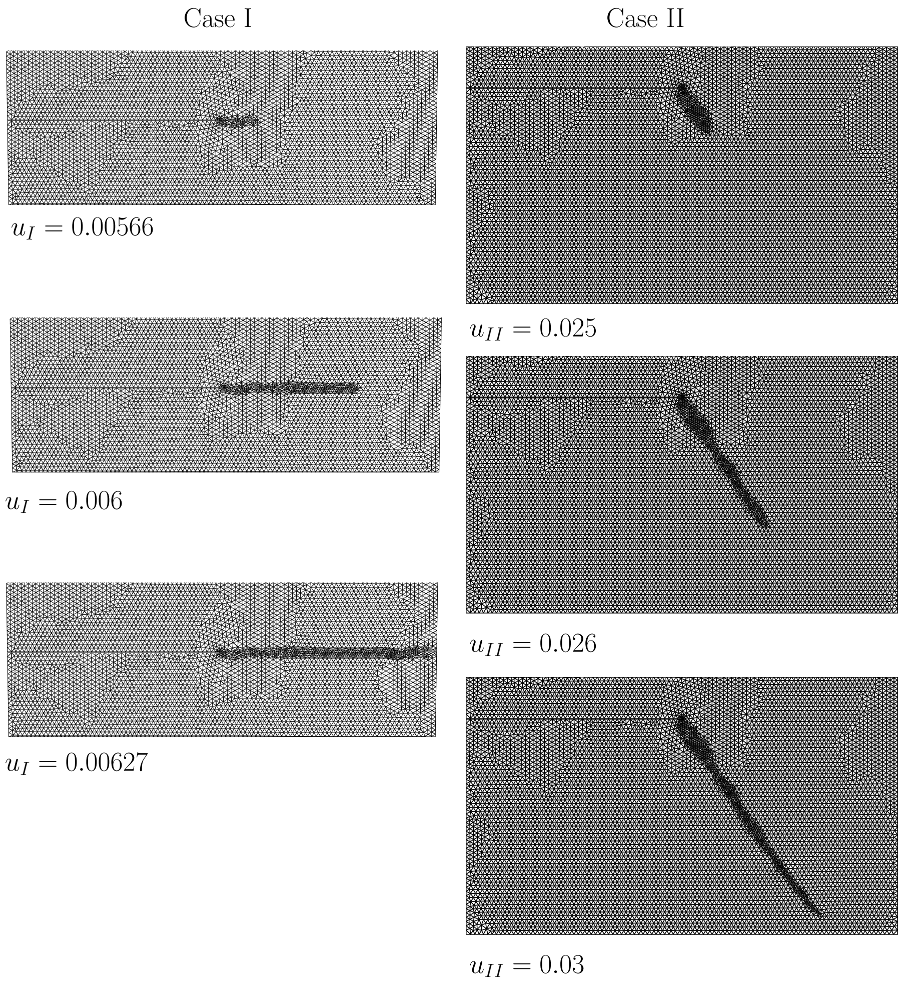

Figure 5.15: Test of Ambati *et al.*: mesh evolution with local remeshing ($l_{\text{min}} = 5 \times 10^{-3}$ *mm*).

5.5.3 L-shaped panel

We make use of a classical problem in crack path tracking: the L-shaped panel. Figure 5.16 shows the relevant data for the simulation and damage evolution in states A and B, depicted in the graph. In Figure 5.17, we show a comparison between the cases $\Delta t = 0.001$ (2000 steps),$\Delta t = 0.002$ (1000 steps) and $\Delta t = 0.004$ (500 steps). Note that, for this particular problem, *unload to origin* is enforced. Ambati *et al.* used 2000 steps with their hybrid model and show very similar results to ours (Figure 5.17). Since no remeshing was employed in this problem, damage distribution is wide for the mesh (only 8762 nodes) and does not represent a realistic crack. However, results are sufficiently close to the experimental envelope.

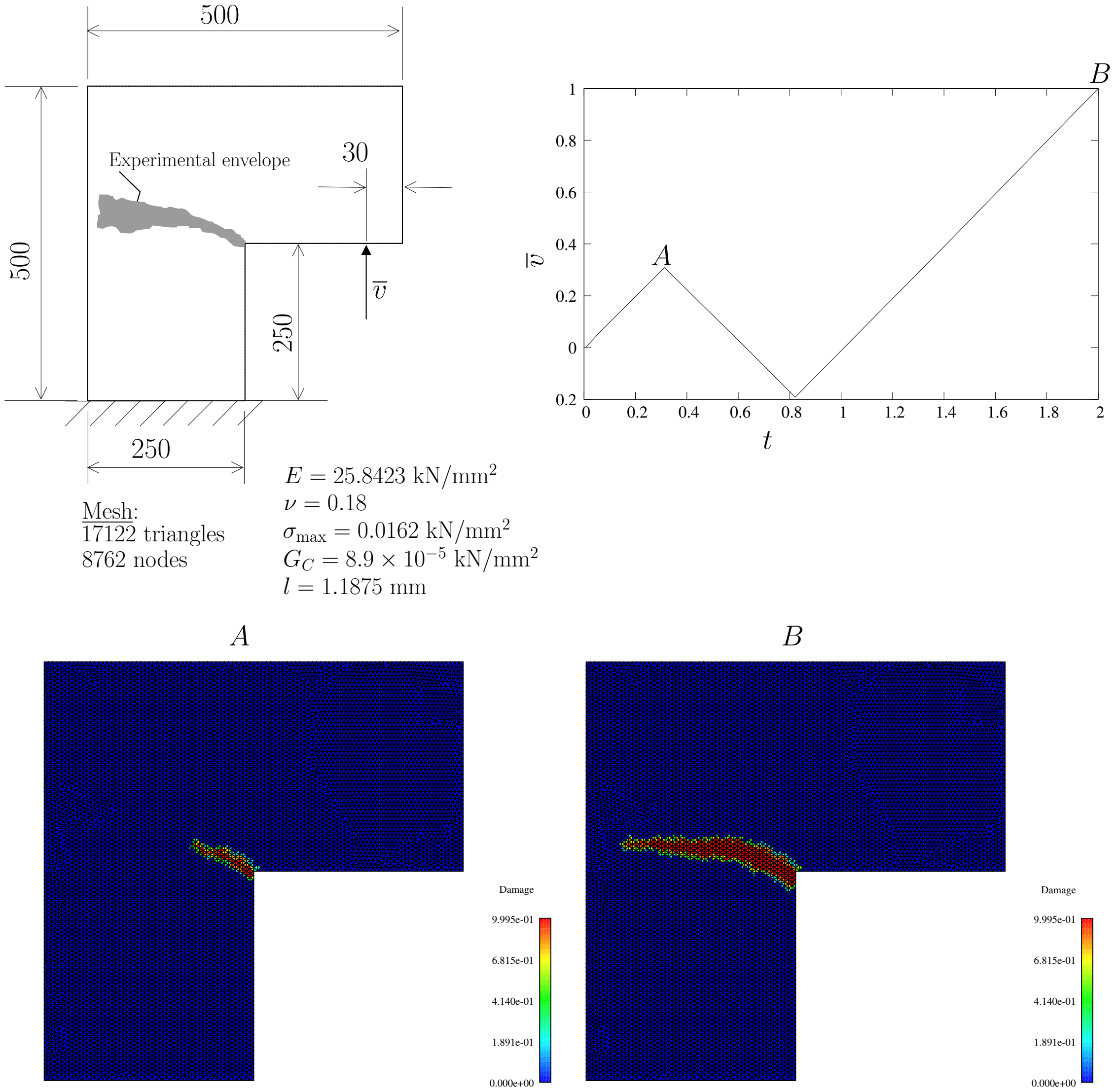

Mesh:
17122 triangles
8762 nodes

$E = 25.8423\ \mathrm{kN/mm^2}$
$\nu = 0.18$
$\sigma_{\max} = 0.0162\ \mathrm{kN/mm^2}$
$G_C = 8.9 \times 10^{-5}\ \mathrm{kN/mm^2}$
$l = 1.1875\ \mathrm{mm}$

Figure 5.16: L-shaped panel: relevant data and damage region obtained from our model.

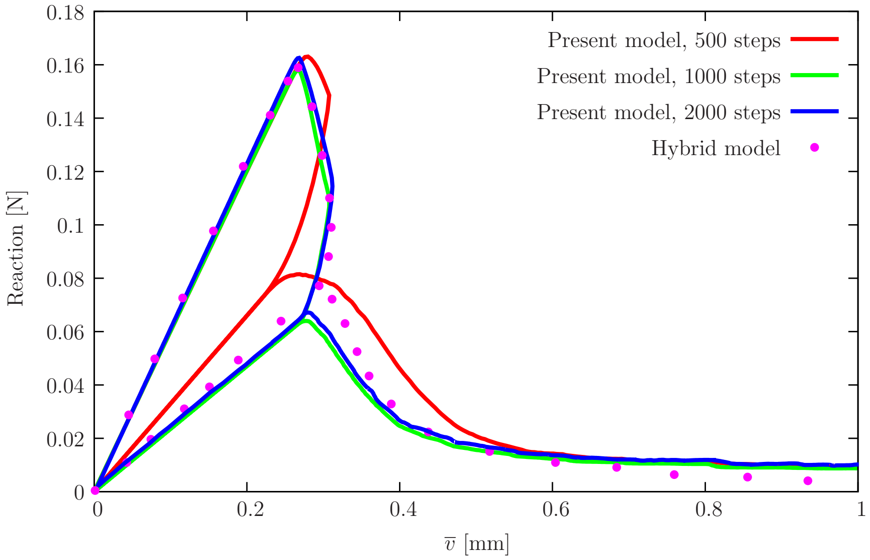

Figure 5.17: L-shaped panel: comparison with the results of Ambati *et al.* (4) hybrid model.

5.5.4 Localization and assessment of l parameter

We use a plane stress panel with two holes to inspect the effect of l on localization with the GTN ductile model. Relevant data for this problem is shown in Figure 5.18. Also shown are the effective plastic strain and void fraction contour plots for the two main localization stages. Relevant constitutive properties are given in Table 5.3 and we use $f_{\text{max}} = 0.6$ for the erosion criterion. Two values of l_{min} are adopted: $l_{\text{min}} = 0.2$ *mm* and $l_{\text{min}} = 0.4$ *mm*. Figure 5.19 shows the mesh evolution in the undeformed configuration for $l_{\text{min}} = 0.2$ *mm*. A relatively smooth crack path is observable since the small parameter is used. Note that l_{min} has a relatively diminutive effect in the reactions. Reaction-displacement results are compared in Figure 5.20 where it can be observed that the results are somehow sensitive to the value of l_{min} but *only in the post-localization* region. Also, complete collapse of the panel is possible without the load spikes often appearing in ductile fracture with enrichment methods.

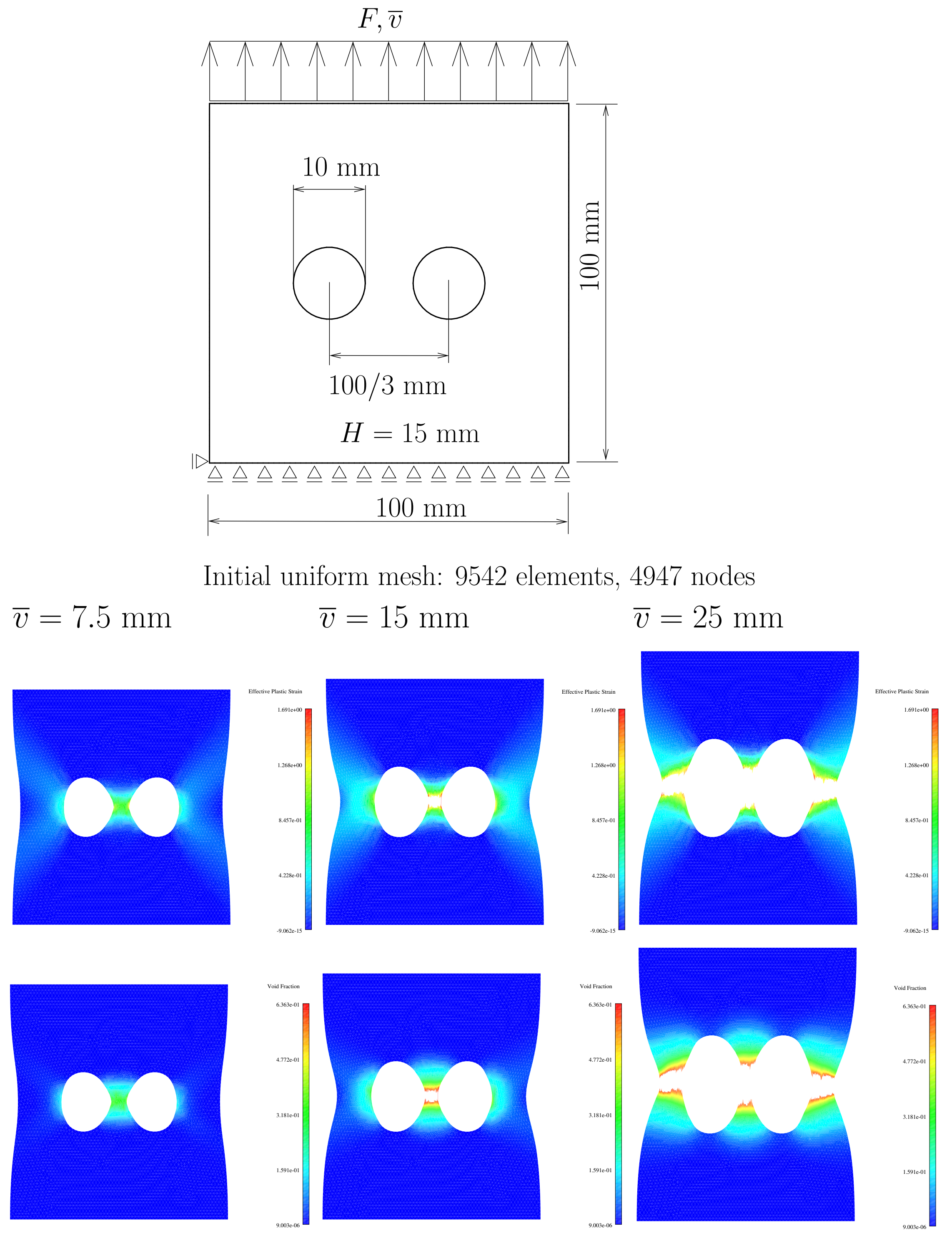

Figure 5.18: Two-hole specimen: data (see also Table 5.3) and localization in the inner region between the holes followed by the full-section localization and collapse ($l_{\text{min}} = 0.2$ mm). GTN results depicted.

Table 5.3: Properties for 2024-T351 Aluminum

Notation	**Value**
E	72400
ν	0.33
y	$352+668\varepsilon_p^{0.63302}$
f_0	0.0
q_1	1.5
q_2	1.0
q_3	2.25
f_N	0.042
S_N	0.1
ε_N	0.2
q_6	0.01
f_c	0.06
f_m	0.99

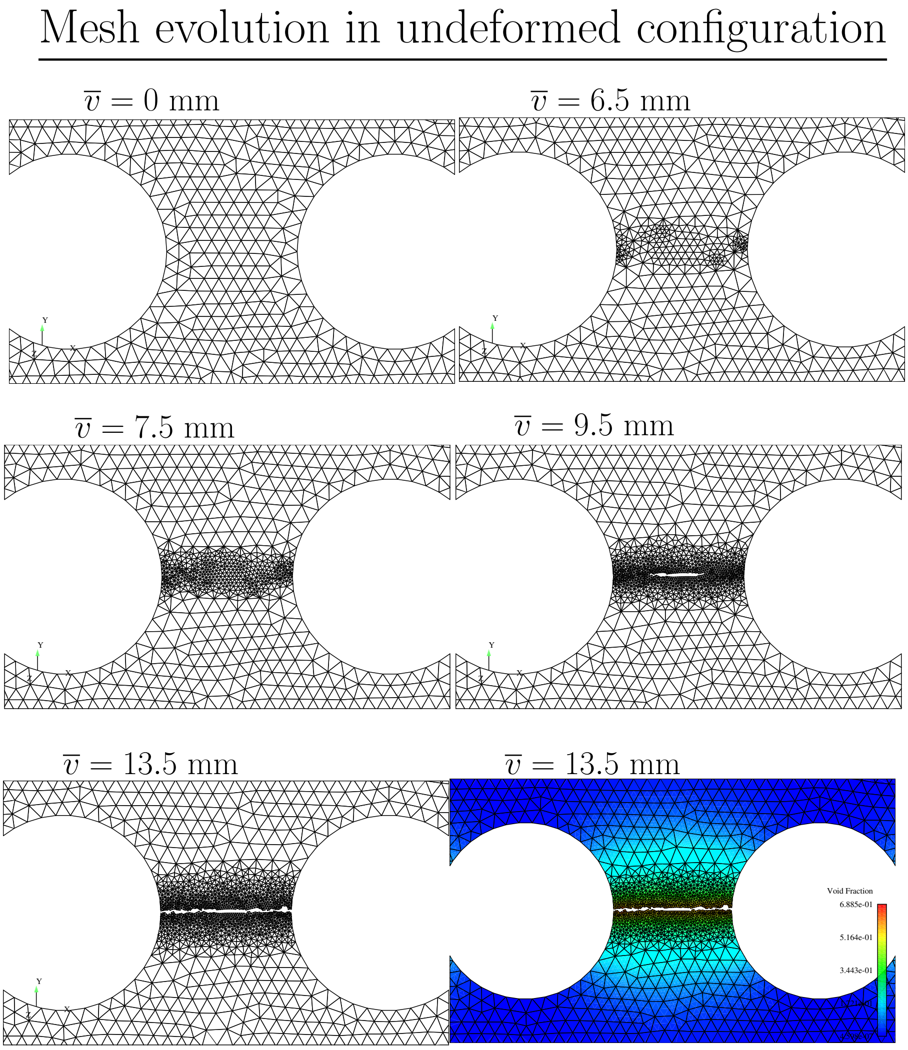

Figure 5.19: Two-hole specimen: detail of the central region crack nucleation and propagation. Undeformed configuration is used ($l_{\text{min}} = 0.2$ *mm*). GTN results depicted.

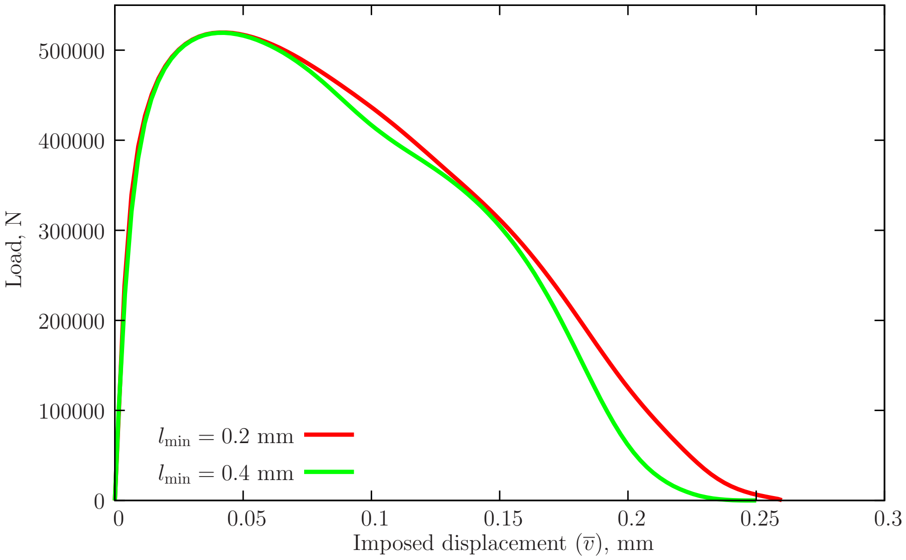

Figure 5.20: Two-hole specimen: Load–displacement results for $l_{\text{min}} = 0.2$ and $l_{\text{min}} = 0.4$ mm.

5.5.5 Single edge notched beam

The single edge notched (SEN) beam originally tested by Schlangen (5) is here numerically assessed with the model of section 5.1.3. A description of this problem, with constitutive properties and boundary conditions is shown in Figure 5.21. Three uniform meshes are adopted, containing 10194, 22776 and 40726 initial elements. The arc-length method is used, with monotonically increasing CMSD (crack mouth sliding displacement). The damage contour plot for the three meshes is shown in Figure 5.22 where a good correspondence can be observed, which further confirms the appropriateness of the remeshing process. The crack path reproduces adequately the experimental envelope, as can be observed in Figure 5.23; even near the support the experimental observations are accurately reproduced. A comparison with the experimental results (151, 152), along with a study of mesh and step size influence is effected. As can be observed in Figure 5.24, after the peak load is reached (where a slightly overshooting of the measurements is observed), the numerical results follow closely the experimental results. In terms of step-size sensitivity, we found that an assessment must be performed (here 2.4×10^{-3} *mm* was found to be a too large step size for CMSD). We found minor mesh size sensitivity (Figure 5.24) but similar to what is reported in other problems.

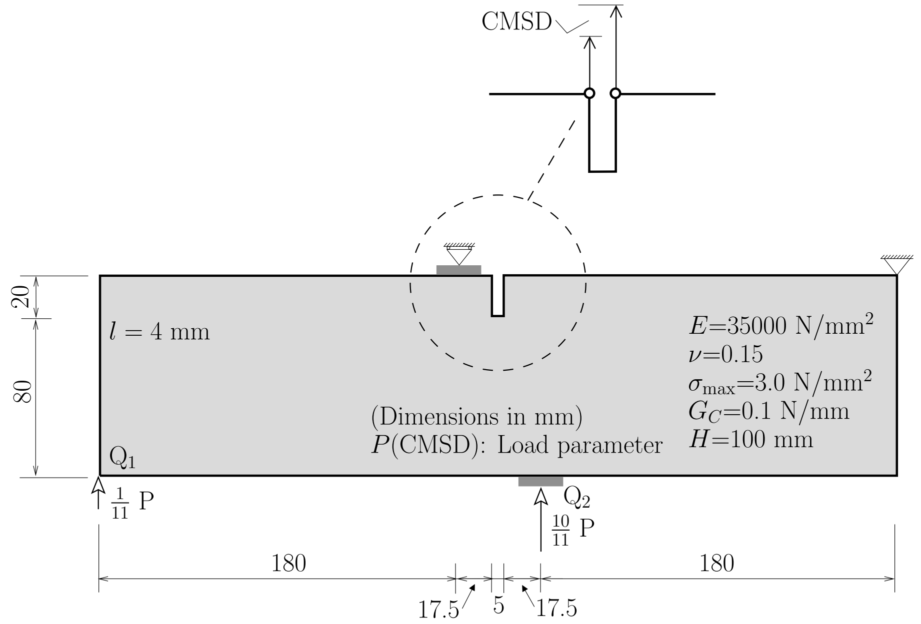

Figure 5.21: Schlangen's SEN test: geometry, boundary conditions and material properties.

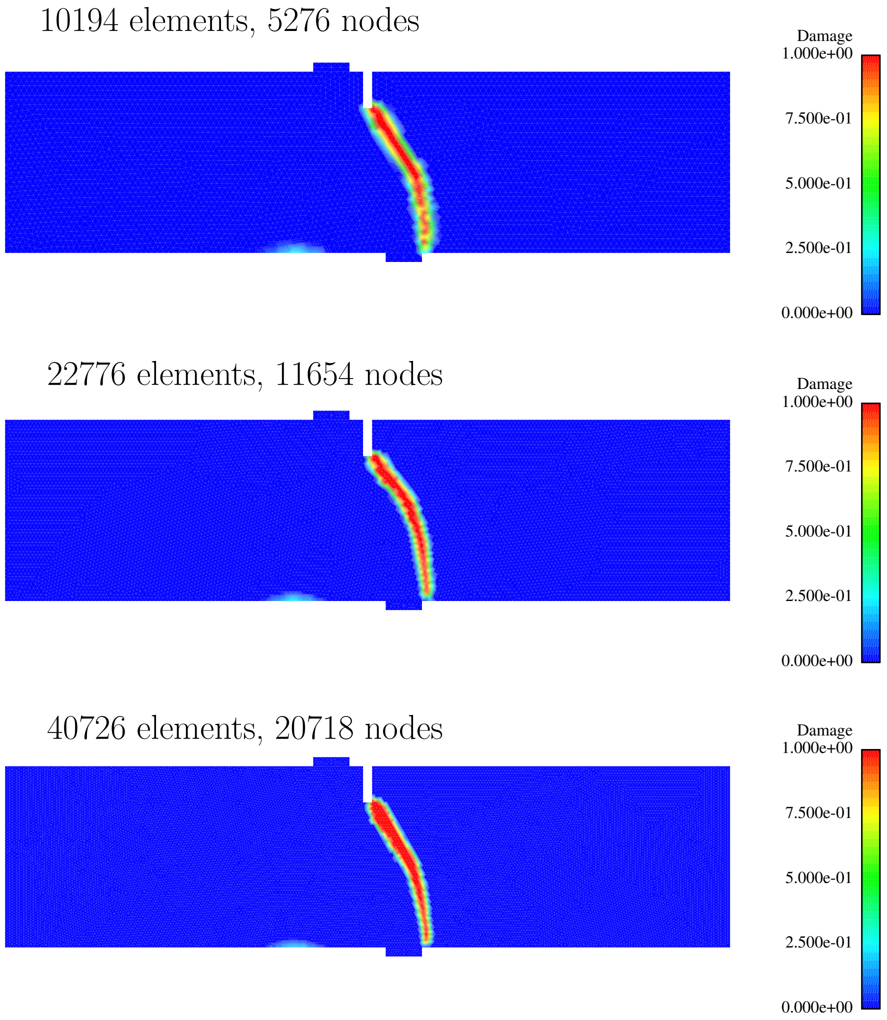

Figure 5.22: SEN test: damage distribution around the crack faces.

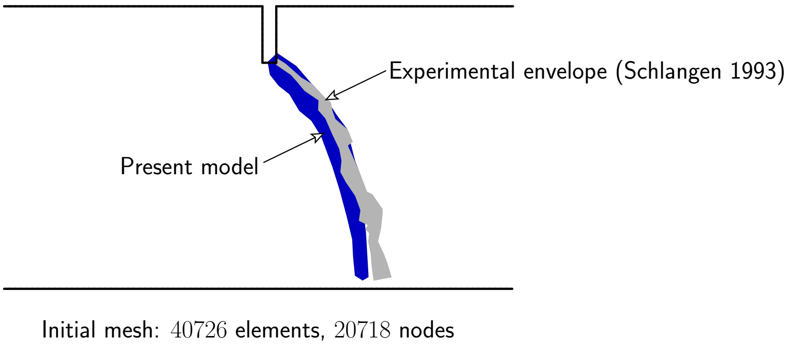

Figure 5.23: SEN test: crack path comparison.

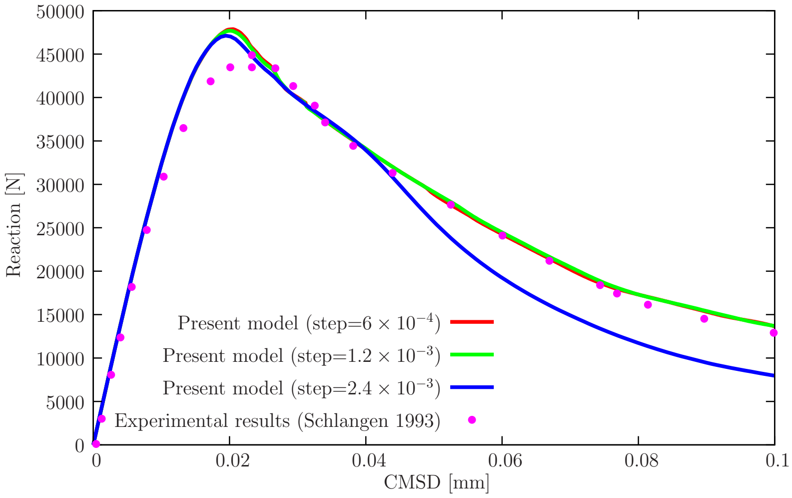

(a) Load-CMSD results for several CMSD increment sizes.

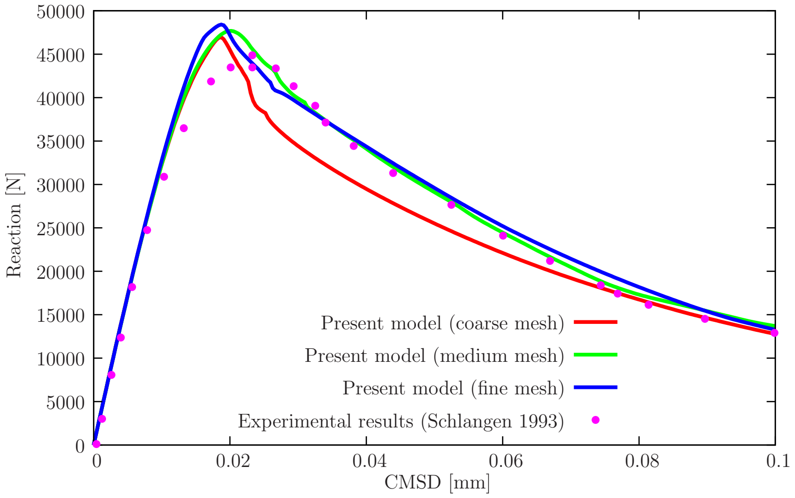

(b) Load-CMSD results for three mesh densities.

Figure 5.24: SEN test: load-CMSD results: comparison with the experimental results by Schlangen (5) and effect of step and mesh sizes.

5.5.6 Drilled panel

We assess a problem discussed by Ambati *et al.* (4) who performed an experiment with a cement-mortar pre-notched plate containing three holes. Four specimens were reportedly employed. Figure 5.25 shows the geometry and constitutive properties as discussed in that paper. The notch acts as a initiation site and it is worth noting that the largest-diameter hole introduces asymmetry and induces mixed-mode conditions. Displacement control is applied, with 500 equally-sized steps up to 2.5 *mm*. The largest-diameter hole acts as an attractor for the crack emerging from the notch. The initial crack coalesces with the hole and subsequently a second crack initiates at opposed site in the hole and propagates to the specimen edge. Three mesh policies are used: fixed (coarse) mesh containing 8529 nodes and 16545 triangles, fixed (fine) mesh 23399 nodes and 45944 triangles and a third mesh with 10583 initial node and 20596 initial triangles. In Figure 5.25, the contour plots for f, ε_p and $\overline{\varepsilon}_p$ are also shown. We can observe the regularization effect of the screened Poisson equation in $\overline{\varepsilon}_p$. Figure 5.26 shows the results with three mesh strategies and also results reported by Ambati *et al.* (4) using their hybrid model and also Miehe *anisotropic* model (2, 46). Differences occur in the final collapse region, where our model localizes earlier than both Miehe's and Ambati and we found that this is caused by our much finer local discretization after remeshing. Ambati *et al.* used for both models a *fixed* mesh containing 25085 quadrilateral elements with refinement in the areas where the crack is expected to form (4). With localized mesh refinement, we avoid a-priori predictions of crack paths. Mesh evolution and corresponding crack path are shown in Figure (5.27) where reasonable agreement can be observed with the experimental envelope corresponding to the reported four specimens. Mesh evolution is reported in Table (5.4).

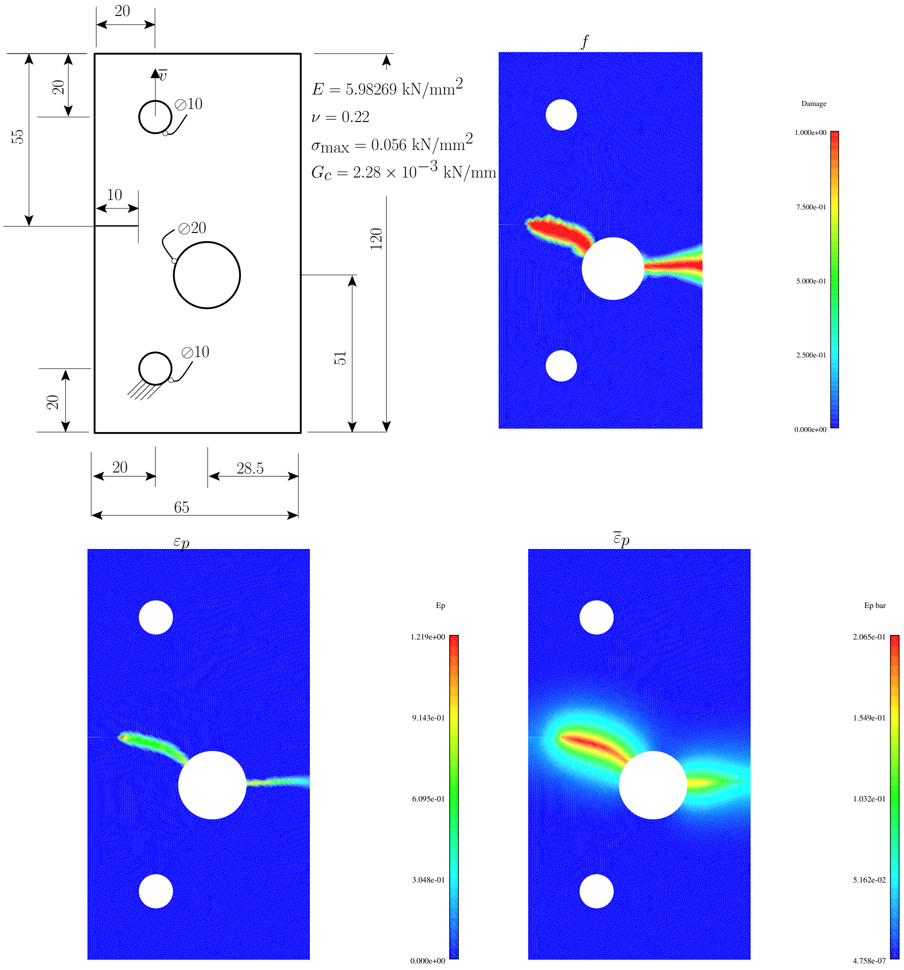

Figure 5.25: Drilled panel: relevant data.

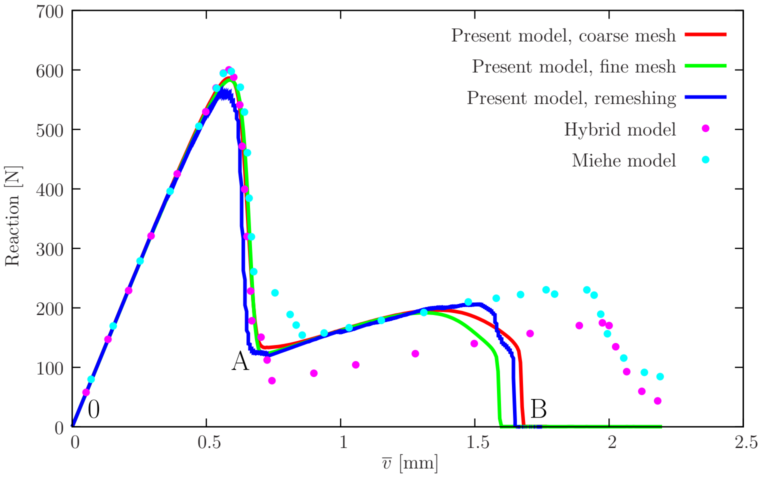

Figure 5.26: Drilled panel: results using a coarse mesh, a fine mesh and also mesh refinement. Comparison with published results (Ambati *et al.* (4)).

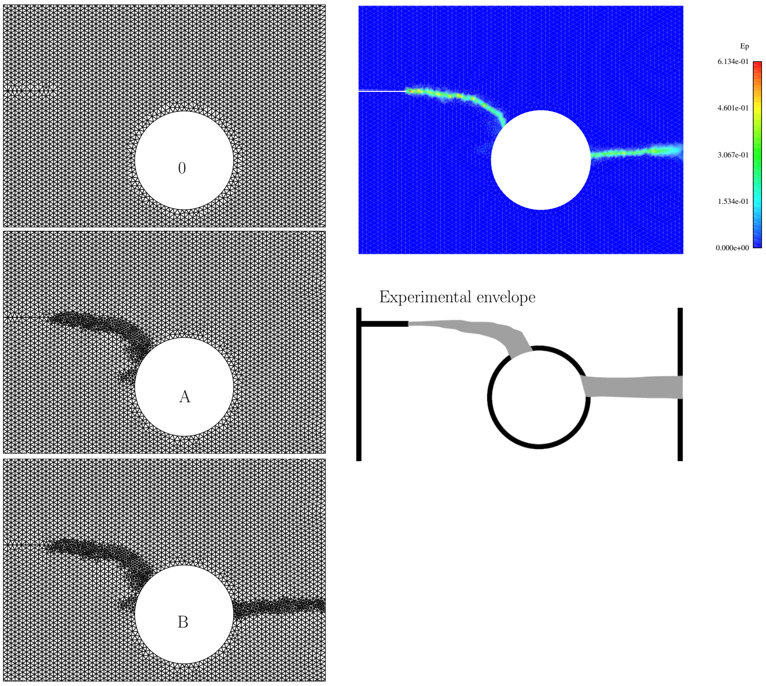

Figure 5.27: Drilled panel: crack path comparison with the experimental crack path envelope of Ambati *et al.* (4).

Table 5.4: Mesh sizes (initial and final) and mesh evolution with time step

	Initial	Final
Number of nodes	10583	12127
Number of triangles	11398	22210

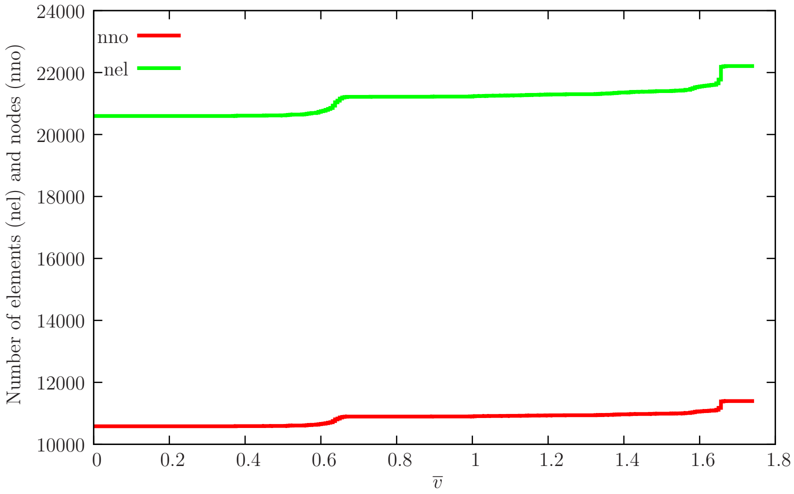

Conclusion

By combining a staggered algorithm with the screened Poisson equation and, optionally, adaptive mesh refinement, we solve well-known benchmarks in computational fracture. A simple algorithm to solve quasi-brittle and ductile crack *nucleation* and *propagation* 2*D* problems was described and tested; observed effects in experiments such as crack curving and ductile coalescence were observed. In comparison with the classical approaches, this staggered algorithm was found to be applicable to other discretizations and constitutive cases. Excellent crack path agreement with experiments was systematically obtained. Good load-deflection and load-CMSD results were also observed.

Chapter 6

Polymer Nanocomposites Properties and Modeling

This chapter aims to outline the PNCs material physical and chemical properties in addition to describe the generation of the representative volume element (RVE) of PNCs.

6.1 Polymer layered silicates

The higher Young's modulus and strength can be easily detected in polymer layered silicate than in the non-filled polymer or traditional composites. The enhancement in the composite is due to the bonding of the fillers and the matrix. These enhanced properties in PNCs come from the vast interfacial area between clays and the polymeric matrix and from the increase in the interfacial area and decrease in the average wall-to-wall distance between fillers due to a decrease in the size of the filler at the same volume fraction (153).

Dispersing the clay platelets into the polymer matrix can be chemically controlled to ensure an interface that lead to either a well-bonded or poorly-bonded composite. The PNCs with strongly or poorly bonding interfaces act differently. The difference come from the neat epoxy behavior that can be "brittle" or "ductile" in some cases of poorly bonded composite, depending on the percentage of the nano–filler material (153).

PLS nanocomposites as a relatively new type of nanoscale material are originated from minerals that regularly assemble with the unit crystalline layer. It comes in three different forms: intercalated nanocomposites, flocculated nanocomposites, and exfoliated nanocomposites. The differences between these types depend on how the silicate layers are distributed in the polymer matrix. Figure 6.1(a) shows the intercalated type of PNCs where the layered silicate structure is crystallographically regular. Figure 6.1(b) shows the flocculated PNCs where the stacked silicate layers are flocculated because of the hydroxylated edge to edge interactions of the silicate layers.

The exfoliated type of PLS is shown in Figure 6.1(c) where the silicate layers are separated in the polymer matrix (154). The techniques used to produce these types of PLS are: Solution Process, In-Situ Polymerization, and Melt Blending. The final characteristics and properties of the nanocomposites are influenced by each technique (72).

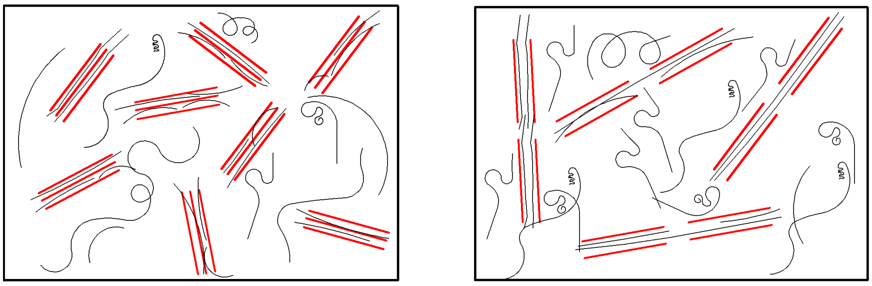

(a) Intercalated (b) Intercalated-Flocculated

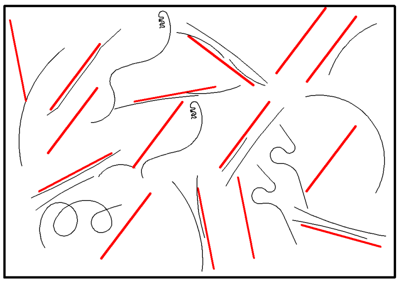

(c) Exfoliated

Figure 6.1: Three different types of polymer/layered silicate nanocomposites.

The layered materials can be divided into several categories. In particular, the layered silicates are classified as either Magadiite, bentonite, kaolinite, montmorillonite, clay saponite, sepiolite, vermiculite, talc (OH), hectorite, attapulgite, fluoromica, illite, or chlorite

The PNCs specimens taken into consideration in this work contain layered silicates designed in situ dispersion into polymer matrixes by intercalation method. Whereby the composites are intercalated into the gallery space of layered silicates to cause the exfoliation of the layers when the polymerization reaction is initiated. Further details can be seen in (155).

6.1.1 Montmorillonite

Most of the PNCs studies used MMT as a layered silicate filler because it is an expandable dioctahedral smectite, has both nanoscale size and intercalation/exfoliation properties (156, 157). MMT clay sheet silicate material consists of Si, O, and various other metals such as Al, Mg, and Ca. The chemical composition of MMT is made up of the general formula $M_x(Al_{4-x}Mg_x)Si_8O_{20}(OH)_4$ (156).

The crystal structure of silicate layers needed to prepare the PLS nanocomposite is $(2:1)$ layered or phyllosilicates being characterized that have greater than 50% octahedral charge. So, The crystal structure contains layers which form two tetrahedrally coordinated silicon atoms that create an edge–shared octahedral sheet of aluminum or magnesium hydroxide. The layer is approximately 1 *nm* thick with different length depending on layered silicate. There are two particular characteristics of layered silicates that are considered for PLS nanocomposites: first, the ability of the silicate particles to disperse into individual layers; and second, the ability of layered silicates to adjust their surface chemistry through ion exchange reactions with organic and inorganic cations (154). Hence, the exfoliation (dispersion) of a single platelet of MMT about 1 *nm* thick stacked together provides a high surface to volume ratio (157). The new composite has exhibited remarkable material property improvements when compared to the matrix polymers alone or conventional micro– and macro–composite materials at low levels of MMT.

6.2 Modeling of PNCs

The experimental results of Wang *et al.* (1) and the recent work in (92, 93, 158, 159) indicate that the silicate clay platelets are much stiffer than the epoxy matrix and can be considered as a linear elastic isotropic material. The epoxy matrix and the IP zones as a brittle material, are modeled by the quasi–brittle fracture model of phase field approach that described in chapter 3. In chapter 7, we assume a rigid bond between the clay reinforcement and the polymer matrix. The interfacial effects between the clay and the matrix is considered by adding the IP zones in chapter 8. The generation of the input file for the sample discretization of the PNCs is performed by Abaqus using a Python script that initiates the model to be formatted for the UEL subroutine.

6.2.1 Generation of the representative volume element of PNCs

6.2.1.1 Fully bonded PNCs

The microstructure of the RVE is generated by the algorithm proposed by Silani *et al.* (88). The generation starts with the definition of the initial numerical parameters (e.g. RVE size, clay volume, clay's aspect ratio, mesh size, element type). The clays are generated randomly and positioned in the RVE with a uniform probability distribution function preventing overlapping and intersecting of the clay fibers to produce realistic PNCs containing fully exfoliated clays. RVEs of the PNC material in 2D and 3D are shown in Figure 6.2. A Flowchart of the sample generation procedure is depicted in Figure 6.3. Different values for the clay wt.% contents and aspect ratios of clay are generated to study the material behavior and the effect of these parameters on the ultimate load of the PNC sample.

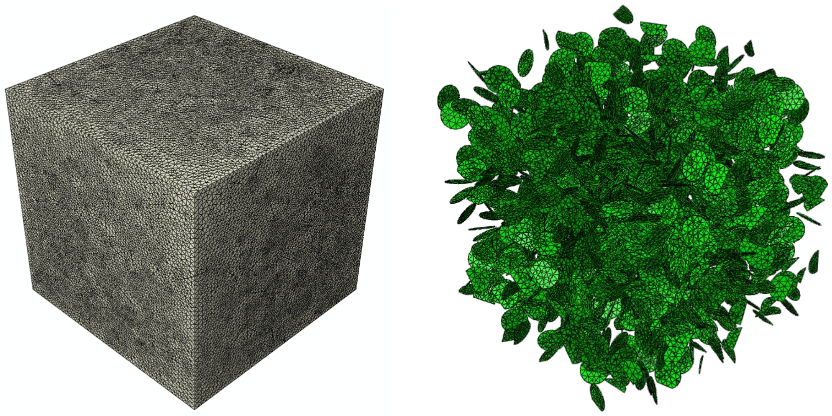

(a) 3D RVE of the PNCs.

(b) Clay platelets in the 3D RVE.

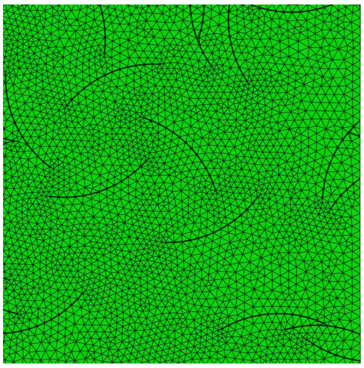

(c) An enlarged zone in 2D representation of the RVE.

Figure 6.2: Three and Two dimensional representation of the PNCs material.

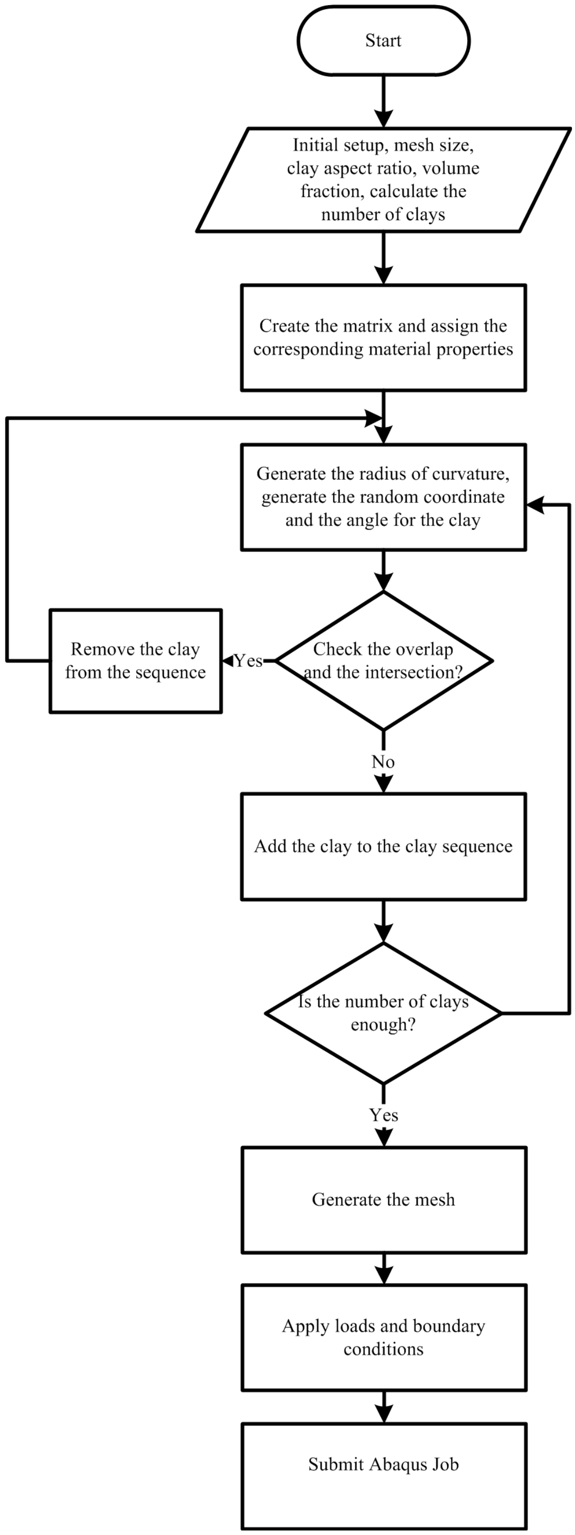

Figure 6.3: Python script flow chart for the fully bonded PNCs generation.

6.2.1.2 PNCs with interphase zones

The interphase zone position in 2D is shown in Figure 6.4. The RVEs with fully exfoliated clay with IP zones surrounding the clay platelets are created by the algorithm shown in Figure 6.5. The algorithm initiates the setup of the PNC sample starts by defining the RVE size, clay weight content (wt.%), clay aspect ratio, IP thickness, mesh size, and finite element type. By using these parameters, we tested the influence of the IP zones thicknesses, different material properties, and the clay distribution on the tensile strength and *J* integral, surface energy and cracks surface area. Also, an intersection checker depending on the volume fraction of the components is implemented to prohibit the intersection of clay platelets and to ensure a full exfoliation for the clay platelets in the generated samples.

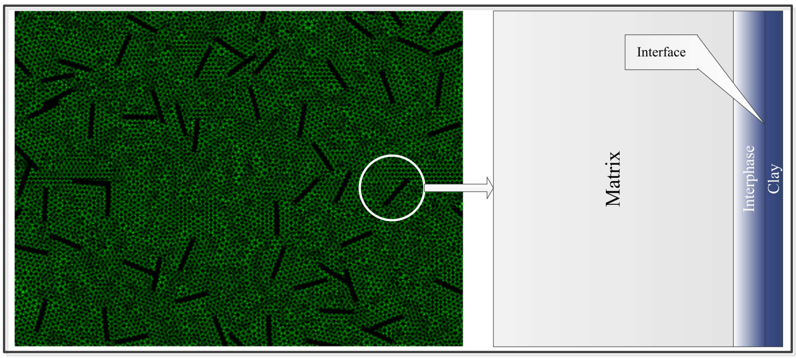

Figure 6.4: Two dimensional representation of the PNCs with interphase zone.

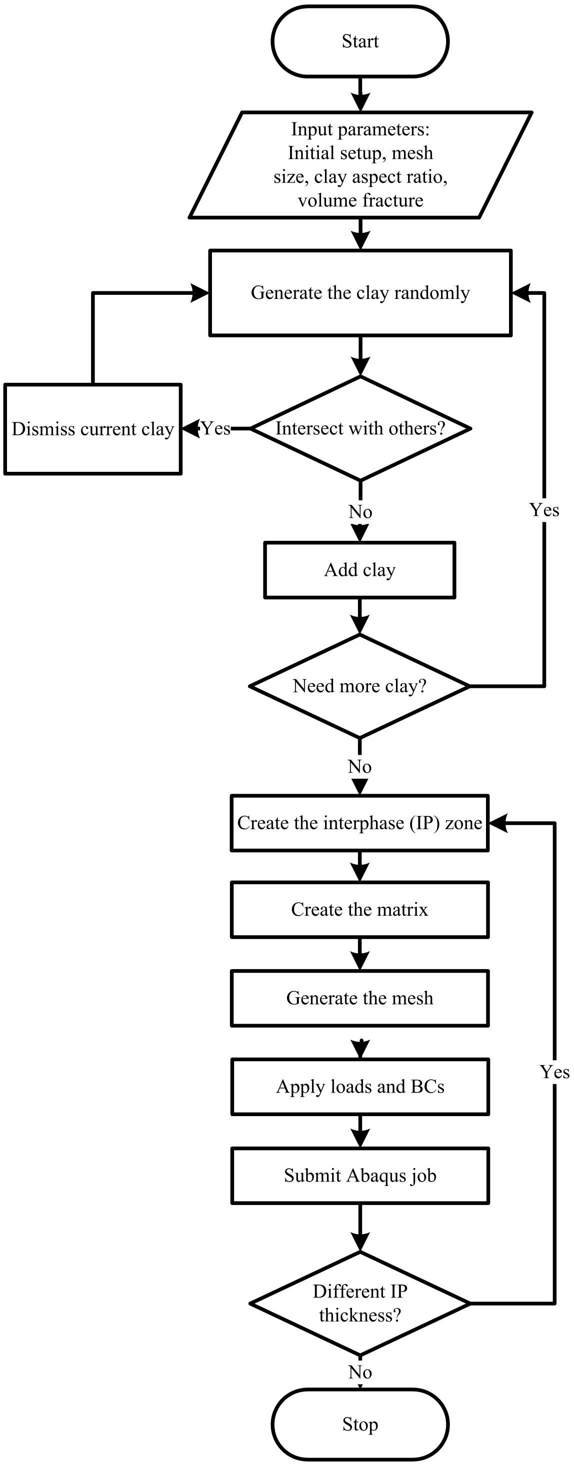

Figure 6.5: Python script flow chart for the PNC including IP zone generation.

Chapter 7

Predictions of Young's Modulus, *J* Integral, Tensile Strength, and Surface Energy of Fully Bonded Clay/Epoxy Nanocomposites Material

The goal of this chapter is to provide a method to computationally design polymeric nanocomposites, in particular clay/epoxy nanocomposites. The studied samples are fully bonded PNCs that have rigidly connected clays to the matrix, in another word, the interfacial effect between the heterogeneous materials of the composite is not taken into consideration. This kind of the composite is a possible outcome according to the production techniques of polymer layered silicates and the adhesion between the clay fibers and the matrix. Obviously, most molecular dynamic simulations are limited in size and not relevant to engineering applications (13). In this approach, we employ a mesoscopic fine-scale model to account for the meso-structure of the composite material in order to extract the macroscopic tensile strength and *J* integral. The effects of the clay weight content, clay platelets aspect ratio, and the energy release rate of the epoxy are studied as stochastic input parameters.

To demonstrate the potential of this approach and its suitability for the application, the material and fracture properties of PNCs such as Young's modulus, tensile strength, and fracture toughness in addition to studying the surface energy dissipation during fracture are investigated in details. The computational technique elaborated in the present work is expected to be an efficient tool for evaluating the overall size-dependent fracture behavior of PNCs.

7.1 Mechanical properties

The exfoliated clay is a plate-like structure of $1-2$ *nm* thickness and hundred nanometres in-plane direction. Platelets with aspect ratio in the range of $50-300$ *nm* have an extremely large surface area of 750 m^2/g (72). In this work the aspect ratio of clay ranged from $150-300$ *nm* with clay thickness of 1 *nm*, while the clay wt.% is between $2\%-4\%$. Chen *et al.* (160) reported Young's moduli values for clay around $178-265$ *GPa*. Young's moduli in our study is 234 *GPa* and the Poisson's ratio is 0.25 (88). Young's modulus of the epoxy/resin is 1.9 *GPa* with Poisson's ratio equal to 0.35. The energy release rate of the matrix is equal to 216 N/m (1).

7.2 Predictions of fracture energy

The fracture toughness is an important material property. The J integral is a parameter to describe the crack tip conditions and is used as fracture criterion to give nearly size independent measures of the fracture toughness (161) if the specimen is large enough. Of course, fracture at different levels would be driven by different mechanisms and different fracture energy or toughness.

The fracture energy or toughness at any scale must be the sum of the fracture energy at all the scales where fracture is taking place. Fracture in the PNCs is dominated by fracture in the matrix material. In order to reliably extract J, a specimen with high stress gradient is needed. The single edge notched and double notched tension specimens are considered in this work. Two approaches are studied which are: 1.) *The work of fracture* and 2.) *Size effect method*. In *the work of fracture* the total work done by the load until the specimen is completely fractured is measured. The work is divided by the area of the ligament in the front of the notch tip using the compact tension specimen loaded by a wedge, see Figure 7.1. The minimum dimension of the specimen needs to be greater than five times of the maximum size of the inhomogeneity, i.e. five times of the length of a nanoparticle.

The applicability limits of using the J integral is exceeded when there is excessive plasticity or significant crack growth. After these limits the fracture toughness and J integral will depend on the size and the geometry of the structure or the test specimen. The contour integral presented by Rice (162) showed that the value of the J integral is equal to the energy release rate in a nonlinear elastic body that contains a crack, except that $\mathscr{G}_c$ is replaced by J:

$$J = -\frac{d\Pi}{dA}\,, \tag{7.1}$$

where Π is the potential energy and A is the crack area; U^* is the complementary strain energy for a plate under load control. Then it can be shown that J is given by

$$J = -\left(\frac{dU^*}{da}\right)_P \tag{7.2}$$

If the crack propagates under displacement control, J is

$$J = -\left(\frac{dU}{da}\right)_\Delta \tag{7.3}$$

According to Figure 7.1, the difference between dU^* for load control and $-dU$ for displacement control is negligible compared to dU which is equal to $(\frac{1}{2}dPd\Delta)$.

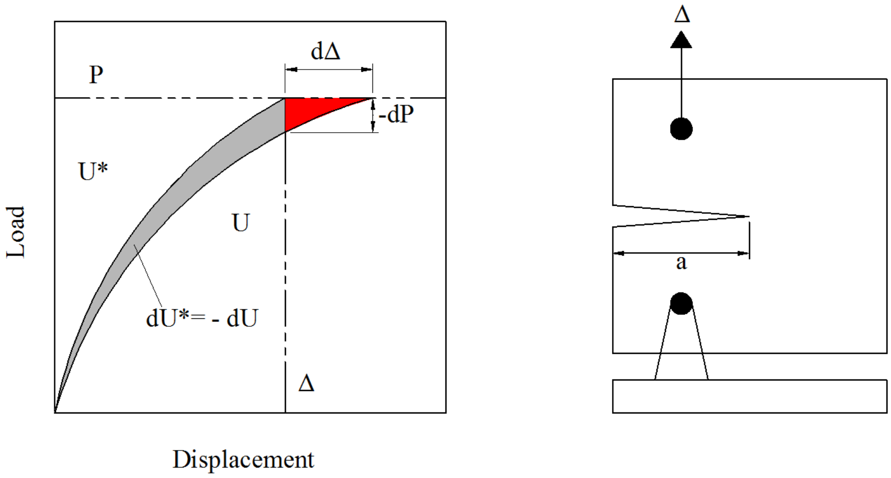

Figure 7.1: Nonlinear energy release rate.

Recalling the value of U and U^*, the J integral can be expressed by:

$$J = \int_0^P \left(\frac{\partial \Delta}{\partial a}\right)_P dP = -\int_0^\Delta \left(\frac{\partial \Delta}{\partial a}\right)_\Delta d\Delta \tag{7.4}$$

Computing the J integral is difficult when the material is nonlinear as there is no simple relationship between J, the load and the crack length. A more practical experimental approach was developed by Landes and Begley (161). This method can be summarized by obtaining a series of test specimens of the same size, geometry and material with different initial crack lengths. The area under the load–displacement curves of these specimens is equal to U, the energy absorbed by the specimen. For a plate with side notch as depicted in Figure 7.1, the J integral is given by

$$J = -\frac{1}{B}\left(\frac{dU}{da}\right)_{\Delta} \tag{7.5}$$

where dU is the change in the energy absorbed by the specimens and da is the change in the initial crack length and B is the thickness of the plate.

7.3 Numerical examples

Before we predict fracture related properties of fully exfoliated PNCs, we verify our model by predicting elastic properties in the bulk. The macroscopic Young's modulus E of the PNCs is extracted by computational homogenization (163) and then compared to results obtained with the Halpin-Tsai model. Young's modulus of the Halpin-Tsai method is estimated by (84):

$$E = \frac{1+\zeta\eta V_f}{1-\zeta\eta V_f}E_m \tag{7.6}$$

where ζ is the shape factor, V_f is the volume fraction of clay particles and η is given as:

$$\eta = \left(\frac{E_f}{E_m}-1\right)\Big/\left(\frac{E_f}{E_m}+\zeta\right) \tag{7.7}$$

E_m is Young's modulus of the matrix containing no silicate clay and Young's modulus of clay silicate is E_f. The shape factor ζ is depicted as $\zeta = 2w/t$ where w/t is the aspect ratio of the clay.

7.3.1 Predictions of Young's modulus

Let us consider a specimen with dimensions 1500 $nm \times$ 1500 nm with different clay weight content (2%, 2.5%, 3%, 3.5% and 4%). The setup of the specimen is shown in Figure 7.2. The plane stress problem is discretized using T3 elements with different element sizes (12, 24 and 36 nm). The load was applied in minimum load increments of $\Delta u = 1\times10^{-5}$ nm and maximum load increments of $\Delta u = 1\times10^{-3}$ nm using the automatic step-size control available in Abaqus. Figure 7.3 depicts the load–displacement curve for different meshes as well as the slight increase in the ultimate load when the element size increases. Note that only the initial slope of the load–displacement curve is of interest for extracting Young's modulus of the composite. Nevertheless, we loaded the specimen until complete fracture.

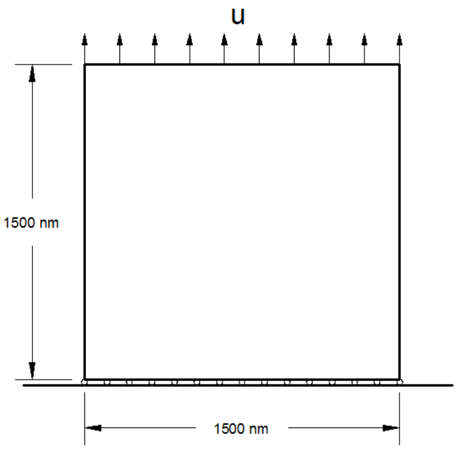

Figure 7.2: Geometric setup of the specimen.

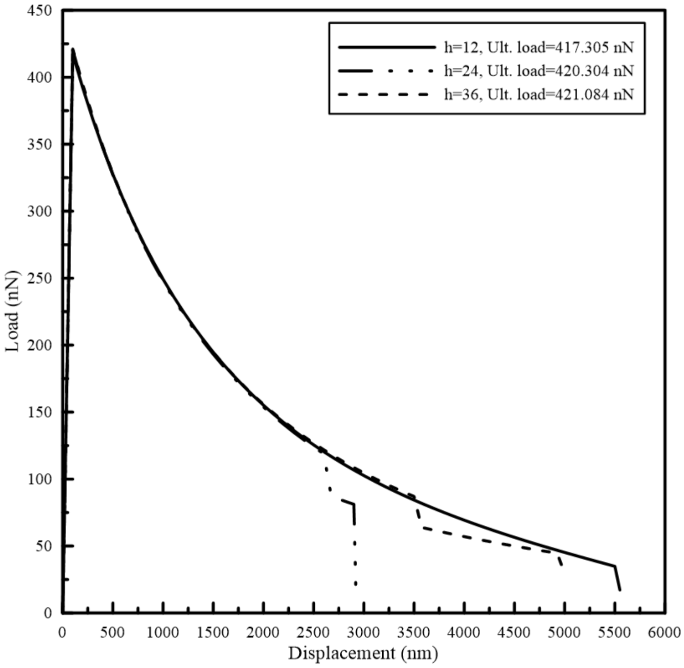

Figure 7.3: Load–displacement curves for different mesh size h, $h = 12$ nm (51334 elements), $h = 24$ nm (14890 elements), $h = 36$ nm (7755 elements).

Figure 7.4 shows the load–displacement curves of specimen with different clay content. The effect of clay wt.% is clearly noticed on the ultimate load. The values of the ultimate load for different percentages of clay weight contents extracted from Figure 7.4 are plotted in Figure 7.5. Contour plots of the phase field variable are depicted in Figure 7.6.

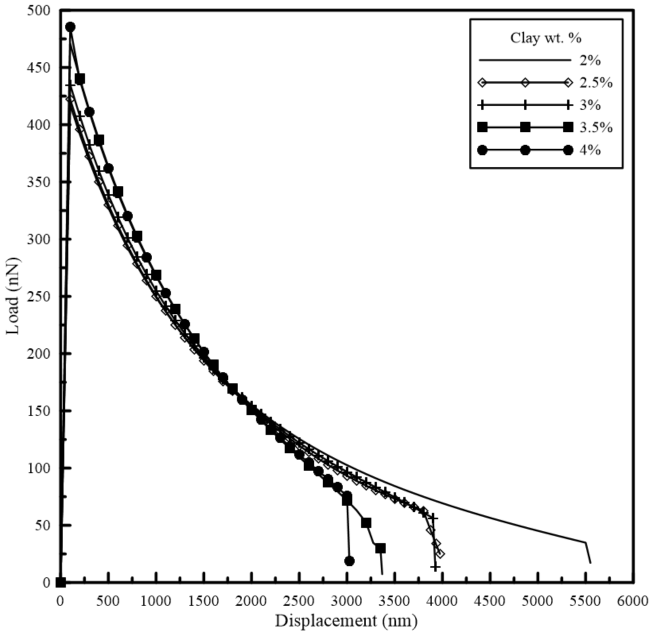

Figure 7.4: Load–displacement curves for different clay wt. %. 24% (51334 elements), 2.5% (53425 elements), 3% (52520 elements), 3.5% (53596 elements), 4% (53916 elements).

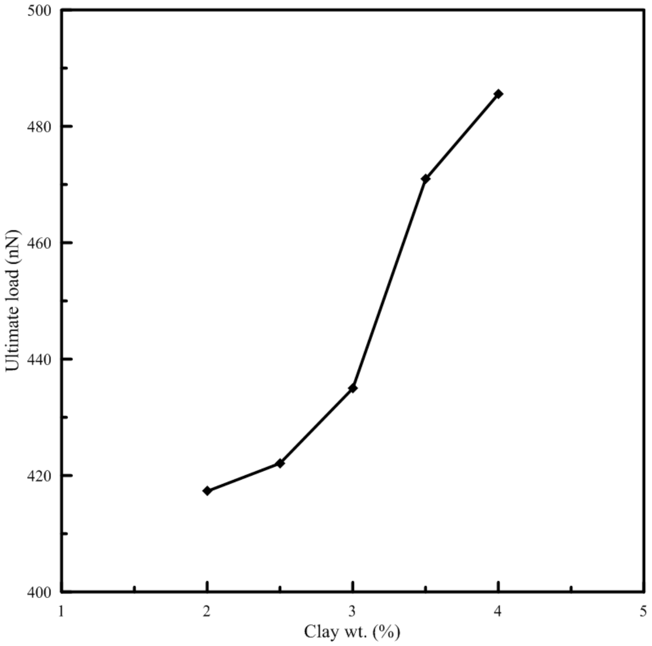

Figure 7.5: Ultimate load values for different clay wt.%.

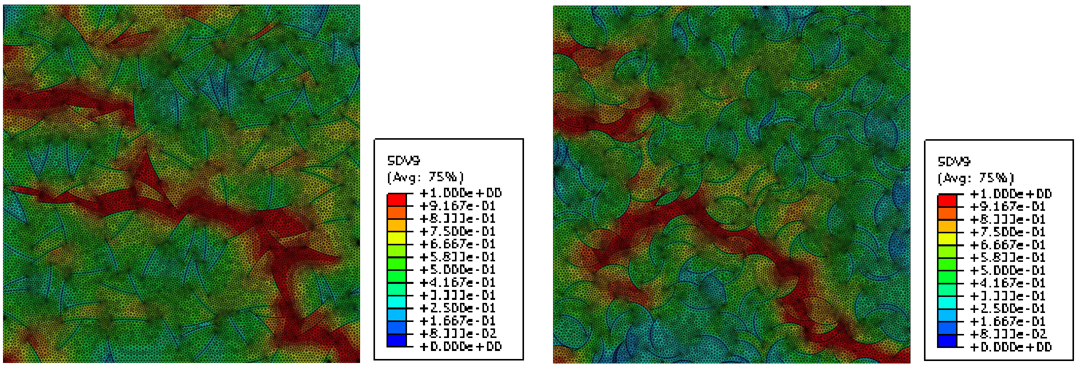

(a) Clay content 2%, 51334 elements.

(b) Clay content 2.5%, 53425 elements.

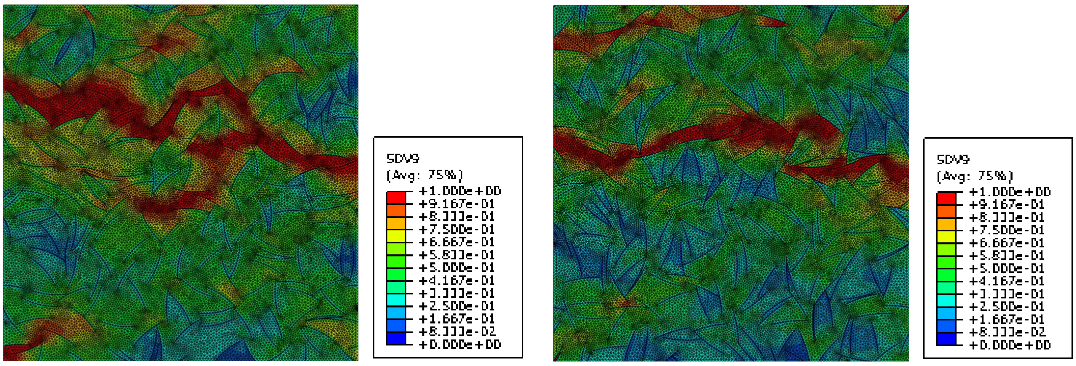

(c) Clay content 3%, 52520 elements.

(d) Clay content 3.5%, 53596 elements.

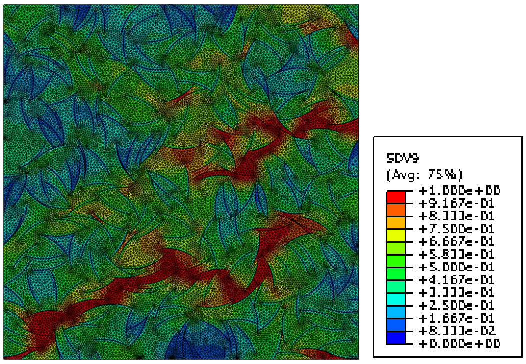

(e) Clay content 4%, 53916 elements.

Figure 7.6: Cracks patterns of the intact square PNCs specimens with different clay wt.%. SDV9 = phase field.

Figure 7.7 compares the predicted Young's modulus E of the composite obtained by the Halpin-Tsai model (Equation 7.6) and our computational model for different clay ratios. We extracted the Young's modulus through computational homogenization by simulation at RVEs of different size. The predicted Young's modulus of our model (computational homogenization) and the Halpin-Tsai model are in fair agreement. The percentage difference between these results ranges from 2.06% -18.02%.

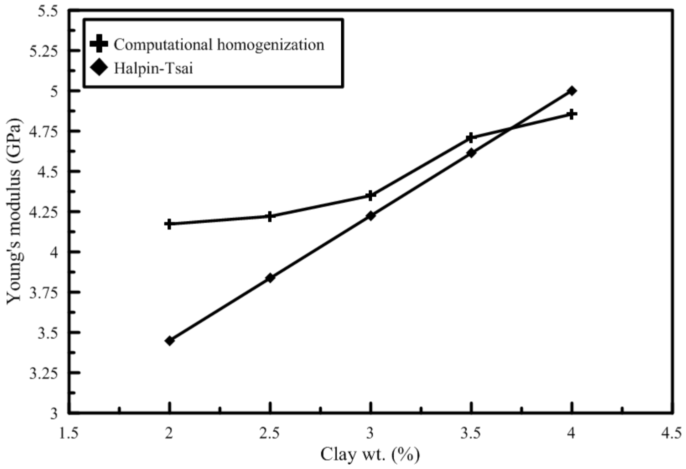

Figure 7.7: Young's modulus versus the clay wt.%.

The change in the aspect ratio of the clays changes the number of clays when the thickness of the clay platelets is set constant to 1 *nm*. Accordingly, the increase in the number of the clay platelets leads to an increase of the contact surface between the clay and the matrix which accelerates crack initiation on the surface of the clay platelets as the crack initiation often starts from the surface of the clays. Figure 7.8 shows the increase of the PNC strength with increasing the aspect ratio. When the aspect ratio exceeds a value of 250, the maximum load decreases since increasing the aspect ratio leads to an increased clay–free epoxy area. Note also that the interfacial interaction between the highly exfoliated clay and the epoxy decreases when the number of clay platelets decreases. Figure 7.9 shows the effect of the clay platelet distribution on the crack propagation. The phase field variable (SDV9) is shown in Figure 7.9. With an increasing clay aspect ratio, the number of dominant cracks can be observed.

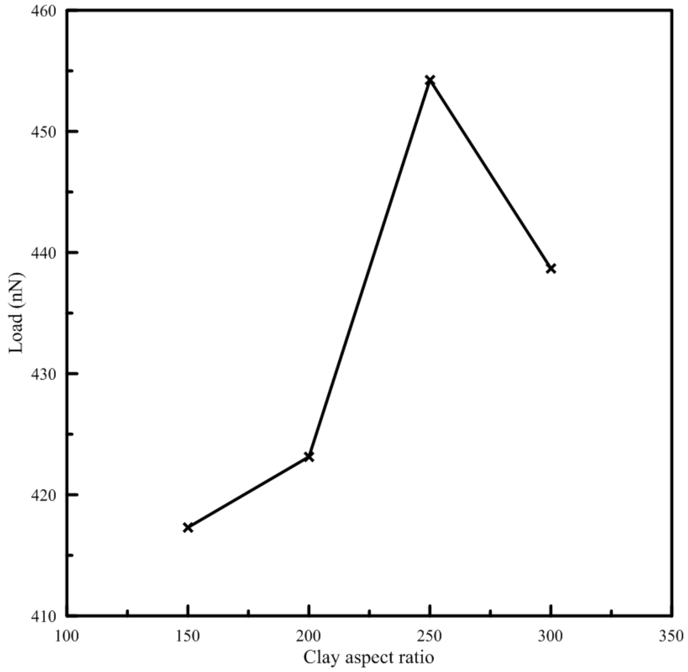

Figure 7.8: Ultimate load versus aspect ratio.

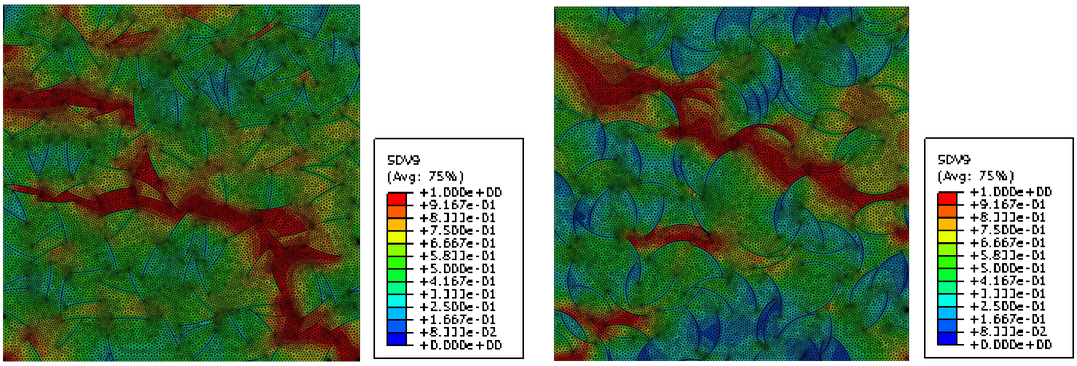

(a) Clay aspect ratio 150, 51334 elements. (b) Clay aspect ratio 200, 46888 elements.

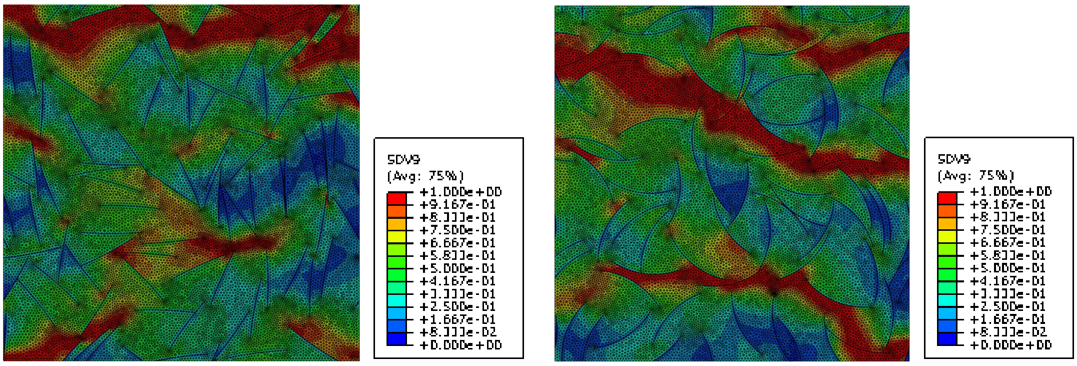

(c) Clay aspect ratio 250, 44304 elements. (d) Clay aspect ratio 300, 43006 elements.

Figure 7.9: Cracks patterns of the intact square PNCs specimens with different aspect ratio of clay with 2% clay wt. %. SDV9 = phase field.

7.3.2 Predictions of tensile strength and fracture toughness

7.3.2.1 Side notched specimen

We test four side notch specimens and compute J according to Equation (7.5). If a is half of the specimen width, the initial cracks of the specimens used are $a, 3/4\ a, 1/2\ a, 1/4\ a$. The specimen geometry is shown in Figure 7.10 with a specimen width b equal to 750 nm and height h equal to 1500 nm. The deformed shapes of the specimens are shown in Figure 7.11. The clay wt.% of these specimens is 2% with an aspect ratio 150 of clay platelets. The load–displacement curves shown in Figure 7.12 indicate that the specimen with the smallest initial crack carried the higher load which is reasonable. The J integral values are listed in the Table 7.1. They are determined between any two specimens with different initial crack length $(a_1,\ a_2)$ using the equation $(J = Area(\Delta)/(a_2 - a_1)B)$, where $Area(\Delta)$

is the area between the two curves of $a_1,\ a_2$ (164). As there is no rule to select the initial crack increment (difference in the length of initial crack), different values were used with a ratio of 12.5% - 37.5% of the specimen width with random clay distribution.

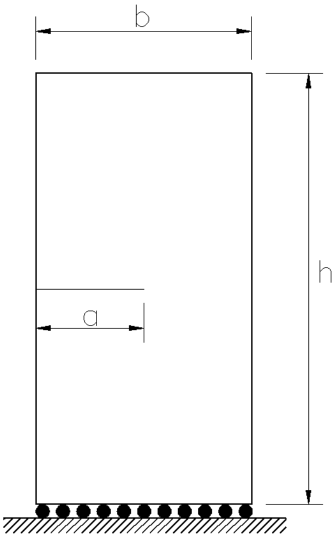

Figure 7.10: Side notch specimen geometry.

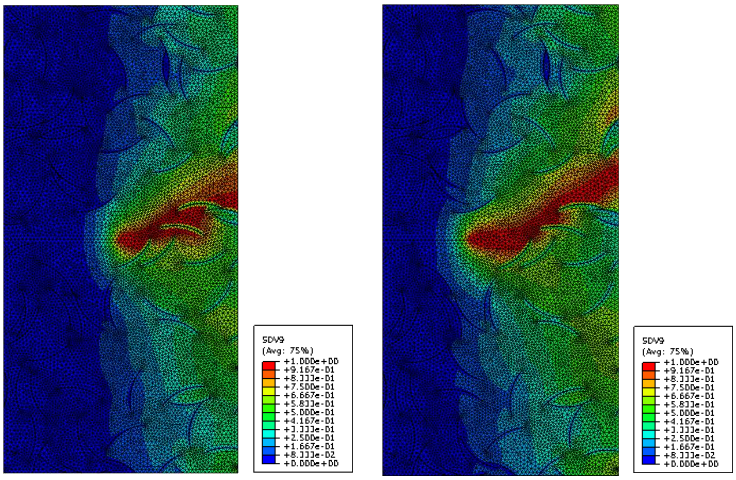

(a) Sample 1, crack = a.

(b) Sample 2, crack = 3/4 a.

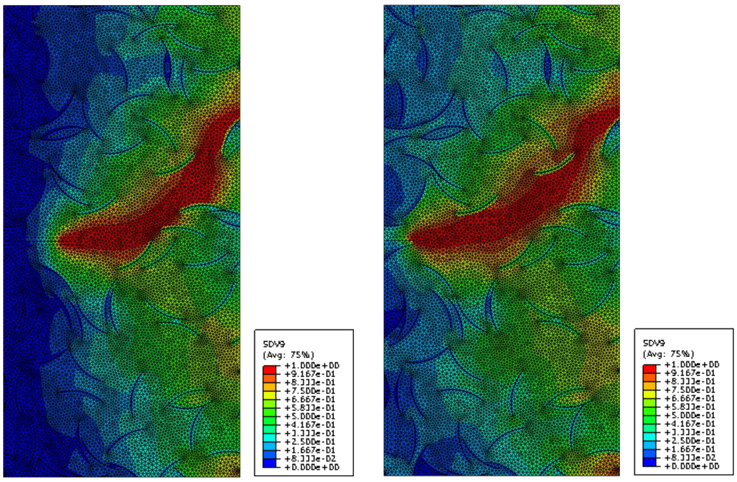

(c) Sample 3, crack = 1/2 a.

(d) Sample 4, crack = 1/4 a.

Figure 7.11: Cracks patterns of the side notched PNCs specimens with different initial crack length. SDV9 = phase field.

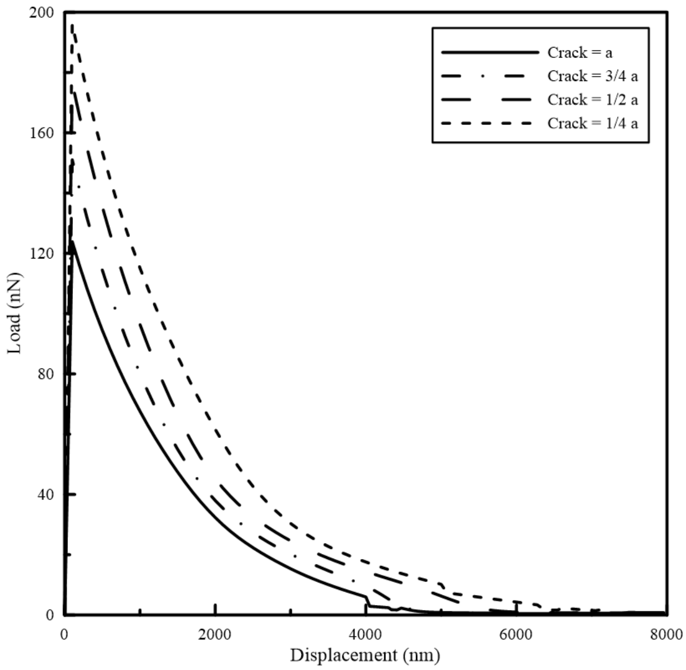

Figure 7.12: Load–displacement curves of PNCs with different initial crack length, $a = 375\ nm$.

Table 7.1: J Integral values for different samples. S1=Sample 1, S2=Sample 2, S3=Sample 3, and S4=Sample 4.

Sample No.	S1	S2	S1	S3	S1	S4	S2	S3	S2	S4	S3	S4
Crack Increment (nm)	93.75		187.5		281.25		93.75		187.5		93.75	
J integral N/m	408.95		459.82		498.6		513.15		544.63		579.02	

The results of J vary between $408.95 - 579.02\ N/m$. The results show an increase in the J value when the sample 3 and 4 (see Figure 7.11) are considered. This happens because of the crack elongation and change in the path as shown in Figures 7.11(a) and 7.11(b) causing an increase in the area under the load–displacement curve. The concern is the overall crack path in sample 3 and 4 since it is not in the directions that we aimed before the test as well as the size of the sample with respect to the clay platelets length and initial crack length. Hence, the fracture energy can not be predicted with sufficient high accuracy. To ensure high stress gradients, the double edge notched tension specimen is considered next.

7.3.2.2 Double notched specimen

For the same geometry, three double notch specimens with clay wt.% (2, 3 and 4) are tested to study the effect of the clay weight content on the J integral. The specimen dimensions are $b = 750$ nm and $h = 1500$ nm with initial crack $a = b/4$. Young's moduli for the specimens of clay wt.% 2, 3 and 4 are 4.17, 4.34 and 4.85 GPa respectively, as illustrated in Figure 7.7. We use a mesh size $h = 12$ nm in all simulations with characteristic length scale variable l_0 equal to 96.

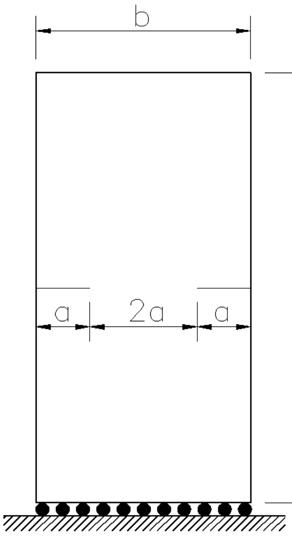

Figure 7.13: Double notch specimen geometry.

The crack path of the specimen depicted in Figure 7.14 indicates the failure process zone is matured before the complete failure of the specimen.

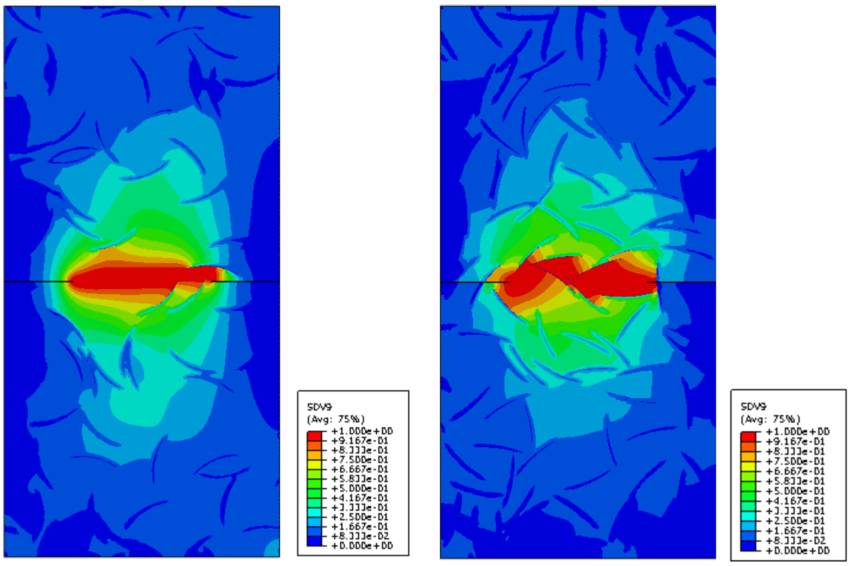

(a) Clay wt.=2 %, 25578 Elements.

(b) Clay wt.= 3%, 25651 Elements.

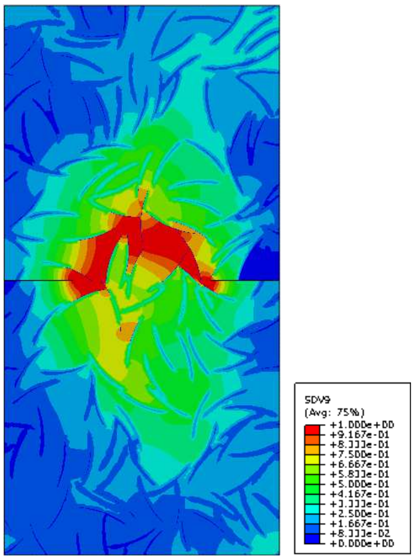

(c) Clay wt.= 4%, 26674 Elements.

Figure 7.14: Cracks patterns of the double notch PNCs specimens with different clay wt.%. SDV9 = phase field.

The load–displacement curves illustrated in Figure 7.15 showing convergence when the mesh is refined. Testing PNC samples with different clay wt.% shows that the clay wt.% is influencing the ultimate load and tensile strength of the PNCs sample, see Figures 7.16 and 7.17. The bulk and surface energy of PNC samples are notably determined by the clay wt.%. Figure 7.18 explains the determination of the clay content on the bulk and surface energy of the PNCs. Consequently, it is due to the variation in properties and fracture parameters of the samples that arise from the change in volume fraction.

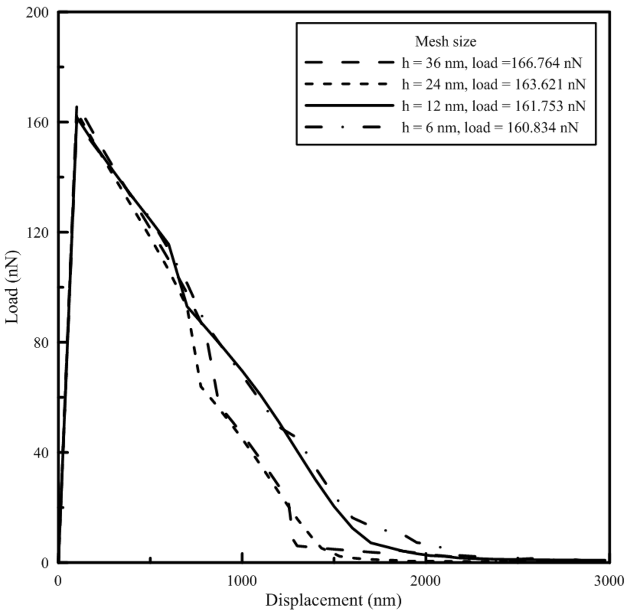

Figure 7.15: Load–displacement curves for different mesh sizes, clay wt. 2%.

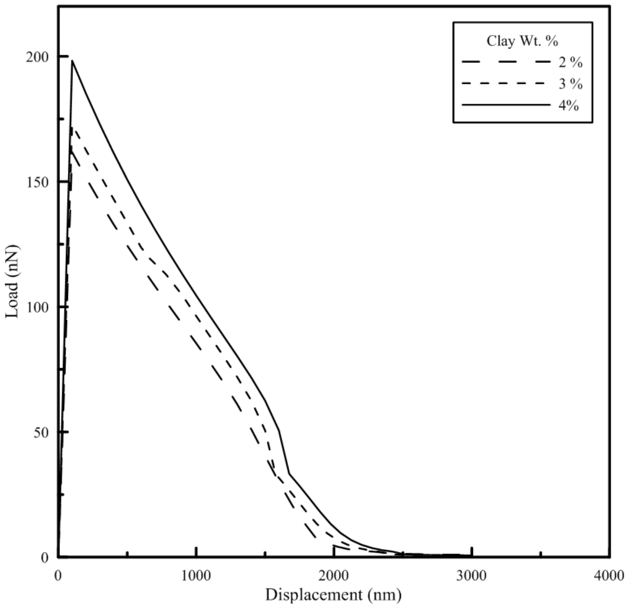

Figure 7.16: Load–displacement curves for different clay wt.%.

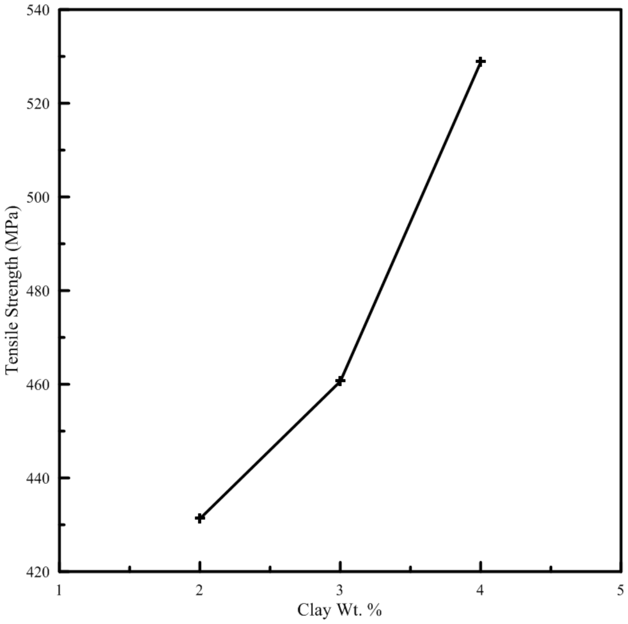

Figure 7.17: Tensile strength versus clay wt.%.

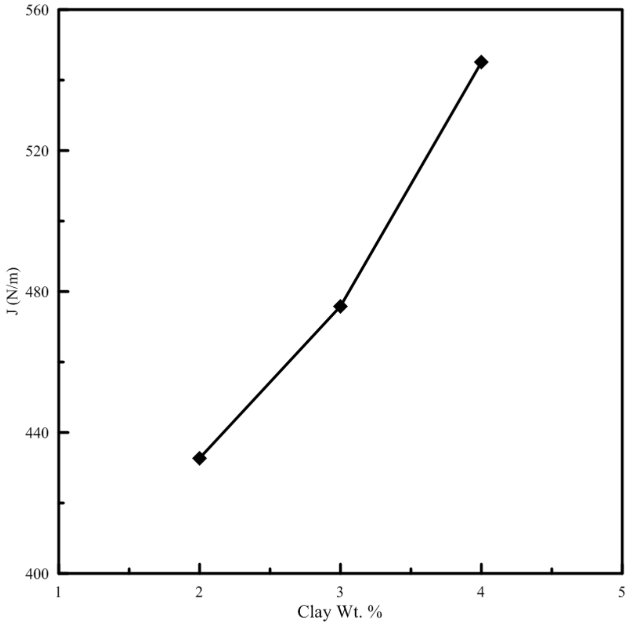

Figure 7.19: *J* integral versus clay wt.%.

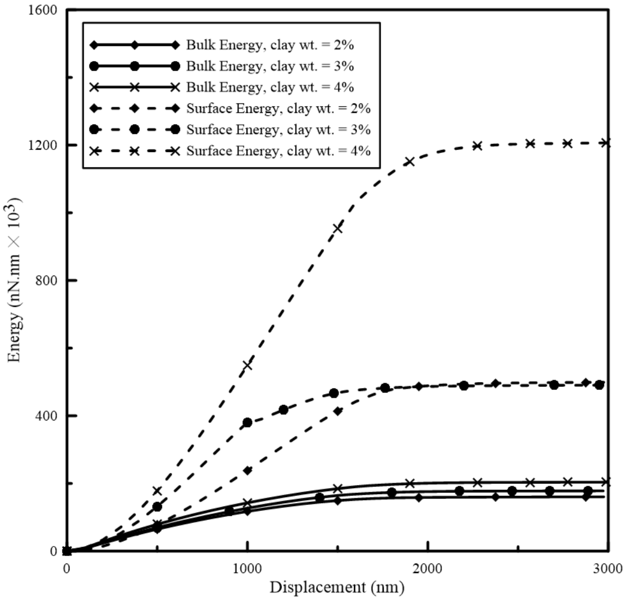

Figure 7.18: Bulk and surface energy of PNCs with different clay wt.%.

The extracted *J* values based on equation 7.5 are depicted in Figure 7.19. The results revealed that the *J* integral increases when the clay wt.% of the PNCs increase.

Figure 7.18 shows the change in the bulk and surface energy for different clay wt. %.

The total surface energies for clay wt. 2% and 3% are close to each other since the crack path and length shown in Figures 7.14a and 7.14b are approximately the same. However, a drastic increase for a clay wt. of 4% due to the increased crack length is observed. Figure 7.17 shows the tensile strength for the different clay weight ratios.

7.3.2.3 Strain energy release rate

We also study the effect of the strain energy release rate on the ultimate load of the PNCs specimen. Different values for $\mathscr{G}_c$ are used (100, 216 and 300 J/m^2) for the PNCs specimen of clay wt. 2%. The crack path were nearly identical for all the values of $\mathscr{G}_c$. Figure 7.20 shows the effect of $\mathscr{G}_c$ on the load–displacement curves while Figures 7.22 and 7.23 present the increase in the tensile strength and ultimate load when $\mathscr{G}_c$ increases. Figure 7.21 illustrates the effect of the $\mathscr{G}_c$ value on the surface energy to create new cracks. It also shows the rate of surface energy dissipation increase when $\mathscr{G}_c$ decreases. Figure 7.24 depicts the dependence of the J Integral on the strain energy release rate $\mathscr{G}_c$.

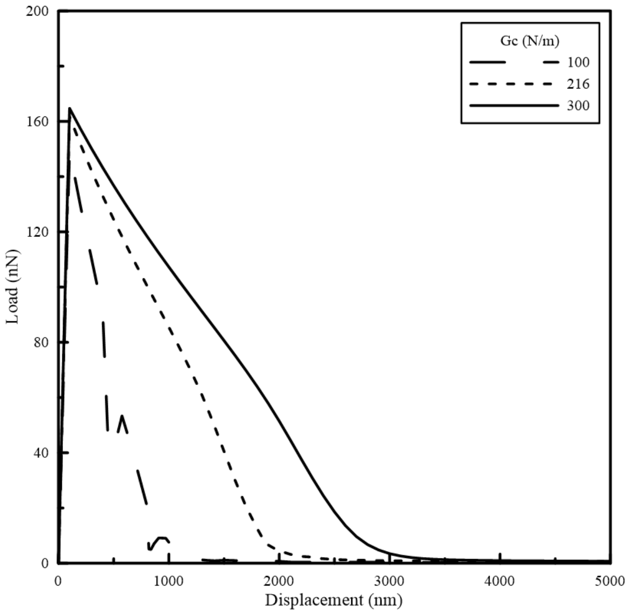

Figure 7.20: Load–displacement curves for PNCs with different matrix $\mathscr{G}_c$.

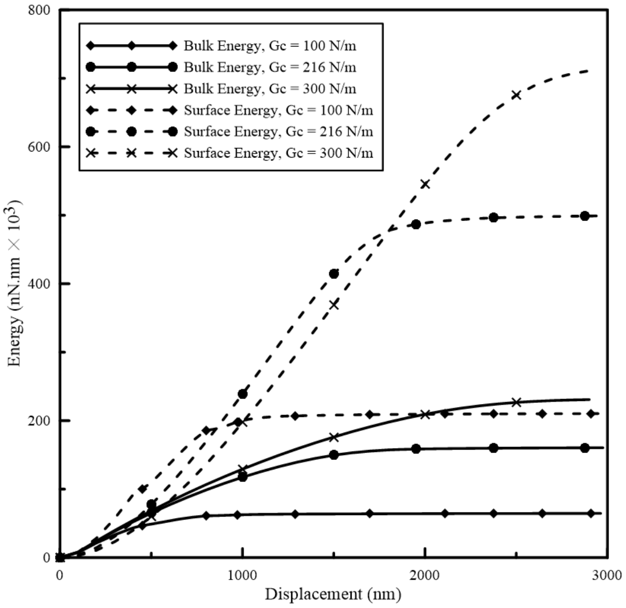

Figure 7.21: Bulk and surface energy for PNCs with different matrix $\mathscr{G}_c$.

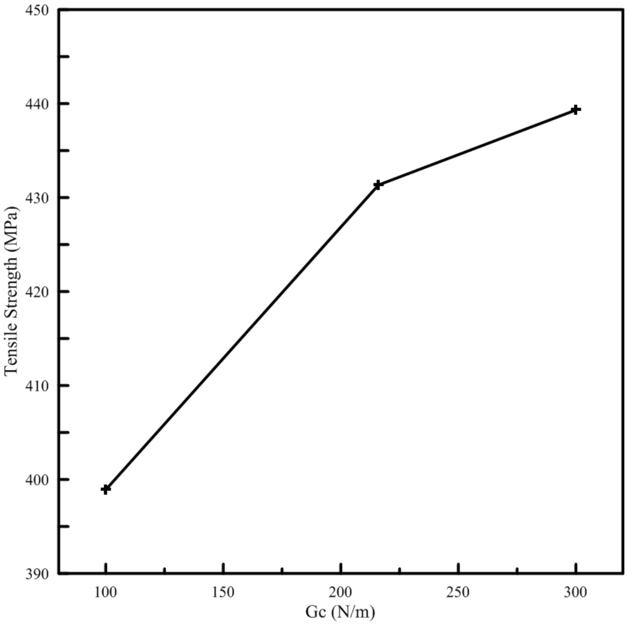

Figure 7.22: Tensile strength of PNCs versus matrix $\mathscr{G}_c$.

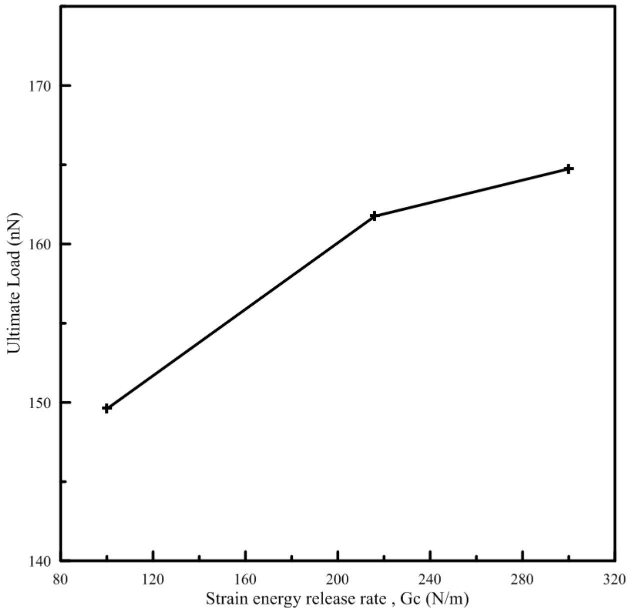

Figure 7.23: Ultimate load of PNCs versus matrix $\mathscr{G}_c$.

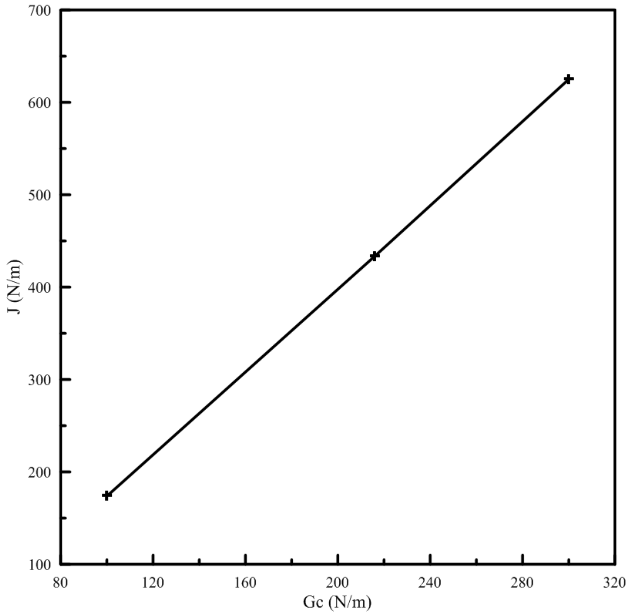

Figure 7.24: *J* integral versus matrix strain energy release rate $\mathscr{G}_c$.

7.3.2.4 Size effect

In order to study the size effect and characteristic length of different material properties (Young's Modulus, *J* Integral, and tensile strength), the size of the specimen presented in Figure 7.13 is increased by a factor of 2 yielding the dimensions $b = 1500\ nm$ and $h = 3000\ nm$. The clay wt. is kept at 2% and clay aspect ratio equal to 150. The initial crack length is $a = 375\ nm$. The load–displacement curve for different size specimens is plotted in Figure 7.26. The results indicate there is no difference in the slope of the linear elastic part of the curve which means the size doesn't affect the Young's modulus. However, a significant difference in the area under the curve between the two specimens can be observed. The calculations show a noticeable size effect on the values of the J integral (434.2 and 697.63 N/m) and tensile strength (431.34 and 228.33 MPa) for the small and big specimens, respectively, which is expected. The crack of both specimens are shown in Figure 7.25. The bulk and surface energy are shown in Figure 7.27. Clearly, the rate of surface energy dissipation in the small sample is higher than the surface energy dissipation rate in the bigger sample at the same load.

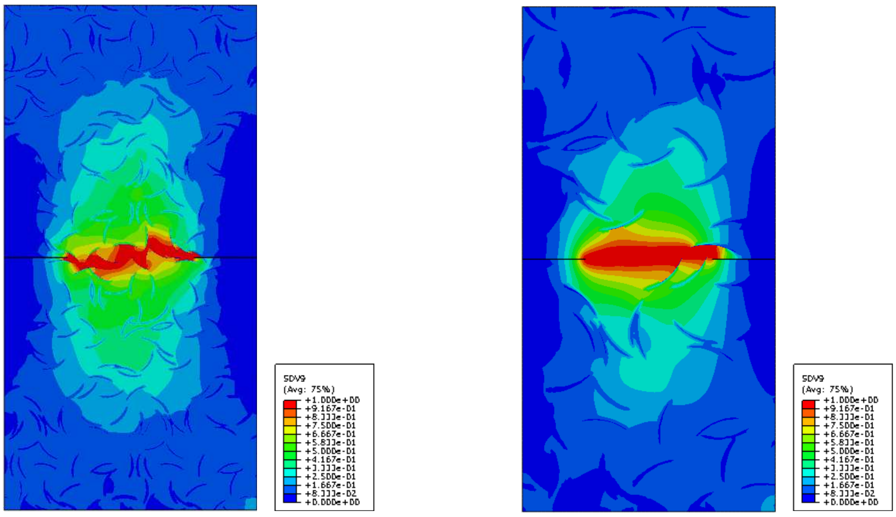

(a) Specimen with size $1500 \times 3000\ nm$, 105605 elements.

(b) Specimen with size $750 \times 1500\ nm$, 25578 elements.

Figure 7.25: Tension test of PNCs double notch specimen with different sizes. SDV9 = phase field.

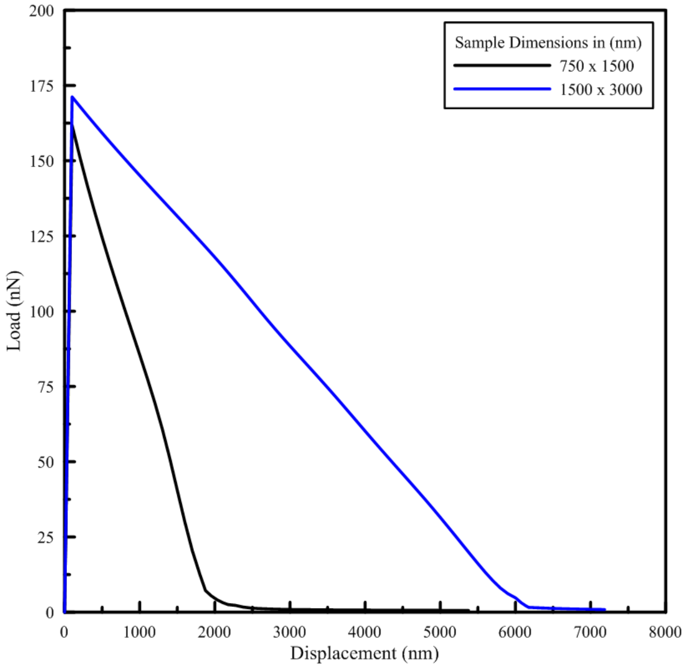

Figure 7.26: Load–displacement curves of different size specimens.

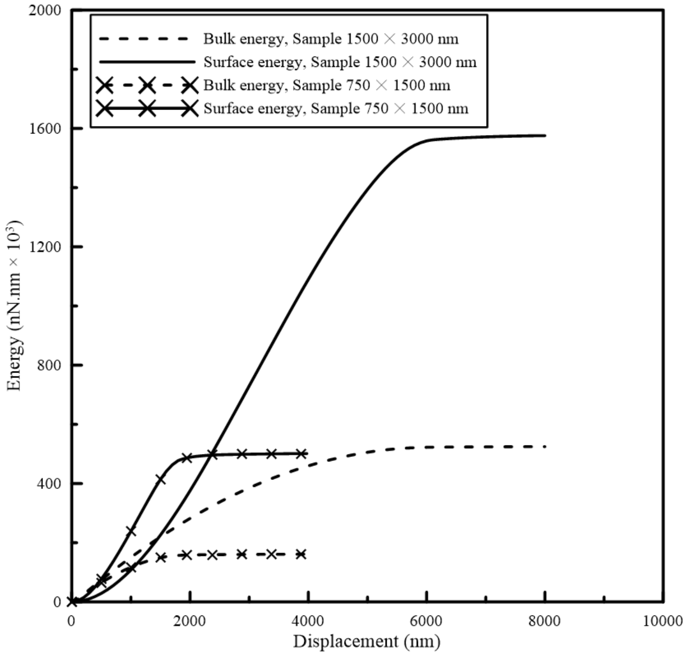

Figure 7.27: Bulk and surface energy.

Conclusion

Different samples of PNCs were tested with different geometric distribution of clay platelets which came from various clay weight percentage content and varied aspect ratios. Note that, the generation of PNCs samples itself is not straightforward and the computational memory is controlling the size and clay platelets percentage of the PNCs. The phase field method elegantly captured the cracks propagation in PNCs without any limitation. Even though, cracks path is not known in advance in the PNCs due to the random distribution and inclination of the clay platelets in the matrix. The analysis shows the change in the crack path depending on the clay platelet distribution at the same boundary conditions and under the same load. Phase field model as a deterministic model shows that the cracks initiated in three locations of the sample: the edges of PNCs samples when there are no clay platelets nearby; at the clay platelet edges, in particular when it is near another clay platelet; and at the supports of the samples. After the crack initiates from one of those positions, it continues propagating in the matrix under the load increments towards other cracks until the sample is completely split. In the analysis, different issues were addressed; for example the percentage increase in the tensile strength of the PNCs was 10.12% when the strain energy release rate of the matrix increased from 100 N/m to 300 N/m. The clay wt. % increasing from 2% - 4% causes a percentage increase 22.6% in the tensile strength and 16.35 % in Young's modulus of the composite, while the J integral increased by 25.95%.

Chapter 8

Predictions of Young's Modulus, *J* Integral, Tensile Strength, and Surface Energy of Clay/Epoxy Nanocomposites Material with Interphase Zones

The influence of the IP zone properties and its interfacial effects are studied in this chapter. This chapter proposes a numerical approach to examining the IP zone effects on PNCs and to predicting Young's modulus, tensile strength, fracture toughness, and surface energy dissipation of PNCs in the presence of IP zones. A comprehensive study of the crack areas at different thicknesses of IP zones and matrix material is also presented.

8.1 Mechanical properties

The mechanical properties of interface layers have been predicted using different methods including molecular dynamics and analytical estimations (77) with contradictory results. By using the molecular dynamic modeling and multi-scale modeling, the IP zone considered softer than the epoxy in (165, 166). And stiffer in (167–169). Peng *et al.* (77) proposed the approximation model "graded effective interface". The results of this model were the same of the molecular dynamic simulations as reported by (165). The graded effective interface model estimates the IP's Young's modulus as following:

$$E_{IP} = (1-x)^n E_c + x^m E_m \ , \tag{8.1}$$

where E_{IP}, E_c, and E_m are the Young's modulus of the IP, the clay, and the matrix respectively; x is the normalized distance from the clay surface to the boundary between the matrix and the IP zone, i.e. it is equal to 0 at the clay surface and 1 at the IP/matrix boundary. Equation 8.1 is the rule of mixture to the relation of the elastic properties of the material in the interface to the density of the corresponding material atoms. The m and n are parameters related to the properties of the IP. The values of these parameters were selected from a distribution by (77) to represent the different properties of the IP, and equal to:

$$\left\{ \begin{array}{cc} \mathrm{n} = 200,\ \mathrm{m} = 0.2 & \text{for weak interphase} \\ \mathrm{n} = 40,\ \mathrm{m} = 0.1 & \text{for stiff interphase} \end{array} \right\}.$$

Young's modulus of the matrix, clay nano platelets, IP, and Poisson's ratios are summarized in Table 8.1 as listed in (1, 158, 160). The critical energy release rate of the matrix is equal to 216 N/m as proposed by Wang *et al.* (1). The energy release rate of the IP is used between 1 N/m as in (170) and 25 N/m as in (6).

Table 8.1: Elastic and fracture properties of epoxy, clay and IP zone

	Epoxy	Clay	IP Zone		
			Weak	Soft	Stiff
E (GPa)	1.9	234.9	1.0	2.75	7.45
υ	0.35	0.25	0.35	0.35	0.35
$\mathscr{G}_c$ (N/m)	216	-	1, 10, and 25		

The experimental determination of the IP thickness is difficult. For organically modified montmorillonite clay immersed in different epoxies (such as Polyamide 6, Polylactic Acid, High–Density Polyethylene, Polypropylene, and Polyamide 12), the relationship between the IP thickness to the clay platelets thickness varies between (1–4.5) (105). Akay (171) and Pukanszky (104) recorded an IP thickness of 3.6 nm for silicate clays immersed in a high–density Polyethylene and Polypropylene matrix polymer. To investigate the effect of the IP thickness, we used different values of the IP thicknesses: 1, 2, 3, and 4nm. The aspect ratio of clay platelets in all simulations is used equal to 50 nm (72).

8.2 Numerical examples

8.2.1 Crack diffusion length (ℓ_0) of the phase field model

The crack diffusion property is a recognized drawback in phase field model since it requires a specific mesh density that constrain the simulations' size (2). To avoid the influence of the diffusion length and maintaining the condition of selecting it's quantity in the PNCs intensive mesh configuration. The IP zone have been discretized to have at least four elements in depth as noted in Figure 8.1. By using this meshing technique, the influence of the diffusion is kept small as reported in Figure 8.2. Moreover, the crack diffusion length has not been influencing the PNCs' tensile strength as determined in Figure 8.3. Additionally, the crack diffusion length is used constant in all the simulations unless mentioned.

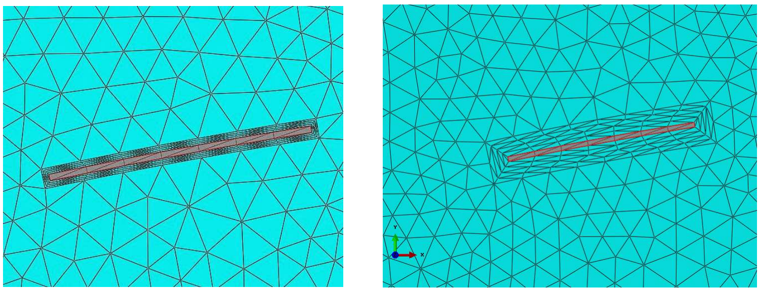

IP = 1 *nm* IP = 4 *nm*

Figure 8.1: Mesh discretization

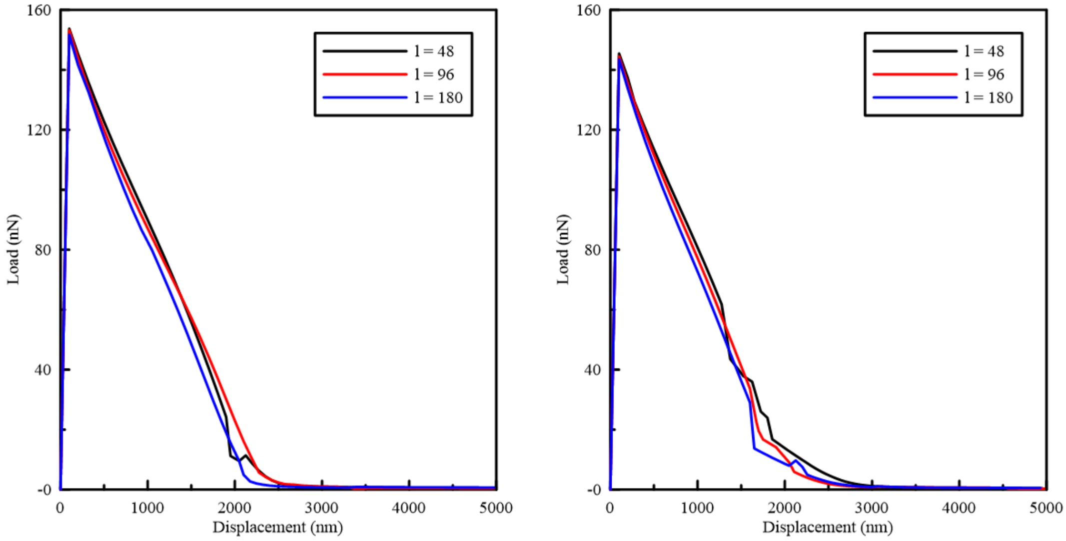

IP = 1 *nm* IP = 4 *nm*

Figure 8.2: Load–displacement curves of PNCs samples with 2 % clay wt. and different crack diffusion lengths, $\mathscr{G}_c = 25\ N/m$, $E = 1.0\ GPa$.

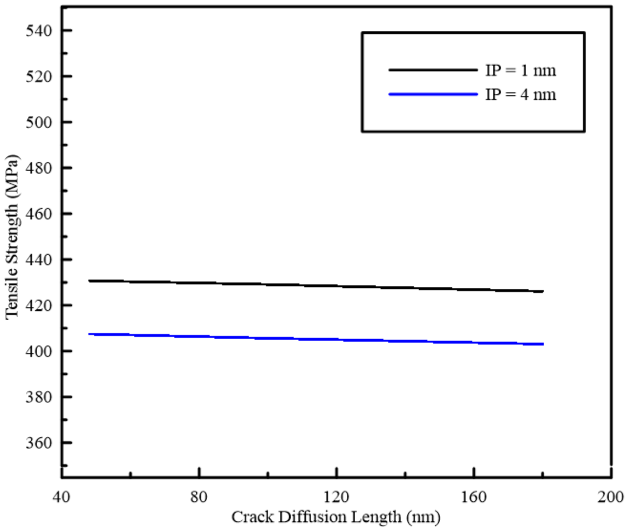

Figure 8.3: Tensile strength versus crack diffusion length.

8.2.2 Predictions of Young's modulus

Prediction of Young's modulus of PNCs is necessary to predict the tensile strength and fracture toughness of PNCs for different IP thickness and properties. Therefore, four PNC specimens with a 2% clay ratio and IP thicknesses of 1, 2, 3, and 4 *nm* have been tested under pure tension loads in different directions. The phase field model is not necessary for these simulations since there is no need to fracture modeling. The macroscopic Young's modulus E of the PNCs has been extracted by computational homogenization. The composite Young's moduli for different IP thicknesses and Young's moduli are compared to the fully bonded PNCs in Figure 8.4.

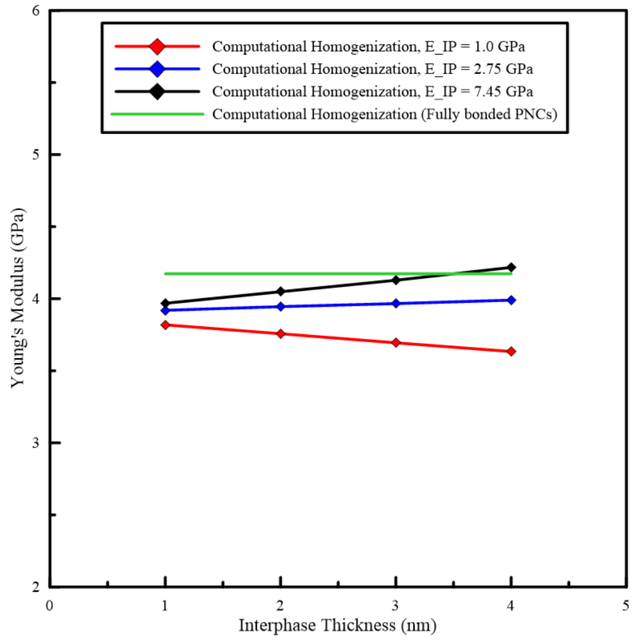

Figure 8.4: Young's modulus of PNCs for different IP thickness and properties.

8.2.3 Predictions of tensile strength and fracture toughness

The double notch sample under tension load (DENT) is used to predict the tensile strength and fracture toughness of PNCs. The geometric setup is shown in Figure 8.5. We have generated randomly different clay distributions as described in 6.2. For a clay wt. of 2%, Figure 8.6 shows exemplary for four samples with two different IP zone thickness, that the load-deflection curve is fairly independent on the random clay distribution. The associated crack evolution in two samples can be observed in Figure 8.7.

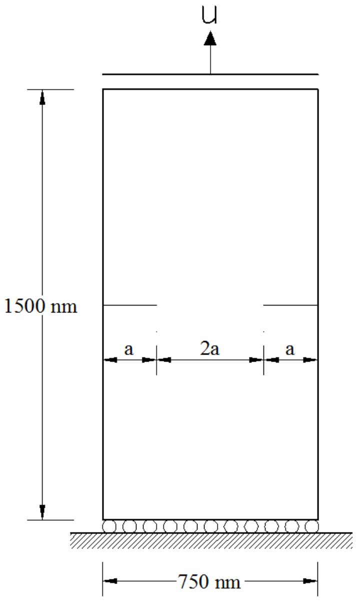

Figure 8.5: DENT sample geometric setup.

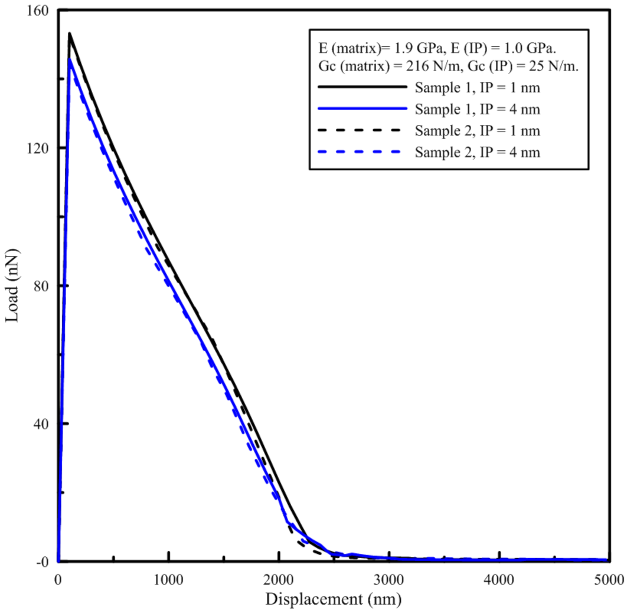

Figure 8.6: Load–displacement curves for samples with different clay distribution.

The crack patterns of the two samples at different load steps and IP thickness of 1 *nm* are shown in Figure 8.7.

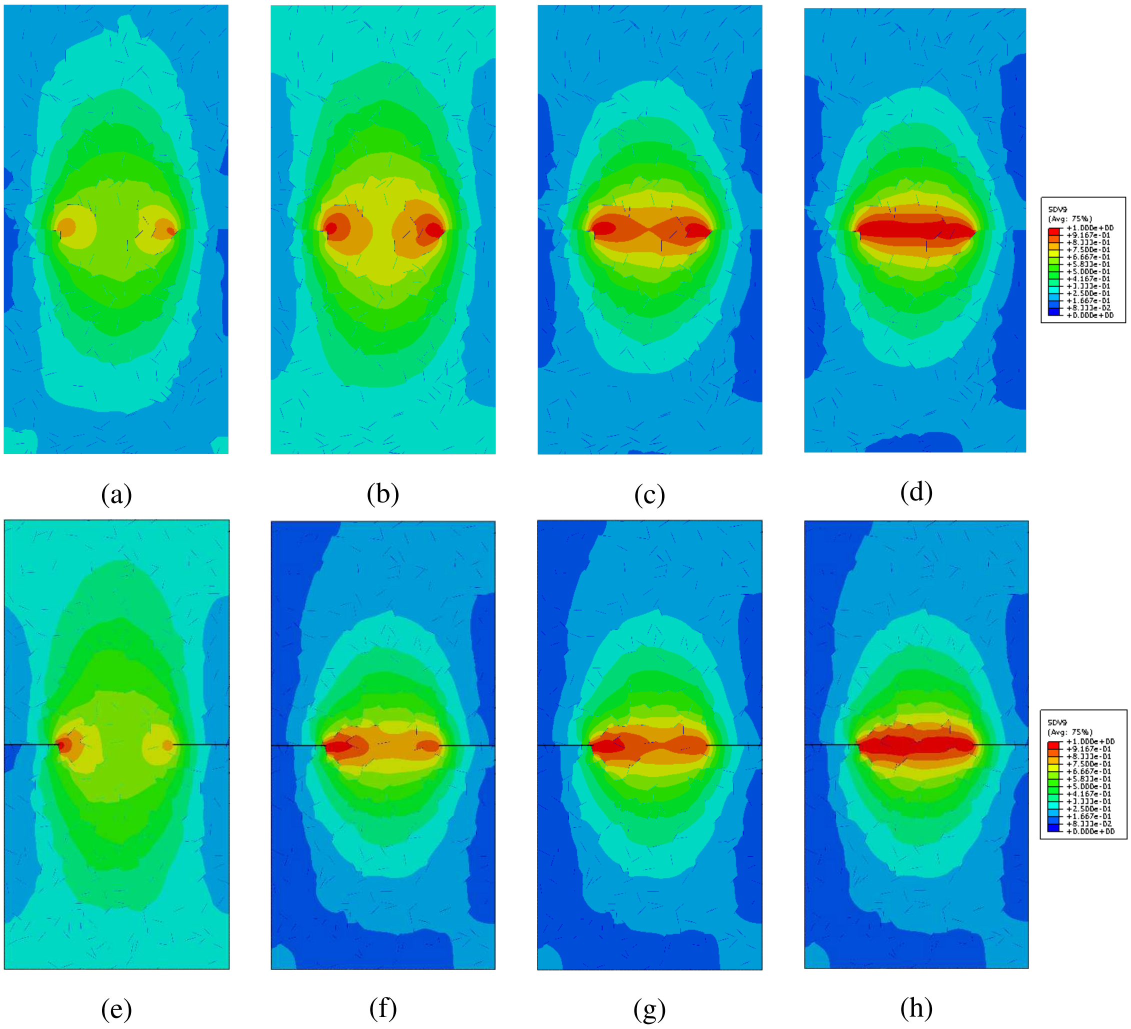

(a) (b) (c) (d)

(e) (f) (g) (h)

Figure 8.7: Crack pattern of DENT sample at different load steps for different clay distribution in samples. Distribution 1 (a–d), distribution 2 (e–h). IP=1 *nm*. SDV9= phase field.

Next, we consider four PNCs samples with a clay weight ratio of 2% and IP thicknesses of 1, 2, 3, and 4 *nm*. We also test the influence of varying properties on the tensile strength of the PNC. In all samples, the crack starts at the IP nearest to the notch and extends into the matrix towards the nearby IPs and the notch edge. Figure 8.7, for example, records the slight change in crack path and propagation when the clay platelets distribution between the notches changes.

The load–displacement curves with an IP zone thickness of 1 *nm* with different Young's moduli and constant $\mathscr{G}_c = 1.0\ N/m$ are depicted in Figure 8.8.

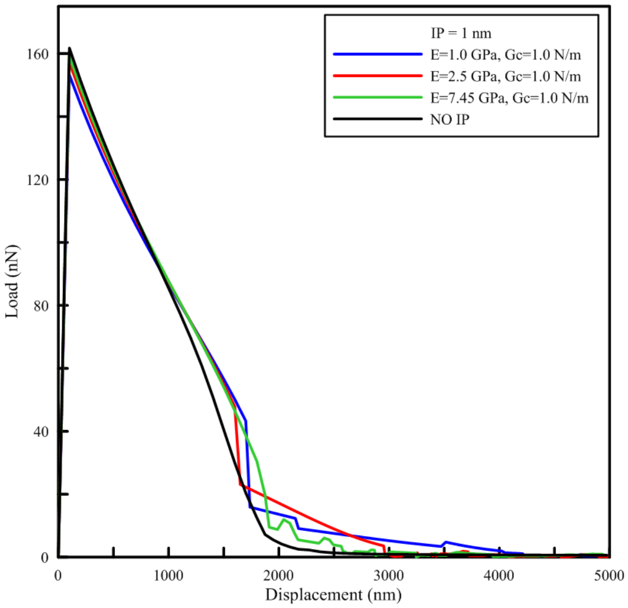

Figure 8.8: Load–displacement curves of 1 *nm* IP zone thickness for different Young's modulus E and constant strain energy release rate $\mathscr{G}_c = 1.0\ N/m$.

The effect of IP' elastic moduli on tensile strength is shown in Figure 8.9. Increasing Young's modulus of the IP causes an increase in the composite elastic moduli and tensile strength. This effect is most pronounced with increasing IP thickness. Furthermore, the conclusion was the same for the results of IP thicknesses of 2 *nm*, 3 *nm*, and 4 *nm*. However, the strain energy release rate of the IP zone does not show a remarkable influence on the PNCs tensile strength as exposed in Figure 8.10.

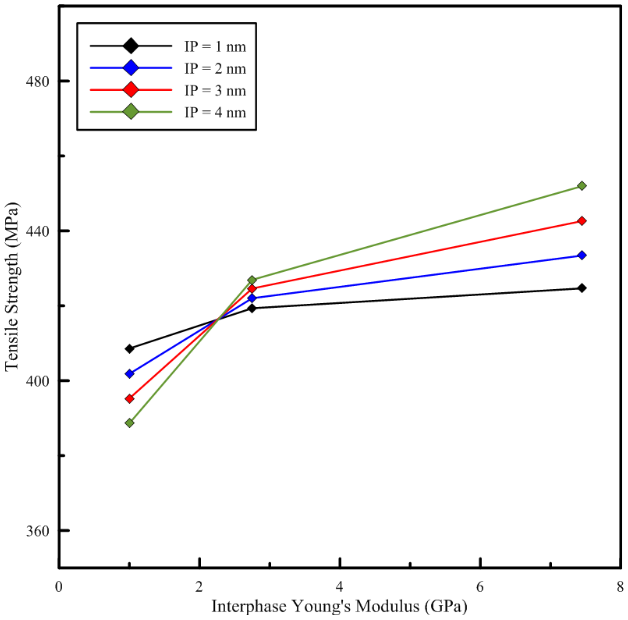

Figure 8.9: PNCs tensile strength for different IP thickness and Young's modulus, $\mathscr{G}_c = 25\ N/m$.

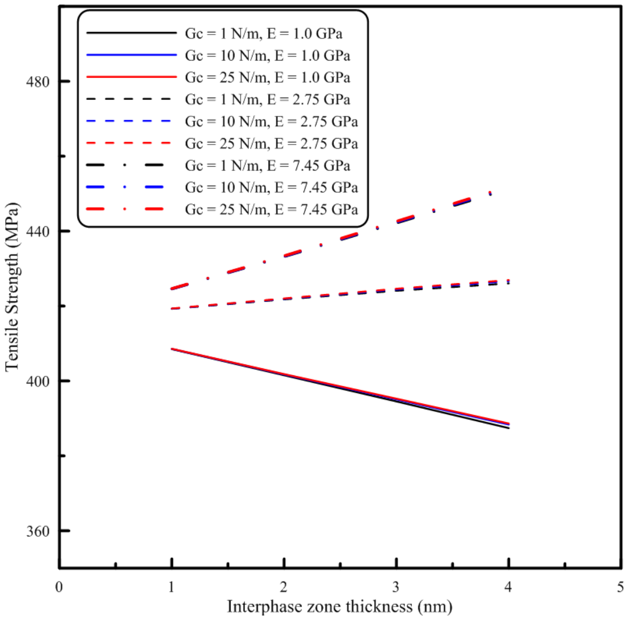

Figure 8.10: PNCs tensile strength for different $\mathscr{G}_c$, thicknesses, and IP zone Young's moduli.

The critical property of fracture toughness is calculated using the procedure detailed in section 7.2. In PNCs, evaluating the J integral through domain integral is difficult since the crack tip cannot be clearly located due to the excessive “micro-cracking” in the sample (161, 172).

The predicted J integral values for different Young’s moduli and constant $\mathscr{G}_c$ of the IP zones are depicted in Figure 8.11. The results show that the J integral decreases as the IP thickness increases. The results also reveal that the J integral decreases when the Young’s modulus of the IP increases. The maximum decrease in the J integral is 5.49% with an IP of 4 *nm*, whilst the minimum percentage of difference in the J integral is 0.99% with an IP of 1 *nm*. The dashed line in Figure 8.11 indicates the value of the J integral without the IP when the clay is fully bonded to the epoxy matrix (7). The results show a difference in J integral values for various configuration of PNCs in addition to the deviation from the fully bonded PNCs. Differences are due to the influence of the different IP zone parameters. For example, IPs’ Young’s modulus affect the composite Young’s modulus and tensile strength which leads to change the J integral of the sample.

The effect of varied values of $\mathscr{G}_c$ on J integral with 2% clay wt. PNCs are shown in Figure 8.12 for different values of Young’s modulus and different IP thickness. J integral increases by increasing the IP’s strain energy release rate $\mathscr{G}_c$, this change significantly appears at thicker IP thickness.

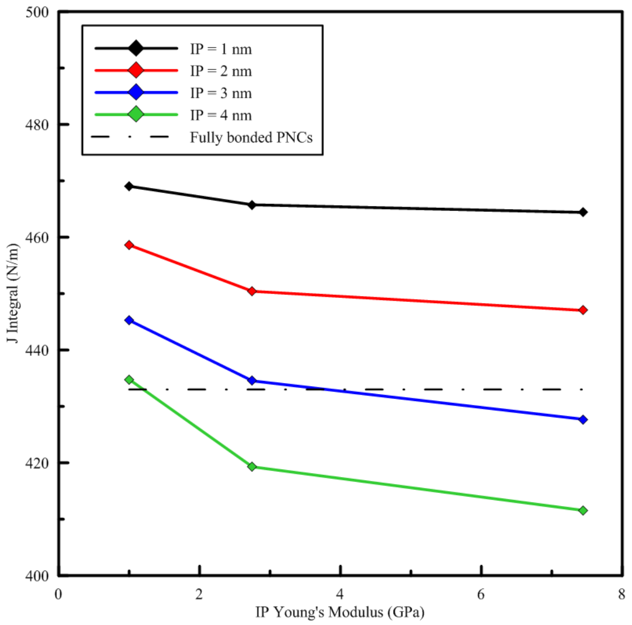

Figure 8.11: J integral versus Young’s modulus of IP zone thickness.

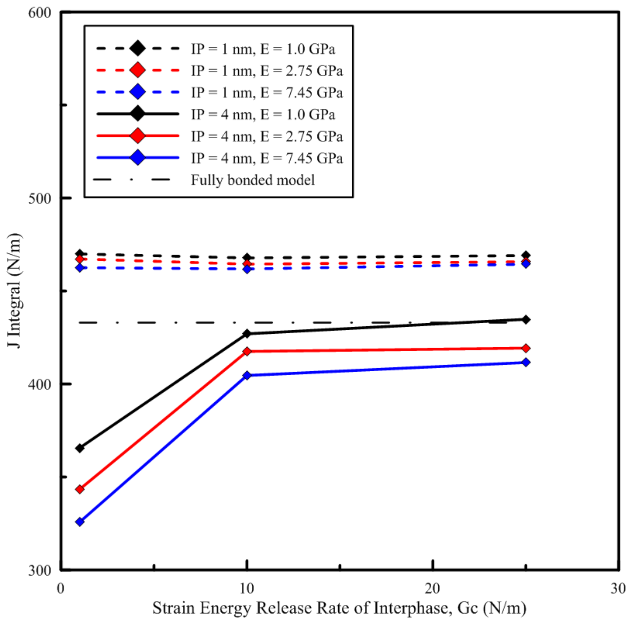

Figure 8.12: J integral versus $\mathscr{G}_c$ of IP zone.

8.2.3.1 Surface energy dissipation of PNCs

The surface energy value and the associated crack surface values can be extracted through the phase field model from Equation 3.17. Varying the IP critical strain energy release rate and the IP thickness significantly affect the surface energy dissipation of the PNCs specimens. Figure 8.13 illustrates the effect of the critical strain energy release rate and Young's modulus of the IP on the surface energy dissipation in the PNCs of the same clay distribution. Despite the lower $\mathscr{G}_c$ value of the IP with respect to the matrix which is 216 N/m, the total dissipated surface energy is significantly higher compared to the fully bonded model where the IP is not considered. This increase in surface energy dissipation can be explained by the crack diffusion around the clay platelets which causes more "micro–cracks" compared to the fully bonded PNC sample. Figure 8.14 shows the influence of the IP thickness on the surface energy exemplary for an IP critical energy release rate of $\mathscr{G}_c = 25$ N/m. An increase in the IP thickness leads to a decrease in the slope of the surface energy-displacement curve. Interestingly, the fracture energy increases as the IP thickness decreases which is counter-intuitive considering that the dissipated energy is lowest for an IP thickness of 0. We attribute this affect to crack diffusion around clay platelets which occurs as the IP thickness increases. The extension of cracks from the IP to the matrix in samples of IP=1 nm produces an increase in the surface energy, part of this increase is due to the higher fracture energy value of the matrix (216 N/m) with respect to the IP which is $(1-25\ N/m)$.

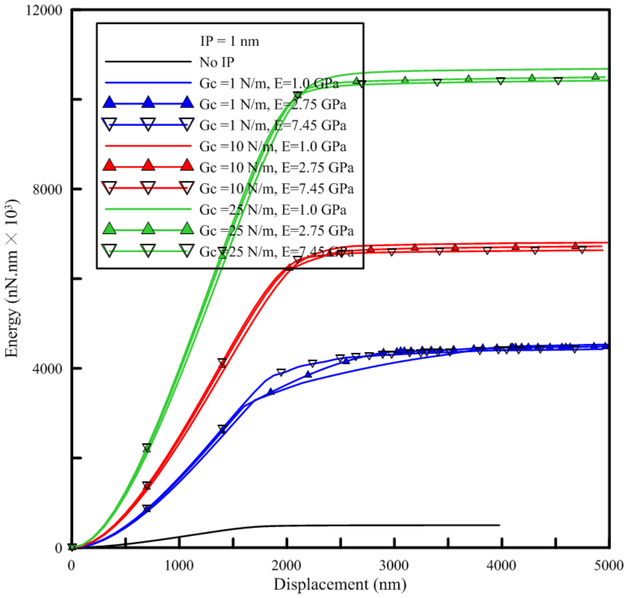

Figure 8.13: Surface energy for different $\mathscr{G}_c$ and E of IP.

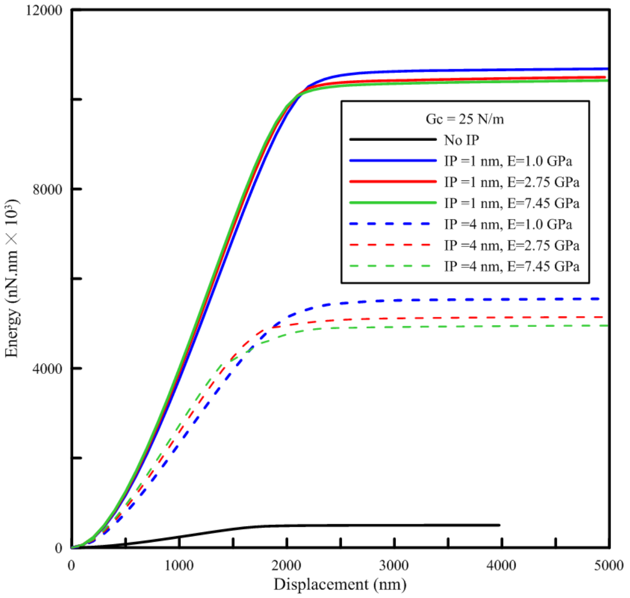

Figure 8.14: Surface energy for different IP thickness and Young's modulus E.

The total cracks surface area of the matrix and the IP zones for different material properties and IP zone thicknesses are illustrated in Figure 8.16. The analyses find that the IP zone thickness is affecting the area of phase field diffusion and provides that most of the cracks occur in the weaker IP zones. Therefore, the cracks surface area in IP zones and the matrix are individually evaluated in Figure 8.17. The highest crack surface area appears in the IP zone and is drastically affected by the IP thickness. The crack surface in the epoxy matrix depends less on the IP thickness. In PNCs with an IP 1 *nm* thick, the cracks surface area is higher than in PNCs which have a 4 *nm* of IP thickness. This observation indicates that; at a certain applied load, fewer IP zones of high thickness can provide the deformation of more IP zones with thin thicknesses as the IP zone areas are representing the weakness in the composite. The reduction in cracks area when the IP changes are also clearly noticed in the tension test of intact samples presented in Figure 8.15(a–d). These intact samples have the same clay distribution and properties aside from the thickness of the IP. The variation in the diffusion of the phase field values over all samples of different IP thicknesses is also describing the phenomenon.

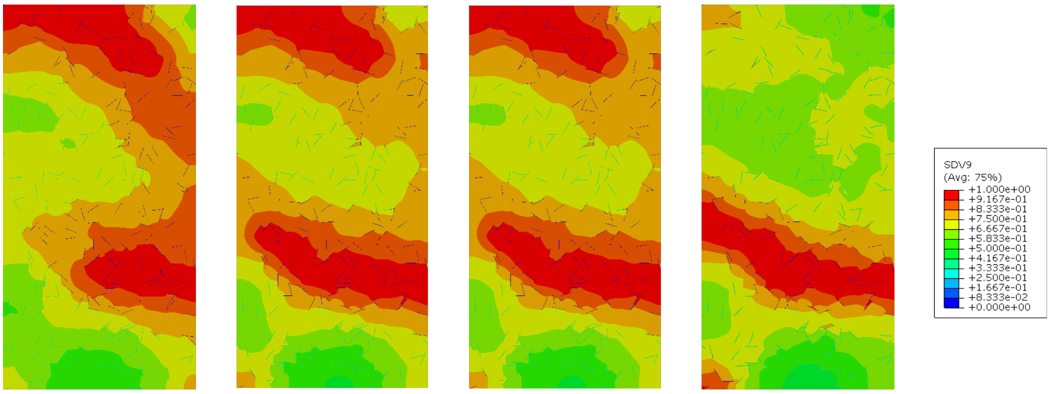

(a) IP= 1 nm (b) IP= 2 nm (c) IP= 3 nm (d) IP= 4 nm

Figure 8.15: Crack patterns in PNCs samples with different IP zone thicknesses. (a) 53797 elements; (b) 48091 elements; (c) 50478 elements; (d) 46834 elements.

To precisely estimate the crack surface area in different areas of the PNC sample, a new geometric setup is presented in Figure 8.18. In this figure, the hatched area is selected to compute the cracks surface area in addition to the complete area of the cracks in the entire sample. The results for samples with different IP thicknesses are reported in Figure 8.19. The consequences signify that there is a large area of cracks settled near the notches within the matrix and the IP zones. The percentage difference in cracks surface area for the different zones of the sample ($400\ nm \times 750\ nm$ and $1500\ nm \times 750\ nm$) are 29.7% and 15.1% for IP of 1 *nm* and 4 *nm*, respectively.

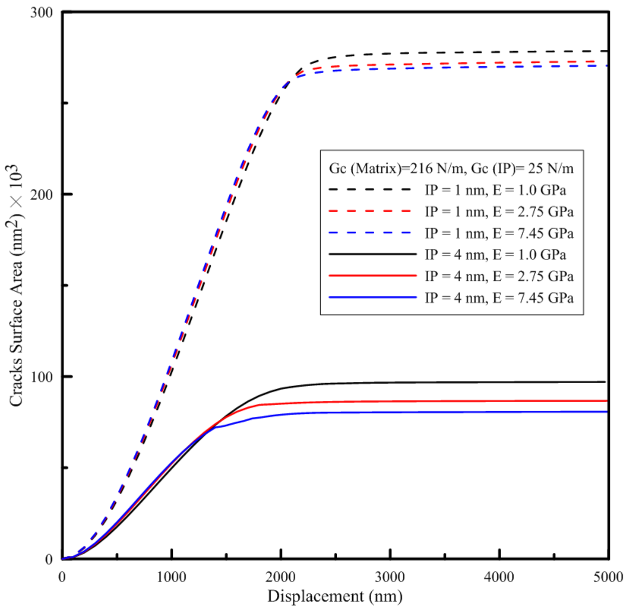

Figure 8.16: Total cracks surface area of PNCs with IP = 1 *nm* and 4 *nm* with different Young's modulus.

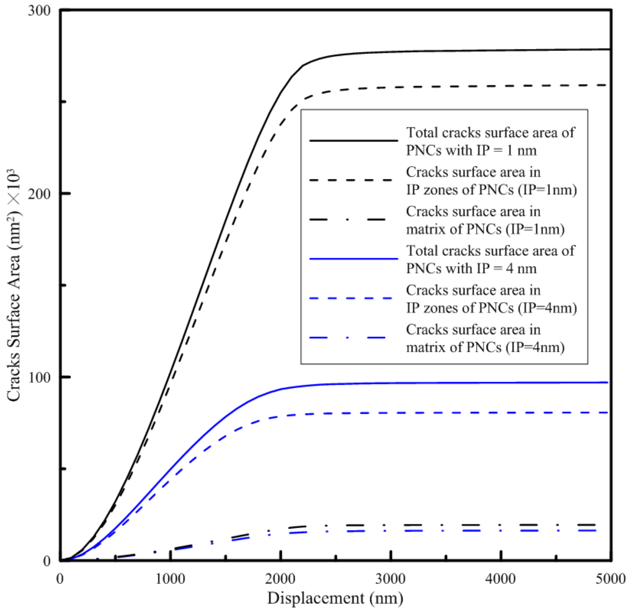

Figure 8.17: Cracks surface area in IP, matrix, and PNCs.

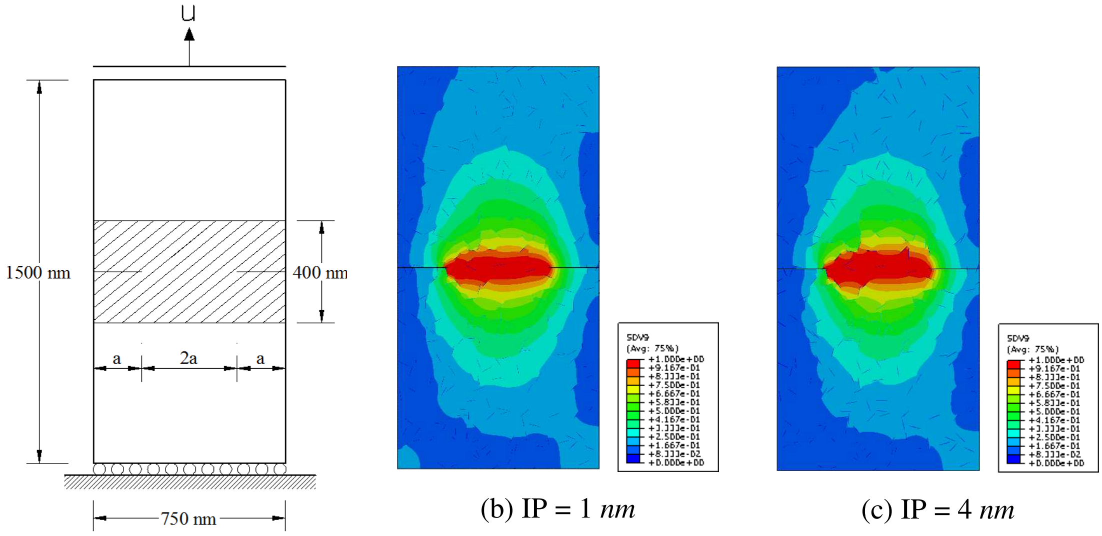

(b) IP = 1 *nm*

(c) IP = 4 *nm*

(a) Geometric setup

Figure 8.18: DENT sample geometry and phase field, SDV9 = phase field.

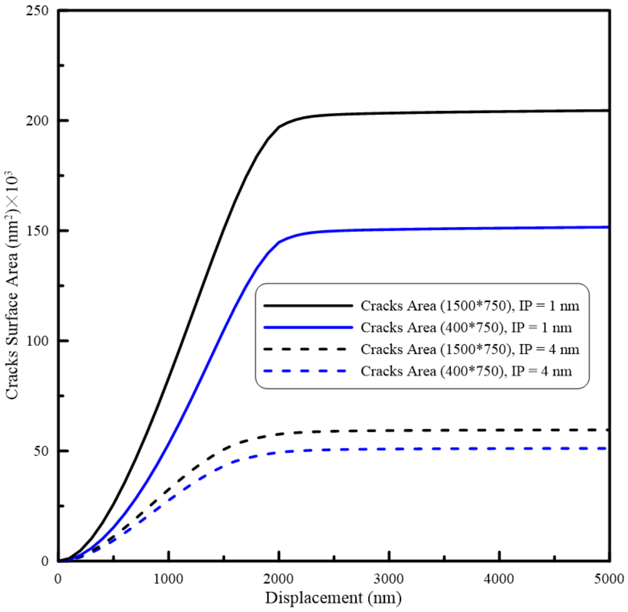

Figure 8.19: Cracks surface area in PNCs for different depths.

8.3 Prediction of macroscopic fracture energy of PNCs

Since the cracks are mainly matured between the DENT specimen notches regardless the IP thickness and properties. We introduce a new configuration of DENT specimen to observe the crack propagation at the interface regions in addition to manage the high computation cost required for the analysis. Hence, the RVE of the PNC material contains 2% wt. of clay is plugged in the DENT sample between the initial notches of the test specimen as shown in Figure 8.20. The material properties of the IP zone, matrix and clays are listed in Figure 8.20. Regardless the RVE, the properties of the other parts of the specimen are selected from the computational homogenization for PNC sample of IP = 10 *nm* with Young's modulus of 1.0 *GPa*, for instance, Young's modulus is 2.9 *GPa* and Poisson's ratio is 0.35.

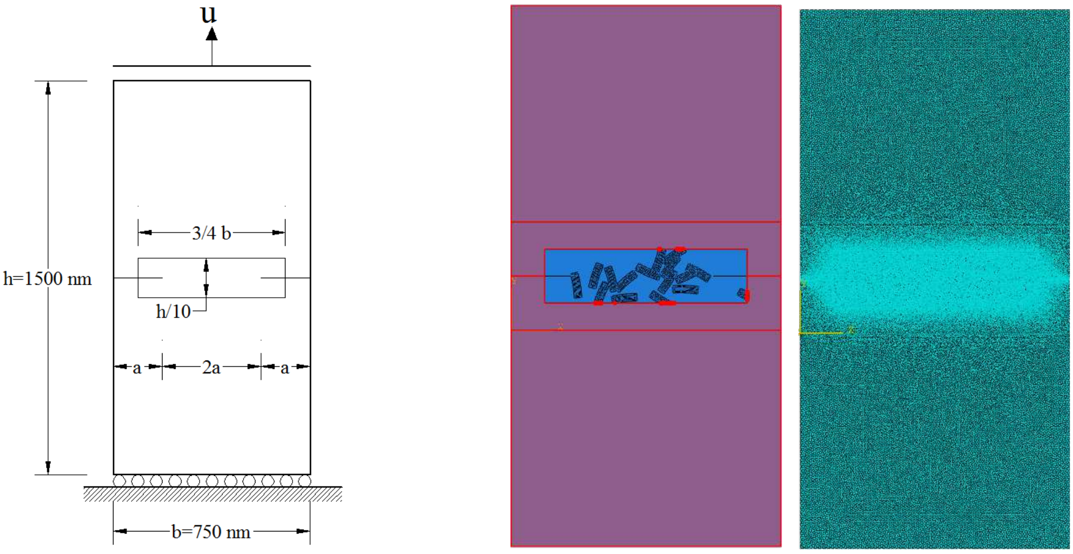

(a) Geometric setup.

(b) Mesh discretization, 264408 Elements, $\ell_0 = 10$

Figure 8.20: Specimen Configuration (Matrix: $E = 1.9\ GPa$, $\nu = 0.35$, and $\mathscr{G}_c = 216\ N/m$. Clay: $E = 234\ GPa$ and $\nu = 0.25$. IP: $\mathscr{G}_c = 25\ N/m$).

The load–displacement curve and the total surface energy of the sample under loading increments are given in Figures 8.21 and 8.22, respectively. The jumps in the load–displacement curve labeled (A–F) have occurred when the new crack propagates from the IP zone and touches the matrix which has a higher critical energy release rate $\mathscr{G}_c$ and Young's modulus E as depicted in Figures 8.23(A–F).

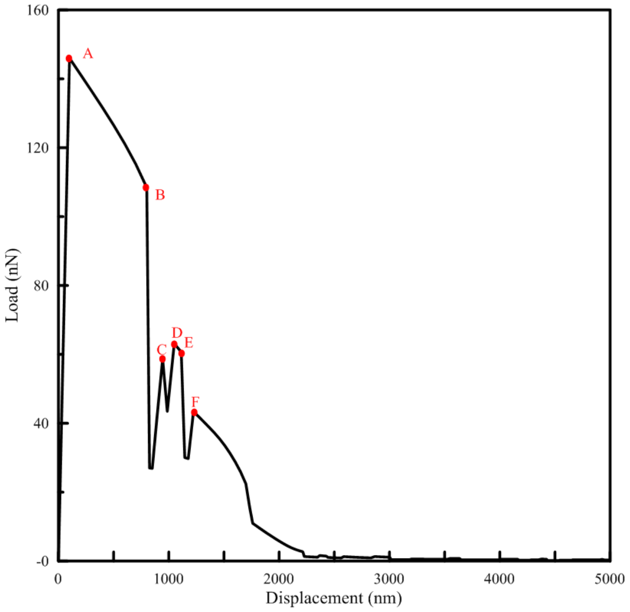

Figure 8.21: Load–displacement curve.

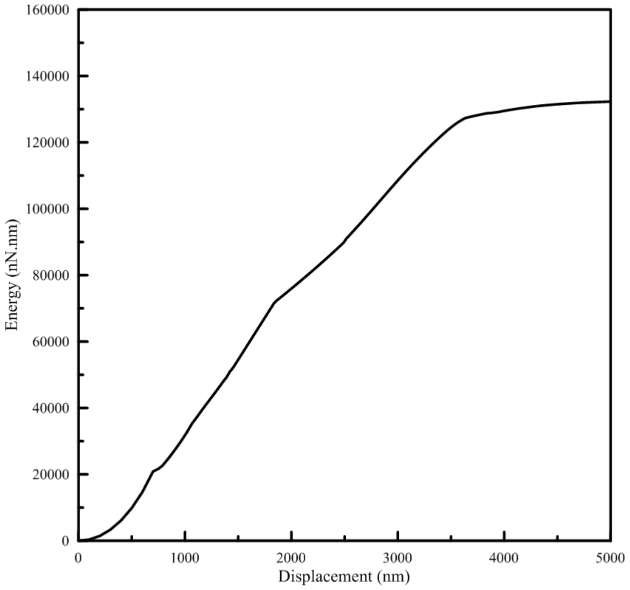

Figure 8.22: Surface energy dissipation.

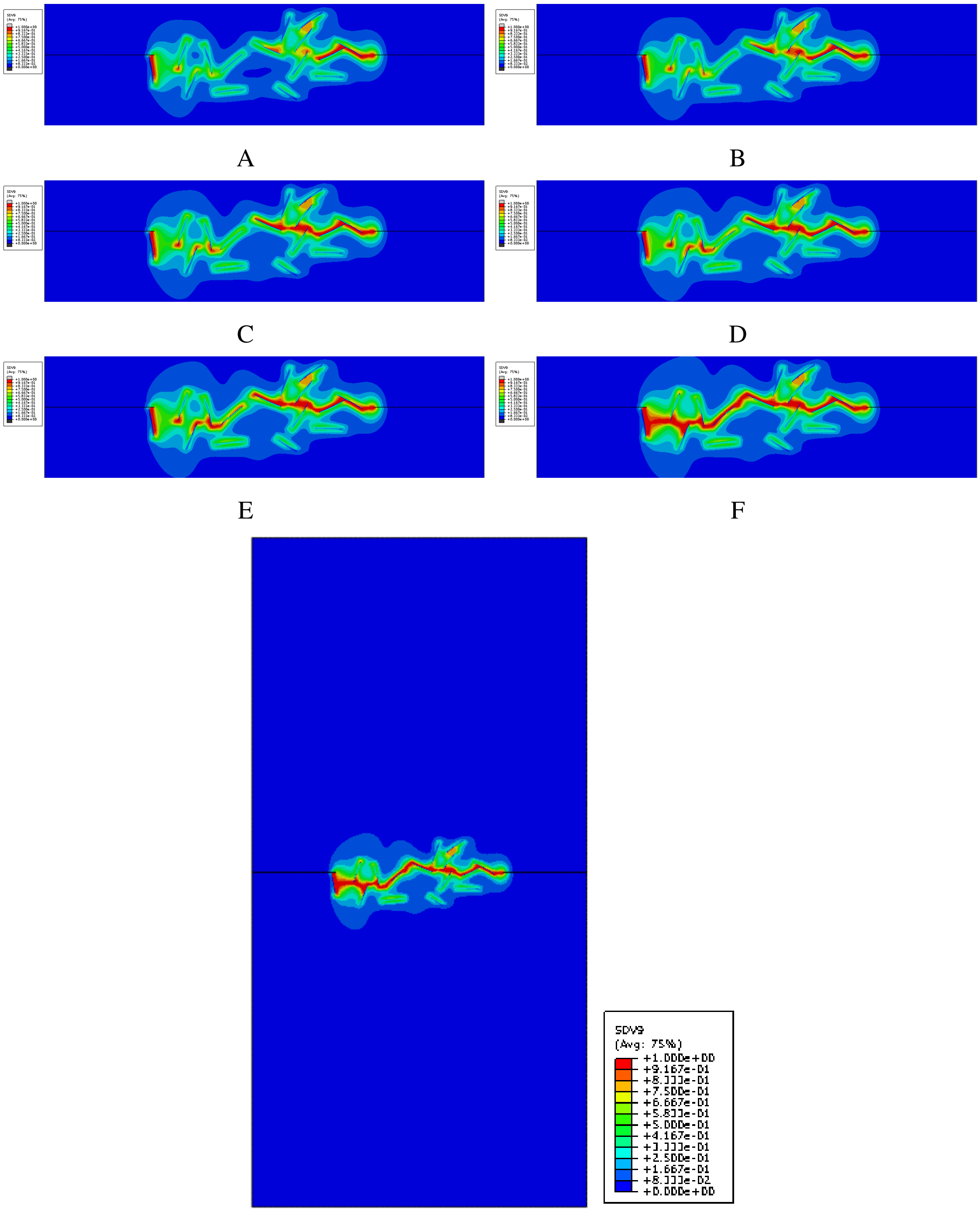

Figure 8.23: Crack propagation steps in the specimen.

It is obvious from the surface dissipation results, after the cracks start, there is a constant rate of energy dissipation before dispersing the total surface energy and splitting the sample. Since the model is linear elastic fracture model, the macroscopic energy dissipation is associated with the micro-cracks propagation in the PNC. So that, the area under the load–displacement curve represents the sum of the elastic energy and the energy dissipation due to fracture process.

The macroscopic fracture energy can be predicted from the microscopic measures using the energy conservation law. The principal of energy conservation implies an equivalence between the total microscopic surface energy and the macroscopic dissipative energy of the specimen. After verifying the equivalence between the macroscopic energy of the sample and the total dissipative surface energy, the constant rate of the microscopic surface energy dissipation is considered to predict the fracture energy of macro-scale specimens of PNCs.

By considering the same geometry of Figure 8.20a but in macro-scale, the predicted macroscopic fracture energy for different lengths can be calculated by dividing the constant dissipation rate by these crack lengths. Note that the macro crack length is the distance between the two notch tips. The results of prediction are presented in Figure 8.24.

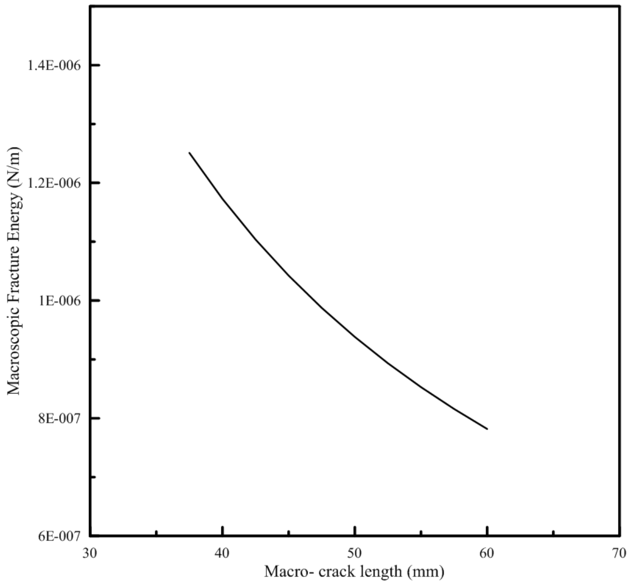

Figure 8.24: Predictions of macroscopic fracture energy.

Conclusion

Intact specimens with different IP thicknesses and properties were used to predict the computational homogenized Young's modulus of PNCs. The IP thickness plays a strong role in Young's modulus and the tensile strength. DENT specimens have been used to evaluate the *J* integral, tensile strength, and surface energy dissipation of PNCs when the IP thickness and properties change. Crack initiation and propagation are the controlling micro deformation and fracture mechanism in PNCs. The crack propagation behavior aligns with the experiment description by Wang *et al.* (1), where the cracks initiate from the IP between clay layers and extend into the epoxy matrix in different directions to connect the nearby cracks when the strain increases. Considering the IP zone is critical to properly investigate the parameters of the composite material during the design process. The analysis findings can be understood as follows:

- The test results pointed that the predicted Young's modulus and the tensile strength remained the same for samples have different clay distribution and same of clay wt.%.
- The IP Young's modulus for different thicknesses has almost no impact on the *J* integral and surface energy dissipation. For example, the maximum percentage difference of the average values of the *J* integral for various values of the IP Young's moduli and thicknesses is 3.06%.
- Depends on the IP zone properties with respect to the matrix, the tensile strength increased with decreasing the IP thickness in the case of weaker IP comparing to the matrix. At the same properties of IP, the percentage increase in tensile strength was 5.13% when the IP thickness changed from 4 *nm* to 1 *nm*. The percentages increase in tensile strength of PNCs by changing the IP zones' Young's modulus from 1.0 *GPa* to 7.45 *GPa* are 3.93%, 7.86%, 11.98%, and 16.29% for IPs thicknesses of 1 *nm*, 2 *nm*, 3 *nm*, and 4 *nm*, respectively.
- The strain energy release rate did not influence the *J* integral when it changed from 1.0 N/m to 25 N/m in IP zone thickness of 1 *nm*. However, it significantly increased the *J* integral in the case where IP = 4 *nm*. The percentages of increase in the *J* integral were 18.91%, 22.09%, and 26.33% in the case where IP = 4 *nm* and Young's modulus was 1.0 *GPa*, 2.75 *GPa*, and 7.45 *GPa*, respectively.
- The strain energy release rate of IP does not affect the PNCs' tensile strength, but it notably changed the surface energy dissipation. Comparatively, the surface en-

ergy dissipation increased drastically in PNCs with an IP zone rather than the fully bonded PNCs. Hence, it is important to account for IP.

- The surface energy dissipation and phase field diffusion in PNCs explained an important behavior regarding the IP thickness; first, the surface energy and crack diffusion matured greatly in the IP zones rather than the matrix, due to the lower value of strain energy release rate of the IP comparing to the matrix. Second, the surface energy dissipation and phase field diffusion were high in PNCs with an IP thickness of 1 *nm* rather than those with an IP of 4 *nm*.

As a result, future experimental or nano-scale studies should aim in particular to determine the IP thickness. An accurate determination for this zone may change the assumption of the constant thickness of the IP, as assumed in PNCs modeling of this work.

Chapter 9

Conclusions

9.1 Summary of Achievements

This work is dedicated to developing the commercial software Abaqus to adopt phase field model for brittle fracture simulation in 2D and 3D. Many problems with complicated crack patterns is reached using the model. Phase field model as an efficient fracture model could capture complex crack patterns elegantly. In the same context of quasi-brittle fracture, the thesis proposed a new damage algorithm worked as an effective approach to detect the cracks propagation in 2D geometries independent of the constitutive law and element technology. It consists of a localization limiter in the form of the screened Poisson equation and local mesh refinement.

Consequently, phase field model for fracture is used to study the fracture behavior of the polymer nanocomposites material. The polymer nanocomposites as a filler–enhanced polymer nanocomposite technology, are one of the dominant influences in motivating and sponsoring nanotechnology improvement. Currently, nanotechnology has expanded into many aspects of science and technology. The invention of filler–enhanced materials has led to significantly enhanced properties and uses which cannot be gained using classical macro and micro technology with normal filler loading levels. Furthermore, studying the fracture behavior of the polymer nanocomposites material is performed in addition to: first, the prediction of elastic and fracture parameters of PNCs; second, prediction of surface energy dissipation and crack surface area for different PNCs properties and geometry. From the work that has been done, the conclusions are summarized as follows:

Continuum modeling of fracture

- The phase field model for fracture, is defined as the generalized concept of configurational forces that connects the crack evolution in the phase field model and the energetic crack propagation law of Griffith's theory.
- The interpretation of the crack field as an auxiliary indicator for cracks, is relevant. Hence, irreversibility constraints in terms of boundary conditions have been determined to produce the correct amount of surface energy upon unloading.
- The proposed technique overcomes the irreversibility constraints at the element level. This is an advantage because the modification of the global boundary conditions during the simulation is not required. This would be complicated from a technical point of view, because it requires interrupting the finite element framework on the global level.
- The implicit time integration scheme has been used for the integration of the evolution equation. Because of the fast change in the crack field, the fracture processes need to be determined using very small time steps. Therefore, an automatic step size control has been applied for the simulations. This combination of implicit time integration and automatic step size control has produced a very robust simulation strategy. In addition, Abaqus provides a wide and efficient solver tool because it is designed to solve complex multi-physics problem. So, with Abaqus the fully coupled solver scheme is used.
- The implementation of quasi-brittle fracture model in the commercial software in 2D and 3D, were comprehensive and flexible for fracture simulations. This means that applying of the model to many examples does not require much expertise on the subject. Simulations also showed that the 3D modeling is manageable without utilizing the parallel computing techniques although they were computationally expensive.
- Staggered algorithm with the screened Poisson equation and mesh refinement can be combined to model quasi-brittle and ductile crack *nucleation* and *propagation*. An excellent crack path and load-displacement curves were obtained systematically in this regard.
- Phase field model with controlled element deactivation can be used. If elements are sufficiently small, either from a fine mesh or a mesh refinement algorithm, this produces realistic results. From the energy balance perspective (specifically localized

strain energy density loss), displacement discontinuities can be replaced by inactive elements or explicit boundaries. In alternative, localization limiters with strain softening constitutive laws produce a similar effect.

- Our model show that a gradient-enhanced formulation with a staggered scheme is able to achieve: very good mesh-size independence, excellent length-scale independence for values compatible with the mesh, moderate step-size independence, reproduction of curved crack paths, and application to both quasi-brittle and ductile problems.

Fracture in polymer nanocomposites

- The generation of PNCs samples themselves is not straightforward and the computational memory controls the size and clay platelet percentage of the PNCs. Additionally, the strategy used to generate the samples according the volume fraction or weight needs to be validated if it reflects material with an isotropic properties.
- Even though the crack path is not known in advance in the PNCs due to the random distribution and inclination of the clay platelets in the matrix, the analysis showed that the change in the crack path depends on the clay platelet distribution with the same boundary conditions and under the same load.
- In fully bonded PNCs, the analysis proved that the cracks had initiated in three locations of the sample: at the edges of PNCs samples when there are no clay platelets nearby; at the clay platelet edges, in particular when it is near another clay platelet. Following their initiation, the cracks continue propagating in the matrix under the load increments towards other cracks until the sample is completely split.
- The analytical Halpin–Tsai and the effective interface models are used as a reference to compare the predicted Young's modulus of the computational approach between fully bonded and poorly bonded PNCs. As a result, computational homogenization is still the best and most accurate method for extracting macroscopic material parameters. This is due to the limitations of the analytical models and the linear relation between the model parameters, which has no physical meaning because of the force interactions under loading steps.
- In solid mechanics, the interphase/interface energy is usually negligible in comparison to the bulk energy. However, in PNCs, one cannot neglect to take the IP zone

energy into consideration due to the high ratio of IP to volume.

- The computational techniques can examine the IP zone effects on PNCs and predicted the Young's modulus, tensile strength, fracture toughness, surface energy dissipation, and crack surface area in PNCs.
- In PNCs with interphase zones, the IP thickness acted as a substantial part in material properties and fracture parameters. Plus, the surface energy dissipation and cracks' surface area of the composite were drastically altered when the IP thickness changed.
- The crack propagation behavior aligns with the experimental description of fracture tests of PNCs; the cracks initiate from the IP between clay layers and extend into the epoxy matrix in different directions to connect nearby cracks when the strain increases.
- Observed phenomenon in the simulations: The rise of the IP thickness reduces the development of cracks in the matrix. This behavior can be clearly recognized in surface energy and cracks surface area calculations.
- The macroscopic fracture energy of PNCs is predicted from the microscopic measures using the energy conservation law. After verifying the equivalence between the macroscopic energy of the sample and the total dissipative surface energy, this approach is a good tool to predict the macroscopic fracture energy of any heterogeneous material from its fine scale features.

9.2 Scope for future work

In the work presented, different fracture models are introduced, implemented in 2D and 3D, and used to study the material and fracture properties of PNCs. Some suggested extensions to the current work could be:

- Phase field method could be implemented in a straightforward manner by coupled multi–field finite element solvers. PNCs is widely applied for thermal purposes. So, this approach could make a useful contribution in this manner.
- Since there is a size effect on fracture properties, larger sizes are required to obtain convergence in fracture toughness values. The computational cost does not allow

the simulation of such large–sized experiments. A multiscale approach could be used to increase the size of the specimen. Additionally, a homogenization approach to the PNCs could be adopted in this regard; in this case, modeling PNCs in 3D could be reached with a lower computational cost.

- Since the IP zone had a significant effect on the cracks dissipation in the composite and surface energy dissipation, future experimental or nano-scale studies should aim in particular to determine the IP thickness. An accurate determination for this zone may change the assumption of the constant thickness of the IP, as assumed in PNCs modeling of this work.

References

[1] Ke Wang, Ling Chen, Jingshen Wu, Mei Ling Toh, Chaobin He, and Albert F Yee. Epoxy nanocomposites with highly exfoliated clay: mechanical properties and fracture mechanisms. *Macromolecules*, 38(3):788–800, 2005. ix, 2, 3, 97, 104, 129, 147

[2] C Miehe, F Welschinger, and M Hofacker. Thermodynamically consistent phase-field models of fracture: Variational principles and multi-field FE implementations. *International Journal for Numerical Methods in Engineering*, 83(10):1273–1311, 2010. x, 10, 19, 20, 21, 25, 32, 33, 39, 51, 79, 91, 130

[3] TN Bittencourt, PA Wawrzynek, AR Ingraffea, and JL Sousa. Quasi-automatic simulation of crack propagation for 2D LEFM problems. *Engineering Fracture Mechanics*, 55(2):321–334, 1996. x, 38, 39

[4] Marreddy Ambati, Tymofiy Gerasimov, and Laura De Lorenzis. A review on phase-field models of brittle fracture and a new fast hybrid formulation. *Computational Mechanics*, 55(2):383–405, 2015. xi, xii, 11, 79, 80, 83, 90, 91, 93

[5] HEJG Schlangen. *Experimental and numerical analysis of fracture processes in concrete*. TU Delft, Delft University of Technology, 1993. xii, 87, 90

[6] Zita Dominkovics. *Polymer/layered silicate nanocomposites: structure formation, interactions and deformation mechanisms*. PhD thesis, Budapest University of Technology and Economics, 2011. 3, 14, 129

[7] Dassault Systémes. Abaqus, `http://www.3ds.com`. 4, 30

[8] Christian Miehe, Lisa-Marie Schänzel, and Heike Ulmer. Phase field modeling of fracture in multi-physics problems. part i. balance of crack surface and failure

criteria for brittle crack propagation in thermo-elastic solids. *Computer Methods in Applied Mechanics and Engineering*, 2014. 4

[9] Christian Miehe, M Hofacker, L-M Schänzel, and F Aldakheel. Phase field modeling of fracture in multi-physics problems. part ii. coupled brittle-to-ductile failure criteria and crack propagation in thermo-elastic–plastic solids. *Computer Methods in Applied Mechanics and Engineering*, 2014.

[10] Alexander Schlüter, Charlotte Kuhn, Ralf Müller, Marilena Tomut, Christina Trautmann, Helmut Weick, and Carolin Plate. Phase field modelling of dynamic thermal fracture in the context of irradiation damage. *Continuum Mechanics and Thermodynamics*, pages 1–12, 2015. 4

[11] Christian Miehe, Steffen Mauthe, and Stephan Teichtmeister. Minimization principles for the coupled problem of darcy-biot-type fluid transport in porous media linked to phase field modeling of fracture. *Journal of the Mechanics and Physics of Solids*, 2015. 4

[12] Arun Raina and Christian Miehe. A phase-field model for fracture in biological tissues. *Biomechanics and modeling in mechanobiology*, pages 1–18, 2015. 4

[13] QH Zeng, AB Yu, and GQ Lu. Multiscale modeling and simulation of polymer nanocomposites. *Progress in Polymer Science*, 33(2):191–269, 2008. 4, 16, 103

[14] Olgierd Cecil Zienkiewicz, Robert Leroy Taylor, and J Z Zhu. *The Finite Element Method: Its Basis and Fundamentals*, volume 7. Elsevier Ltd, 2013. 6

[15] AA Griffith. The Phenomena of Rupture and Flow in Solids. *Philosophical Transactions of the Royal Society of London A*, 221:163–198, 1921. 7, 17

[16] D Ngo and AC Scordelis. Finite element analysis of reinforced concrete beams. *Journal of the American Concrete Institute*, 64:152–163, 1967. 7

[17] AR Ingraffea and V Saouma. *Fracture mechanics of concrete*, chapter Numerical modeling of discrete crack propagation in reinforced and plain concrete, pages 171–225. Martinus Nijhoff Publishers, Dordrecht, 1985. 7

[18] JR Rice. Elastic Fracture Mechanics Concepts for Interfacial Cracks. *Journal of Applied Mechanics*, 55:98–103, 1988. 7

[19] X-P Xu and A Needleman. Numerical simulations of dynamic crack growth along an interface. *International Journal of Fracture*, 74:289–324, 1996. 7

[20] F Zhou and JF Molinari. Dynamic crack propagation with cohesive elements: a methodology to address mesh dependency. *International Journal for Numerical Methods in Engineering*, 59:1–24, 2004. 7

[21] Nicolas Moës, John Dolbow, and Ted Belytschko. A finite element method for crack growth without remeshing. *International Journal for Numerical Methods in Engineering*, 46:131–150, 1999. 7

[22] N Moës, A Gravouil, and T Belytschko. Non-planar 3D crack growth by the extended finite element and level sets—Part I: Mechanical model. *International Journal for Numerical Methods in Engineering*, 53:2549–2568, 2002. 7

[23] Pedro Areias and Ted Belytschko. Analysis of three-dimensional crack initiation and propagation using the extended finite element method. *International Journal for Numerical Methods in Engineering*, 63(5):760–788, 2005. 8

[24] L Chen, T Rabczuk, S Bordas, GR Liu, KY Zeng, and P Kerfriden. Extended finite element method with edge-based strain smoothing (ESm-XFEM) for linear elastic crack growth. *Computer Methods in Applied Mechanics and Engineering*, 209–212:250–265, 2012. 8

[25] Timon Rabczuk, Stéphane Bordas, and Goangseup Zi. On three-dimensional modelling of crack growth using partition of unity methods. *Computers and Structures*, 88:1391–1411, 2010. 8

[26] JJC Remmers, R de Borst, and A Needleman. A cohesive segments method for the simulation of crack growth. *Computational Mechanics*, 31:69–77, 2003. 8

[27] T Rabczuk and T Belytschko. Cracking particles, a simplified meshfree method for arbitrarily evolving cracks. *International Journal for Numerical Methods in Engineering*, 61:2316–2343, 2004. 8

[28] Timon Rabczuk, Goangseup Zi, Stephane Bordas, and Hung Nguyen-Xuan. A simple and robust three-dimensional cracking-particle method without enrichment. *Computer Methods in Applied Mechanics and Engineering*, 199:2437–2455, 2010. 8

[29] YR Rashid. Ultimate strength analysis of prestressed concrete pressure vessels. *Nuclear Engineering and Design*, 7:334–344, 1968. 8

[30] RJ Cope, PV Rao, LA Clark, and P Norris. Modelling of reinforced concrete behaviour for finite element analysis of bridge slabs. In C Taylor, E Hinton, and DRJ Owen, editors, *Numerical Methods for Non-linear Problems I*, pages 457–470. Pineridge Press, 1980. 9

[31] Luigi Cedolin and Zdeněk P Bažant. Effect of finite element choice in blunt crack analysis. *Computer Methods in Applied Mechanics and Engineering*, 24:305–316, 1980. 9

[32] A Hillerborg, M Modéer, and PE Petersson. Analysis of crack formation and crack growth in concrete by means of fracture mechanics and finite elements. *Cement Concrete Research*, 6:773–782, 1976. 9

[33] Zdeněk P Bažant and B H Oh. Crack band theory for fracture of concrete. *Materials and Structures*, 16:155–177, 1983. 9

[34] Timon Rabczuk. Computational methods for fracture in brittle and quasi-brittle solids: state-of-the-art review and future perspectives. *ISRN Applied Mathematics*, 2013, 2013. 9, 15

[35] GA Francfort and J-J Marigo. Revisiting brittle fracture as an energy minimization problem. *Journal of the Mechanics and Physics of Solids*, 46(8):1319–1342, 1998. 9

[36] Alain Karma, David A Kessler, and Herbert Levine. Phase–field model of mode iii dynamic fracture. *Physical Review Letters*, 87(4):45501, 2001. 10

[37] Vincent Hakim and Alain Karma. Crack path prediction in anisotropic brittle materials. *Physical review letters*, 95(23):235501, 2005.

[38] Vincent Hakim and Alain Karma. Laws of crack motion and phase-field models of fracture. *Journal of the Mechanics and Physics of Solids*, 57:342–368, 2009.

[39] Robert Spatschek, Efim Brener, and Alain Karma. Phase field modeling of crack propagation. *Philosophical Magazine*, 91(1):75–95, 2011. 10

[40] Charlotte Kuhn and Ralf Müller. A continuum phase field model for fracture. *Engineering Fracture Mechanics*, 77:3625–3634, 2010. 10

[41] Charlotte Kuhn and Ralf Müller. A new finite element technique for a phase field model of brittle fracture. *Journal Of Theoritical and Applied Mechanics*, 49(4):1115–1133, 2011. 10

[42] B Bourdin, GA Francfort, and J-J Marigo. Numerical experiments in revisited brittle fracture. *Journal of the Mechanics and Physics of Solids*, 48:797–826, 2000. 10

[43] Blaise Bourdin, Gilles A Francfort, and Jean-Jacques Marigo. The variational approach to fracture. *Journal of Elasticity*, 91:5–148, 2008. 10

[44] Giovanni Lancioni and Gianni Royer-Carfagni. The Variational Approach to Fracture Mechanics. A Practical Application to the French Panthéon in Paris. *Journal of Elasticity*, 95:1–30, 2009. 10

[45] Hanen Amor, Jean-Jacques Marigo, and Corrado Maurini. Regularized formulation of the variational brittle fracture with unilateral contact: Numerical experiments. *Journal of the Mechanics and Physics of Solids*, 57:1209–1229, 2009. 10

[46] Christian Miehe, Martina Hofacker, and Fabian Welschinger. A phase field model for rate-independent crack propagation: Robust algorithmic implementation based on operator splits. *Computer Methods in Applied Mechanics and Engineering*, 199:2765–2778, 2010. 10, 32, 79, 91

[47] Michael Johns Borden. *Isogeometric Analysis of Phase-Field Models for Dynamic Brittle and Ductile Fracture*. PhD thesis, University of Texas at Austin, August 2012. 10, 32

[48] Michael J Borden, Thomas JR Hughes, Chad M Landis, and Clemens V Verhoosel. A higher-order phase-field model for brittle fracture: Formulation and analysis within the isogeometric analysis framework. *Computer Methods in Applied Mechanics and Engineering*, 273:100–118, 2014. 10

[49] Dominik Schillinger, Michael J Borden, and Henryk K Stolarski. Isogeometric collocation for phase-field fracture models. *Computer Methods in Applied Mechanics and Engineering*, 284:583–610, 2015. 11

[50] F Amiri, D Millán, Y Shen, T Rabczuk, and M Arroyo. Phase-field modeling of fracture in linear thin shells. *Theoretical and Applied Fracture Mechanics*, 69:102–109., 2014. 11

[51] Clemens V Verhoosel and René Borst. A phase-field model for cohesive fracture. *International Journal for Numerical Methods in Engineering*, 96(1):43–62, 2013. 11

[52] Julien Vignollet, Stefan May, René de Borst, and Clemens V Verhoosel. Phase-field models for brittle and cohesive fracture. *Meccanica*, 49(11):2587–2601, 2014. 11

[53] Fernando P Duda, Angel Ciarbonetti, Pablo J Sánchez, and Alfredo E Huespe. A phase–field/gradient damage model for brittle fracture in elastic–plastic solids. *International Journal of Plasticity*, 65:269–296, 2015. 11

[54] QH Zeng, AB Yu, GQ Lu, and DR Paul. Clay-based polymer nanocomposites: research and commercial development. *Journal of nanoscience and nanotechnology*, 5(10):1574–1592, 2005. 11

[55] Michael Alexandre and Philippe Dubois. Polymer-layered silicate nanocomposites: preparation, properties and uses of a new class of materials. *Materials Science and Engineering: R: Reports*, 28(1):1–63, 2000.

[56] Pethrick R. Polymer clay nanocomposites. In TJ Pinnavaia and GW Beall, editors, *Polymer International*, page 464. John Wiley and Sons Inc., 2002.

[57] S Pavlidou and CD Papaspyrides. A review on polymer–layered silicate nanocomposites. *Progress in polymer science*, 33(12):1119–1198, 2008.

[58] YC Ke and Pieter Stroeve. Polymer-layered silicate and silica nanocomposites. In , page 398. Elsevier Inc., 2005.

[59] Hong-Yuan Liu, Gong-Tao Wang, Yiu-Wing Mai, and Ying Zeng. On fracture toughness of nano-particle modified epoxy. *Composites Part B: Engineering*, 42(8):2170–2175, 2011. 11

[60] Richard A Vaia, Gary Price, Patrick N Ruth, Hieu T Nguyen, and Joseph Lichtenhan. Polymer/layered silicate nanocomposites as high performance ablative materials. *Applied Clay Science*, 15(1):67–92, 1999. 11

[61] Emmanuel P Giannelis. Polymer-layered silicate nanocomposites: synthesis, properties and applications. *Applied Organometallic Chemistry*, 12:675–680, 1998. 11

[62] Rishikesh K Bharadwaj. Modeling the barrier properties of polymer-layered silicate nanocomposites. *Macromolecules*, 34(26):9189–9192, 2001. 11

[63] Serge Bourbigot, Michel Le Bras, Francois Dabrowski, Jeffrey W Gilman, and Takashi Kashiwagi. Pa-6 clay nanocomposite hybrid as char forming agent in intumescent formulations. *Fire and Materials*, 24(4):201–208, 2000. 11

[64] Mai Yiu Wing, Yu Zhongzhen, XiE Xaolin, Zhang Qingxin, and MA Jun. Polymer nanocomposites and their applications. *HKIE Transactions*, 10(4):67–73, 2003. 11

[65] Bohayra Mortazavi, Fatima Hassouna, Abdelghani Laachachi, Ali Rajabpour, Said Ahzi, David Chapron, Valérie Toniazzo, and David Ruch. Experimental and multiscale modeling of thermal conductivity and elastic properties of pla/expanded graphite polymer nanocomposites. *Thermochimica Acta*, 552:106–113, 2013. 12, 14

[66] Bohayra Mortazavi, Olivier Benzerara, Hendrik Meyer, Julien Bardon, and Said Ahzi. Combined molecular dynamics-finite element multiscale modeling of thermal conduction in graphene epoxy nanocomposites. *Carbon*, 60:356–365, 2013. 14

[67] Bohayra Mortazavi, Majid Baniassadi, Julien Bardon, and Said Ahzi. Modeling of two-phase random composite materials by finite element, mori-tanaka and strong contrast methods. *Composites Part B: Engineering*, 45(1):1117–1125, 2013. 12

[68] Fengge Gao. *Advances in polymer nanocomposites: types and applications*. Elsevier, 2012. 12

[69] Joseph H Koo. *Polymer nanocomposites*. McGraw-Hill Professional Pub., 2006. 12

[70] Michael Alexandre and Philippe Dubois. Polymer-layered silicate nanocomposites: preparation, properties and uses of a new class of materials. *Materials Science and Engineering*, 28:1–63, 2000. 12

[71] K Hbaieb, QX Wang, YHJ Chia, and B Cotterell. Modelling stiffness of polymer/clay nanocomposites. *Polymer*, 48(3):901–909, 2007. 12

[72] MT Albdiry, BF Yousif, H Ku, and KT Lau. A critical review on the manufacturing processes in relation to the properties of nanoclay/polymer composites. *Journal of Composite Materials*, 47(9):1093–1115, 2013. 12, 96, 104, 129

[73] Asif Abdul Azeez, Kyong Yop Rhee, Soo Jin Park, and David Hui. Epoxy clay nanocomposites–processing, properties and applications: a review. *Composites Part B: Engineering*, 45(1):308–320, 2013. 12

[74] Carsten Zilg, Rolf Mülhaupt, and Jürgen Finter. Morphology and toughness/stiffness balance of nanocomposites based upon anhydride-cured epoxy resins and layered silicates. *Macromolecular Chemistry and Physics*, 200(3):661–670, 1999. 13

[75] Adam S Zerda and Alan J Lesser. Intercalated clay nanocomposites: morphology, mechanics, and fracture behavior. *Journal of Polymer Science Part B: Polymer Physics*, 39(11):1137–1146, 2001.

[76] Man-Wai Ho, Chun-Ki Lam, Kin-tak Lau, Dickon HL Ng, and David Hui. Mechanical properties of epoxy-based composites using nanoclays. *Composite structures*, 75(1):415–421, 2006. 13

[77] RD Peng, HW Zhou, HW Wang, and Leon Mishnaevsky. Modeling of nano-reinforced polymer composites: Microstructure effect on Young's modulus. *Computational Materials Science*, 60:19–31, 2012. 13, 128, 129

[78] S Kunz-Douglass, Peter WR Beaumont, and MF Ashby. A model for the toughness of epoxy-rubber particulate composites. *Journal of Materials Science*, 15(5):1109–1123, 1980. 13

[79] Anthony Glyn Evans, ZB Ahmad, DG Gilbert, and PWR Beaumont. Mechanisms of toughening in rubber toughened polymers. *Acta metallurgica*, 34(1):79–87, 1986.

[80] Y Huang and AJ Kinloch. Modelling of the toughening mechanisms in rubber-modified epoxy polymers. *Journal of materials science*, 27(10):2753–2762, 1992. 13

[81] Marco Salviato, Michele Zappalorto, and Marino Quaresimin. Plastic shear bands and fracture toughness improvements of nanoparticle filled polymers: a multiscale analytical model. *Composites Part A: Applied Science and Manufacturing*, 48:144–152, 2013. 13

[82] Bernd Lauke. On the effect of particle size on fracture toughness of polymer composites. *Composites Science and Technology*, 68(15):3365–3372, 2008. 13

[83] JG Williams. Particle toughening of polymers by plastic void growth. *Composites Science and Technology*, 70(6):885–891, 2010.

[84] TH Hsieh, AJ Kinloch, K Masania, AC Taylor, and S Sprenger. The mechanisms and mechanics of the toughening of epoxy polymers modified with silica nanoparticles. *Polymer*, 51(26):6284–6294, 2010. 106

[85] TH Hsieh, AJ Kinloch, K Masania, J Sohn Lee, AC Taylor, and S Sprenger. The toughness of epoxy polymers and fibre composites modified with rubber microparticles and silica nanoparticles. *Journal of materials science*, 45(5):1193–1210, 2010.

[86] Marino Quaresimin, Marco Salviato, and Michele Zappalorto. Strategies for the assessment of nanocomposite mechanical properties. *Composites Part B: Engineering*, 43(5):2290–2297, 2012.

[87] M Quaresimin, M Salviato, and M Zappalorto. A multi-scale and multi-mechanism approach for the fracture toughness assessment of polymer nanocomposites. *Composites Science and Technology*, 91:16–21, 2014.

[88] Mohammad Silani, Hossein Talebi, Saeed Ziaei-Rad, Pierre Kerfriden, Stéphane PA Bordas, and Timon Rabczuk. Stochastic modelling of clay/epoxy nanocomposites. *Composite Structures*, 118:241–249, 2014. 13, 98, 104

[89] M Silani, S Ziaei-Rad, M Esfahanian, and VBC Tan. On the experimental and numerical investigation of clay/epoxy nanocomposites. *Composite Structures*, 94(11):3142–3148, 2012.

[90] Khader M Hamdia, Tom Lahmer, Trung Nguyen-Thoi, and Timon Rabczuk. Predicting the fracture toughness of PNCs: A stochastic approach based on ANN and ANFIS. *Computational Materials Science*, 102:304–313, 2015.

[91] Roham Rafiee, Timon Rabczuk, Reza Pourazizi, Junhua Zhao, and Yancheng Zhang. Challenges of the modeling methods for investigating the interaction between the CNT and the surrounding polymer. *Advances in Materials Science and Engineering*, 2013, 2013. 13

[92] N. Vu-Bac, R. Rafiee, T. Lahmer, X. Zhuang, and T. Rabczuk. Uncertainty quantification for multiscale modeling of polymer nanocomposites with dependent parameters. *Int. J. Solid Struct.*, 2014. 13, 97

[93] N Vu-Bac, M Silani, T Lahmer, X Zhuang, and T Rabczuk. A unified framework for stochastic predictions of mechanical properties of polymeric nanocomposites. *Computational Materials Science*, 96:520–535, 2015. 13, 97

[94] Arthur W Adamson, Alice Petry Gast, et al. Physical chemistry of surfaces. 1967. 13

[95] Lawrence T Drzal. The interphase in epoxy composites. In *Epoxy resins and composites II*, pages 1–32. Springer, 1986. 14

[96] PJ Herrera-Franco and LT Drzal. Comparison of methods for the measurement of fibre/matrix adhesion in composites. *Composites*, 23(1):2–27, 1992. 14

[97] Andrzej Galeski. Strength and toughness of crystalline polymer systems. *Progress in Polymer Science*, 28(12):1643–1699, 2003. 14

[98] JM Gloaguen and JM Lefebvre. Plastic deformation behaviour of thermoplastic/clay nanocomposites. *Polymer*, 42(13):5841–5847, 2001. 14

[99] Zita Dominkovics, József Hári, János Kovács, Erika Fekete, and Béla Pukánszky. Estimation of interphase thickness and properties in pp/layered silicate nanocomposites. *European Polymer Journal*, 47(9):1765–1774, 2011. 14

[100] Béla Pukánszky. Interfaces and interphases in multicomponent materials: past, present, future. *European Polymer Journal*, 41(4):645–662, 2005. 15

[101] Roham Rafiee, Abdolhossein Fereidoon, and Meghdad Heidarhaei. Influence of non-bonded interphase on crack driving force in carbon nanotube reinforced polymer. *Computational Materials Science*, 56:25–28, 2012. 15

[102] Roham Rafiee and Reza Pourazizi. Influence of cnt functionalization on the interphase region between cnt and polymer. *Computational Materials Science*, 96:573–578, 2015. 15

[103] Xiang Ling Ji, Jiao Kai Jing, Wei Jiang, and Bing Zheng Jiang. Tensile modulus of polymer nanocomposites. *Polymer Engineering & Science*, 42(5):983–993, 2002. 15

[104] B Pukanszky. Influence of interface interaction on the ultimate tensile properties of polymer composites. *Composites*, 21(3):255–262, 1990. 15, 129

[105] Yasser Zare and Hamid Garmabi. Thickness, modulus and strength of interphase in clay/polymer nanocomposites. *Applied Clay Science*, 105:66–70, 2015. 15, 129

[106] Yasser Zare. Determination of polymer–nanoparticles interfacial adhesion and its role in shape memory behavior of shape memory polymer nanocomposites. *International Journal of Adhesion and Adhesives*, 54:67–71, 2014. 15

[107] Bohayra Mortazavi, Julien Bardon, and Said Ahzi. Interphase effect on the elastic and thermal conductivity response of polymer nanocomposite materials: 3d finite element study. *Computational Materials Science*, 69:100–106, 2013. 15

[108] Saeed Saber-Samandari and Akbar Afaghi Khatibi. The effect of interphase on the elastic modulus of polymer based nanocomposites. *Key Engineering Materials*, 312:199–204, 2006. 15

[109] Ray S Fertig and Mark R Garnich. Influence of constituent properties and microstructural parameters on the tensile modulus of a polymer/clay nanocomposite. *Composites science and technology*, 64(16):2577–2588, 2004. 15

[110] Julian YH Chia, Kais Hbaieb, and QX Wang. Finite element modelling epoxy/clay nanocomposites. *Key Engineering Materials*, 334:785–788, 2007. 15

[111] Julian YH Chia. Finite element modelling clay nanocomposites and interface effects on mechanical properties. In *IUTAM Symposium on Modelling Nanomaterials and Nanosystems*, pages 241–248. Springer, 2009. 15

[112] René De Borst, Miguel A Gutiérrez, Garth N Wells, Joris JC Remmers, and Harm Askes. Cohesive-zone models, higher-order continuum theories and reliability methods for computational failure analysis. *International Journal for Numerical Methods in Engineering*, 60(1):289–315, 2004. 15

[113] PR Budarapu, B Javvaji, VK Sutrakar, D Roy Mahapatra, G Zi, and T Rabczuk. Crack propagation in graphene. *Journal of Applied Physics*, 118(6):064307, 2015. 15

[114] Nuo Sheng, Mary C Boyce, David M Parks, GC Rutledge, JI Abes, and RE Cohen. Multiscale micromechanical modeling of polymer/clay nanocomposites and the effective clay particle. *Polymer*, 45(2):487–506, 2004. 15

[115] Yu Chen, YH Chia, TE Tay, and VBC Tan. *Multiscale modeling of polymer-clay nanocomposites*. LAP LAMBERT Academic Publishing, 2013. 15

[116] Shaoning Song, Yu Chen, Zhoucheng Su, Chenggen Quan, and Vincent BC Tan. Multiscale modeling of damage progression in nylon 6/clay nanocomposites. *Composites Science and Technology*, 100:189–197, 2014. 15

[117] P Areias, T Rabczuk, and PP Camanho. Initially rigid cohesive laws and fracture based on edge rotations. *Computational Mechanics*, 52(4):931–947, 2013. 15

[118] Yi-Lin Gui, Ha H Bui, Jayantha Kodikara, Qian-Bing Zhang, Jian Zhao, and Timon Rabczuk. Modelling the dynamic failure of brittle rocks using a hybrid continuum-discrete element method with a mixed-mode cohesive fracture model. *International Journal of Impact Engineering*, 2015. 15

[119] Simão Pedro Pereira, Giulio Scocchi, Radovan Toth, Paola Posocco, Daniel R Nieto, Sabrina Pricl, and Maurizio Fermeglia. Multiscale modeling of polymer/clay nanocomposites. *Journal of Multiscale Modelling*, 3(03):151–176, 2011. 16

[120] Timon Rabczuk, Roham Rafiee, and Xiaoying Zhuang. Preface to the special issue computational modeling of polymeric composites. *Computational Materials Science*, (96):381, 2015. 16

[121] Robert J Dorgan. *A Nonlocal Model For Coupled Damage-Plasticity Incorporating Gradients Of Internal State Variables At Multiscales*. PhD thesis, Department of Civil and Enviromental Engineering, Graduate Faculty of the Louisiana State University and Agricultural and Mechanical College, May 2006. 31

[122] C Hesch and K Weinberg. Thermodynamically consistent algorithms for a finite-deformation phase-field approach to fracture. *International Journal for Numerical Methods in Engineering*, 99(12):906–924, 2014. 32, 33

[123] Anthony R Ingraffea and Mircea Grigoriu. Probabilistic fracture mechanics: A validation of predictive capability. Technical Report 90–8, Structural Engineering, School of Civil and Environmental Engineering, Cornell University Ithaca, New York, 1990. 38

[124] Pedro, Areias. Simplas, `http://www.simplas-software.com`. 52, 75

[125] Jean Lemaitre. *A course on damage mechanics*. Springer Science & Business Media, 2012. 52

[126] Alexander L Fetter and John Dirk Walecka. *Theoretical mechanics of particles and continua*. Courier Corporation, 2003. 52, 68

[127] RW Ogden and Non-linear Elastic Deformations. Dover. *New York*, 1997. 53

[128] Juan C Simo and Thomas JR Hughes. *Computational inelasticity*, volume 7. Springer Science & Business Media, 2006. 55

[129] Pedro Areias, D Dias-da Costa, EB Pires, and J Infante Barbosa. A new semi-implicit formulation for multiple-surface flow rules in multiplicative plasticity. *Computational Mechanics*, 49(5):545–564, 2012. 58

[130] Chunhui Chen and Olvi L Mangasarian. A class of smoothing functions for nonlinear and mixed complementarity problems. *Computational Optimization and Applications*, 5(2):97–138, 1996. 58

[131] FJP Reis, Paulo MST de Castro, Gustavo V Guinea, L Malcher, FM Andrade Pires, and JMA César de Sá. A comparison of shear mechanisms for the prediction of ductile failure under low stress triaxiality. *International Journal of Structural Integrity*, 1(4):314–331, 2010. 60

[132] CC Chu and A Needleman. Void nucleation effects in biaxially stretched sheets. *Journal of Engineering Materials and Technology*, 102(3):249–256, 1980. 61

[133] Arthur L Gurson. Continuum theory of ductile rupture by void nucleation and growth: Part i–yield criteria and flow rules for porous ductile media. *Journal of engineering materials and technology*, 99(1):2–15, 1977. 61

[134] Liang Xue. Constitutive modeling of void shearing effect in ductile fracture of porous materials. *Engineering Fracture Mechanics*, 75(11):3343–3366, 2008. 61

[135] K Nahshon and JW Hutchinson. Modification of the gurson model for shear failure. *European Journal of Mechanics-A/Solids*, 27(1):1–17, 2008.

[136] Ken Nahshon and Zhenyu Xue. A modified gurson model and its application to punch-out experiments. *Engineering fracture mechanics*, 76(8):997–1009, 2009. 61

[137] Viggo Tvergaard and Alan Needleman. Analysis of the cup-cone fracture in a round tensile bar. *Acta metallurgica*, 32(1):157–169, 1984. 63

[138] Thomas JR Hughes. *The finite element method: linear static and dynamic finite element analysis*. Courier Corporation, 2012. 65

[139] PMA Areias, JMA César de Sá, CA Conceição António, and AA Fernandes. Analysis of 3d problems using a new enhanced strain hexahedral element. *International Journal for Numerical Methods in Engineering*, 58(11):1637–1682, 2003. 65

[140] Douglas N Arnold, Franco Brezzi, and Michel Fortin. A stable finite element for the stokes equations. *Calcolo*, 21(4):337–344, 1984. 65, 75

[141] Klaus-Jürgen Bathe. *Finite element procedures*. Klaus-Jurgen Bathe, 2006. 65

[142] Pedro Areias, Nicolas Van Goethem, and EB Pires. A damage model for ductile crack initiation and propagation. *Computational Mechanics*, 47(6):641–656, 2011. 65

[143] Wolfram Research Inc. Mathematica. 66, 69

[144] Joze Korelc. Multi-language and multi-environment generation of nonlinear finite element codes. *Engineering with computers*, 18(4):312–327, 2002. 66, 69

[145] RHJ PEERLINGS R DE and JHP DE VREE. Gradient enhanced damage for quasi-brittle materials. *International Journal for numerical methods in engineering*, 39:3391–3403, 1996. 68

[146] PMA Areias, JMA César de Sá, and CA Conceição António. A gradient model for finite strain elastoplasticity coupled with damage. *Finite Elements in Analysis and Design*, 39(13):1191–1235, 2003. 68, 75

[147] René de Borst, Jerzy Pamin, and Marc GD Geers. On coupled gradient-dependent plasticity and damage theories with a view to localization analysis. *European Journal of Mechanics-A/Solids*, 18(6):939–962, 1999. 68

[148] David Lasry and Ted Belytschko. Localization limiters in transient problems. *International Journal of Solids and Structures*, 24(6):581–597, 1988. 68

[149] Pedro Areias and T Rabczuk. Finite strain fracture of plates and shells with configurational forces and edge rotations. *International Journal for Numerical Methods in Engineering*, 94(12):1099–1122, 2013. 70

[150] PJ Frey and PL George. *Mesh generation. Application to finite elements. Hermes Science Publ., Paris*. Oxford, 2000. 72

[151] J Alfaiate, A Simone, and LJ Sluys. A new approach to strong embedded discontinuities. In *Computational modelling of concrete structures, EURO-C*, 2003. 87

[152] PMA Areias, JMA Cesar de Sa, CA Conceicao Antonio, JASAO Carneiro, and V MP Teixeira. Strong displacement discontinuities and lagrange multipliers in the analysis of finite displacement fracture problems. *Computational Mechanics*, 35(1):54–71, 2004. 87

[153] Vasyl Michael Harik and Manuel D Salas. *Trends in Nanoscale Mechanics*. Springer, 2003. 95

[154] Suprakas Sinha Ray and Masami Okamoto. Polymer/layered silicate nanocomposites: a review from preparation to processing. *Progress in polymer science*, 28(11):1539–1641, 2003. 96, 97

[155] YC Ke and Pieter Stroeve. *Polymer–layered silicate and silica nanocomposites*. Elsevier, 2005. 96

[156] Vikas Mittal. *Characterization Techniques for Polymer Nanocomposites*. John Wiley & Sons, 2012. 97

[157] PM Visakh, Sabu Thomas, Kristiina Oksman, and Aji P Mathew. Crosslinked natural rubber nanocomposites reinforced with cellulose whiskers isolated from bamboo waste: Processing and mechanical/thermal properties. *Composites Part A: Applied Science and Manufacturing*, 43(4):735–741, 2012. 97

[158] Mohammad Silani, Hossein Talebi, Saeed Ziaei-Rad, Pierre Kerfriden, Stéphane PA Bordas, and Timon Rabczuk. Stochastic modelling of clay/epoxy nanocomposites. *Composite Structures*, 118:241–249, 2014. 97, 129

[159] Mohammad Silani, Saeed Ziaei-Rad, Hossein Talebi, and Timon Rabczuk. A semi-concurrent multiscale approach for modeling damage in nanocomposites. *Theoretical and Applied Fracture Mechanics*, 74:30–38, 2014. 97

[160] Biqiong Chen and Julian RG Evans. Elastic moduli of clay platelets. *Scripta materialia*, 54(9):1581–1585, 2006. 104, 129

[161] Ted L Anderson. *Fracture mechanics: fundamentals and applications*. CRC press, 2005. 104, 105, 137

[162] James R Rice. A path independent integral and the approximate analysis of strain concentration by notches and cracks. *Journal of applied mechanics*, 35(2):379–386, 1968. 104

[163] Vinh Phu Nguyen, Oriol Lloberas-Valls, Martijn Stroeven, and Lambertus Johannes Sluys. Homogenization-based multiscale crack modelling: from micro-diffusive damage to macro-cracks. *Computer Methods in Applied Mechanics and Engineering*, 200(9):1220–1236, 2011. 106

[164] C-LI Victor. *Multiscale Deformation and Fracture in Materials and Structures*, chapter J-Integral Applications to Characterization and Tailoring of Cementitious Materials, pages 385–406. Springer Netherlands, 2002. 114

[165] GM Odegard, TC Clancy, and TS Gates. Modeling of the mechanical properties of nanoparticle/polymer composites. *Polymer*, 46(2):553–562, 2005. 128

[166] L Adam, K Delaere, M Kaszacs, J-S Grard, R Assaker, and I Doghri. Multi-scale modeling of polymer nanocomposites. *Nanotech Conference and Expo*, 2:515–518, 2009. 128

[167] Rui Qiao and L Catherine Brinson. Simulation of interphase percolation and gradients in polymer nanocomposites. *Composites Science and Technology*, 69(3):491–499, 2009. 128

[168] A Mesbah, Fahmi Zaïri, S Boutaleb, Jean-Michel Gloaguen, Moussa Naït-Abdelaziz, S Xie, T Boukharouba, and Jean-Marc Lefebvre. Experimental characterization and modeling stiffness of polymer/clay nanocomposites within a hierarchical multiscale framework. *Journal of applied polymer science*, 114(5):3274–3291, 2009.

[169] Hua Liu and L Catherine Brinson. Reinforcing efficiency of nanoparticles: a simple comparison for polymer nanocomposites. *Composites Science and Technology*, 68(6):1502–1512, 2008. 128

[170] Kevin Kendall. Fracture of particulate filled polymers. *British Polymer Journal*, 10(1):35–38, 1978. 129

[171] G Akay. Flow induced polymer-filler interactions: Bound polymer properties and bound polymer-free polymer phase separation and subsequent phase inversion during mixing. *Polymer Engineering & Science*, 30(21):1361–1372, 1990. 129

[172] Dietmar Gross and Thomas Seelig. *Fracture mechanics: with an introduction to micromechanics*. Springer Science & Business Media, 2011. 137

Ehrenwörtliche Erklärung

Ich erkläre hiermit ehrenwörtlich, dass ich die vorliegende Arbeit ohne unzulässige Hilfe Dritter und ohne Benutzung anderer als der angegebenen Hilfsmittel angefertigt habe. Die aus anderen Quellen direkt oder indirekt übernommenen Daten und Konzepte sind unter Angaben der Quellen gekennzeichnet.

Weitere Personen waren an der inhaltlich-materiellen Erstellung der vorliegenden Arbeit nicht beteiligt. Insbesondere habe ich hierfür nicht die entgeltliche Hilfe von Vermittlungs-bzw. Beratungsdiensten (Promotionsberater oder anderer Personen) in Anspruch genommen. Niemand hat von mir unmittelbar oder mittelbar geldwerte Leistungen für Arbeiten erhalten, die im Zusammenhang mit dem Inhalt der vorgelegten Dissertation stehen.

Die Arbeit wurde bisher weder im In-noch im Ausland in gleicher oder ähnlicher Form einer anderen Prüfungsbehörde vorgelegt.

Ich versichere ehrenwörtlich, dass ich nach bestem Wissen die reine Wahrheit gesagt und nichts verschwiegen habe.

Mohammed Abdulrazzak Msekh
Weimar, Jan. 2016

Mohammed Msekh

Curriculum Vitae

Address: Marine Str. 15, Weimar, Germany
Email: mohammed.msekh@uni-weimar.de

Education

2011-2016	Ph.D. Candidate in Chair of Computational Mechanics-Institute Structural Mechanics/Faculty of Civil Engineering, Bauhaus University-Weimar, Germany.
2000-2003	Masters of Civil Engineering/Structures, Al-Nahrain University, Baghdad, Iraq.
1997-2000	Bachelor of Civil Engineering, Al-Nahrain University, Baghdad, Iraq.

Academic Experience:

10/2011- 01/2016	Research Assistant, Bauhaus University-Weimar, Germany.
01/2006-06/2011	Faculty Member/ Lecturer, University of Babylon, Iraq.

Languages: Arabic (Mother tongue), English (Fluent), and Deutsch (Upper-Intermediate).

Academic Interests

Fracture Mechanics, Continuum Mechanics, Engineering Software, Programming, Structural Analysis and Design of Buildings and Bridges, Project Managements, Materials Modeling, Sensitivity Analysis, Simulation and Modeling, CAD.

Scholarships

DAAD (Deutscher Akademischer Austauschdienst) scholarship award as a doctoral candidate.

Links

ResearchGate: https://goo.gl/W4KKDU
Google Scholar: https://goo.gl/LTiSCL
ORCID: https://goo.gl/p3YDXc
Scopus: https://goo.gl/FBRDy7

Publications in Science Citation Index (SCI) Journals

1. Msekh, M.A., Sargado, J.M., Jamshidian, M., Areias, P.M. and Rabczuk, T., 2015. Abaqus implementation of phase-field model for brittle fracture. Computational Materials Science, 96, pp.472-484.
2. Msekh, M.A., Silani, M., Jamshidian, M., Areias, P., Zhuang, X., Zi, G., He, P. and Rabczuk, T., 2016. Predictions of J integral and tensile strength of clay/epoxy nanocomposites material using phase field model. Composites Part B: Engineering, 93, pp.97-114.
3. Areias, P., M. A. Msekh, and T. Rabczuk. "Damage and fracture algorithm using the screened Poisson equation and local remeshing." Engineering Fracture Mechanics 158 (2016): 116-143.

4. Areias, P., T. Rabczuk, and M. A. Msekh. "Phase-field analysis of finite-strain plates and shells including element subdivision." Computer Methods in Applied Mechanics and Engineering 312 (2016): 322-350.
5. Hamdia, K.M., Msekh, M.A., Silani, M., Vu-Bac, N., Zhuang, X., Nguyen-Thoi, T. and Rabczuk, T., 2015. Uncertainty quantification of the fracture properties of polymeric nanocomposites based on phase-field modeling. Composite Structures, 133, pp.1177-1190.
6. Liu, G., Li, Q., Msekh, M.A. and Zuo, Z., 2016. Abaqus implementation of monolithic and staggered schemes for quasi-static and dynamic fracture phase-field model. Computational Materials Science, 121, pp.35-47.